UNIVERSITY OF CALIFORNIA

SANTA CRUZ

SIMULATED GALAXY REMNANTS PRODUCED BY BINARY AND MULTIPLE MERGERS

A dissertation submitted in partial satisfaction of the
requirements for the degree of

DOCTOR OF PHILOSOPHY

in

ASTRONOMY & ASTROPHYSICS

by

Gregory S. Novak

September 2008

The Dissertation of Gregory S. Novak
is approved:

Professor Joel R. Primack, Chair

Professor Sandra M. Faber

Professor Piero Madau

Lisa C. Sloan
Vice Provost and
Dean of Graduate Studies

Table of Contents

List of Figures

List of Tables

Abstract

Simulated Galaxy Remnants Produced by Binary and Multiple Mergers

by

Gregory S. Novak

I compute simulated integral field kinematic data for the remnants produced in a large suite of hydrodynamic binary galaxy merger simulations in order to compare to the galaxies observed as part of the SAURON survey. I find that binary mergers are plausibly the formation mechanism for the ∼80% of SAURON galaxies with fast rotation velocities, in agreement with previous studies. However, the simulations of gas-rich binary mergers produce virtually no slow rotators observed to make up ∼20% of the SAURON galaxies.

In order to identify the origin of these slow rotators, I perform a new set of galaxy merger simulations involving merger histories more complex than single binary mergers of disk galaxies. I set up simple, idealized simulations with four or eight progenitor galaxies in order to build intuition about how a simulated galaxy's merger history affects its kinematic structure. I find that if the merger tree consists solely of roughly equal mass binary mergers, then the remnant is a fast rotator similar to that produced by a single binary merger of disk galaxies. However, if the progenitors merge with the central galaxy one after another in a sequence of mergers with decreasing mass ratios, then the remnant does not rotate. This is a plausible formation scenario for the observed SAURON slowly-rotating galaxies.

To see how frequently this happens with realistic initial conditions, I extract halos from a large-scale cosmological simulation and re-simulate the region with higher resolution. These simulations include intergalactic gas that is able to replenish the galaxies' gas supply as the simulation runs. In all cases, I get rapidly rotating remnant galaxies in spite of having

several halos with diverse merger histories.

For my teachers, academic and otherwise.

Acknowledgments

Thanks to Sandy and Joel for more second chances than anyone can reasonably expect. Thanks to my family for many years of support and for giving me the space to figure things out for myself. Thanks to Jen for seeing something in me and sticking with me all these years.

Thanks to colleagues for useful discussions over the years: Andreas Burkert, Thorsten Naab, Adam Bolton, Avishai Dekel, Patrik Jonsson, T.J. Cox, Laura Parker, Mike J. Hudson. Thanks to the whole gang of astrograds for making Santa Cruz such a nice place to live.

This research was supported by the Computational Science Graduate Fellowship and NASA. I made extensive use of the NASA's Columbia and Pleiades computers as well as UCSC's Pleiades cluster, funded by the NSF. This work relies on simulations performed at NERSC and using the UpsAnd cluster at UCSC.

I also made extensive use of Free Software, including Gadget[1], Emacs[2], Python[3], Numerical Python, Scientific Python, and the interactive shell IPython[4]. Many plots in this document were produced with PyX[5] or Splash[6]. This document itself was prepared using the LaTeX document processing system.

[1] http://www.mpa-garching.mpg.de/galform/gadget/index.shtml
[2] http://www.gnu.org/software/emacs/
[3] http://www.python.org
[4] These three all available from http://www.scipy.org/
[5] http://pyx.sourceforge.net/
[6] http://www.astro.ex.ac.uk/people/dprice/splash

Chapter 1

Introduction

Three quarters of the stellar mass in the universe is in spheroids (Fukugita & Peebles, 2004), yet there are many open questions about how these systems came to be as we see them today. Since the pioneering papers by Toomre & Toomre (1972; 1977), the "Major Merger Hypothesis" has been the dominant explanation of the formation of these spheroids. In the intervening years, the hypothesis has remained just that: a plausible hypothesis where one can verify that the results of simulated galaxy mergers are broadly consistent with the properties of observed galaxies.

The Major Merger Hypothesis has remained "plausible" rather than "proven" or "disproven" because it is difficult to test the idea quantitatively. For many years computers lacked sufficient computational power to address the question in detail. Even today, there are important physical processes that are only included through sub-resolution recipes that purport to model the underlying physics—in particular the roles of the cosmological environment, feedback from active galactic nuclei (AGN), and feedback from star formation. Nevertheless, the state of the art with respect to simulations has progressed to the point where it is useful

to attempt detailed quantitative comparisons between actual galaxies and simulated galaxy merger remnants.

Although it is widely believed that many elliptical galaxies (Es) and most classical galactic bulges formed via mergers, many aspects remain unclear. When did the mergers occur? Can the structure of the spheroids be explained by simple binary mergers of spiral galaxies, or are more complex assembly histories necessary? What was the nature of the progenitors, and how much gas dissipation was involved? How were the super-massive black holes (SMBHs) associated with galactic spheroids affected by the merger? When did the SMBHs grow by gas accretion producing bright AGN, and how did they in turn affect the evolution of the remnant galaxies? How did all these processes result in the observed color bimodality of galaxies, and in the Fundamental Plane defining the observed correlations between structural properties of Es? How did they produce the entire evolving population and spatial distribution of early-type galaxies?

The overall goal of all of this is to turn the "Major Merger Hypothesis" into the quantitative "Major Merger Theory." While galaxy merger simulations certainly produce plausible galaxy remnants, it remains unknown whether or not they produce accurate, realistic predictions in fine quantitative detail.

The plausibility of the Major Merger Hypothesis based as it is on simulations with incomplete implementations of the relevant physics indicates that the gross properties of stellar spheroids are well explained by very simple physics. Toomre & Toomre got useful results using only restricted-three-body simulations. However, observations of stellar spheroids have grown ever more detailed and there is discriminatory power in those fine details. The fact that the Major Merger Hypothesis has remained plausible but not proven *also* indicates that tests it has passed have not been very demanding.

1.1 History

The Atlas of Peculiar Galaxies (Arp, 1966) highlighted the diversity of stellar systems in the universe. The role of mergers in generating this diversity was pointed out in the papers by Toomre & Toomre (1972; 1977). Since then the "Major Merger Hypothesis" that elliptical galaxies primarily form by major mergers of spiral galaxies has remained plausible and has become the dominant model of how these galaxies formed.

Toomre & Toomre (1972) emphasized the importance of running *simple, computationally cheap* simulations as a way of gaining insight in into the vast space of input parameters to a galaxy merger simulation. They restricted 3-body simulations and showed that their (admittedly vastly oversimplified) simulations nevertheless reproduced the gross features of both interacting galaxies (tidal tails) and early type galaxies (spheroidal merger remnants).

Hernquist et al. (1993) argued on the basis of phase space density that gas physics and dissipation must be essential to elliptical galaxy formation, and the need for hydrodynamics effectively put a floor on the computational cost associated with a minimally realistic simulation. In the mid 90's it become possible to run hydrodynamic simulations with reasonable parameterizations of sub-resolution physics (Mihos & Hernquist, 1996; Weil & Hernquist, 1996; Springel, 2000)

Naab & Burkert (2003) ran a large set of gas-free (and thus computationally relatively cheap) simulations and extensively analysed the diskiness/boxiness of the isophotes of the resulting galaxies. Cox (2004) ran ~ 100 hydrodynamic simulations of gas-rich spiral galaxy mergers, focusing on the star formation history of galaxies during the interactions. Dekel et al. (2005) used those simulations to show that simulated galaxy mergers are plausibly similar to early type galaxies using a variety of kinematic observables.

The most interesting recent results in our understanding of the role that mergers play

in galaxy formation concern the role of cosmological environment and the effects of AGN on galaxy merger remnants. The background on these issues is discussed below as it relates to the proposed research.

Another important source of uncertainty in early galaxy merger simulations was that there was little guidance about the cosmologically likely orbits of merging galaxies, dark halo concentrations, and time between mergers. The past ten years have seen revolutionary advances in the precision measurement of cosmological parameters. At the same time, cosmological simulations of large-scale structure formation have reached a point where it is possible to extract realistic probability distributions for orbit geometries (Khochfar & Burkert, 2006).

The past decade has seen a confluence of observational and theoretical information that makes this problem ripe for revisiting. 1) The computational cost of a single hydrodynamic simulation of sufficient resolution to determine many detailed observables has become low enough that it can be thought of as cheap. 2) The cosmological parameters are now known to high precision and simulations of structure formation can give needed information about the cosmological context in which galaxies form. This removes a significant source of uncertainty from galaxy-scale simulations.

Detailed testing of hydrodynamic simulations using observational data is vital because of the many modeling uncertainties, such as the treatment of include supernova and AGN feedback. It is often possible to show that astrophysical simulations satisfy gross constraints, for example that the galaxies resulting from merger simulations fall on the Fundamental Plane (Robertson et al., 2006; Boylan-Kolchin et al., 2006) Moreover, we have shown in detail (Dekel et al., 2005) that the remnants of our hydrodynamic binary major mergers accurately match the observations of planetary nebular velocity dispersions around typical nearby elliptical galaxies. However, ever-richer data sets provide ever-more-detailed quantitative comparisons with the

simulated galaxy merger remnants.

There are two general goals when analyzing the output of numerical simulations. One goal is purely theoretical: What are the characteristics of the galaxy produced by a given initial state? What were the important features of that initial state that led to each property of the final state? A single simulation does not teach the simulator anything since he does not yet know which aspects of the simulation contributed to the success and which were extraneous. Therefore it is important to develop an understanding of which simulation input parameters determine which properties of the final galaxy.

The second goal connects with the actual universe: Does the final state of this simulation correspond to galaxies that we see in the universe? The first step in comparison with observed galaxies is to focus on particular observables, one at a time, in order to see if simulated and observed galaxies occupy the same region of the observable space with similar distributions.

In this thesis I will characterize the structure and kinematics of a large set of hydrodynamics binary merger remnants. I will also take the first steps toward an understanding of how a galaxy's mass build-up history affects its final structure, and how a galaxy's cosmological environment influences its properties.

Chapter 2

Properties of Simulated Remnants

The starting point for this study is the set of hydrodynamic binary major merger simulations done by Cox as part of his Ph.D. thesis (Cox, 2004; Cox et al., 2006b). In this chapter I briefly describe these simulations, the code used to run them, and the major assumptions that were made in order to model star formation and gas heating due to supernovae.

The goal of this chapter is to characterize the shapes and density profiles of the simulated merger remnants. This is interesting in its own right in order to understand how the progenitor galaxies, merger orbits, and numerical code each influence the properties of the merger remnant. It is also necessary to have a good understanding of the properties of binary merger remnants in order to make sense of the simulations incorporating multiple galaxy mergers to be discussed in Chapter 4.

I will show that these merger remnants have density profiles that are very close to isothermal profiles with a logarithmic density slope -2. There is little if any feature in the total

density profile at the point where the remnant switches from being dominated by baryonic matter to being dominated by dark matter.

There is a robust and easily understood correlation between the shapes of stellar merger remnants and their dark halos. This correlation has interesting implications for the interpretation of observations of galaxy-galaxy gravitational lensing. The procedure in galaxy-galaxy lensing is to build up an observational signal by optically aligning and stacking many foreground galaxies and then to look for systematic effects in the shapes of the background galaxies in order to measure dark halo masses and shapes. I calculate the effect of the intrinsic correlation between the shapes of simulated stellar remnants and their dark halos on galaxy-galaxy lensing surveys.

2.1 Previous Work

Detailed testing of hydrodynamic simulations using observational data is vital because of the many modeling uncertainties, such as the treatment of include supernova and AGN feedback. It is often possible to show that astrophysical simulations satisfy gross constraints, for example that the galaxies resulting from merger simulations fall on the Fundamental Plane (Robertson et al., 2006; Boylan-Kolchin et al., 2006). Moreover, Dekel et al. (2005) showed in detail that the remnants of these hydrodynamic binary major mergers accurately match the observations of planetary nebular velocity dispersions around typical nearby elliptical galaxies, contrary to the claims (Romanowsky et al., 2003) that these galaxies do not have massive dark matter halos.

Naab & Burkert (2001, 2003) performed a large suite of dissipationless disk galaxy merger simulations with a variety of orbits and mass ratios from 1:1 to 4:1. They found that equal mass mergers produce remnants that can show boxy or disky isophotes (Bender et al.,

1988) depending on viewing angle, but that higher mass ratio mergers produce disky isophotes.

Naab et al. (2006b) used merger simulations paired with a semi-analytic model of galaxy formation (e.g. Cole et al., 1994, 2000; Somerville & Primack, 1999) to argue that nearly dry mergers between two early-type progenitors are necessary to produce massive, slowly rotating elliptical galaxies with boxy isophotes.

Naab et al. (2006a) found that mergers with gas fractions 10% have observable properties that are significantly different from gas-free merger remnants. In particular, the presence of gas favors tube orbits at the expense of box orbits in the remnants, leading to galaxies with disky isophotes.

Cox et al. (2006a) extensively analysed the kinematic structure of dissipationless and dissipational simulated galaxy merger remnants, including where remnants fall in the v/σ vs. ellipticity diagram, the frequency of kinematic misalignments, and the three-dimensional shapes of remnants. Regarding shapes, they found that dissipationless remnants had triaxial shapes while increasing gas fractions resulted in more oblate remnants.

Naab & Trujillo (2006) and Hopkins et al. (2008b) analysed the surface brightness profiles of simulated merger remnants. Naab & Trujillo (2006) used dissipationless simulations where the progenitors had or did not have bulges. They found that mass ratios of 1:1 and 2:1 lead to Sérsic parameters between 3 and 4, characteristic of elliptical galaxies. However, higher mass ratios (3:1, 4:1, and 6:1) have disk-like components with exponential surface-brightness profiles. Hopkins et al. (2008b) and found that their remnants had centrally concentrated populations populations of young stars produced in a starburst during the merger. A two-component surface-brightness formula consisting of the sum of an inner exponential and an outer Sérsic profile allowed them to separate the two populations in the photometric profile of the merger remnant. They went on to apply their fitting formula to merger remnants in

the nearby universe and claim that i) their formula results in better fits than a single Sérsic function, and ii) that the light in the inner exponential profile accurately recovers the amount of gas converted to stars in the last major merger experienced by a given galaxy.

González-García & Balcells (2005) looked at equal- and unequal-mass dissipationless mergers and found that the presence or absence of bulges had a large effect of the structure of remnants. Bulges in the progenitors led to remnants with higher rotation velocities and less triaxiality. Their progenitors with bulges had stellar bulge mass fractions of 1:3.

Bournaud et al. (2005) used a particle-mesh code with hydrodynamics implemented via a sticky-particle scheme to study merger remnants with mass ratios up to 10:1. They looked at surface brightness profiles, isophotal shapes, and rotation velocities, concluding that mergers with mass ratios from 1:1 to 3:1 produce elliptical remnants while mass ratios above 4:1 produce hybrid objects that have some of the properties of elliptical galaxies and some of the properties of spirals.

2.2 Numerical Simulations

I analyse the binary merger simulations performed by Cox in his Ph.D. thesis and in subsequent years, specifically minor merger simulations described in (Cox et al., 2008). In chapter 4 I analyze simulations of multiple galaxy mergers with idealized and cosmologically motivated initial conditions that I performed. In order to gain some understanding of what is going on in the binary merger case and, by comparison, the multiple merger case, for now I restrict my attention to the binary mergers.

Simulations were performed using the entropy-conserving version of the SPH code GADGET (Springel et al., 2001; Springel & Hernquist, 2002; Springel, 2005) with a gravitational smoothing length of 100 pc. The progenitor galaxies have baryonic masses from 1.6×10^9

	Sbc	*G*3	*G*2	*G*1	*G*0
$M_{\rm dark}$	81.2	116	51.0	20	5.10
$M_{\rm disk}$	3.92	4.11	1.35	0.470	0.0980
$M_{\rm bulge}$	1.00	0.889	0.150	0.0300	0.00200
$M_{\rm gas}$	5.36	1.22	0.480	0.200	0.0600
$f_{\rm baryon}$	12.7	5.46	3.88	3.5	3.14
$f_{\rm gas}$	52.2	19.6	24.2	28.6	37.5
$f_{\rm bulge}$	20.3	17.8	10.0	6.00	2.00
$N_{\rm dark}$	100	120	80	50	30
$N_{\rm disk}$	30	50	30	20	10
$N_{\rm bulge}$	10	20	10	5	1
$N_{\rm gas}$	30	50	30	20	10
$R_{\rm vir}$	241	272	207	151	96.0
$R_{\rm disk}$	5.5	2.85	1.91	1.48	1.12
$R_{\rm bulge}$	0.45	0.62	0.43	0.33	0.25
$R_{\rm gas}$	16.5	8.55	5.73	4.44	3.36
C	11	6	9	12	14

Table 2.1: Basic properties of merger simulation progenitors. $M_{\rm dark}$, $M_{\rm disk}$, $M_{\rm bulge}$ and $M_{\rm gas}$ are the masses of the dark matter, stellar disk, stellar bulge, and gas disk respectively, in units of $10^{10} M_{\odot}$. The values $f_{\rm baryon}$, $f_{\rm gas}$, and $f_{\rm bulge}$ are the baryonic-to-dark, gas-to-baryonic, and bulge-to-stellar mass ratios in percent, respectively. The values $N_{\rm dark}$, $N_{\rm disk}$, $N_{\rm bulge}$, $N_{\rm gas}$ are the number of dark matter, stellar disk, stellar bulge, and gas particles respectively, in thousands. The values $R_{\rm vir}$, $R_{\rm disk}$, $R_{\rm bulge}$, and $R_{\rm gas}$ are the virial radius, the stellar disk exponential scale length, the stellar bulge exponential scale length, and gas disk exponential scale length in kiloparsecs, respectively.

to $2 \times 10^{11} M_{\odot}$, gas fractions between 20% and 70%, consist of ∼100,000 particles, and use a parameterization of star formation feedback from supernovae tuned to match the empirical Schmidt law (Kennicutt, 1998).

There are five progenitor galaxies considered here: *G*3, *G*2, *G*1, *G*0 and *Sbc*. The *G* series progenitors are designed to resemble low-redshift galaxies as observed by the Sloan Digital Sky Survey (SDSS, York et al., 2000). These progenitors follow the trends with mass of gas fraction, bulge-to-disk ratio, disk scale lengths, and so forth seen in the SDSS. The *Sbc* progenitor is a massive, gas-rich, spiral galaxy designed to resemble galaxies at higher redshift than the Sloan survey. Table 2.1 summarizes the properties of the progenitors.

2.2.1 Star Formation and Supernovae

The simulations include a sub-resolution scheme to model star formation and supernova energy injection into the interstellar medium. Motivated by the empirical Schmidt law Schmidt (1959) relating star formation rate to three-dimensional gas density, the star formation rate is:

$$\frac{d\rho_*}{dt} = \begin{cases} c_* \rho_{\rm gas}/t_{\rm dyn} & : \quad \rho_{\rm gas} \geq \rho_{\rm th} \\ 0 & : \quad \rho_{\rm gas} < \rho_{\rm th} \end{cases} \tag{2.1}$$

where rho_* is the density of stars, $\rho_{\rm gas}$ is the density of gas, and $t_{\rm dyn} = (4\pi G \rho_{\rm gas})^{-1/2}$ is the gas dynamical time, $\rho_{\rm th}$ is the minimum density for gas to form stars, and c_* is a constant. The threshold density used here is 0.0171 $M_\odot\,{\rm pc}^{-3}$, motivated by Kennicutt's finding that star formation rates drop significantly for gas surface densities of less than 10 $M_\odot\,{\rm pc}^{-3}$. The value of c_* is chosen so that the galaxies lie on the Tully-Fisher relation.

Every star above 8 $M_\odot$ is assumed to instantaneously explode as a supernova, injecting 10^{51} ergs of energy into an ad-hoc reservoir separate from the thermal energy of the gas particle. One may think of this separate energy reservoir as the energy in sub-resolution turbulent motions of the gas. The turbulent energy contributes to the pressure of the gas particle, but does not, for example, affect the temperature (and therefore cooling) of the gas particle. This turbulent energy is then slowly transferred back to the thermal energy of the gas particle.

$$\frac{dq}{dt} = \frac{\epsilon_{\rm SN}}{\rho_{\rm gas}} \left(\frac{d\rho_*}{dt} \right) - \frac{q}{\tau_{\rm fb}} \left(\frac{\rho_{\rm gas}}{\rho_{\rm th}} \right)^{(1-n)/2} \tag{2.2}$$

where q, is the specific energy in the turbulent reservoir, $\epsilon_{\rm SN}$ is the energy injected by supernovae per solar mass of stars formed, $\tau_{\rm fb}$ is the timescale over which turbulent energy is thermalized, and n is a constant that sets the polytropic index of the effective equation of state

of star forming gas. The first term represents energy injection into the turbulent reservoir due to star formation, and the second represents thermalization of the turbulent energy. When the gas density is below ρth, the value of n is fixed to 2 in order to avoid long thermalization timescales for non-star-forming gas.

Thus the uncertain parameters in the supernova feedback recipe are n and $\tau_{\rm fb}$. Three possibilities for each value are considered: $n = 0$, 1, or 2 and $\tau_{\rm fb}$= 0.827, 8.27, and 82.7 Myr. These values of $\tau_{\rm fb}$ are named *low*, *med*, *high*, respectively. I will not always explore all nine of the resulting possibilities, because some of the parameter values are very expensive to simulate. Lower values of $\tau_{\rm fb}$ and n result in higher computational costs. The most common value used in the simulations considered here is $n2med$; those are the parameters used unless otherwise indicated.

A scheme like this is necessary because star formation takes place in cold, dense gas, where the energy loss from radiative cooling is high. Early simulations of galaxy mergers with star formation found that purely thermal feedback had little effect in stabilizing the gas against runaway star formation because the energy injected into the the temperature of the gas was radiated away very quickly (Navarro & White, 1993; Springel, 2000)

There are two sets of simulations of binary mergers considered here. The *Sbc* series consists of equal mass mergers between two identical *Sbc* progenitors on a variety of orbits. the *G* series focuses on the effect of different galaxy mass ratios. Only a few orbits are considered. Table 2.2 gives a list of the merger orbits considered and their sometimes convoluted naming scheme. I will usually refer to orbits by their characteristics rather than their simulation names so that Table 2.2 will not often be necessary.

Given the large number of simulations under consideration, it is sometimes useful to focus on a single simulation in order to avoid being overwhelmed by a large number of plots.

Name	θ_1	ϕ_1	θ_2	ϕ_2	$R_{\rm peri}$	e	Description
*Sbc*201	0	0	30	60	11.0	1.0	P-P
*Sbc*202	180	0	30	60	11.0	1.0	R-P
*Sbc*203	180	0	210	60	11.0	1.0	R-R
*Sbc*206	90	0	30	60	11.0	1.0	T-P
*Sbc*207	270	0	30	60	11.0	1.0	T-P
*Sbc*217	90	0	90	60	11.0	1.0	T-T
*Sbc*204	0	0	30	60	5.5	1.0	P-P, small impact parameter
*Sbc*208	180	0	30	60	5.5	1.0	R-P, small impact parameter
*Sbc*209	180	0	210	60	5.5	1.0	R-R, small impact parameter
*Sbc*205	0	0	30	60	44	1.0	P-P, large impact parameter
*Sbc*211	180	0	210	60	44.0	1.0	R-R, large impact parameter
*Sbc*212	0	0	30	60	11.0	0.9	P-P, bound orbit
*Sbc*218	180	0	210	60	11.0	0.9	R-R, bound orbit
*Sbc*213	0	0	30	60	25.0	0.8	P-P, lower energy orbit, large impact parameter
*Sbc*214	0	0	30	60	44.0	0.8	P-P, lower energy orbit, even larger impact parameter
*Sbc*216	0	0	30	60	100.0	0.8	P-P, lower energy orbit, largest impact parameter
*Sbc*210	150	0	150	180	2.918	1.0	R-R, zero angular momentum
*Sbc*219	150	0	150	180	2.89	0.97	R-R, zero angular momentum

Table 2.2: Orbits for in the *Sbc* series of galaxy simulation. From Cox (2004), reproduced here for convenience. The two progenitor disk galaxies are initially in the $x-y$ plane and are rotated about the x axis by θ and then about the z axis by ϕ. Abbreviations in the Description column refer to the spin of each galaxy relative to the orbit, and are P for prograde, R for retrograde, and T for tilted such that the disk is perpendicular to the orbit plane.

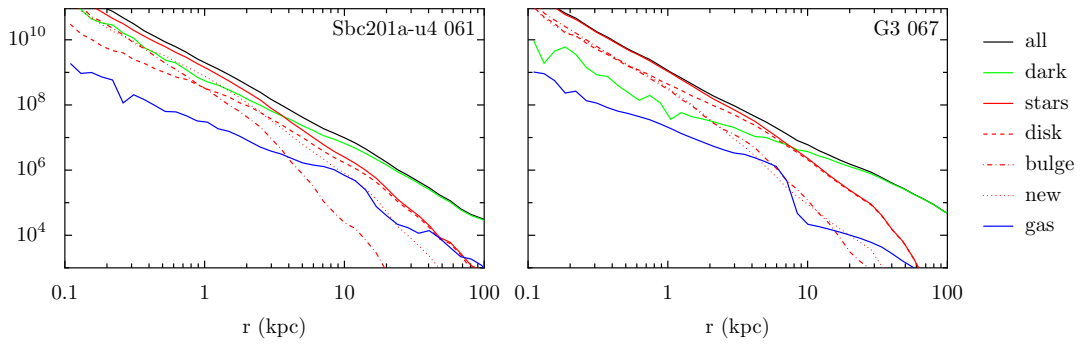

Figure 2.1: Density profiles of the two fiducial simulations with each type of matter indicated. The 3D effective radii of the remnants are 5.25 and 5.05 kpcrespectively. These profiles are typical of those for the binary galaxy merger remnants. Chapter 5 will explore the density profiles of all of the remnants in greater detail.

The *Sbc*201a-u4 and *G*3*G*3b-u1 simulations are therefore christened the "fiducial" simulations.

Cox (2004) and Cox et al. (2006b) contain more detailed information about the code, simulations, star formation, and feedback schemes.

2.3 Results

In this section I seek to briefly characterize the density profiles, shapes, and velocity profiles of the simulated binary merger remnants.

2.3.1 Density Profiles

Figure 2.1 shows 3D density profiles for two of the binary merger remnants. A few features to note are that the centers are dominated by stars that started out in the bulge or stars that were formed during the simulation, that the outer parts of the stellar remnants are dominated by stars that started out in the stellar disks, and that the dark matter density becomes larger than the stellar density at 0.8 to 1.6 effective radii for these two simulations.

Furthermore, the total mass density profile is extremely close to a power law, with

virtually no feature where the density transitions from being dominated by baryons to being dominated by dark matter. This is the old disk-halo conspiracy (Burstein & Rubin, 1985; Bahcall & Casertano, 1985; Kent, 1987) arising naturally in simulations. A precise understanding of the origin of these nearly-perfect power laws in spite of the different physics that governs the evolution of the stellar, dark, and gaseous components of the simulation is an interesting question that unfortunately remains unaddressed in this work. Violent relaxation (Lynden-Bell, 1967; Shu, 1978) would seem to provide part of the understanding since it describes how energy is transferred between individual stars through global potential fluctuations during violent collapse in spite of the lack of two-body collisions in stellar systems. However, Lynden-Bell's analysis considered dissipationless collapse of a single type of matter (that is, no dark matter or gas), and most simulations focusing on violent relaxation (e.g. van Albada, 1982) have done the same. The dynamics that robustly lead to this property of simulated remnants remains unclear.

Given the the total mass density profile is strikingly close to a power law, and that the dark matter and stellar density profiles individually are not far from power laws, simple power law fits to the density profiles are a compact way to summarize the density profiles of the remnants.

Figure 2.2 shows power-law fits to the *central* densities of all of the G and Sbc series mergers. The fit runs from 500 pc to the 3D effective radius of the baryonic component. Thus the fit to all of the different matter components is over the same radial range. This radial range is chosen to provide a close comparison to the gravitational lensing data discussed in Chapter 6, which typically extends to half of an effective radius. The zero-point of all of the fits is the density at half of the effective radius.

Focusing on the central density does not do justice to the full density profile of the

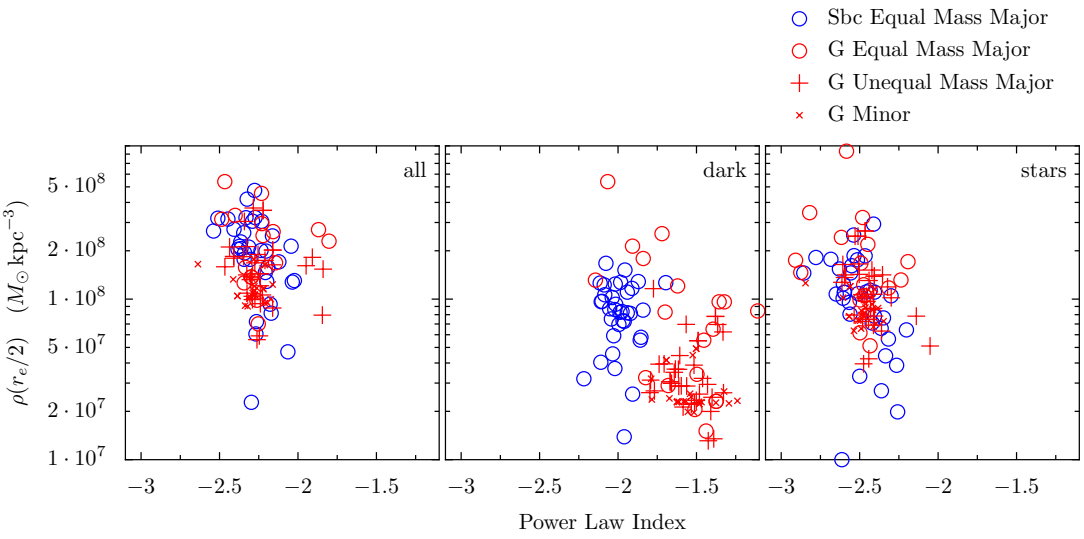

Figure 2.2: Central slopes and densities of matter by type. From the left: all matter, dark matter, and stellar matter. All remnants have quite similar density structure in spite of the large number of orbits, progenitors, and gas fractions. The power-law index of the stellar density profiles are slightly steeper than isothermal profiles (for which the power-law index is -2). The densities at half of the effective radius (the zero-point of the fits) very by about an order of magnitude. This figure introduces a convention that will be used throughout this thesis: In scatter plots, the *Sbc* major mergers are represented by blue circles, *G* series equal mass major mergers by red circles, *G* series unequal mass major mergers by red crosses, and *G* series minor mergers by small red Xs. The legend will not be repeated in every figure.

dark matter, which extends to much larger radius. However, the dynamical time falls rapidly with radius and the dark halos have not relaxed by the time these simulations are stopped. Therefore the density profile of the dark matter at large radius has more to do with the initial conditions of the model galaxies than the dynamics at play during the simulation. Most observational information about galaxies comes from the central parts, so I do not further consider the large-radius behavior of the remnant density profiles.

The density structure of the total mass density of all of the remnants is quite remarkably similar, and in agreement with the assertion in Bolton et al. (2008) that singular isothermal ellipsoids are the best mass models for elliptical galaxies. The most obvious difference between the *G* and *Sbc* series is in the dark matter density profiles. The *Sbc* remnants

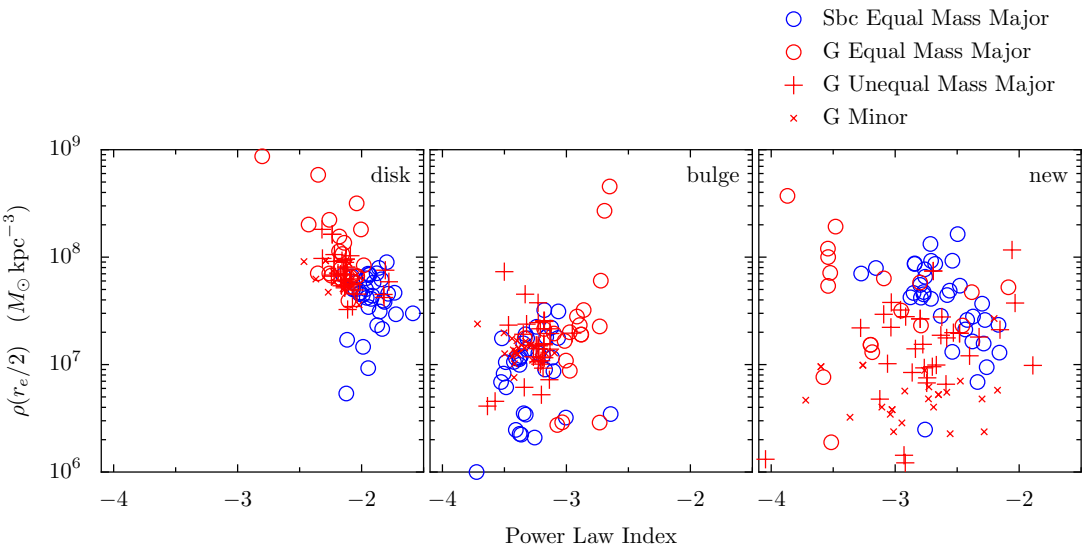

Figure 2.3: Central slopes and densities of stars by type. From the left, stars that were originally in the disk, originally in the bugle, and stars that were created during the simulation. Bulge stars and new stars have quite steep density profiles while disk stars are close to isothermal. For stars created in the simulation, there is wide variation in both the slope and the density at $r_e/2$.

have steeper, denser dark matter profiles than most of the *G* series simulations. This is because the *Sbc* progenitor has a high halo concentration and adiabatic contraction of the halo due to baryonic infall was taken into account. By contract, the *G* series progenitors did *not* use adiabatically contracted halos.

Figure 2.3 shows the density structure split by type of star. Bulge stars have a steep density profile because they start out in a small, tightly-bound spherical structure and are not much disturbed by the merger. New stars have steep density profiles because their formation is a strong function of gas density. Finally, disk stars end up with a nearly isothermal distribution, with the *G*-series mergers having systematically slightly steeper density profiles.

Figure 2.4 shows a histogram of the the dark matter fractions (either projected or 3D) for all of the merger remnants. There are significant differences between major and minor mergers as well as between *G* and *Sbc* series mergers. *G* series minor and unequal-mass major

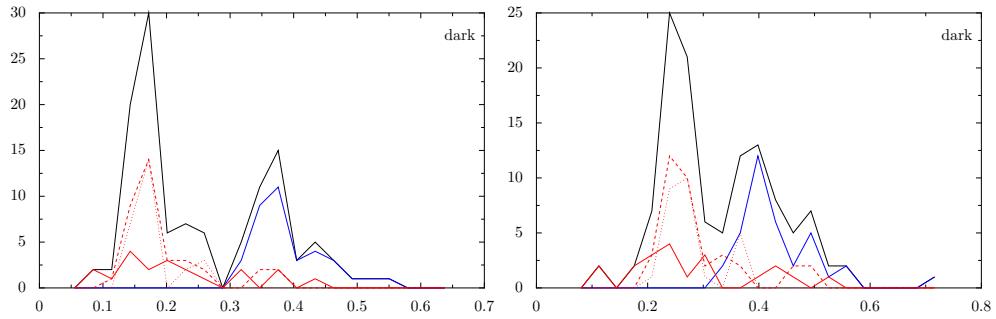

Figure 2.4: Histograms of the dark matter fractions within one effective radius. On the left, within one 3D effective radius, and on the right, projected mass fraction within one projected effective radius. There is a distinct difference between the G and Sbc series of mergers, with the Sbc series having larger central dark matter fractions than the G series minor and unequal-mass-major mergers.

mergers show lower dark matter fractions than Sbc equal mass major mergers. The G series equal mass major mergers span a wide range of DM fractions.

Remnants thus show some diversity in their mass profiles, but one remarkable regularity is the slope of the total mass profile near one stellar effective radius. Figure 2.2 shows that in spite of very different initial galaxy models, orbits, and feedback recipes, the density structure remains very consistent.

2.3.2 Shapes of Stellar Remnants and Dark Halos

I find that stellar remnants are mostly oblate while dark matter halos are mostly prolate or triaxial. The stellar minor axis and the halo major axis are almost always nearly perpendicular. This can be understood by considering the influence of angular momentum and dissipation during the merger. If binary mergers of spiral galaxies are responsible for the formation of elliptical galaxies or some subpopulation thereof, these galaxies can be expected to be oblate and inhabit their halos with the predicted shapes and orientations. These predictions are relevant to observational studies of weak gravitational lensing, where one must stack many optically aligned galaxies in order to determine the shape of the resulting stacked mass

distribution. The simple relationship between the dark and luminous matter presented here can be used to guide the stacking of galaxies to minimize the information lost.

The shapes and mass profiles of dark matter halos from cosmological N-body simulations have long been studied (Dubinski & Carlberg, 1991; Navarro et al., 1996; Allgood et al., 2006, and references therein). Cosmological simulations still lack sufficient resolution to track the shape and orientation of galaxies within their dark matter halos. There is no reason to believe that the shapes of galaxies and dark matter halos should be similar. It has only recently become feasible to perform large suites of high-resolution binary galaxy merger simulations (Naab & Burkert, 2003; Cox, 2004; Cox et al., 2006b; Robertson et al., 2006), and here I use such simulations in order to study the shapes of the resulting galaxies and their host halos statistically.

Observationally, the intrinsic shapes of elliptical galaxies have remained elusive. It has long been known that there seem to be at least two classes of elliptical galaxies: massive, anisotropic galaxies and lower mass, oblate rotators (Bender et al., 1988, 1992). However, allowing the possibility of triaxiality leads to degeneracies in deprojection (Franx et al., 1991). Alam & Ryden (2002) and Vincent & Ryden (2005) have used Sloan Digital Sky Survey (SDSS) data to conclude that not all elliptical galaxies can be oblate.

The relative orientations of galaxies and their dark halos is relevant to studies of weak gravitational lensing. Observers stack many images of galaxies in order to use the average deformation of the shapes of background galaxies to infer properties of the foreground mass distribution. It is important to stack galaxies coherently in order to build up a detectable signal. The model presented here represents a physically well-motivated *Ansatz* to help interpret the results of weak lensing observations. Section 2.3.2.1 gives a description of the galaxy merger simulations and our method of determining the shape of merger remnants, §2.3.2.1

gives our results, and §2.4 summarizes our conclusions.

2.3.2.1 Methods

In order to reduce the dependence on the progenitor galaxy model, here I only consider major mergers with mass ratios of 1:1 (*G*3-*G*3, *G*2-*G*2, *G*1-*G*1, and *G*0-*G*0) and roughly 3:1 (*G*3-*G*2, *G*2-*G*1, and *G*1-*G*0). I also analyze the *Sbc* series of merger simulations.

To calculate the shape of a merger remnant, I iteratively diagonalize a moment of inertia tensor using an ellipsoidal window (Dubinski & Carlberg, 1991):

$$M_{ij} = \Sigma_k m_k r_{i,k} r_{j,k} \tag{2.3}$$

where $r_{i,k}$ is the position vector, i, j refer to coordinates, and k refers to particle number. The triaxial radius is given by Franx et al. (1991):

$$\zeta = \sqrt{x^2/a^2 + y^2/b^2 + z^2/c^2} \tag{2.4}$$

where a, b, and c are the major, intermediate, and minor axis lengths, respectively. The sum over k includes all particles for which r lies within the ellipsoid $\zeta = 1$. The iteration is started with a spherical window ($a = b = c =$ baryonic half-mass radius), and after each iteration a,b, and c are scaled so that half of the baryonic mass is enclosed. The result does not appreciably change if equation (2.3) is modified to include ζ^2 in the denominator. Using a spherical window rather than an ellipsoidal one results in systematically larger axial ratios but does not change the main result.

When shapes are calculated in this way, sometimes equation 2.3 is modified to include ζ^2 in the denominator. This has the effect of giving equal weight to a given mass independent of its position within the remnant. However, it has the undesirable side-effect that it mixes information at all radii with equal weight. That is, if a remnant has axis ratios that change

with radius, then the calculated shape at large radius will be significantly affected by the mass at small radius. Our goal in calculating these shapes is to cheaply find an isodensity surface. Therefore I would like the shape calculated at each radius to include *mostly* information *near* the radius under consideration.

Three-dimensional shapes of galaxies can be quantified with the triaxiality parameter $T = (a^2 - b^2)/(a^2 - c^2)$. I call an object oblate, triaxial, or prolate if $T < 0.25$, $0.25 < T < 0.75$, or $0.75 < T$, respectively. Shapes of galaxies can also be quantified by ellipticity $\epsilon = 1 - b/a$. Ellipticities are most often used to describe two-dimensional shapes; I occasionally refer to the three-dimensional ellipticity of perfectly prolate or oblate ($T = 0$ or 1) objects since there is no ambiguity about the use of the equation.

Figure 2.5 illustrates that most stellar remnants are oblate, while the dark matter halos in which they reside are mostly prolate or triaxial. Figure 2.6 shows that the short axis of the stellar system and the long axis of the dark matter halo are almost always nearly perpendicular. This can be understood simply in terms of angular momentum and dissipation, as shown in Figure 2.7.

This model helps interpret the findings from studies of weak gravitational lensing. Hoekstra et al. (2004) find that the ellipticity of dark halos is $0.77^{+0.18}_{-0.21}$ times the ellipticity of the light (i.e., halos are somewhat less flattened than galaxies), assuming that the two are aligned. According to our result, elliptical galaxies would either show an elliptical halo (if the long axis of the prolate halo is in the plane of the sky) or a circular halo (if the long axis of the halo is pointed toward the observer). Thus, the flattening of the dark matter would follow that of the luminous matter, in agreement with these observations.

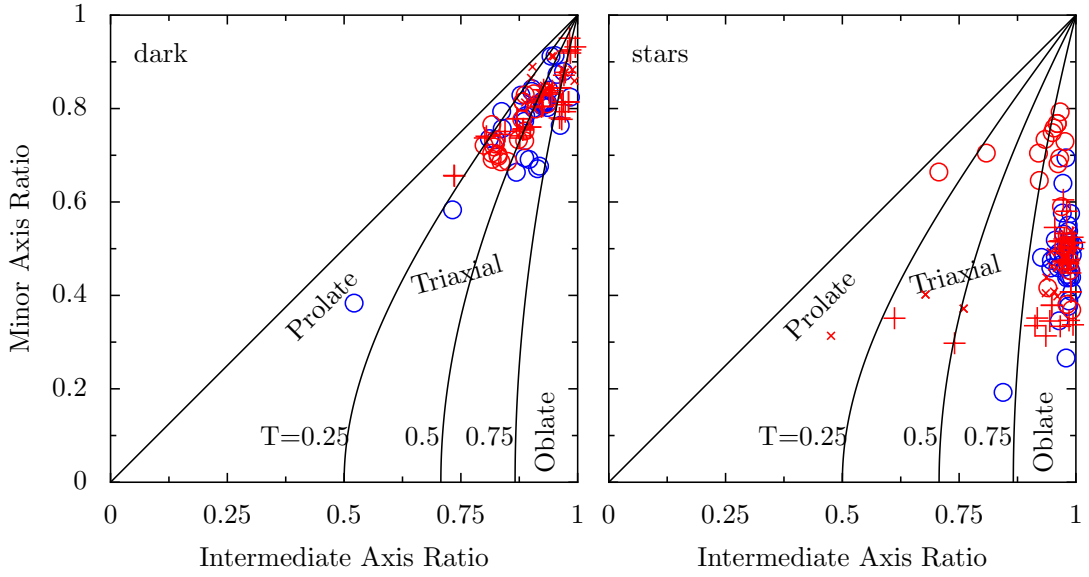

Figure 2.5: Shapes of the luminous and dark components of simulated merger remnants. *Left*: the intermediate-to-major axis ratio vs. the minor-to-major axis ratio for stars. *Right*: Same as left panel, but for dark matter halos. Objects near the diagonal line are prolate spheroids, objects near $b/a = 1$ are oblate spheroids, and objects in between are triaxial. Dotted lines indicate constant triaxiality T. Most stellar remnants are oblate with $\epsilon = 0.5$. Most dark matter halos are either prolate or triaxial.

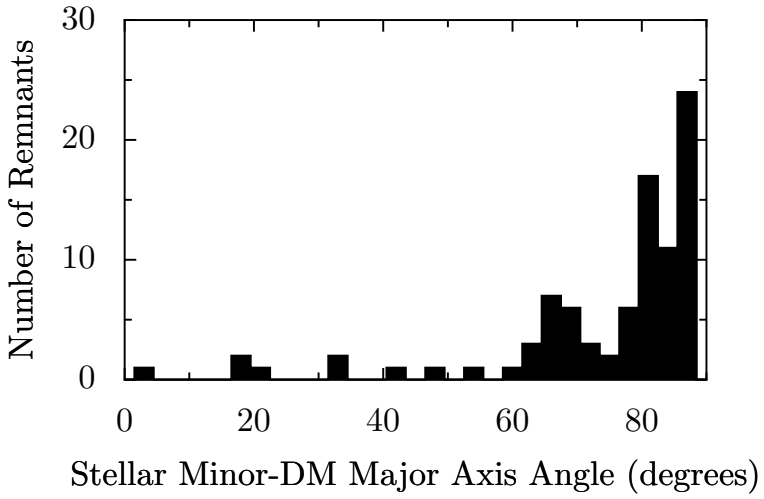

Figure 2.6: The angle between the *minor* axis of the stars and the *major* axis of the dark matter. The stellar material is mostly oblate, the dark matter halos are mostly prolate, and the "preferred" axes of the two shapes are nearly always perpendicular.

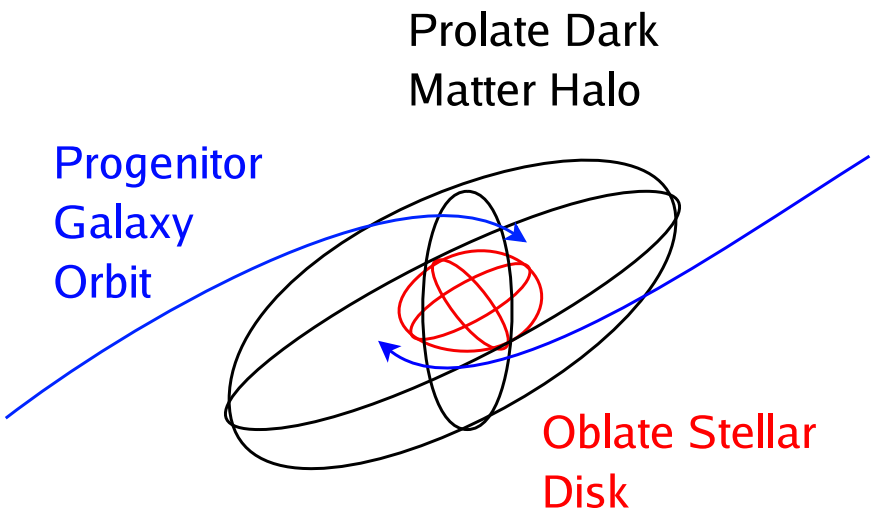

Figure 2.7: The physical interpretation of Figs. 2.5 and 2.6 in terms of angular momentum and dissipation. The total angular momentum in a merger simulation is usually dominated by the orbital angular momentum of the two galaxies. As the galaxies merge, both the luminous and dark components acquire angular momentum from the orbits of the progenitors. Their velocity dispersion increases along the axis parallel to the direction of approach, leading to an anisotropic velocity dispersion tensor. Gas in the simulation cools while largely conserving angular momentum so that it spins up to the point where the shape of the resulting stellar system is determined by rotation, not velocity dispersion anisotropy. Meanwhile, the dark matter cannot cool, so its shape is determined by velocity dispersion anisotropy. Therefore, the stellar system is oblate, dark matter halos are prolate, and the angle between the "preferred" axes of these two shapes is $\simeq 90°$.

2.3.3 Shapes as a Function of Radius

Using an aperture technique as above will always mix information about all radii. Therefore to compute the shapes of remnants as a function of radius I diagonalize the moment-of-inertia tensor within an ellipsoidal shell. In this case I seek both inner and outer similar ellipsoids such that a specified fraction of the mass is contained within each ellipsoid. The diagonalized moment-of-inertia tensor for the mass within the ellipsoidal shell defines the shape for that radius. In all of the work below I use ellipsoids containing 0, 10, 20, 30, 40, 50, 60, 70, 80, and 90 percent of the mass. I compute shapes for the mass between each adjacent pair of ellipsoids, resulting nine shape measurements per remnant. The simulated remnants have nearly r^{-2} density profiles, for which the enclosed mass as a function of radius is linear. Therefore although I compute the shapes for a specified enclosed mass fraction, the shapes are almost linearly distributed in radius as well.

Figure 2.8 shows the median (over all of the simulated remnants) axis ratios as a function of radius for the simulated remnants. The median is shown to avoid confusion since all of the shape profiles are quite similar. Both stars and dark matter become less spherical at increasing radius. This is expected since the dynamical time is larger at larger radius, so the system will take longer to come to equilibrium. Note, also, that the shape at a specified mass fraction is very different for different types of matter. The shape of dark matter in Figure 2.8 refers to larger radii than the shape of stellar material.

These ellipsoids defining the shape of the remnant are not constrained to be centered on the same point. However, in nearly all cases the distance between the centers of two of these ellipsoids for a given remnant is less than 10% of their radius. Therefore the remnants are close to having a common center at all radii.

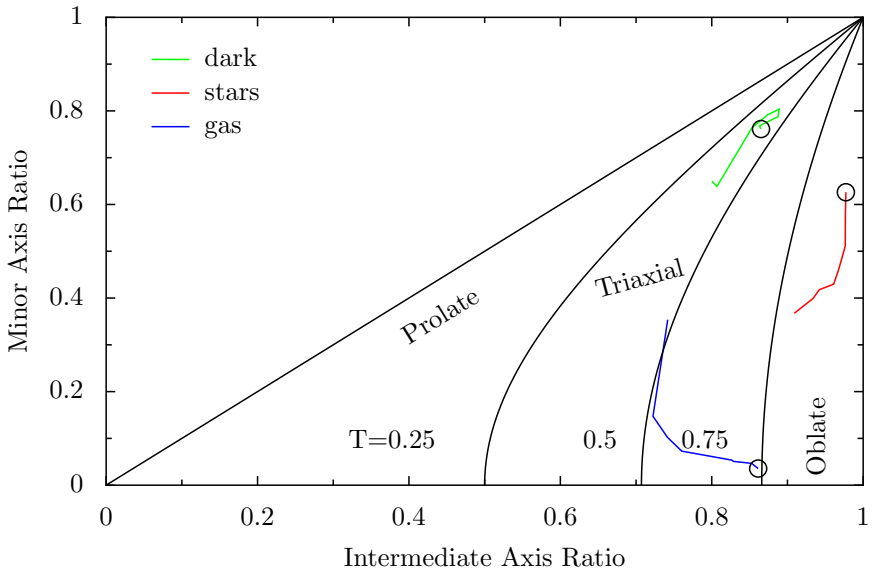

Figure 2.8: Median axis ratios of remnants as a function of radius for different types of matter. The innermost axis ratios are marked with open circles. Both the dark and stellar matter become less round as you get further from the center of the remnant. The gas at the center of each remnant is in a very flattened disk, as expected. At larger radius, the gas is mostly in a hot triaxial halo.

2.3.4 Application to Weak Gravitational Lensing

The interpretation of the Hoekstra et al. data is complicated by the inclusion of spiral as well as elliptical galaxies in the sample. Mandelbaum et al. (2006b,a) have done a similar study using SDSS galaxies separated by Hubble type and found that the projected halo shapes for elliptical galaxies are aligned with the projected stellar shapes, in agreement with Hoekstra et al. Finally, the projected positions of satellite galaxies also seem to indicate that the projected shapes of elliptical galaxies and halos are aligned (Sales & Lambas, 2004; Brainerd, 2005; Yang et al., 2006).

Weak lensing studies necessarily underestimate the flattening of dark matter halos. Figures 2.9 and 2.10 quantify this by simulating the weak gravitational lensing observations. Given assumptions about the three-dimensional shapes and mass profiles of galaxies and their

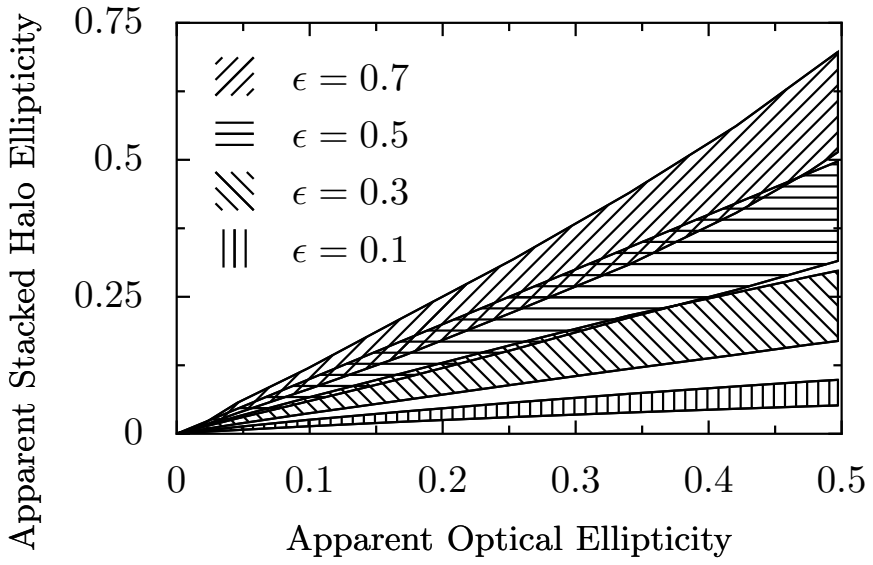

Figure 2.9: Consequences of our model for weak gravitational lensing measurements where one must stack many optically aligned galaxies in order to detect flattening of the dark matter halo. The plot shows the apparent ellipticity of the halo mass surface density vs. the apparent optical ellipticity of the stacked galaxies. Each shaded region shows the range of possible apparent ellipticities given an *intrinsic, three-dimensional* halo ellipticity. The lower bound of each shaded region is given by assuming a prolate halo and the upper bound by assuming an oblate halo. This is the result one would obtain if all galaxies followed the trend noted in this Letter and one stacked galaxies only with a *given* optical ellipticity. The observed halo ellipticity goes to zero for apparent optical ellipticities near zero because the galaxies cannot be oriented so that the stacking is coherent, even though each individual halo will have a nonzero projected ellipticity. The observed halo ellipticity only equals the three-dimensional ellipticity when halos are intrinsically oblate and the galaxies are viewed edge on; otherwise the flattening is underestimated.

halos and a scheme for combining many galaxies into a single mass surface density, these two figures show shapes of the projected halo mass surface densities. They allow observers to translate their two-dimensional measurements to a range of possibilities for the three-dimensional structure of dark matter halos.

The hydrodynamic simulations discussed here do not represent a cosmologically unbiased sample, so they are *not* used as input to the simulated lensing observations. Instead I adopt a slightly idealized version of the correlation between halos and galaxies noted in this Letter. Nearly all of the baryonic components of the simulated galaxies are close to 2:1 oblate

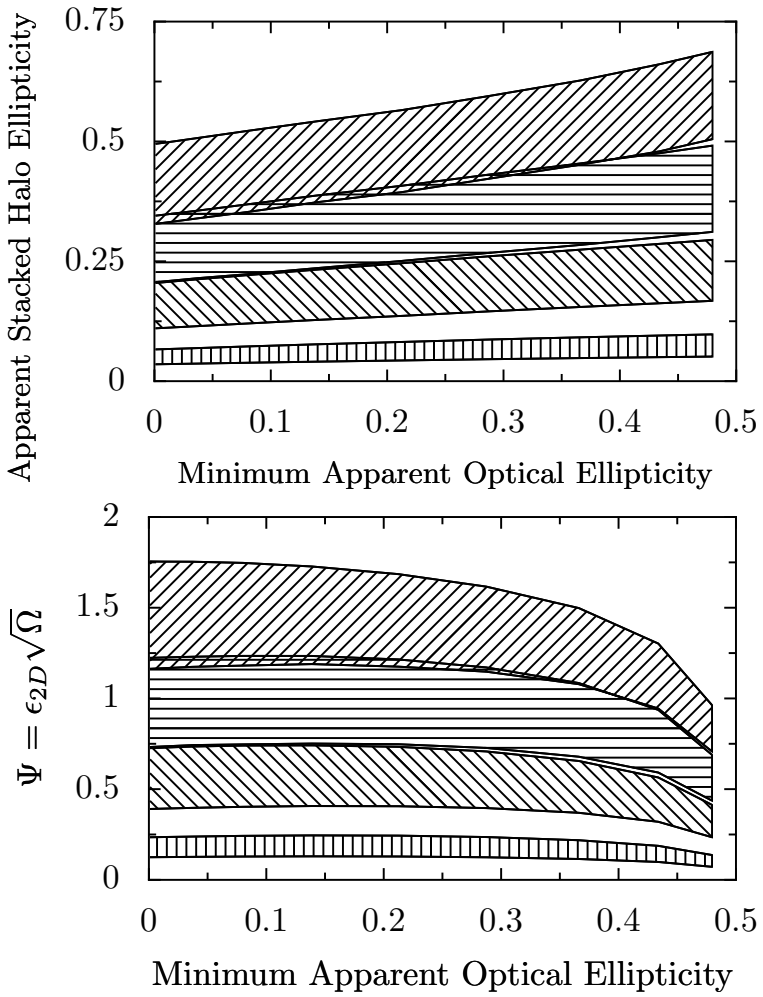

Figure 2.10: Weak gravitational lensing measurements when all galaxies with optical ellipticities greater than some value are included in the stacking. The shaded regions are defined as in Fig. 2.9. In both panels the x-axis is the minimum apparent optical ellipticity of galaxies included in the stacking. *Left*: The y-axis shows the apparent ellipticity of the stacked halo mass surface density. This is the halo ellipticity that would be measured if one stacked *all* galaxies with optical ellipticity greater than the given value. *Right*: Effect of different optical ellipticity requirements on the S/N ratio of the halo ellipticity measurement. Increasing the minimum optical ellipticity increases the signal (as seen in the right panel) but also increases the noise by reducing the number of galaxies included in the stack. The y-axis is Ψ defined by Equation (2.6). For small optical ellipticity cuts, the increase in signal is almost exactly canceled by the decrease in available solid angle, meaning that nothing is lost (or gained) by removing round galaxies from the stack. In reality, there is an advantage to removing low-ellipticity galaxies since their position angle is ill-defined. (This analysis assumes no error in position angle.) Above a minimum ellipticity of ~ 0.25 the quality of the measurement declines rapidly because of smaller solid angle of available viewing directions.

spheroids, so I assume that all early-type galaxies are so described. Thus, there is a simple mapping between viewing angle and optical ellipticity. We assume all galaxies follow the correlation between halos and galaxies noted here and that the halo mass density is given by a triaxial Navarro-Frenk-White profile: $\rho = \rho_0/(\zeta/r_s)(1+\zeta/r_s)^2$, where ρ is the mass density and ρ_0 is a constant (Navarro et al., 1996; Jing & Suto, 2002).

Contopoulos (1956) showed that for a triaxial ellipsoid with constant three-dimensional axis ratios, the contours of constant projected surface density are ellipses with constant ellipticity and position angle, independent of the radial density profile. I only use the ellipticity and position angle of the baryonic component, so the radial profile of the baryons does not matter. The Contopoulos (1956) analysis does not apply to the stacked dark matter halos, so Figures 2.9 and 2.10 depend on the radial density distribution of the halos. In practice the difference is not large.

To simulate weak lensing measurements, I align the projected mass distributions based on projected light distributions, stack the projected halo mass distributions, and fit an ellipse to the halo mass surface density distribution where the area of the ellipse is constrained to equal $\pi(3r_s)^2$. This size for the ellipse is motivated by the approximate radius at which weak lensing observations are sensitive to the halo shape (M. J. Hudson 2006, personal communication). The stacking either assumes a given inclination of the optical galaxy, averaging over the azimuthal angle (as in Fig. 2.9), or assumes that some *minimum* optical ellipticity is required to be included in the stack, averaging over the portion of the unit sphere that gives rise to sufficient optical ellipticities (as in Fig. 2.10).

Figure 2.9 shows that galaxies with low optical ellipticities will have low halo ellipticities because there is no preferred axis to use to stack galaxies. The only situation where the projected halo ellipticity equals the three-dimensional halo ellipticity is when all stacked

galaxies are viewed edge-on and halos are intrinsically oblate. Flattening is underestimated in all other cases.

Figure 2.10 shows the result of the more realistic scenario where all galaxies with optical ellipticities greater than some value are included in the stack. This allows one to transform projected ellipticities to three-dimensional ellipticities. For example, if an observer sets the minimum optical ellipticity to 0.2 and measures a stacked halo ellipticity of 0.25, one can conclude that the three-dimensional ellipticity of halos is either 0.3 (for oblate halos), 0.5 (for prolate halos), or somewhere in between.

As one enforces tighter constraints on the optical ellipticity, the halo ellipticity goes up, but the cost is that fewer galaxies will make it into the stack. Under simple assumptions, one can estimate the signal-to-noise ratio (S/N) of the halo ellipticity measurement to be

$$(\mathrm{S/N})_{\mathrm{tot}} = \epsilon_{\mathrm{2D}} \sqrt{\Omega N_{\mathrm{tot}}} / \sigma_1 \tag{2.5}$$

where ϵ_{2D} is the apparent ellipticity of the stacked halo mass surface density, Ω is the solid angle of viewing angles for which a galaxy will be included in the stack, N_{tot} is the total number of galaxies in the survey, and σ_1 is the error on the halo ellipticity when only *one* galaxy is used. We define Ψ as the part of this expression which depends on the signal and the available solid angle:

$$\Psi = \epsilon_{\mathrm{2D}} \sqrt{\Omega} \tag{2.6}$$

Figure 2.10 thus also allows observers to estimate the quality of their measurement given the size of their survey and an estimate of the one-galaxy error on the halo ellipticity. In reality, observers do not know Ω, but they could estimate it from the from the minimum ellipticity of galaxies in their sample as long as our assumption that the stellar remnants are 2:1 oblate spheroids is not far wrong.

2.4 Conclusions

In this chapter I have characterized the three-dimensional shapes and density profiles of remnants produced by hydrodynamic simulations of binary galaxy mergers. Stellar remnants are nearly all oblate, with a few examples of triaxiality in the most gas-poor mergers. Dark matter halos are either prolate or triaxial, and the short axis of the baryons is perpendicular to the long axis of the dark matter. All of these facts can be understood in terms of the effects of angular momentum and dissipation during the merger. If there is a class of elliptical galaxies that were formed by gas-rich binary galaxy mergers, they can be expected to display these characteristics.

Given the three-dimensional correlation between galaxy shapes and halo shapes, I have calculated the expected projected halo flattening when galaxies are stacked based on their optical orientation. This information can be used to help interpret data on halo shapes from weak galaxy-galaxy lensing surveys such as the one by Parker et al. (2007).

Real galaxies in a ΛCDM universe are thought to have experienced many mergers over the course of their history, and these multiple mergers can be expected to weaken the relationship between the shapes of galaxies and their halos described here. The extent to which the effects of large-scale structure, such as mass accretion along filaments, tend to preserve the relationship between galaxies and their halos is an interesting and open question.

The density profiles of remnants are quite regular in their structure. The slopes of the baryonic and total density profiles are confined to a small range, although the densities at $r_e/2$ vary by about an order of magnitude. The dark matter density profiles of the *Sbc* simulations are significantly different from the *G* series, attributable to the initial configuration of the halos of the progenitors.

2.4.1 Future Work

The material in this chapter is far from being either the first or the last word on the properties of simulated galaxy merger remnants. Questions to be resolved in immediate future work to prepare the most interesting parts of this chapter for publication are:

- Is the difference in the central dark matter fractions between the *Sbc* and *G* series simulations due to the higher dark halo concentration and adiabatic contraction in the *Sbc* progenitor or due to the fact that gas physics is more important in the *Sbc* simulation owing to its higher gas fraction?

- What is the exact physical mechanism by which remnants come to have a density profile that very nearly goes as r^{-2}? Is gas physics important? Under what circumstances will remnants *not* have this profile?

- Why does the dark matter density profile in both the *Sbc* and *G* series simulations steepen? Is this because of adiabatic contraction due to radiative gas cooling during the simulation?

- Exactly how do remnants avoid a feature in the density profile at the transition between baryonic domination and dark matter domination? Is this related to the Blumenthal et al. (1986) explanation of the featureless rotation curves in spiral galaxies?

Chapter 3

Comparison with Integral Field Observations

Rich observational data sets allow powerful tests of the extent to which simulated galaxy merger remnants resemble early-type galaxies. One such set is the SAURON survey, which uses a purpose-built integral field unit with a 41x33 arcminute field-of-view on the 4.2 meter William Herschel Telescope (Bacon et al., 2001). The team observed 48 nearby early-type galaxies out to one effective radius, giving kinematic information from deconvolved stellar absorption line spectra (Emsellem et al., 2004). They are extending the survey to increase the number of galaxies by a substantial factor (Roger Davies, personal communication). The SAURON survey is unique in that it increases not only the quality of the kinematic data available for nearby galaxies, but the dimensionality of the data. This chapter evaluates the extent to which remnants of simulated hydrodynamic mergers of disk galaxies resemble actual early-type galaxies.

I have analysed the merger remnants produced in a series of gas-rich binary galaxy

merger simulations run by T.J. Cox as part of his Ph.D. thesis and subsequent work (Cox, 2004; Cox et al., 2006b, 2008), in order to determine which elliptical galaxies have arisen from binary mergers of spiral galaxies and which have not. Approximately 80% of the SAURON early type galaxies are fast rotators and the remaining 20% of SAURON Es are slowly rotating nearly spherical systems (Emsellem et al., 2007).

Fast-rotating elliptical galaxies appear to be very similar to the remnants from our merger simulations once the simulations are smoothed to the SAURON resolution and the full SAURON data-reduction pipeline including stellar spectrum deconvolution is included. However, these binary gas-rich galaxy merger remnants do *not* make good candidates for relatively high-mass, nearly spherical, non-rotating elliptical galaxies that make up 20% of the early-type galaxies in the SAURON survey. Thus binary mergers of disk galaxies are not a plausible scenario for the formation of these massive elliptical galaxies.

3.1 Previous Work

Bendo & Barnes (2000) used Gauss-Hermite moments (discussed in Section 3.2 below) to analyze the line-of-sight velocity distribution (LOSVD) of sixteen dissipationless merger simulations with mass ratios of 1:1 and 3:1. They found that equal mass mergers display a variety of kinematic features (including kinematically decoupled components, and kinematic misalignments), and that 3:1 mergers result in disk-like kinematics. Their remnants show a positive correlation between the line-of-sight velocity v and the third Gauss-Hermite coefficient h_3, in conflict with observations (Bender et al., 1994).

Naab & Burkert (2001, 2003) analysed the kinematic structure of the remnants produced by a large suite of dissipationless disk galaxy merger simulations with a variety of orbits and mass ratios from 1:1 to 4:1. They found that the majority of equal mass mergers resulted

in slowly rotating objects, with $(v/\sigma)^* < 0.4$ (where σ is the velocity dispersion). However, the three dimensional shapes of these remnants were usually triaxial, and intrinsically triaxial objects have very few viewing angles from which they appear round (Binney & de Vaucouleurs, 1981). Thus the ellipticities of the slowly rotating objects are statistically too large to correspond to the SAURON round slowly-rotating galaxies. They find that 3:1 and 4:1 mergers produce remnants that can be identified with low-luminosity, fast-rotating ellipticals.

Burkert & Naab (2005) further developed the claim that unequal mass major mergers have photometric and kinematic properties that correspond to low-luminosity elliptical galaxies. In particular, they found that rapidly rotating remnants are not flattened solely by their rotation, but also by their anisotropies which range from nearly isotropic to very anisotropic.

Cappellari et al. (2007) used Schwarzschild (1979) modeling to determine the 3D orbital structure of the SAURON galaxies. They found a *positive* correlation between rotation and anisotropy. That is, galaxies with little rotation have nearly isotropic velocity ellipsoids, and hence have spherical 3D shapes. Galaxies with larger rotation velocities *also* have larger anisotropies. The velocity ellipsoid is flattened in the z direction ($\sigma_R > \sigma_z$), so these galaxies have 3D shapes flattened by both rotation *and* anisotropy.

Burkert et al. (2007) made the point that no such correlation between rotation and anisotropy is seen coming from numerical simulations of binary galaxy mergers. They claim that this is a major problem for the idea that early-type galaxies are formed via major mergers.

Cox et al. (2006a) extensively analysed the behavior of a large set of remnants in the v/σ vs. ellipticity plane, but did not focus on two-dimensional kinematics. They found that simulations with sufficient gas produce remnants that match low-luminosity ellipticals in a v/σ vs. ellipticity plot, but that massive ellipticals are not produced.

González-García et al. (2006) studied the LOSVDs of dissipationless merger remnants

and found that central bulges result in higher values of v/σ and in the observed $v - h_3$ anti-correlation.

Jesseit et al. (2007) analysed the LOSVDs of a set of 1:1 and 3:1 merger remnants where the progenitors were either gas-free or contained 10% gas. There was no star formation, no supernova feedback, and no AGN feedback. They found that the presence of gas is necessary to produce the observed $v - h_3$ anti-correlation, in disagreement with the finding of González-García et al. (2006).

3.2 Methods

Hermite polynomials are familiar from the eigenfunctions of the quantum harmonic oscillator. They are useful as a parameterization of LOSVDs in galaxies because the lowest order eigenfunction is the Gaussian distribution with the increasing energy levels of the oscillator being increasingly different from a Gaussian. These functions are preferred over the classical moments (skewness and kurtosis) because the classical moments are most sensitive to the tails of the distribution, where signal-to-noise is low in galaxy LOSVDs, while the harmonic oscillator eigenfunctions parameterize the same deviations from Gaussianity but have decreasing sensitivity in the wings of the line profile. Henceforth $H_i(x)$ refers to the ith eigenfunction of the quantum harmonic oscillator, which is a Gaussian function times the ith Hermite polynomial. The coefficient of the $H_i(x)$ in the expansion of an LOSVD is h_i.

It is important to note that the Hermite polynomials are a complete, orthogonal set of functions and can therefore represent *any* function using *any* choice of the v and σ as long as enough terms are included in the expansion. We know that LOSVDs are nearly Gaussian, so we would like to make an intelligent choice of v and σ so that the extra terms in the expansion parameterize small deviations from Gaussianity. One possibility is to use the computed first

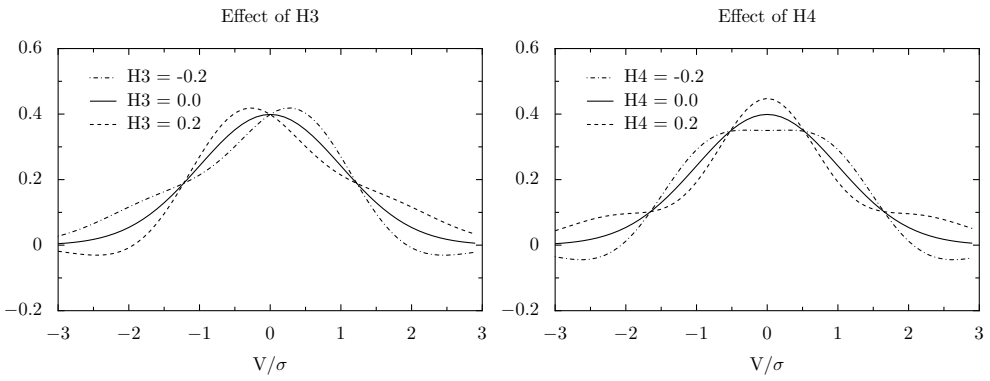

Figure 3.1: The effect of variations in h_3 and h_4 on the line-of-sight velocity distribution. On the left, h_3 parameterizes the skewness of the distribution. On the right, h_4 parameterizes the kurtosis or "peakiness" of the distribution.

and second moments of the distribution ($\int vf(v)\,dv$ and $\int v^2 f(v)\,dv$) (Gerhard, 1993). This approach allows the entire expansion to be computed directly, with no need to minimize any function. A disadvantage is that h_1 and h_2 will be nonzero in general. Therefore to reconstruct the LOSVD to fourth order, one must provide v, σ, h_1, h_2, h_3, and h_4.

Another possibility is to require that v and σ be chosen so that h_1 and h_2 are zero (van der Marel & Franx, 1993; Cappellari & Emsellem, 2004). One must therefore perform a constrained minimization of the difference between the LOSVD and the expansion. However, the advantage is that v and σ are provided by the fit and reconstructing the LOSVD to fourth order only requires knowledge of v, σ, h_3, and h_4.

In looking at the Gauss-Hermite functions, the most natural candidates for measuring skewness and kurtosis are $H_1(x)$ and $H_2(x)$ which have one and two zeros, respectively. The requirement that v and σ be set by requiring that h_1 and h_2 be zero has the slightly non-intuitive effect that skewness and kurtosis are measured by functions that have three and four zeros, respectively. This can be seen in Figure 3.1 where the curves with non-zero H cross the Gaussian curve three and four times, respectively.

As a result, non-zero h_3 and h_4 values indicate something about *both* the center and

the tails of the line profile. With respect to h_4, a positive value indicates a peaky center and heavy tails in the distribution. A negative value indicates a flat-topped center and light tails. Similarly, a positive h_3 value indicates that the LOSVD has a center shifted towards negative values with a light tail on the negative side and a heavy one on the positive side. A negative h_3 value indicates the opposite.

Non-Gaussian LOSVDs can give information about anisotropy or about kinematically distinct populations of the galaxy. Figure 3.2 shows schematically how radial and tangential anisotropy affect the LOSVD. Figure 3.3 shows how two kinematically distinct populations can give non-Gaussian LOSVDs. For very kinematically distinct populations observed at high spectral resolution, Gauss-Hermite moments become a poor representation of the underlying LOSVD. In that case a double-Gaussian fit would be more appropriate. A double-Gaussian fit requires one extra parameter (the relative normalization of the two populations) compared to a Gauss-Hermite fit up to h_4, but it the advantage that the fit coefficients would directly give the relative sizes of the two populations. There us evidence that real early-type galaxies contain distinct kinematically hot and cold components (Cappellari et al., 2007). A double-Gaussian fit appears well-motivated both theoretically and observationally, so we propose that observers and theorists move toward this way of parameterizing LOSVDs. However, I do not pursue the idea further in this work.

This chapter makes extensive use of SAURON-style plots of two-dimensional galaxy kinematics, an example of which is shown in Figure 3.4. For all of the plots in this chapter, the minimum and maximum of the line-of-sight velocity color bar as well as the maximum of the velocity dispersion color bar are set to the projected velocity dispersion (σ_p) within $r_e/8$ for each galaxy, unless otherwise noted in the figure caption. The minimum of the velocity dispersion color bar is set to zero, $\sigma_p/2$, or allowed to float to the minimum value actually

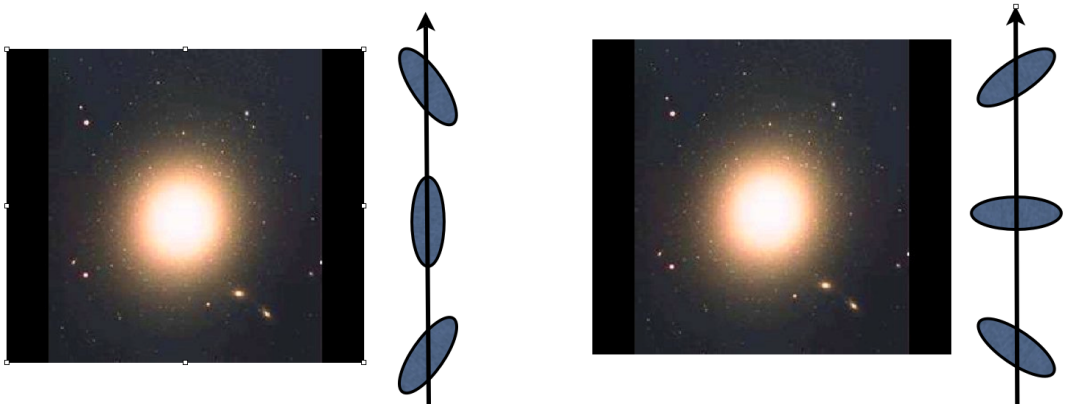

Figure 3.2: Radial and Tangential anisotropy and its contribution to non-Gaussian LOSVDs. Two images of M87 (image credit: David Malin and the Anglo-Australian Observatory) are shown with hypothetical lines of sight through the outskirts of the galaxy. The ellipses represent the velocity ellipsoid at different points along the line of sight assuming radial or tangential anisotropy. The luminosity density drops off rapidly with 3D distance to the center of the galaxy, so the LOSVD is primarily determined by the middle ellipse with small changes introduced by the top and bottom ellipses. On the left, a tangentially anisotropic galaxy. In this case the largest contribution to the LOSVD comes from the region where the velocity dispersion along the line of sight is the highest. Therefore the top and bottom ellipses leave the wings of the profile unchanged but build up a broad center of the profile, leading to negative (flat-topped) h_4 values. On the right, a radially anisotropic galaxy. Here, the brightest contribution to the LOSVD comes from the point where the velocity dispersion along the line of sight is the *smallest*. Therefore the *primary* effect of the top and bottom ellipses is to build up the wings of the profile, leading to positive h_4 values.

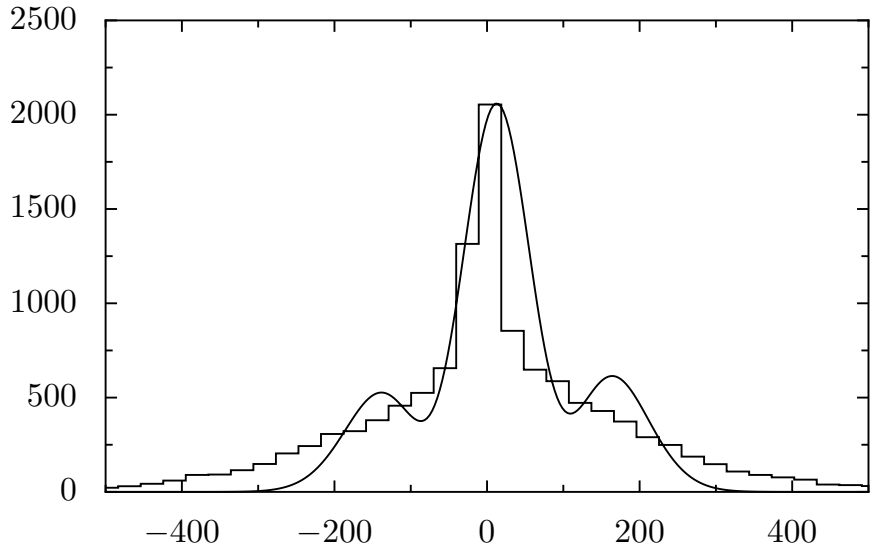

Figure 3.3: The effect of kinematically distinct populations of a galaxy on the LOSVD. Here, a kinematically cold disk component is superimposed upon a kinematically hot bulge component, leading to a very peaky distribution and hence very positive value of h_4. For the merger remnants studied here, this is the primary driver of nonzero h_3 and h_4 values inside one effective radius. The smooth solid line is the best-fitting Gauss-Hermite expansion to forth order. The poor representation of the underlying LOSVD shows that the Gauss-Hermite series becomes a less faithful representation of the LOSVD as systems with very different kinematic populations are observed at high spectral resolution.

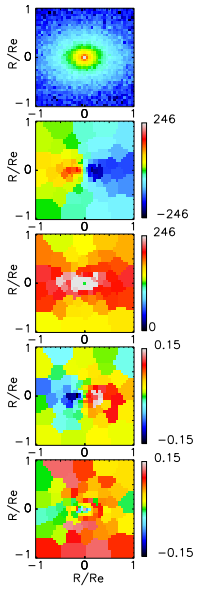

Figure 3.4: A Sample SAURON-style plot, used extensively throughout this section. From top to bottom, the panels are: surface brightness, velocity, velocity dispersion, h_3, and h_4.

appearing in the plot.

One of the principal results of the SAURON survey has been to highlight the division of galaxies into so-called fast-rotators and slow-rotators. It has long been known that there is a systematic trend where more massive elliptical galaxies have lower rotation speeds (Davies et al., 1983), but the division of early-type galaxies into two distinct classes (Kormendy & Bender, 1996), dramatically demonstrated with integral-field data (Emsellem et al., 2007) is new. Figures 3.5 and 3.6 show a selection of SAURON fast and slow rotators, respectively.

3.2.1 Template Spectra

In order to treat the simulations in a manner as close to the observations as possible, we convolve the stellar LOSVD in each pixel with a template stellar spectrum, then use the same code used as part of the SAURON project to recover v, σ, h_3 and h_4 values from the simulated spectrum. Template spectra are taken from Vazdekis (1999). For most of the plots

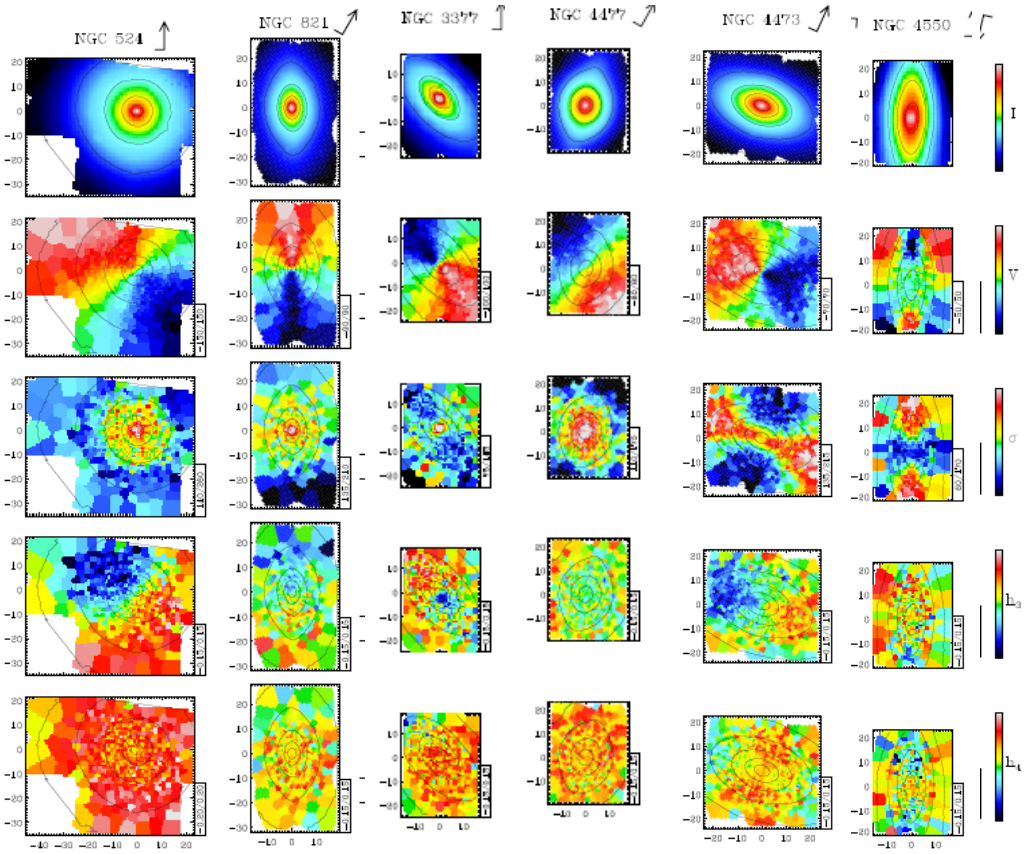

Figure 3.5: A selection of SAURON fast rotators from Emsellem et al. (2004). From left to right, N524, N821, N3377, N4477, N4473, and N4550. The two right-most galaxies (N4473 and N4550) are included as interesting anomalous galaxies – they both have counter-rotating kinematic components. The elongated feature in the velocity dispersion map of N4473 is evidence for a counter-rotating thin disk which must make a sub-dominant contribution to the mass since the feature does not show up in the velocity map (Cappellari & McDermid, 2005; Krajnović et al., 2006). N4550 shows similar bilateral symmetry in the velocity dispersion map as well as tri-fold symmetry in the rotation map. This indicates the presence of both a thick rotating component and a thin counter-rotating component (Rubin et al., 1992).

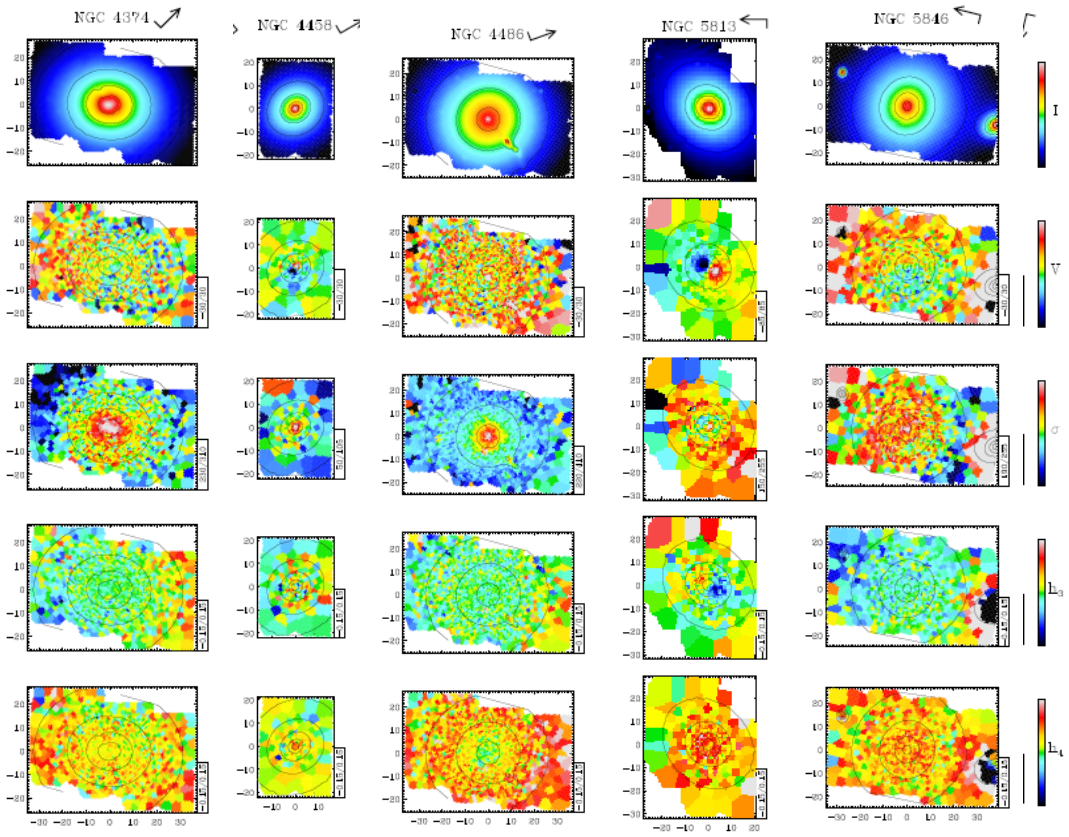

Figure 3.6: A selection of SAURON slow rotators from Emsellem et al. (2004). From left to right, N4374, N4458, N4486, N5813, and N5846.

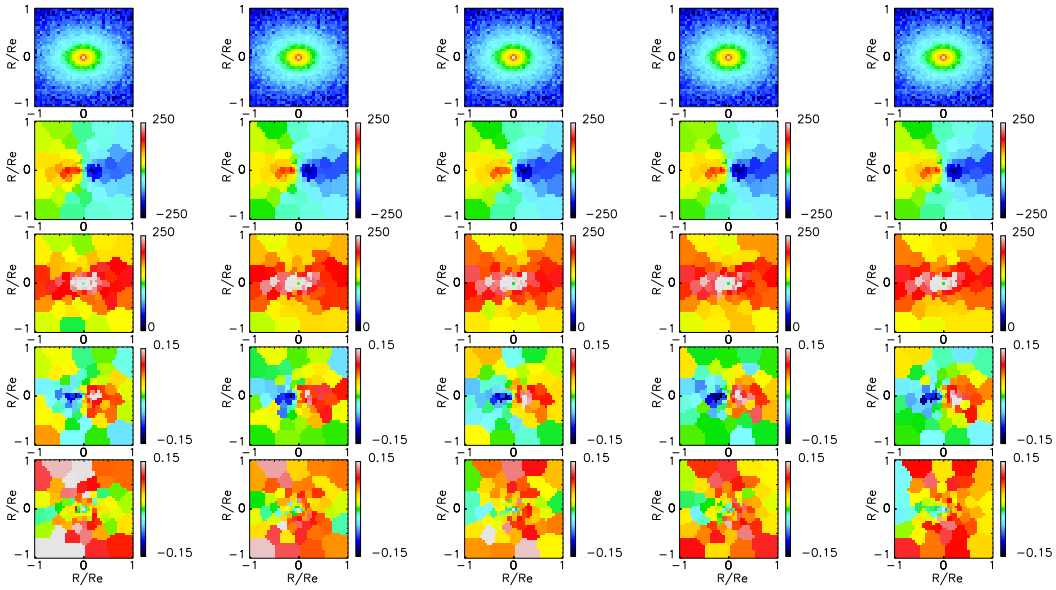

Figure 3.7: Effect of different ages of stellar populations on moment fitting. From the left, assuming a stellar population age of 1, 5, 10, 12.6, and 17.8 Gyr from Vazdekis (1999). The effect is negligible.

here, we use the spectrum corresponding to solar metallicity and a luminosity weighted stellar age of 12.6 Gyr because massive ellipticals typically have old, metal-rich stellar populations. Figures 3.7 and 3.8 show that the choice of stellar template does not make a significant except for very metal poor ([Fe/H] = -0.68) populations. Figures 3.9 and 3.10 show that even template mismatch does not make a significant difference in recovering the LOSVD except in the case where an old stellar population (10 Gyr) is used for the convolution and a very young (1 Gyr) population is used for the LOSVD recovery.

3.3 Results

There are several important regularities visible in Figures 3.5 and 3.6. The slow rotators are systematically rounder than fast rotators Cappellari et al. (2006), the $(v/\sigma)^*$ values are close to unity for fast rotators and very small for slow rotators, there is a distinct

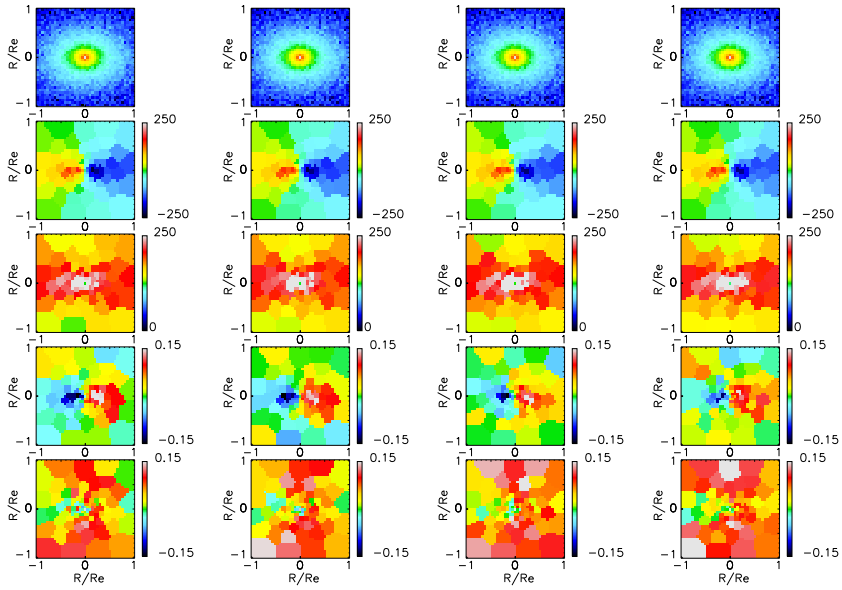

Figure 3.8: Effect of different metallicities of stellar populations on moment fitting. From the left, [Fe/H] = 0.2, 0.0, -0.38, and -0.68. The effect is negligible except for the lowest metallicity case, where the h_3 values are less significant.

anti-correlation between v and h_3, and h_4 is rotationally symmetric with a preference for positive values.

Figures 3.11 and 3.12 take advantage of the symmetry of the remnants and show a sequence of viewing angles in inclination. Each view is separated by 15 degrees, and the very regular kinematic structure of the remnants is visible in these two simulations. The remnants rotate about the short axis of the remnant and the visibility of the rotation is a function of inclination angle. This simple structure describes nearly all of the simulated remnants.

There is a clear and very interesting trend in the h_4 values as a function of inclination shown in Figures 3.11 and 3.12. As the remnant is seen increasingly face-on, the h_4 values rise significantly. This is because of the kinematically cold population of stars formed in a gaseous disk after the merger has finished. The kinematically cold stars are sub-dominant in terms of the total number, so they make their presence felt as deviations from a purely

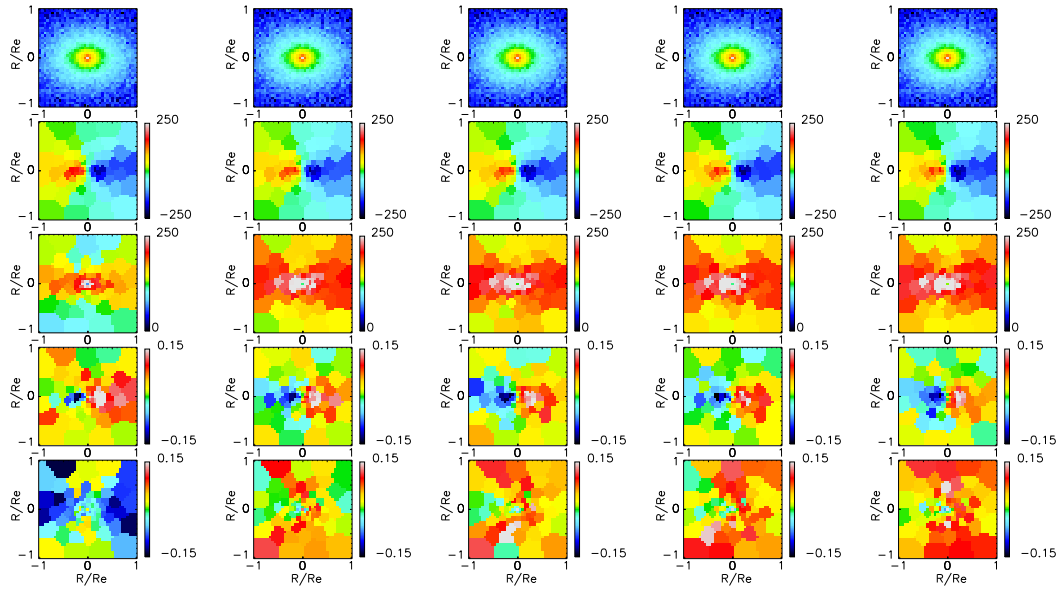

Figure 3.9: The effect of stellar age template mismatch on LOSVD recovery. The LOSVD from the *Sbc*201a-u4 simulation is convolved with a model spectrum from a solar metallicity, 12.6 Gyr old population. The model spectrum used for deconvolution uses the same metallicity and ages of 1, 5, 10, 12.6, and 17.8 Gyr from left to right. Velocities and dispersions are unaffected except for lower velocity dispersions when the deconvolution spectrum is for a 1 Gyr old population. The higher order moments are mostly unaffected except for the 1 Gyr case and slightly elevated h_4 values in the 17.8 Gyr case.

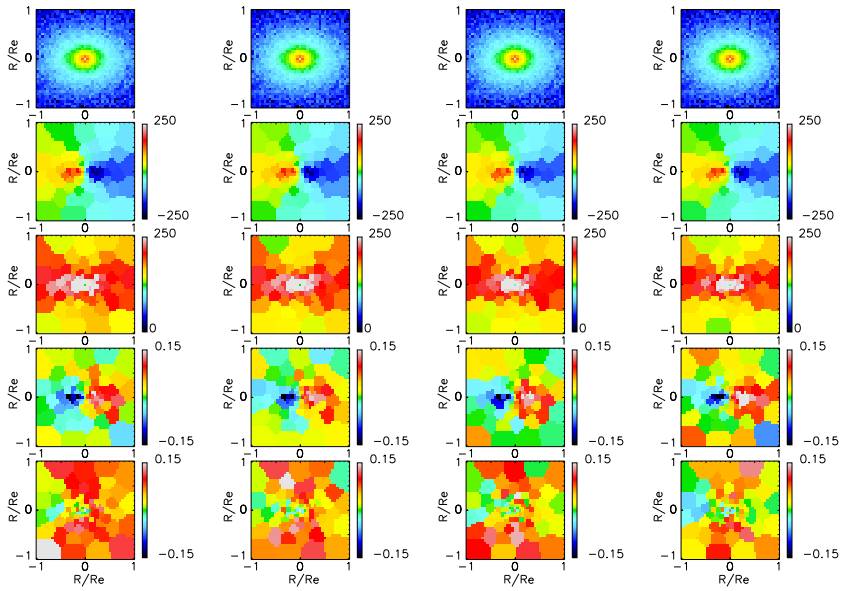

Figure 3.10: The effect of stellar metallicity template mismatch on LOSVD recovery. The LOSVD from the *Sbc*201a-u4 simulation is convolved with a model spectrum from a solar metallicity, 10 Gyr old population. The model spectrum used for deconvolution uses the same age and metallicities of 0.2, 0.0, -0.38, and -0.68 from left to right. The recovered LOSVDs are not dramatically affected.

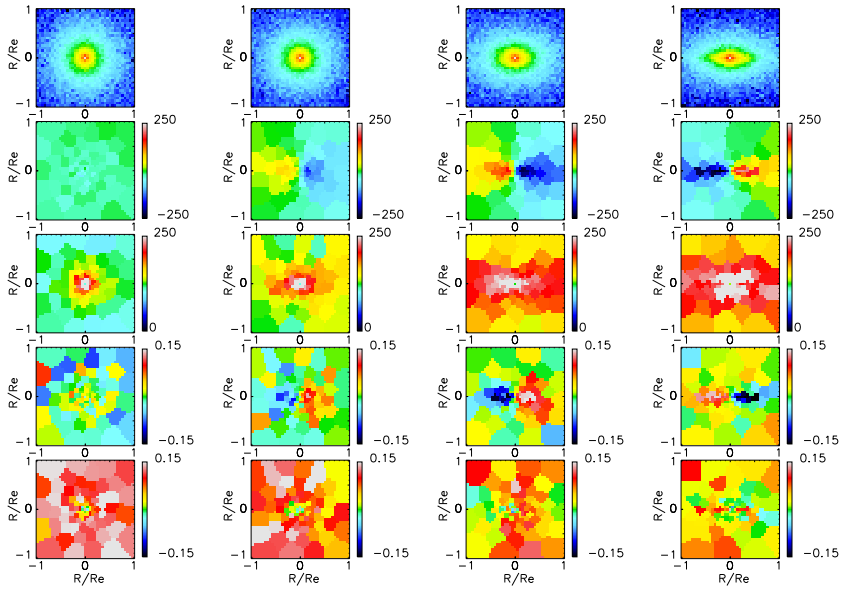

Figure 3.11: The *Sbc*201a-u4 remnant as a function of inclination. From left to right, face-on to edge-on in 30 degree increments. The isophotes are obviously disky as the remnant is viewed increasingly edge-on. The velocity shows the characteristic rotation pattern unless the remnant is viewed very close to face-on. The velocity dispersion drops fairly gently with radius except for the nearly face-on views where it drops dramatically as the fit picks up the kinematically cold disk component. The h_3 coefficient shows the same anti-correlation as the observations. Finally, h_4 shows a preference for positive values, particularly in the face-on case.

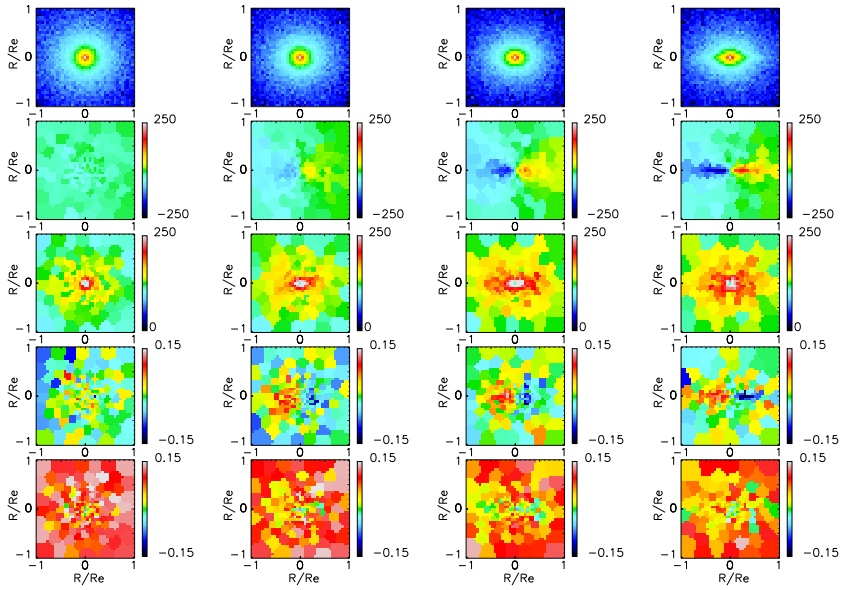

Figure 3.12: The $G3$-$G3$ merger remnant as a function of inclination in 30 degree increments. This remnant is quite similar to the Sbc201a-u4 simulation shown in Figure 3.11 except that the disk is somewhat less prominent in this case. Even so, rotation is clearly visible.

Gaussian line profile as discussed in connection with Figure 3.3. When the disk is seen with some inclination, the primary effect of these stars is to skew the LOSVD, creating the well-known $v - h_3$ anti-correlation (Bender et al., 1994). However, when the disk is viewed face-on, these stars contribute to the LOSVD near the peak of the distribution of kinematically hot stars, albeit with a smaller dispersion. They thus make the LOSVD peakier, hence make h_4 significantly more positive.

Thus the $v - h_3$ anti-correlation and the significantly positive h_4 values when there is no rotation are both indications of a "fossilized" gaseous disk embedded in the merger remnant. The disk is fossilized in the sense that the gas has turned into stars which make their presence known through stellar absorption-line observations.

Figure 3.13 shows the effect of different disk rotation orientations on the resulting remnant. The central velocity dispersion is virtually unchanged, but the retrograde-retrograde

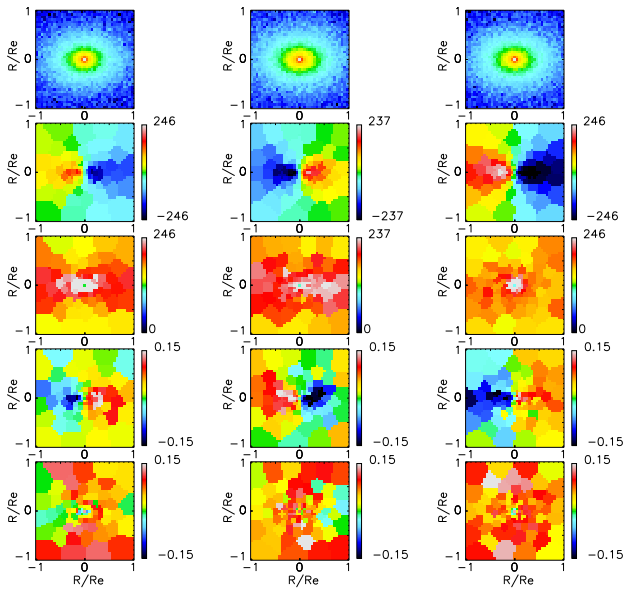

Figure 3.13: The effect of disk rotation orientation on merger remnant kinematics. These mergers have the "fiducial" geometry where one galaxy disk is in the plane of the orbit and the other is inclined by 30 degrees with respect to the plane of the orbit. From left to right, the disk rotations are prograde-prograde, prograde-retrograde, and retrograde-retrograde. Retrograde disks result in more distinct rotation.

mergers show more distinct rotation. This is perhaps counter-intuitive at first glance because retrograde mergers have less total angular momentum since the internal angular momentum of the galaxies is opposite to their merger orbital angular momentum.

The reason for the trend is that merging galaxies with prograde rotation throw out a large fraction of their mass into a tidal tail. The local dynamical time is a strong function of radius, meaning that the tidal material is "frozen" at large radius while the central merging galaxies evolve quickly. The tidal material eventually returns to the remnant, but the location of its infall is no longer correlated to the position and orientation of the merger remnant. Therefore this material is added to the stellar spheroid with less coherent rotation.

By contrast, merging retrograde disks are highly disturbed and show copious star formation, but most of the mass stays near the center of each remnant until they finally

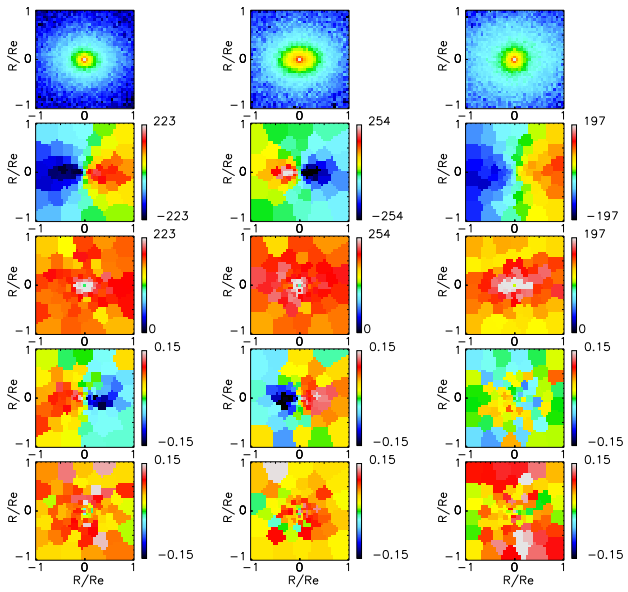

Figure 3.14: The effect of disk orientation on merger remnant kinematics. Here one or both of the disks is perpendicular to the plane of the orbit. From left to right: 1) one disk is perpendicular to the orbit plane and the other is inclined with prograde rotation. 2) The same as 1 except that the rotation of the perpendicular disk is reversed. 3) both disks are perpendicular to the orbital plane. Having both galaxies perpendicular to the orbital plane results in a lower central velocity dispersion and less ordered rotation.

merge. There is enough angular momentum in the orbit of the merging galaxies to overcome the small initial deficit implied by retrograde disk rotation, and the resulting remnant shows distinct, ordered rotation.

Figure 3.14 shows merger remnants where one or both of the galaxies was perpendicular to the orbital plane. These show decreasing rotation as one and both of the galaxies are perpendicular to the orbital plane.

Figure 3.15 shows orbits with impact parameters reduced and increased by a factor of two compared to the previous plots. This figure clearly highlights the fact that conservation of energy and angular momentum do not determine the results of a galaxy merger. This is simply because dark matter, stars, and gas may all exchange energy and angular momentum subject to the constraint that the *total* is conserved. Observations of the stellar remnant only

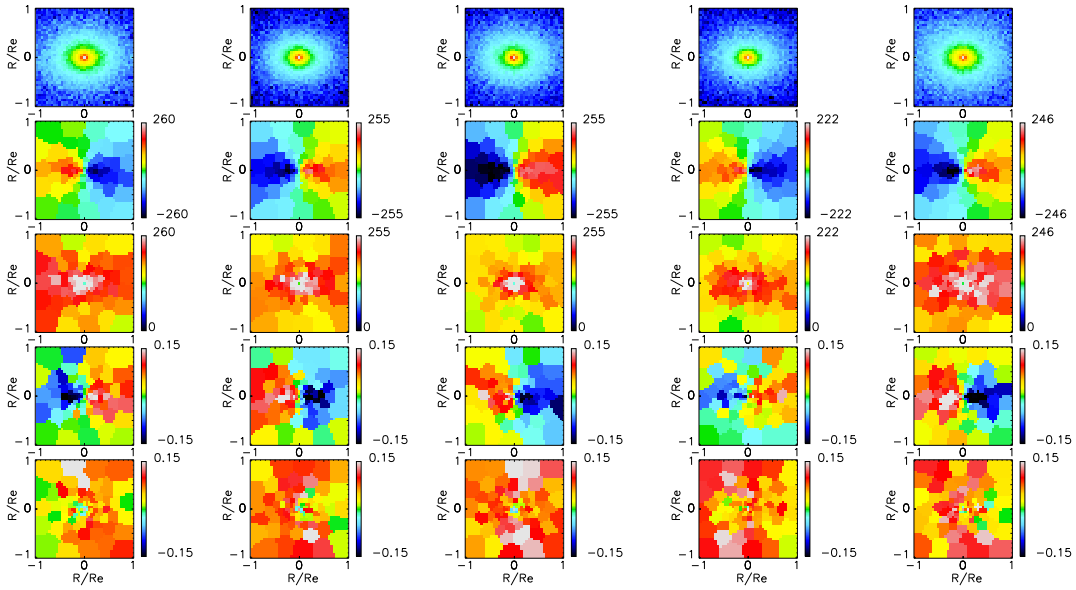

Figure 3.15: The effect of variations in the impact parameter. The left set of remnants has an impact parameter smaller by a factor of 2, and the right set has an impact parameter larger the same factor, both compared to the "fiducial" simulations in Figure 3.13. The remnants also differ in the progenitor disk orientations. From left to right: prograde-prograde, prograde-retrograde, retrograde-retrograde, prograde-prograde, and retrograde-retrograde. As with Figure 3.13, these remnants also demonstrate that retrograde-retrograde mergers show greater rotation. Furthermore, the mergers with smaller impact parameters show higher central velocity dispersions and higher rotation speeds than those with larger impact parameters, in spite of their lower total angular momentum.

probe a small piece of the system, so decreasing the *total* angular momentum in the simulation does not necessarily decrease the resulting angular momentum of the central baryons.

Figure 3.16 shows remnants where the orbits are moderately bound, with eccentricities of 0.8 or 0.9. Decreasing the energy of the orbit results in remnants with lower central velocity dispersions, and the radial fall-off of velocity dispersion seems to be somewhat steeper. However, rotation as a fraction of velocity dispersion is quite similar among all of the remnants. It is somewhat puzzling that all of the $e = 0.8$ orbits show h_3 maps that are nearly zero instead of the usual anti-correlation.

Figure 3.17 shows the two zero angular momentum simulations. If the structure

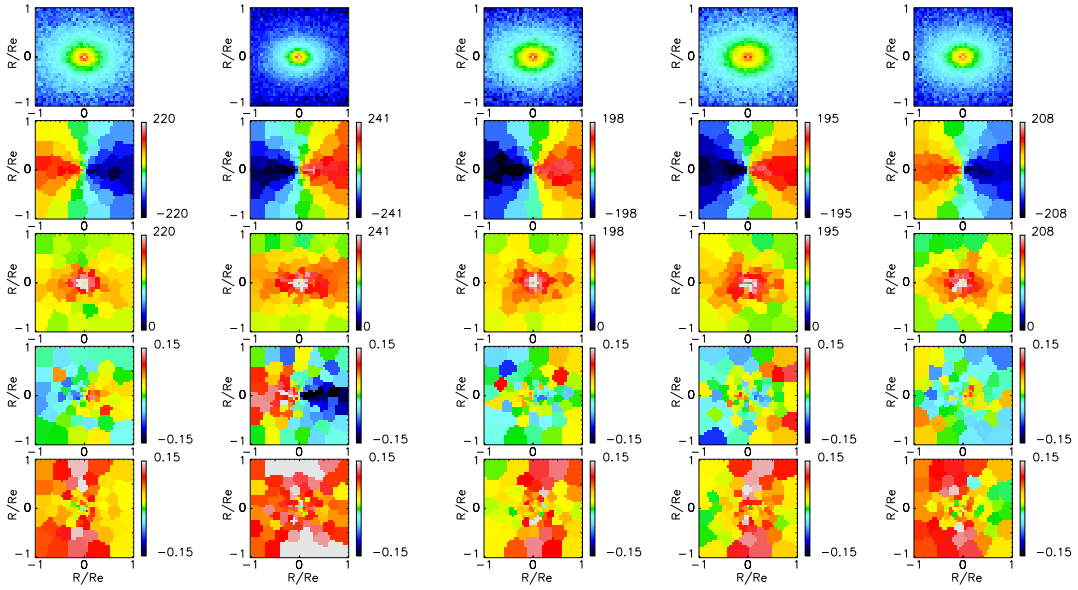

Figure 3.16: Remnants where the progenitors are bound. The left set have eccentricities of 0.9, and the right set have eccentricities of 0.8. For the left set, the left-most is prograde-prograde and the right-most is retrograde-retrograde, both with pericenter distances of 11 kpc. For the right set, all mergers are prograde-prograde, with pericenter distances of 25, 44, and 100 kpc from left to right. The trends are that central velocity dispersion and rotation drop with eccentricity, and central velocity dispersion rises gently with increasing pericenter distance. One remnant (the R-R case with an impact parameter of 11 kpc) shows a significant $v - h_3$ anti-correlation, but the other remnants show a weak or non-existent $v - h_3$ anti-correlation.

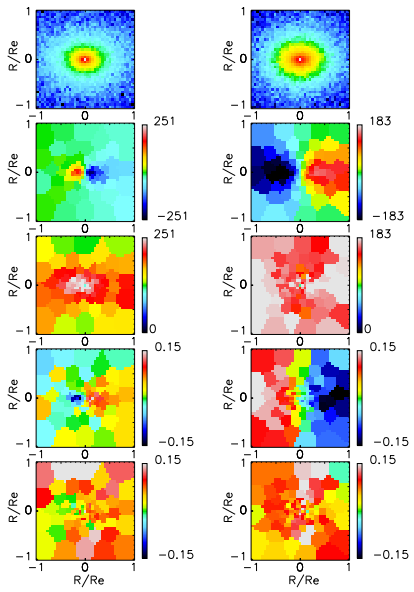

Figure 3.17: Zero angular momentum orbits. On the left, a parabolic orbit with a pericenter distance of 3 kpc. On the right, a bound orbit where the galaxies start out nearly at rest at a distance of 200 kpc.

of galaxy merger remnants were solely determined by conservation of energy and angular momentum, then one would expect that these galaxies would not rotate at all. In one case, that expectation is nearly correct, but in the other there is quite robust rotation.

Figures 3.18 and 3.19 show the effect of the supernova feedback recipe on the kinematic structure of the merger remnants. In these simulations, feedback is parameterized by two parameters: n, giving the effective polytropic index of the equation of state of star forming gas, and τ_{fb}, giving the timescale over which energy injected into the gas by supernovae is thermalized. A particular scheme is specified by choosing one of n0, n1, and n2 (indicating the value of n) as well as one of low, med, high (indicating that $\tau_{fb} = 0.83$, 8.3, and 83 Myr, respectively. See Cox et al. (2006b) for details.

The feedback recipe has its most dramatic effect on the central velocity dispersion of the remnants. The central velocity dispersion declines by 20-30% in going from $\tau_{fb} = 8.3$ Myr

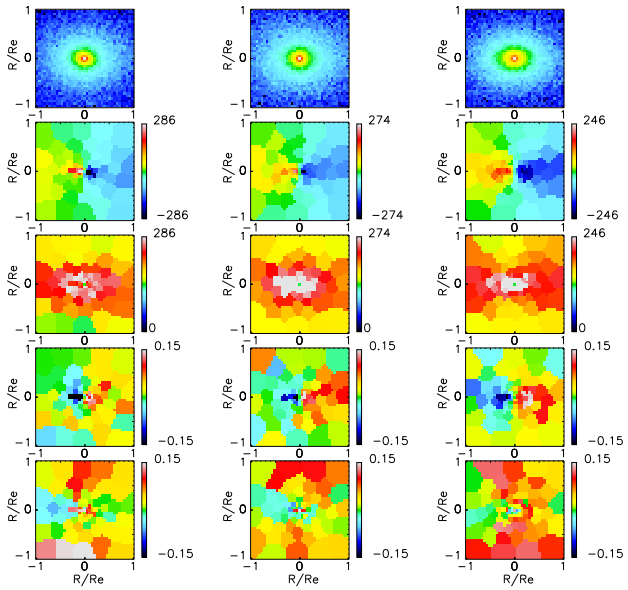

Figure 3.18: Effect of different supernova feedback parameter sets. From the left, the feedback parameter sets are *n0med*, *n1med*, and *n2med*. The main effect is that the central velocity dispersion declines with increasing n

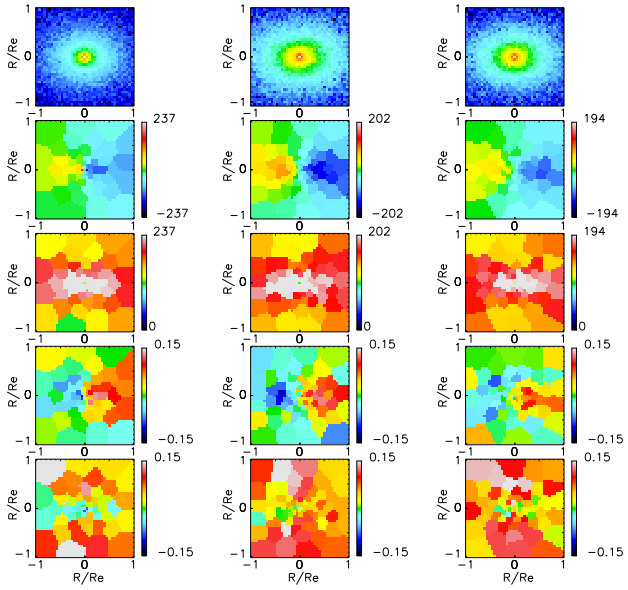

Figure 3.19: Effect of different supernova feedback parameter sets. From the left, the feedback parameter sets are *n0high*, *n1high*, and *n2high*. As in Figure 3.18, the central velocity dispersion declines with increasing n. Comparing to Figure 3.18, it is clear that the central velocity dispersion declines dramatically with increasing τ_{fb}.

to 83 Myr. It also declines somewhat more gently as a function of n: from 5 to 20 %. The velocity structure is similar in all cases, with significant, but not dramatic, variation in v/σ.

Figures 3.20 and 3.21 show equal mass major merger remnants as a function of mass for the series of simulations with G-series progenitors. The G-series remnants generally show less rotation because their gas fractions are lower than the *Sbc*-series of mergers. Gas in a merger simulation is able to cool and sink to the center of the remnant, resulting in a more compact object with higher rotation given the same total angular momentum. Nevertheless, the $G3$-$G3$ and $G2$-$G2$ mergers show clear rotation with one exception: the $G3$-$G3$ merger with bulgeless progenitors. This is in agreement with the González-García & Balcells (2005) result that progenitors with compact bulges result in remnants with higher rotation.

This is surprising given that the bulge contains such a small fraction of the mass of each progenitor. The only thing that makes the bulge special is its density compared to the other components of each remnant. It serves to prevent instabilities near the center of each gas disk. The high density of the two bulges in each galaxy means that the bulges readily "find" each other, merge, and sink to the center (indeed, *define* the center) of the remnant. The lack of such a bulge means that there is less of a preferred location defining the center of the remnant. There is also significantly less mass enclosed in a small sphere near the center, reducing the circular velocity.

The $G1$-$G1$ and $G0$-$G0$ remnants show relatively indistinct kinematic structure. The prograde-prograde mergers show virtually no rotation, while the retrograde-retrograde show clear, but somewhat disordered rotation.

Figure 3.22 shows kinematic data for dissipationless simulations. Note that the scale length of the gas disk in the progenitors is set to three times the scale length of the stellar disk, so changing the gas disk into stars does not correspond to simply erasing the gas disk

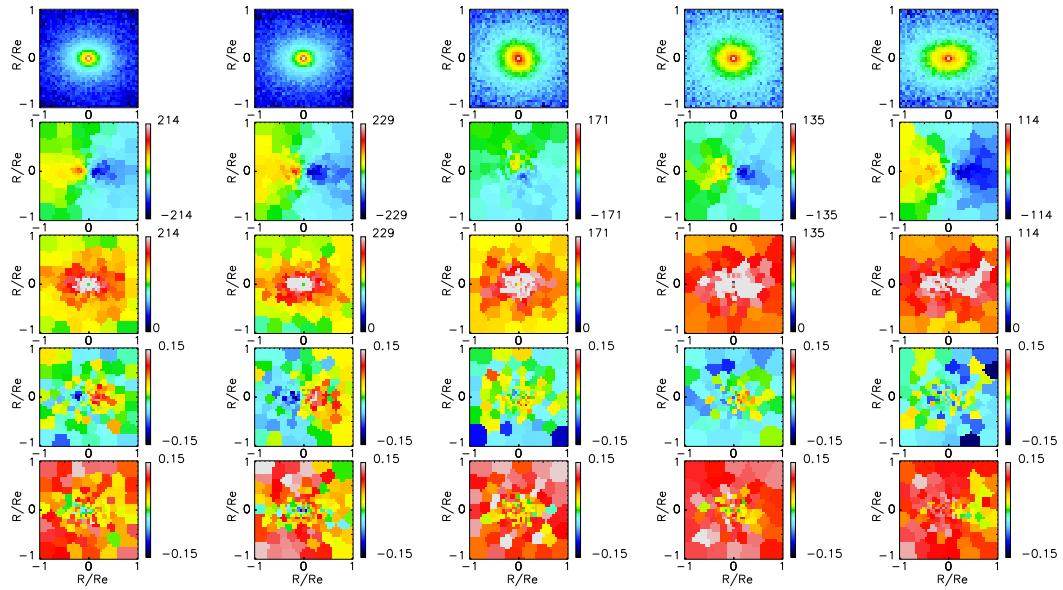

Figure 3.20: $G3$-$G3$ and $G2$-$G2$ equal mass major mergers. The four plots on the left are $G3$-$G3$ mergers, while the two on the right are $G2$-$G2$. From the left: a slightly bound orbit, then retrograde, then bulgeless progenitors. The two remnants on the right are $G2$-$G2$ major mergers, prograde on the left and retrograde on the right.

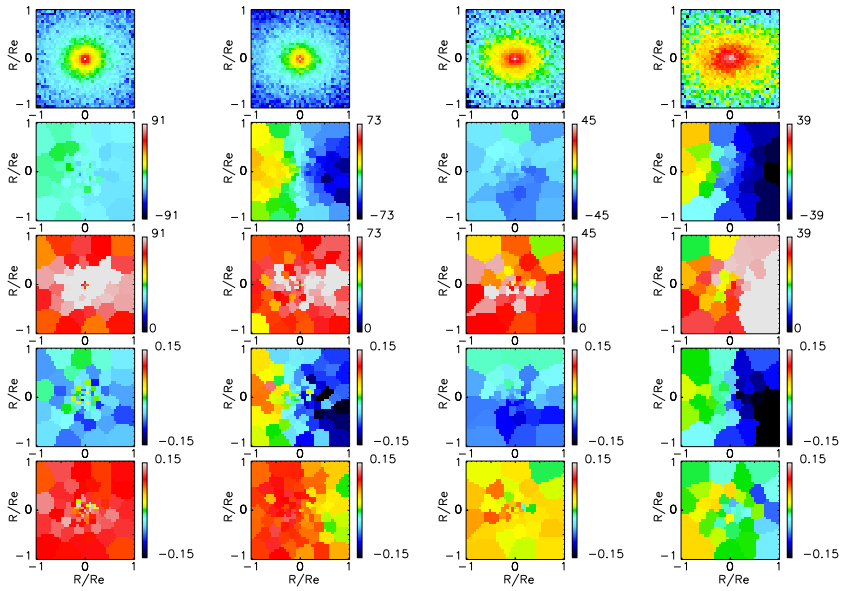

Figure 3.21: $G1$-$G1$ and $G0$-$G0$ equal mass major mergers. All of the orbits are slightly bound, with eccentricities of 0.9. From the left, $G1$-$G1$ prograde, $G1$-$G1$ retrograde, $G0$-$G0$ prograde, and $G0$-$G0$ retrograde.

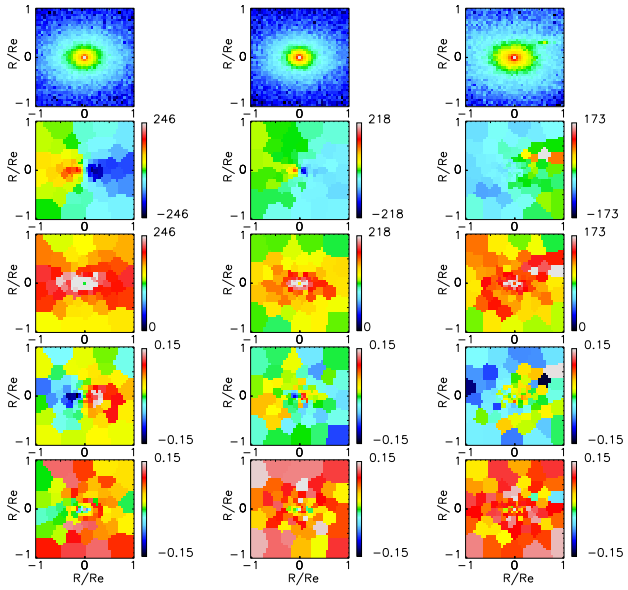

Figure 3.22: Dissipationless *Sbc* merger remnants. Here one or both of the progenitor galaxies has had its gas disk replaced by collisionless particles. From left to right, remnants where both of the progenitors have gas disks, only one has a gas disk, and neither progenitor has a gas disk. To make the progenitors without gas disks, the particles in the *Sbc* gas disk were simply converted to star particles. The projected effective radii of the remnants are from 4.12, 10.4, and 17.8 kpc, respectively. The rotation drops distinctly and the central velocity dispersion drops by a total of 28%.

and scaling up the mass of the stellar disk. Nevertheless the results are illuminating. Gas-free progenitors result in large remnants with little rotation. This is in line with the much more exhaustive study of dissipationless remnants by Naab & Burkert (2003).

Finally, Figure 3.23 shows the effect of varying the gas fraction in the $G3$-$G3$ major merger. Increasing the gas fraction leads to a compact, quickly-rotating stellar remnant.

3.4 Kinemetry

Kinemetry is a generalization of photometry designed to work with higher order moments of the LOSVD (Krajnović et al., 2006). One may think of the luminosity as the zeroth order moment of the LOSVD, simply summing up the light emitted by all stars along

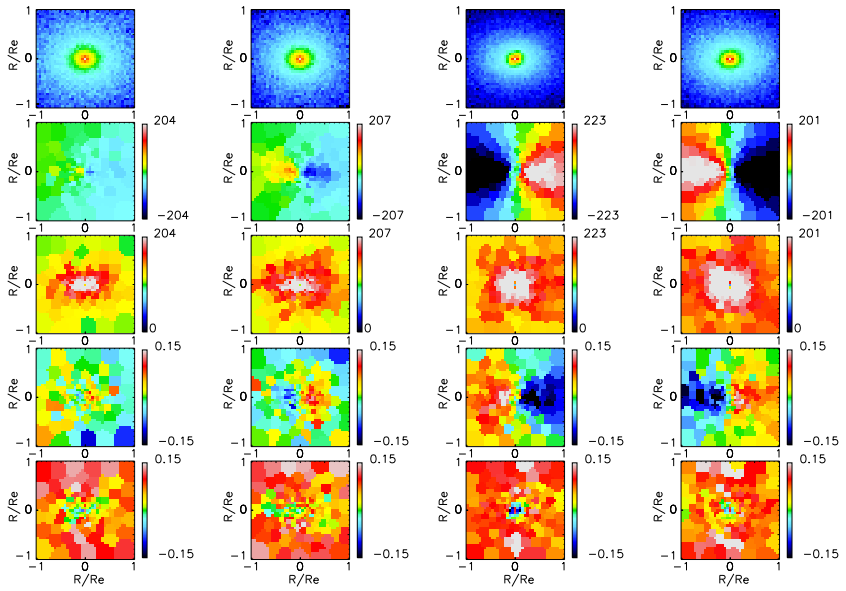

Figure 3.23: The effect of different gas fractions. From the left, gas fractions are 10%, 20%, 58%, and 75%. Note that these plots are scaled to the projected effective radius for each remnant, which is from right to left: 4.6, 3.7, 1.5, and 1.3 kpc. Clearly, gas-rich progenitors lead to very compact, fast-rotating remnants. Increasing gas fractions also make the $v - h_3$ anti-correlation more distinct.

a line of sight: $\int f(v)\,dv$. Streaming velocity, then, is the first moment: $\int vf(v)\,dv$ and so on.

Photometry has been useful in compactly characterising the appearance of early-type galaxies because the isophotes are so close to ellipses. It is then possible to provide a good, quantitative, compact representation of a galaxy's image by specifying the flattening and position angle of the ellipses as a function of radius, perhaps along with a quantity parameterizing deviations from perfect ellipses such as a_4 (Bender et al., 1988).

3.4.1 Method

In order to define a useful representation of LOSVD moments, it is necessary to choose a similar "baseline mode" that is a good representation of the typical behavior of the LOSVD moments. Even moments of the LOSVD ($\int v^n f(v)\,dv$ where n is even) tend to be symmetric under reflections about the projected short axis of the galaxy. Therefore ellipses continue to be a good baseline model for them. The expansion should vary the position angle and flattening of an ellipse to find a curve of constant surface brightness, velocity dispersion, or h_4.

By contrast, the odd moments of the LOSVD are typically antisymmetric under reflections through the projected short axis of the galaxy. Krajnović et al. (2006) therefore chose a cosine law as the baseline model in this case. That is, the algorithm is to vary the position angle and flattening of an ellipse so that the line-of-sight velocity along the ellipse satisfies a cosine law. For flattened, inclined, thin disks, the line-of-sight velocity along a (three-dimensional) circle in the plane of the disk satisfies a cosine law, and the projection of the circle is an ellipse.

Therefore, if the objects under study are thin disks, the choice of a cosine law as the baseline model makes the flattening and position angle of the fitted ellipses readily interpretable

in terms of the inclination and orientation of the disk. Elliptical galaxies are not thin disks, so there is no *a priori* guarantee that the baseline model will provide a good fit to the behavior of integral field data from actual galaxies, and there is no guarantee that the coefficients will be easily interpretable. Nevertheless, in practice the expansion seems to work quite well and compactly summarizes the salient features of the integral field data.

Concretely, for a given LOSVD moment $\psi(x, y)$ where x, y are projected positions on the sky, and a given major axis length a, choose a minor axis length p and position angle ϕ, and center x_0, y_0, determining a parametric curve of x and y values: $(x, y) = (a\cos(t + \phi) + x_0, b\sin(t + \phi) + y_0)$. Extract the value of ψ along the ellipse: $\psi(t) = \psi(x(t), y(t))$. Fourier expand the difference between $\psi(t)$ and the baseline model $M(t)$ (either a constant for even moments or $M(t) = \cos t$ for odd moments) to some order n:

$$\psi(t) - M(t) = A_0 + \Sigma_{k=1}^{n} A_k \sin kt + B_k \cos kt \tag{3.1}$$

Now allow b, ϕ, x_0, and y_0 to change until the ellipse matches the model as closely as possible.

For even moments, the criterion for choosing b, ϕ, x_0, and y_0 is that the combination $A_1^2 + B_1^2 + A_2^2 + B_2^2$ should be minimized. This is easily understood by applying trigonometric identities to re-write these four terms of the expansion in terms of $x = r\cos\theta$ and $y = r\sin\theta$, and then noting that these four terms in the expansion correspond to the first and second moments of position. Thus the ellipse is correctly centered and oriented when the first position moments vanish and the second moments are minimized.

For the odd LOSVD moments, some experimentation led Krajnović et al. (2006) to settle on the requirement that the combination $A_1^2 + A_2^2 + B_2^2 + A_3^2 + B_3^2$ be minimized. The absence of B_1 is related to the fact that a cosine model is being used as the baseline model, and the presence of A_3 and B_3 is simply because empirically these coefficients seem to be sensitive to mis-oriented ellipses in the case of odd moments.

3.4.2 Previous Work

Jesseit et al. (2007) fit kinematic moments to a set of 1:1 and 3:1 mergers where the progenitors were gas-free or had 10% gas. Their analysis focused on doing a kinemetric expansion on the LOSVDs of a few galaxies with fine spacing in projected radius in order to detect kinematically decoupled components. They found that equal mass mergers with a dissipational component were necessary to produce counter rotating cores in merger remnants. Gas-free mergers and unequal mass-major mergers showed more regular kinematic structure, without multiple components.

Jesseit et al. (2007) also found that gas-free mergers do not produce the observed $v - h_3$ anti-correlation. Such merger remnants either have no correlation or else a *positive* correlation between the two quantities.

Krajnovic et al. (2008) fit kinemetric moments as a function of radius to the 48 SAURON early-type galaxies and found very similar behavior to the results presented here for fast rotators. They also found significant differences between slow and fast rotators in all moments of the LOSVDs, which they argue points to a different evolutionary path for the two populations. This is in good agreement with the findings of this study.

3.4.3 Results

Figure 3.24 shows kinemetric moments fit at half of the effective radius. As described above, the output of the kinemetry routine is the shape and orientation of an ellipse such that the line-of-sight velocity extracted along the ellipse is as close as possible to a cosine law. All of the remnants are viewed along the vector $\hat{x} + \hat{y} + \hat{z}$ where $\hat{x}$, $\hat{y}$, and $\hat{z}$ are the principal axes of the remnant.

This figure compactly summarizes the rotation of all of the remnants. A non-rotating,

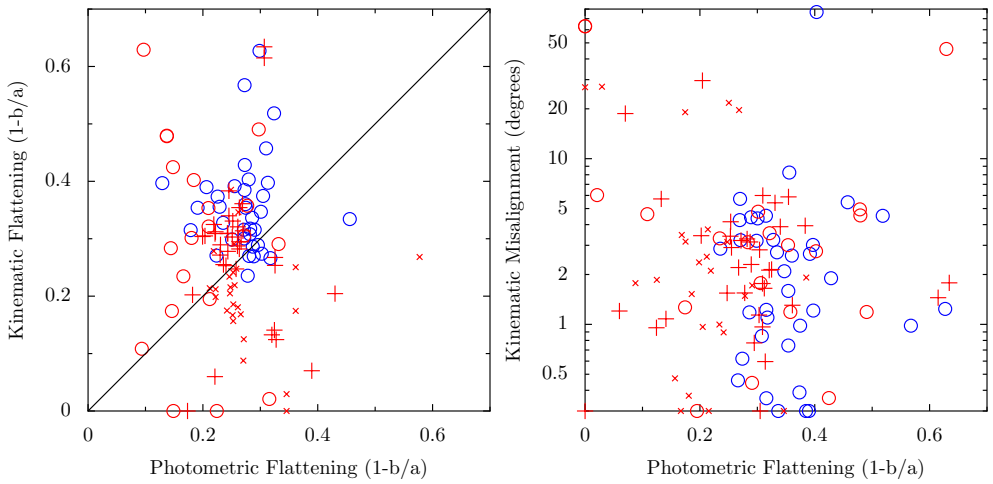

Figure 3.24: Kinemetric moments of the line-of-sight velocity data. On the left, kinemetric flattening versus photometric flattening. These two quantities would be equal if the objects under study were thin, rotating disks. There is not a one-to-one correlation between the two, but about half of the merger remnants do show similar values for the two quantities. On the right, kinematic misalignments. Only a small fraction of merger remnants show kinematic misalignments of greater than 10 degrees.

isotropic remnant would have both a photometric and a kinemetric flattening of nearly zero (near the origin in the left panel). A non-rotating remnant flattened by anisotropy would have non-zero photometric flattening but nearly zero kinemetric flattening (along the x-axis in the left panel). Thin disks should have a one-to-one correspondence between the photometric and kinemetric flattening. The actual merger remnants have non-zero, nearly equal photometric and kinemetric flattenings, with the mean photometric ellipticity around 0.25 and the mean kinemetric flattening around 0.3. This indicates that the great majority of merger remnants are flattened and rotating.

The left panel of Figure 3.24 shows kinematic misalignments in the merger remnants. Only a small fraction of merger remnants have more than 10 degrees between their kinematic and photometric axes.

Taken together, the two panels of Figure 3.24 show that the great majority of gas-

rich binary merger remnants are rotating, and that the axis of rotation is aligned with the photometric axis.

3.5 Conclusions

The many SAURON-style plots in Section 3.3, as well as the kinemetric moments for all merger remnants presented in Section 3.4 show that the current sample of gas-rich hydrodynamic merger remnant simulations plausibly correspond to the SAURON fast-rotators. However, there are very few galaxies in the sample with little rotation, and none at the upper end of the mass range. The origin of massive, non-rotating early-type galaxies remains, at the moment, a mystery.

A standard suggestion is that perhaps these massive galaxies formed via dry mergers. Dry mergers can only decrease their phase-space density (Hernquist et al., 1993), so such mergers have relatively large effective radii. The angular momentum in a typical merger simulation is dominated by the orbit of the two galaxies, so it is reasonable to guess that the remnant produced by a dry merger will have similar total angular momentum to that produced by a gas-rich merger. However, the larger effective radius of the dry merger means that the rotation velocity of the remnant will be smaller. Thus at least the argument goes in the right direction. However, most of the galaxies in Figure 3.6 show *remarkably* little rotation, consistent with zero to the level of $\sim 1\%$. Low but nonzero rotation velocities would have been easily seen by the SAURON survey.

Projection effects on the rotation velocity cannot be the culprit. If the slow rotators were intrinsically rotating (either slowly or quickly) but simply happen to be seen face-on, one would expect at most one case in the SAURON survey. In fact 20% of the SAURON galaxies are slow rotators. The SAURON survey has a non-trivial selection function (de Zeeuw et al.,

2002) and is therefore not a statistically unbiased sample, so this does not mean that 20% of *all* early-type galaxies are slow rotators. However, the number is much too high to be accounted for by projection effects. Therefore the slow rotators must be intrinsically non-rotating.

If the slow-rotators were intrinsically rotating, then their definition as a class of objects would mean they were seen nearly face-on and therefore should have preferentially round projected shapes. However, if they are intrinsically non-rotating as I just argued, then they are not expected to be viewed from a preferred direction and hence their projected shapes are not biased with respect to their three-dimensional shapes. The projected shape of the slow rotators is nearly round (Cappellari et al., 2007), indicating that the three-dimensional shape of these galaxies is nearly spherical. Schwarzschild modeling of the LOSVDs of these galaxies indicates that they do, indeed, have nearly isotropic velocity dispersion tensors (Cappellari et al., 2007), expected if a self-gravitating, non-rotating object is to have a spherical intrinsic shape.

These galaxies thus nearly spherical, nearly isotropic, non-rotating objects. This bears on the possibility of their origin via dry major mergers because such mergers produce *triaxial* remnants (Naab & Burkert, 2003). Objects that are intrinsically triaxial appear round from very few viewing angles (Binney & de Vaucouleurs, 1981), so as a population, the slow rotators cannot have been formed by dry major mergers of galaxies. In Chapter 4 I will try to make headway on this problem.

3.5.1 Future Work

Issues that must be addressed in immediate future work in order to prepare this chapter for publication are:

- I need a compact way of summarizing information about the kinematics of more than

100 merger remnants from many viewing angles. Kinemetry may provide this, but I have not yet fully exploited it.

- I need a better digested, more complete, quantitative understanding of how merger orbit influences the kinematic structure of merger remnants. For example, retrograde-retrograde mergers seem to result in more rotation in the final remnant, and central velocity dispersion seems to increase with n and decrease with $\tau_{\rm fb}$, but I will quantify these trends.

- So far I have only computed kinematic data for seven viewing angles and have not properly averaged them according to the probability with which each configuration will be seen.

- I need to think more carefully about how particle discreteness influences the error estimates in kinemetric moments.

- Do these remnants have velocity dispersion profiles that are in agreement with those seen in real galaxies?

- The bulgeless $G3$ progenitor seems to have quite different kinematics from the $G3$ progenitor that includes a bulge, in agreement with the findings of González-García & van Albada (2003). What is the bulge transition mass between these to outcomes? Does increasing the mass of the bulge result in yet different remnants?

- The low-mass G-series simulations seem to have indistinct kinematic structure. Is this due to the small number of particle in the simulation, or is it a real effect that scales with the mass of the progenitors?

- I have not systematically exploited the h_3 and h_4 coefficients. Many, but not all, of the remnants show the observed $V - h_3$ anticorrelation. Do the remnants that show little

$V - h_3$ anticorrelation have anything in common? The h_4 profiles are generally rotationally symmetric. Is it easier to extract meaningful information from the simulations by averaging h_4 in annuli?

- How accurate are the masses of sub-dominant "fossil" disks recovered from analysis of deviations from Gaussian LOSVDs (particularly positive h_4 values)?

- Some of the simulations have rather large positive h_4 values. Is this a problem?

This work leaves untouched many questions related to the integral-field kinematics of galaxies, some of which will be addressed in future papers:

- What are the kinematic characteristics of remnants produced by unequal-mass major mergers and minor mergers?

- Do integral-field measurements for in-progress simulated mergers correspond to what Puech et al. (2006) and Shapiro et al. (2008) believe to be in-progress mergers at high redshift?

- How do the large-radius (several effective radii) relate to the small-radius kinematics? What does the relationship between the two tell us about the history of the galaxy under study?

- Does a double-Gaussian fit to the LOSVD provide tangible benefits to observers compared to the Gauss-Hermite series?

- Do kinemetric moments as a function of radius reveal interesting information about the remnants?

- What is the effect of subsequent minor mergers on v, σ, and higher order moments?

Chapter 4

Galaxy Formation by Multiple Mergers

I just argued that binary mergers, whether dissipational or dissipationless, do not generate massive elliptical galaxies that are spherical and non-rotating. Binary major mergers of galaxies tend to produce remnants that are aspherical due to anisotropic velocity dispersion (Burkert & Naab, 2005). A more plausible formation mechanism for these massive elliptical galaxies is multiple mergers, either successive minor mergers or roughly simultaneous major mergers that are expected to happen in compact groups of galaxies. Both of these situations lack the "preferred direction" determined by the orbit of the galaxies in a binary merger, where the orbital angular momentum tends to produce fast-rotating systems.

An important goal of this work is to identify the relevant physical processes that lead to the formation of realistic spheroids. Therefore I have also run a series of companion simulations where the initial conditions are not from a cosmological simulation, but rather are idealized cases designed to focus on particular merger histories as possibly determining

the observable properties of the remnant. These will make it possible to effectively interpret the physical processes that are driving the "realistic" simulations to either resemble or not resemble observed massive elliptical galaxies.

There is observational evidence that they are in fact systems of galaxies with multiple mergers taking place simultaneously (Borne et al., 2000).

4.1 Motivation

Ideally, one would run a first-principles cosmological simulation all the way from initial conditions to final galaxies, but a simulation with sufficient resolution (100 pc instead of the 1 kpc that's the state of the art in cosmological simulations today) is computationally prohibitive. Therefore I am taking initial galaxy positions, velocities, and orientations from an adaptive-mesh hydrodynamic cosmological simulation and re-simulating the sub-region with higher resolution using the smoothed-particle-hydrodynamics code Gadget (Springel, 2005). Furthermore, current cosmological simulations have not produced realistic disk galaxies, although there have been some recent near-successes (e.g. Governato et al., 2007). Our method involving resimulation of a sub-region of a large cosmological simulation permits higher spatial resolution, and it allows more realistic initial galaxy models to be used.

The build-up of massive structures in the universe has been effectively characterized by dark matter merger trees from dissipationless simulations. However, cosmological simulations still lack sufficient spatial resolution to study the properties of the resulting galaxies. Therefore we will simulate five qualitatively different scenarios—three are idealized situations designed to cleanly separate the physically distinct possibilities; two are realistic models of how galaxies formed in our universe. They are as follows:

1) Sequential mergers of eight galaxies of identical mass. This is the idealized model

of a galaxy that grows primarily by minor mergers. The smaller galaxies are accreted onto the larger galaxy isotropically. 2) As in 1, but with anisotropic accretion of smaller galaxies along cosmological filaments. 3) Successive binary major mergers of the the same eight progenitor galaxies in a "binary tree," where each merger is between galaxies of equal mass 4) A realistic simulation of the merger history of a galaxy that grew mainly by minor mergers in a dissipationless cosmological simulation. Initial positions, velocities, and masses of the progenitor galaxies will be taken from the cosmological simulation. 5) A realistic simulation of a compact group of galaxies, where all of the mergers are happening simultaneously rather than sequentially.

We feel that simulating these five scenarios will allow us to effectively explore how the properties galaxies with different merger trees are differ (via the idealized situations). This program will also allow us to determine how closely actual galaxies can be expected to approach the idealized situations.

Roughly speaking, there are three ingredients to a simulation of a galaxy merger: 1) Physics included in the simulation, including schemes for implementing sub-resolution processes 2) Initial orbits and orientations of the galaxies, 3) An initial structural model for the progenitor galaxies. It is crucial to understanding that we be able to determine whether a given property of a simulated galaxy remnant depends on a particular one of these three ingredients.

The biggest physical uncertainties in galaxy merger simulations today are the effects of the cosmological environment and the effects of sub-resolution physics, specifically the effects of feedback from star formation and active galactic nuclei.

The cosmological environment must be important because normal star forming galaxies at high redshift have star formation rates of tens of solar masses per year (Noeske et al., 2007). At that rate, the gas consumption timescale for a typical galaxy is so short that merging

galaxies would consume a significant fraction of their before they even have a chance to merge (Cox et al., 2008). Gas must be replenished by the local environment, perhaps as cold flows (Dekel & Birnboim, 2006).

It is important to note that the character of the problem changes considerably when considering minor mergers. With mass ratios between 1:1 and perhaps 1:10, it makes sense to simulate individual galaxy encounters. However, for lower mass encounters the interesting question is not the effect of a single merger but the cumulative effect of many small mergers. Then the parameters of the orbit of an individual small galaxy are not as important as the *distribution* of such parameters. Furthermore, in an individual simulation many such mergers would occur and would help to reduce the dependence of the result on any one small galaxy. That is, if each simulation involves 10 minor mergers, then an impractical approach would be to consider the orbits of each individual small galaxy as separate parameters that must be explored. However, the fact that there are many mergers means that the orbits of the individual mergers are only important in a statistical sense. Thus it is important to run several realizations of a multiple merger simulation, but it is not important to quantify the sensitivity of the result to the exact parameters of each merger orbit. Thus multiple mergers help to reduce the dimensionality of the input space rather than causing it to explode.

4.2 Previous Work

The characteristics of galaxies resulting from multiple simultaneous mergers has been studied in only a few earlier works (Weil & Hernquist, 1996; Bournaud et al., 2007; Li et al., 2007; Naab et al., 2007).

Weil & Hernquist (1996) performed dissipationless simulations of multiple mergers in groups of up to six progenitors as well as mergers of pairs of galaxies for comparison. They

found that multiple merger remnants were nearly spherical, and that multiple mergers resulted in remnants that were less dense than pair mergers.

Li et al. (2007) ran galaxy merger simulations with initial conditions taken from a cosmological simulation and chosen to match the progenitors of the most massive halo at $z = 0$. They are thus focused on very rare objects, studying the material that will make up the most massive galaxy in a rich cluster today.

Naab et al. (2007) ran simulations starting from cosmological initial conditions but with a focus on lower-mass galaxies selected to be similar to typical massive ellipticals today. Their simulations showed very promising results, resulting in a round, nearly isotropic object. Compared to this work, they started at higher redshift, did not insert model galaxies, and did not include star formation feedback. Neither this work nor their work includes the effects of AGN accretion or feedback. I believe that this work is quite complementary to theirs and facilitates interesting comparisons.

Bournaud et al. (2007) considered sequential mergers of galaxies to build up the same total mass independent of the mass ratio of the mergers. That is, they compared remnants produced by a single 1:1 merger, two 2:1 mergers, five 5:1 mergers, ten 10:1 mergers, and so on. Their work is very similar in motivation to the work presented here. The main methodological difference is that they used a sticky-particle scheme to represent gas physics (Bournaud & Combes, 2002). They found that the main difference in building up mass using increasingly small progenitors is that the anisotropy of the remnant rises.

Martig et al. (2008) is currently performing work very similar to this work. They take output from an adaptive-mesh cosmological simulation, replace baryonic density peaks with model galaxies, and re-simulate with higher spatial and mass resolution than the cosmological simulation. The main difference is again that they use a sticky-particle scheme to represent

gas physics.

4.3 Methods

I used the same Smoothed Particle Hydrodynamics code GADGET described in Section 2.2. In addition, some of the simulations described in this chapter use a density dependent pressure floor designed to ensure that each mass element resolves a specified number of Jeans masses (Robertson & Kravtsov, 2008). I implemented this because we were concerned that the large amount of fragmentation of gas into discrete lumps was artificial. I tried setting the pressure floor to ensure that each SPH kernel corresponded to at least 15 or 45 Jeans masses. In both cases, there was little effect on the degree of gas fragmentation. One is left to conclude that the fragmentation in the simulations is caused by the actual Jeans instability rather than a numerical instability caused by insufficient resolution.

Even though there is little effect on the simulations, ensuring that the Jeans mass is resolved makes good sense. Therefore I chose to set the relevant parameter to resolve 15 Jeans masses.

The simulations that use the density-dependent pressure floor are the ones named cos1-2, cos2-2, cos3-2, cos5-2, cos8-2, and cos9-2. This is the "second" series of simulations with cosmological initial conditions described in Section 4.5.5.1. All of the other simulations described here *do not* use this pressure floor.

4.3.1 Mass Build-up Scenarios

I would like to characterize the differences between galaxies whose mass is built up in different ways. Figure 4.1 schematically shows one limiting case where a galaxy is built up via equal mass major mergers. Figure 4.2 shows the opposite limiting case where a galaxy is

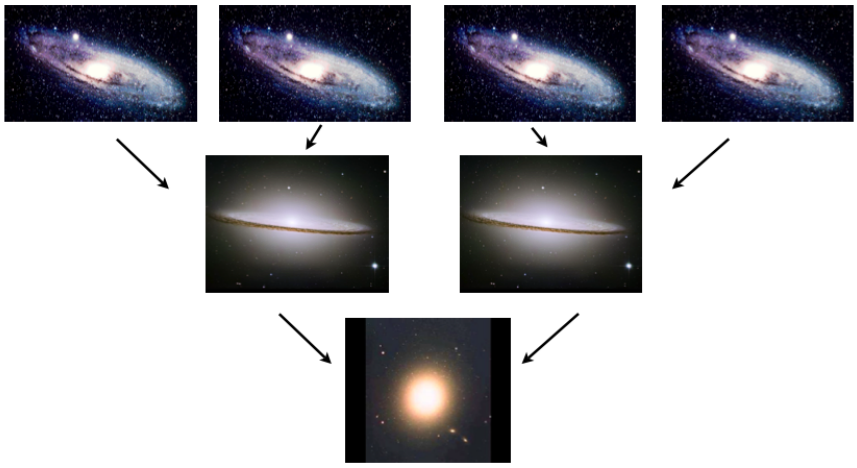

Figure 4.1: Major Mergers

built up via sequential minor mergers.

Minor mergers are thought to be very common. Roughly equal mass major mergers are thought to be rare when structure forms hierarchically. This is especially true as the galaxy's mass increases because equal mass partners with which it can merger get exceedingly rare. Even if major mergers are rare, we saw in Chapter 3 that they have a large effect on the kinematics of the resulting remnant. That is, a single major merger can cancel out the effect of many minor mergers.

Regardless of their frequency, the scenarios outlined above are interesting because they are designed to bracket reality. In the actual universe, both major and minor mergers happen in a haphazard fashion, represented schematically in Figure 4.3.

I have run simulations where the initial conditions are taken from a larger-scale cosmological simulation in order to gain some insight into how much galaxies produced by realistic initial conditions differ from more idealized initial conditions.

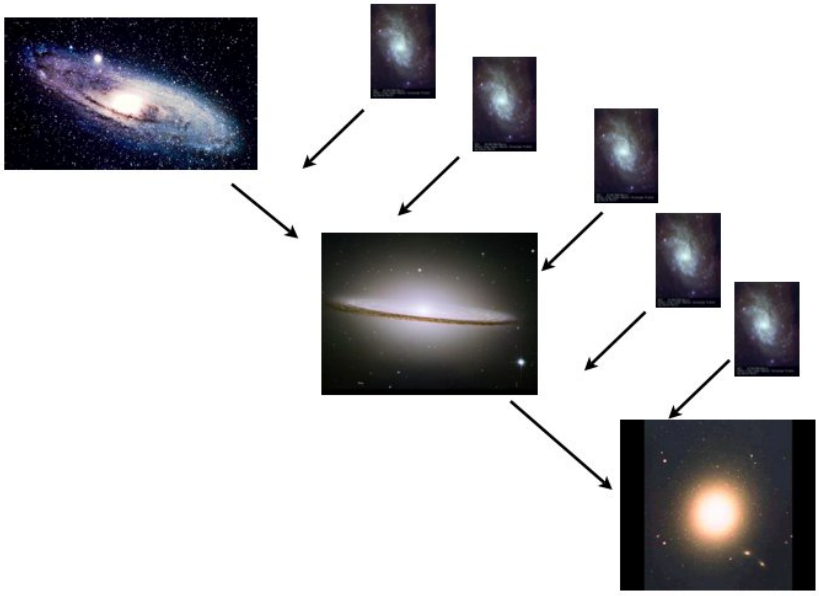

Figure 4.2: Minor Mergers

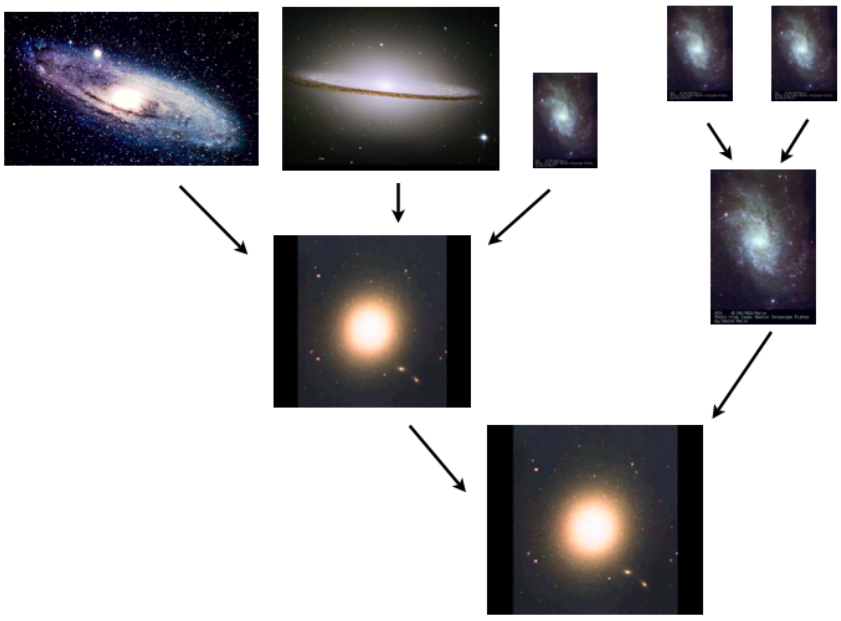

Figure 4.3: Cosmological Initial Conditions

4.4 Idealized Cases

In order to build intuition about the remnants produced by multiple galaxy mergers, I first consider the "idealized" cases represented by Figures 4.1 and 4.2. These are in no sense realistic scenarios given present knowledge of the mass build-up of galaxies through simulation and semi-analytic modeling. The purpose of this part of the study is to learn about the limiting cases to guide our understanding of the more complicated cases to be discussed below.

The most massive binary merger in the G-series of simulations is the $G3$-$G3$ merger, where the remnant has a baryonic mass of $1.2 \times 10^{11} M_{\odot}$ and a dark mass of $2.2 \times 10^{12} M_{\odot}$. In order to end up in the same mass range, I consider simulations involving 4 $G2$ galaxies ($m_b = 7.9 \times 10^{10} M_{\odot}$, $m_d = 2.0 \times 10^{12} M_{\odot}$) and 8 $G1$ galaxies ($m_b = 5.6 \times 10^{10} M_{\odot}$, $m_d = 1.5 \times 10^{12} M_{\odot}$).

The orbit planes and disk orientations are chosen such that the normal vector is uniformly distributed over the unit sphere. The orbits are nearly parabolic, with eccentricities between 0.95 and 1.0. Using only parabolic orbits often resulted in encounters rather than mergers for two reasons. First, as observed in Cox (2004) for binary merger simulations, dynamical friction does not extract much energy in the first pass and the galaxies take a long time to merge. Second, it becomes possible to have a three-body encounter where one of the galaxies is put on a slightly hyperbolic orbit and never comes back. Using slightly bound orbits helps to ensure that all of the galaxies end up in a single remnant at the end of the simulation.

For each set of progenitors ($G2$ and $G1$), I simulated three realizations of the sequential and binary mass build-up schemes. Each realization had different orbit and disk orientations as well as different impact parameters. The impact parameters were chosen to be factor-of-two increases or decreases from the "fiducial" value of 3 kpc. See Table 4.1 for a complete list of simulation names and characteristics

Name	Progenitor	Number	Scheme	r_{peri}
$G1$-8s	$G1$	8	sequential	3.0
$G1$-8s-1	$G1$	8	sequential	1.5
$G1$-8s-3	$G1$	8	sequential	6.0
$G1$-8b	$G1$	8	binary	3.0
$G1$-8b-1	$G1$	8	binary	1.5
$G1$-8b-3	$G1$	8	binary	6.0
$G2$-4s	$G2$	4	sequential	3.0
$G2$-4s-1	$G2$	4	sequential	1.5
$G2$-4s-3	$G2$	4	sequential	6.0
$G2$-4b	$G2$	4	binary	3.0
$G2$-4b-1	$G2$	4	binary	1.5
$G2$-4b-3	$G2$	4	binary	6.0

Table 4.1: Idealized simulation characteristics

4.4.1 Four Galaxies

Figures 4.4 and 4.5 show the projected gas density in the $G2$-4b simulation where four $G2$ galaxies merge in a "binary tree" configuration. These plots show the initial conditions and evolution of the simulation for the purpose of providing some orientation for the reader. This simulation starts out with four $G2$ galaxies. The two pairs merge, and then the two remnants merge.

Figures 4.6 and 4.7 show the gas surface density in the $G2$-4s simulation. In this case the galaxies are supposed to merge one after another. This is basically what happens, but the mergers start to overlap because the next galaxy comes in before the previous one has had a chance to finish its merger. After a violent 2 Gyr, the remnant calms down.

The star formation rates for these two simulations are shown in Figure 4.8. The total star formation rate is peaks at about 10 $M_{\odot}$/yr in both cases, but in the binary merger case it is evenly divided between the two remnants at 1.5 Gyr, whereas in the sequential merger case the star formation is concentrated in the central remnant.

Figures 4.9 and 4.10 show kinematic data major merger and sequential merger cases

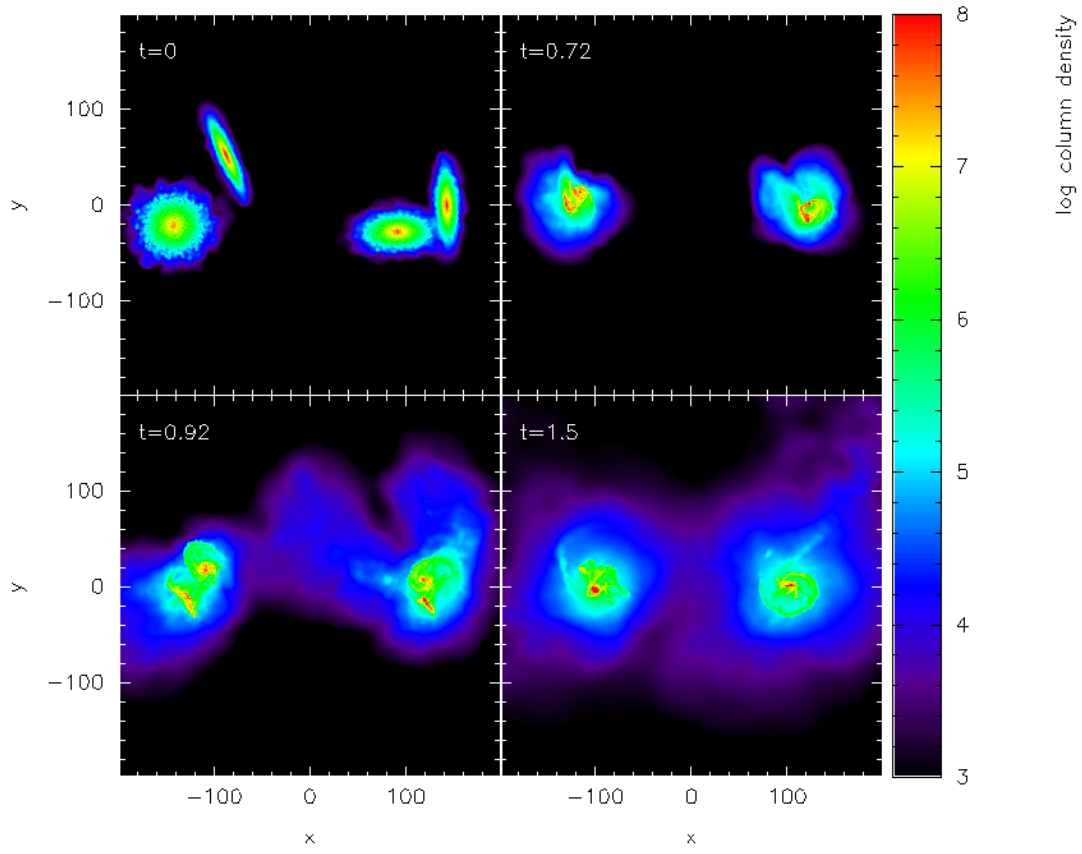

Figure 4.4: First set of mergers in the $G2$-4b simulation. As promised, the two pairs of $G2$ galaxies merge, producing two early-type systems. This and all similar plots show the x and y axis in kiloparsecs. The color shows the base 10 log of the gas column density in $M_{\odot}/\mathrm{kpc}^3$. This and all similar gas-density renderings in this chapter were produced with the software program Splash (Price, 2007)

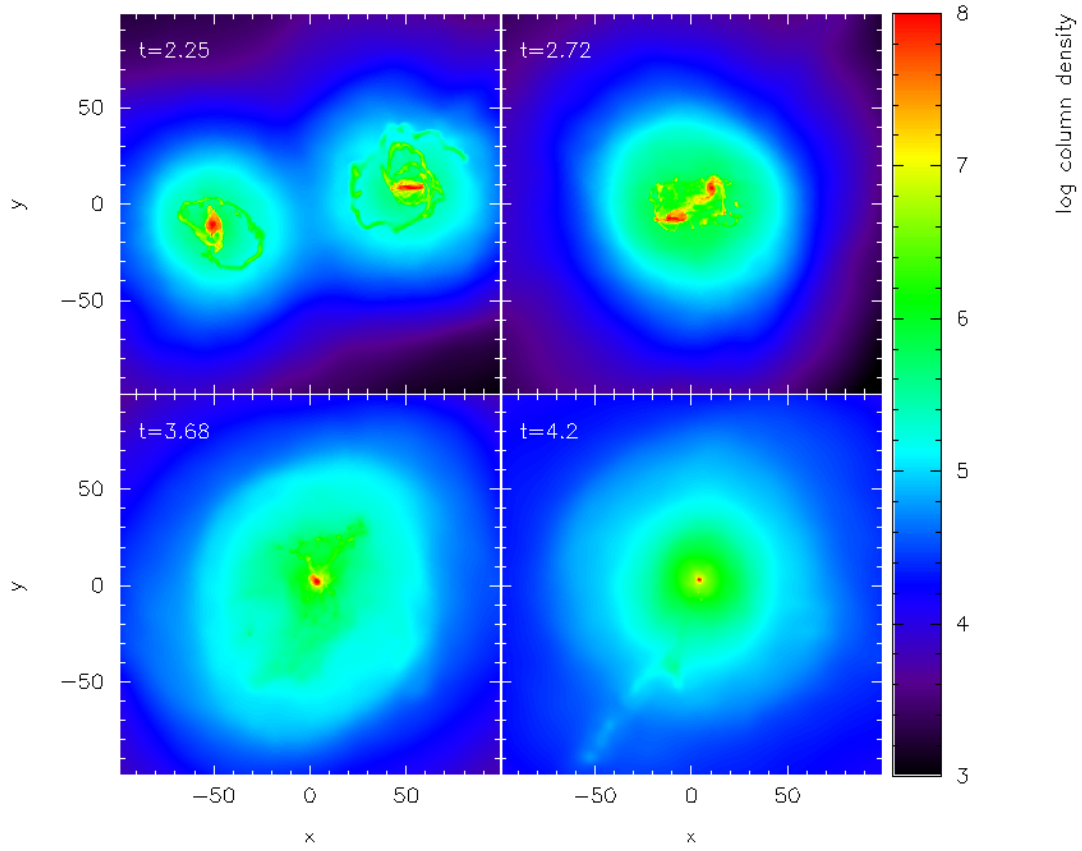

Figure 4.5: Final merger in the $G2$-4b simulation. Note that the scale is slightly zoomed in compared to Figure 4.4.

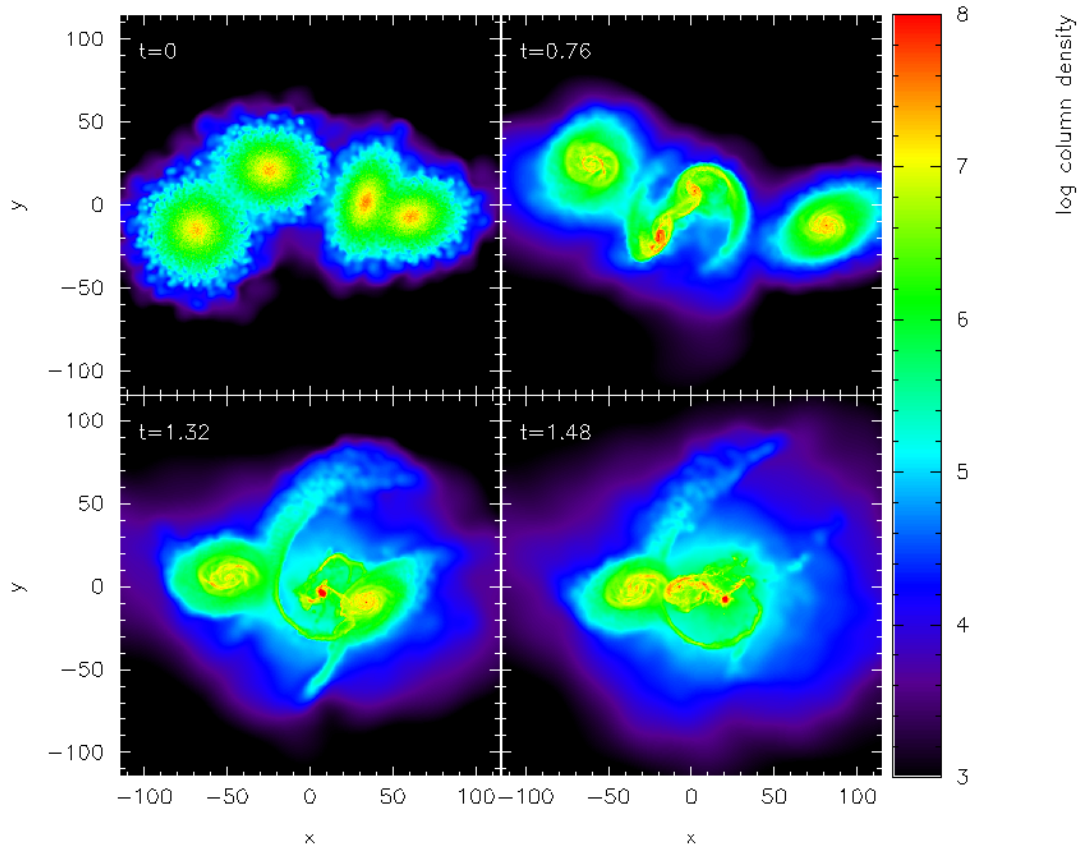

Figure 4.6: The first merger in the $G2$-4s simulation. The central two galaxies merge after 1.32 Gyr. The galaxy in the lower right at 1.32 Gyr has a close encounter with the central galaxy and is flung toward the incoming galaxy in the upper left.

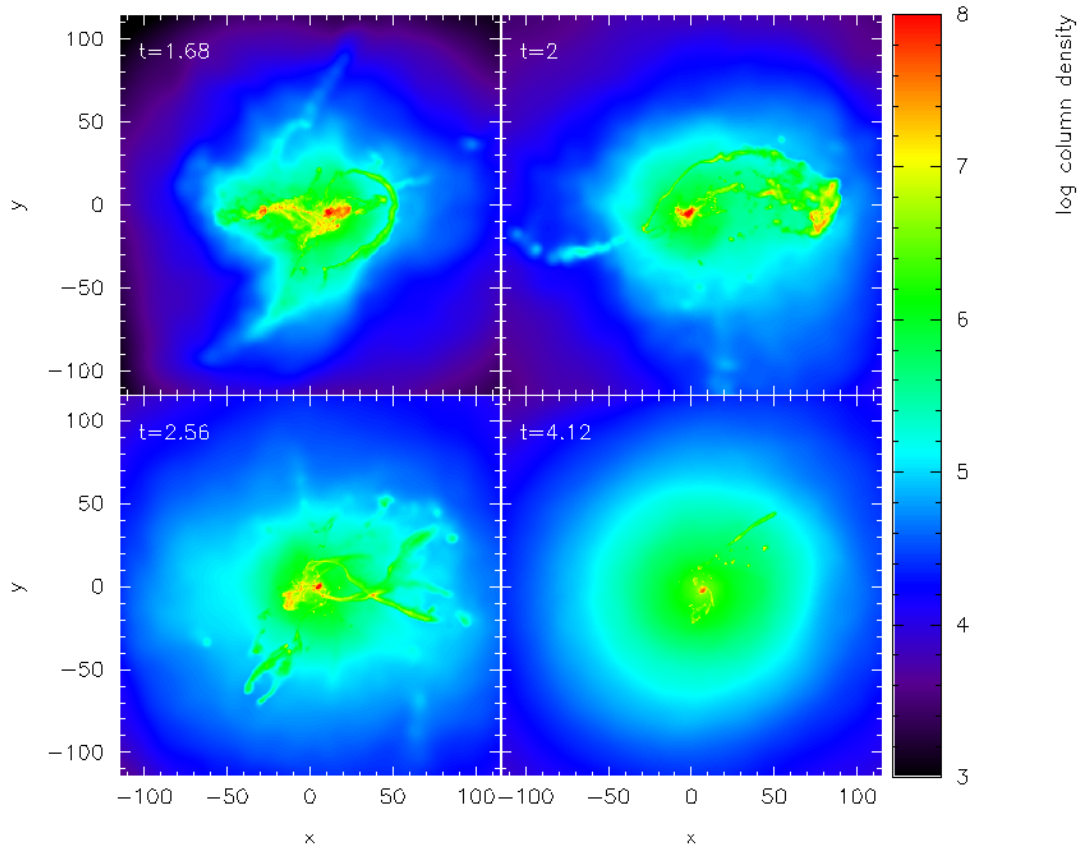

Figure 4.7: The final mergers in the $G2$-4s simulation. At 1.68 Gyr, the last progenitor is undergoing a close-passage with the central galaxy, and is on the right at 2 Gyr. The final merger is happening at 2.56 Gyr and the remnant calms down by 4 Gyr.

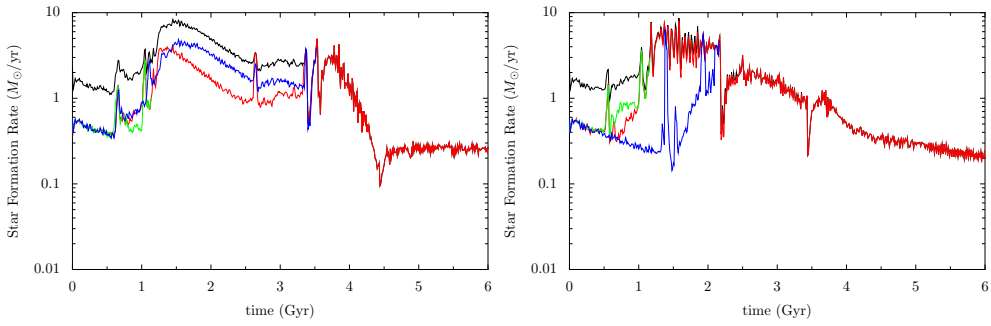

Figure 4.8: Star formation rates for the $G2$-4b simulation (left) and the $G2$-4s simulation (right).

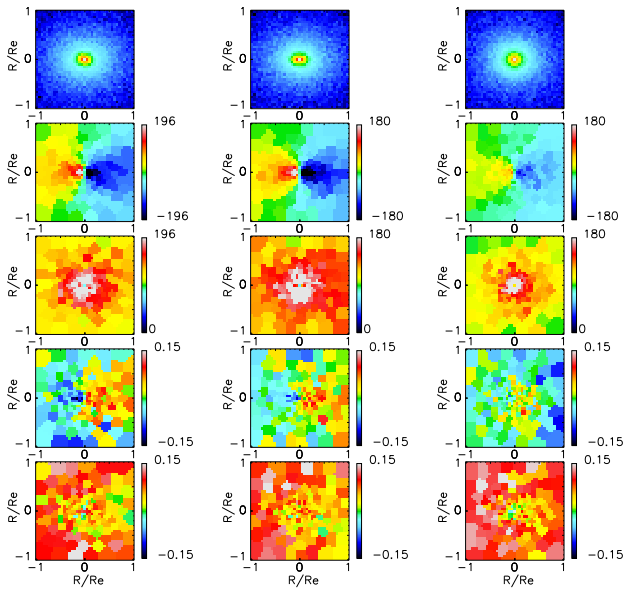

Figure 4.9: Kinematic data on the $G2$-4b simulations. From the left the impact parameters of the orbits are 1.5 kpc ($G2$-4b-1), 3 kpc ($G2$-4b) and 6 kpc ($G2$-4b-3). These remnants show significant rotation except for the case of the largest impact parameter where there is less rotation.

respectively. The trend is that there is *more* rotation in the binary tree of major mergers depicted in 4.1. The rotation also seems to be inversely correlated with the impact parameter, which is at first glance counter-intuitive since larger impact parameters mean larger orbital angular momentum. However, the large impact parameter cases also take longer to merge and have more encounters before finally merging. That is, there is more time and there are more events to change the structure of a disk galaxy into a more slowly rotating early-type galaxy when the impact parameter is large.

4.4.2 Eight Galaxies

Figures 4.11 and 4.12 show the evolution of the $G1$-8b simulation. Note that in the initial snapshot, the positions of the progenitors seem to fall largely along a line. This is an inherent feature of initial conditions where the progenitors are designed to merge in a binary

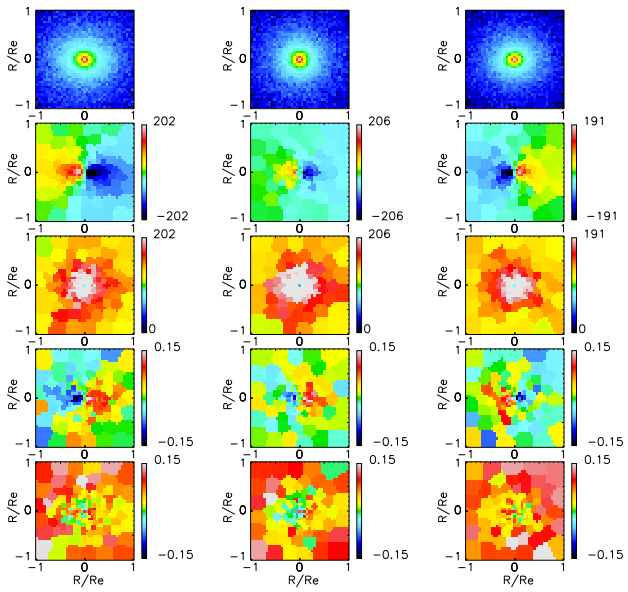

Figure 4.10: Kinematic data for the $G2$-4s simulations. Again, from the left the impact parameters are 1.5 kpc ($G2$-4s-1), 3 kpc ($G2$-4s) and 6 kpc ($G2$-4s-3). These remnants have higher central velocity dispersions and less rotation compared to those in Figure 4.9.

tree. To see this, consider the final merger of two remnants each composed of four previously merged progenitors. The centers of mass of the two sets of four galaxies must be separated by nearly 500 kpc at the start of the simulation to ensure that this is in fact the last merger that occurs. Other mergers in the binary tree must finish sooner, and the progenitors therefore have smaller initial separations. Therefore any realization of a binary tree merger history will start out with two clusters of half of the progenitors separated by a large distance.

Figures 4.13, 4.14, 4.15, and 4.16 show the evolution of the $G1$-8s simulation. With images of sixteen timesteps, I intended to make it possible to follow the path of each galaxy from one frame to the next. However, that is quite difficult and the conclusion is mainly that the galaxies undergo complicated evolution from 1.2 to 4.2 Gyr. Then another 1.5 Gyr passes before the last few galaxies finally merge and the main remnant can settle down.

Figure 4.17 shows the star formation rates for the $G1$-8b and $G1$-8s simulations. As

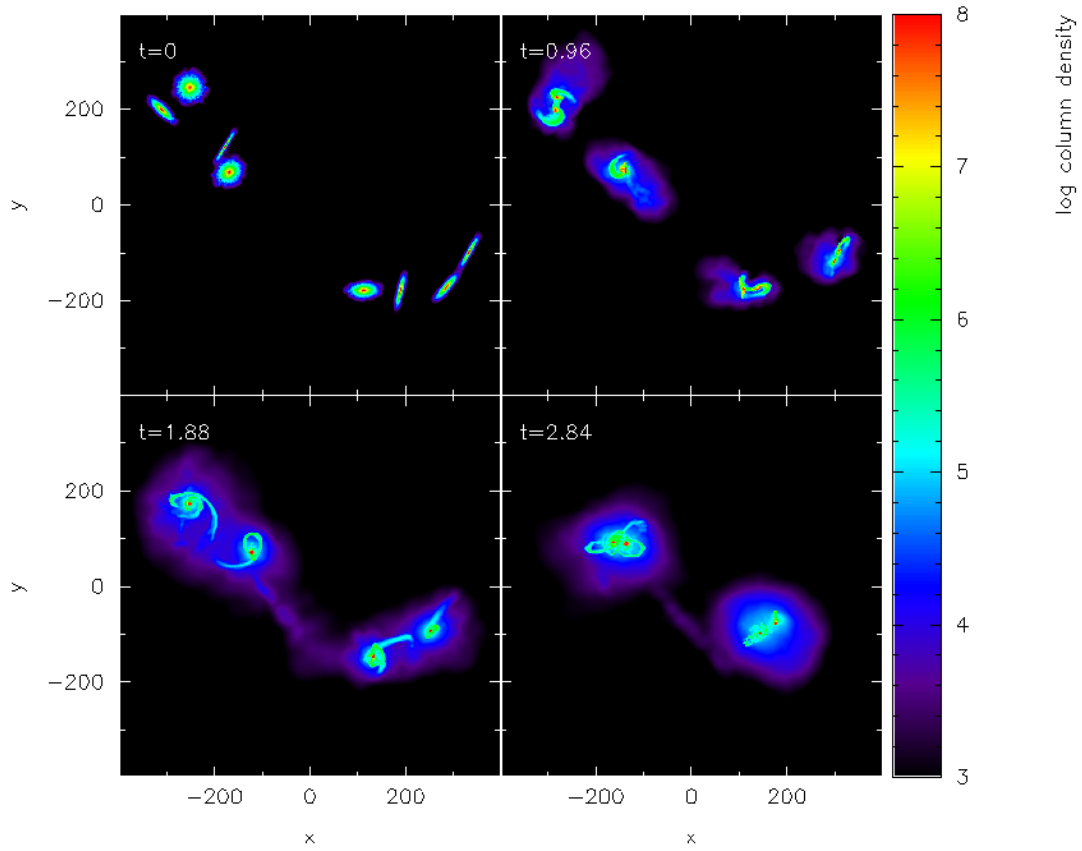

Figure 4.11: The first two sets of mergers in the $G1$-8b simulation with 8 $G1$ galaxies set up to merge in a binary tree. After 1 Gyr, the four pairs have merged, and at 2.8 Gyr the two pairs of remnants have nearly merged.

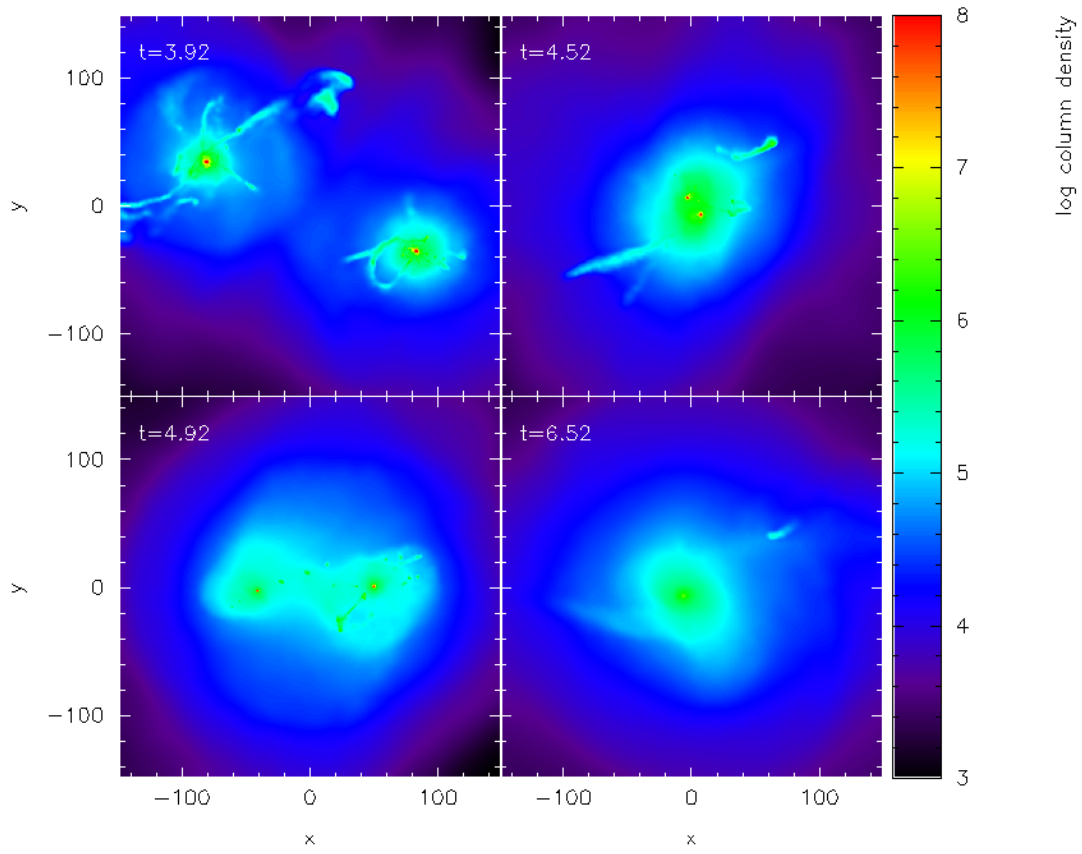

Figure 4.12: The final merger in the $G1$-8b simulation.

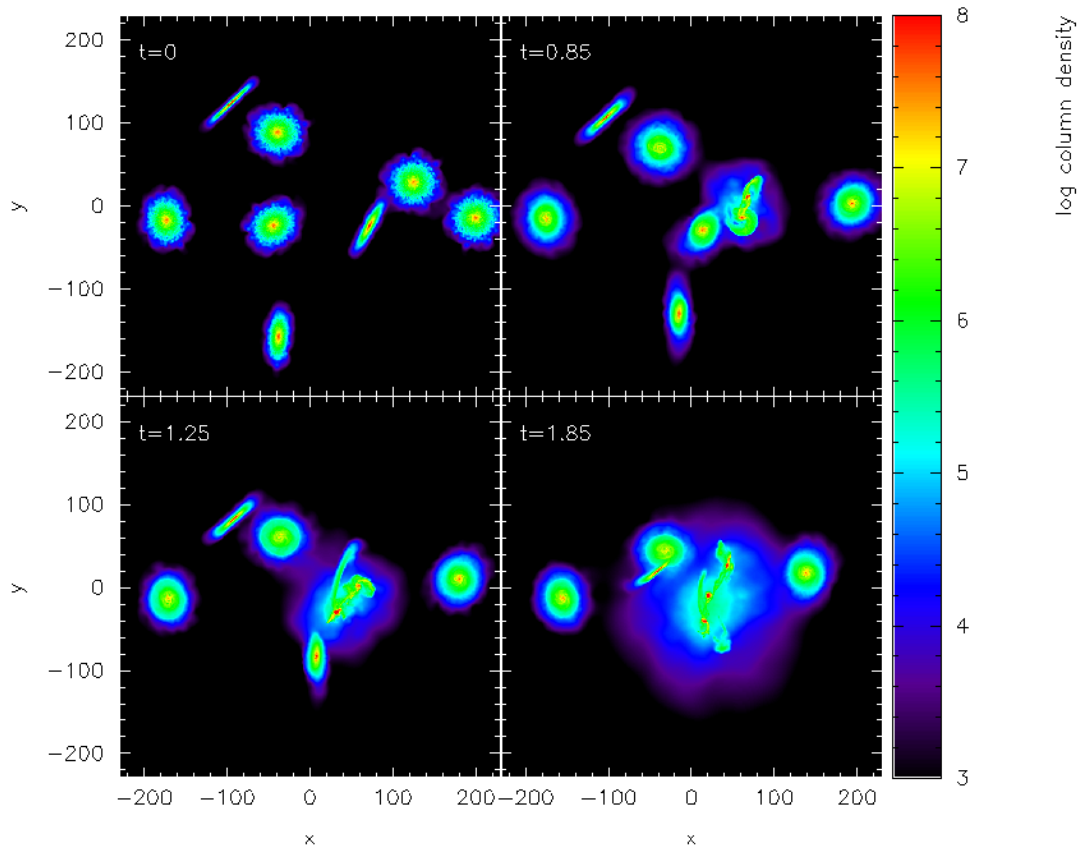

Figure 4.13: The first several mergers in the $G1$-8s simulation.

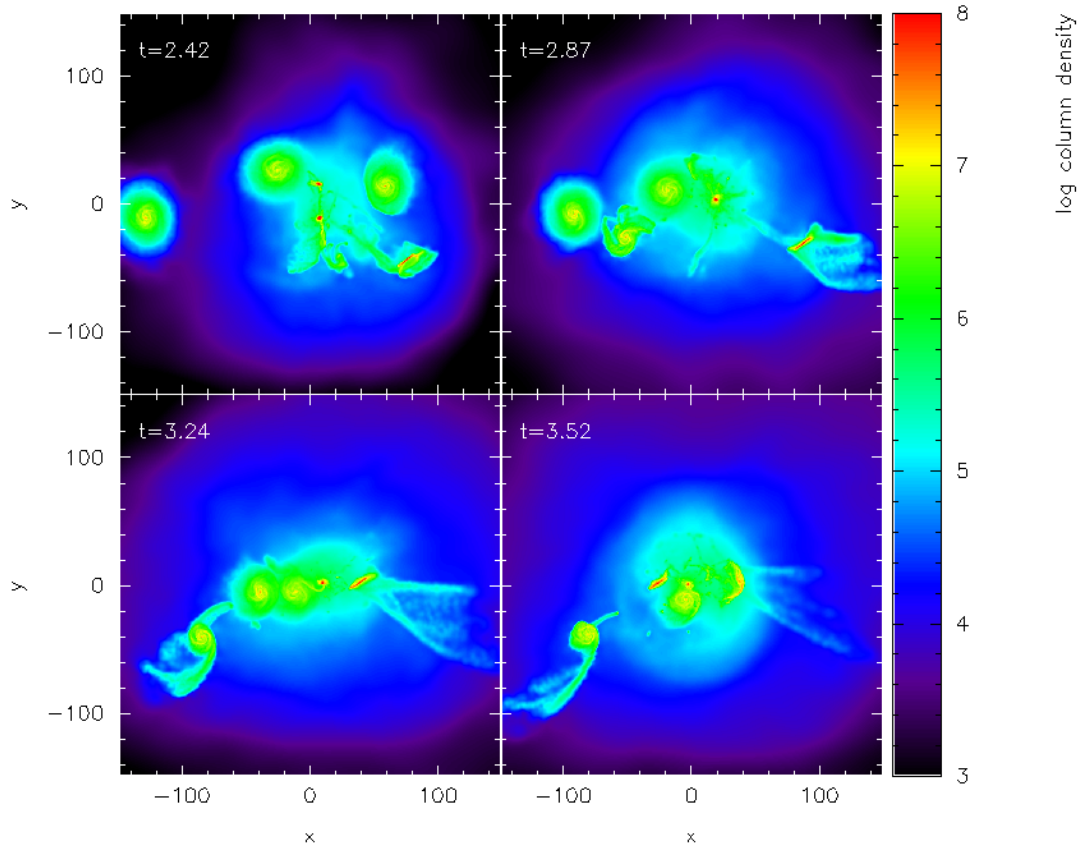

Figure 4.14: Between 2.42 and 3.52 Gyr, all of the progenitors in the $G1$-8s simulation have undergone their first passage close to the central galaxy.

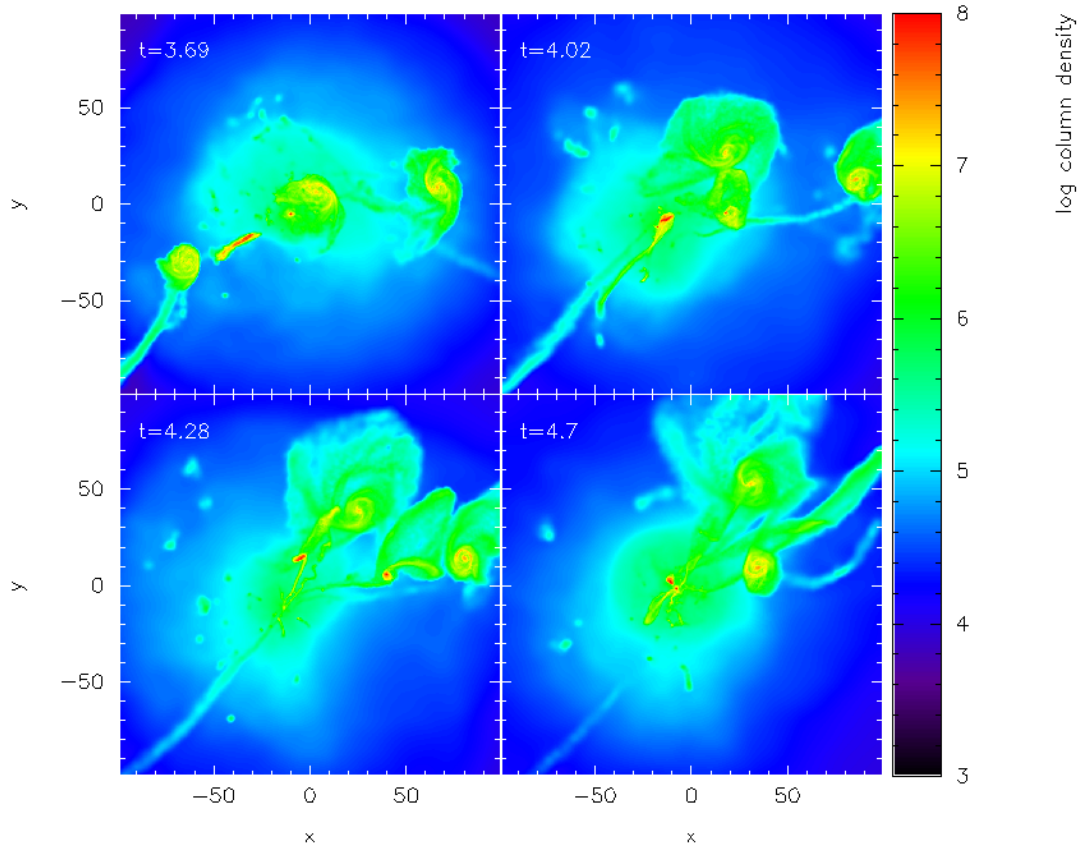

Figure 4.15: The intermediate stages of the *G*1-8s simulation. Many of the progenitors are having interactions with each other as well as with the central galaxy.

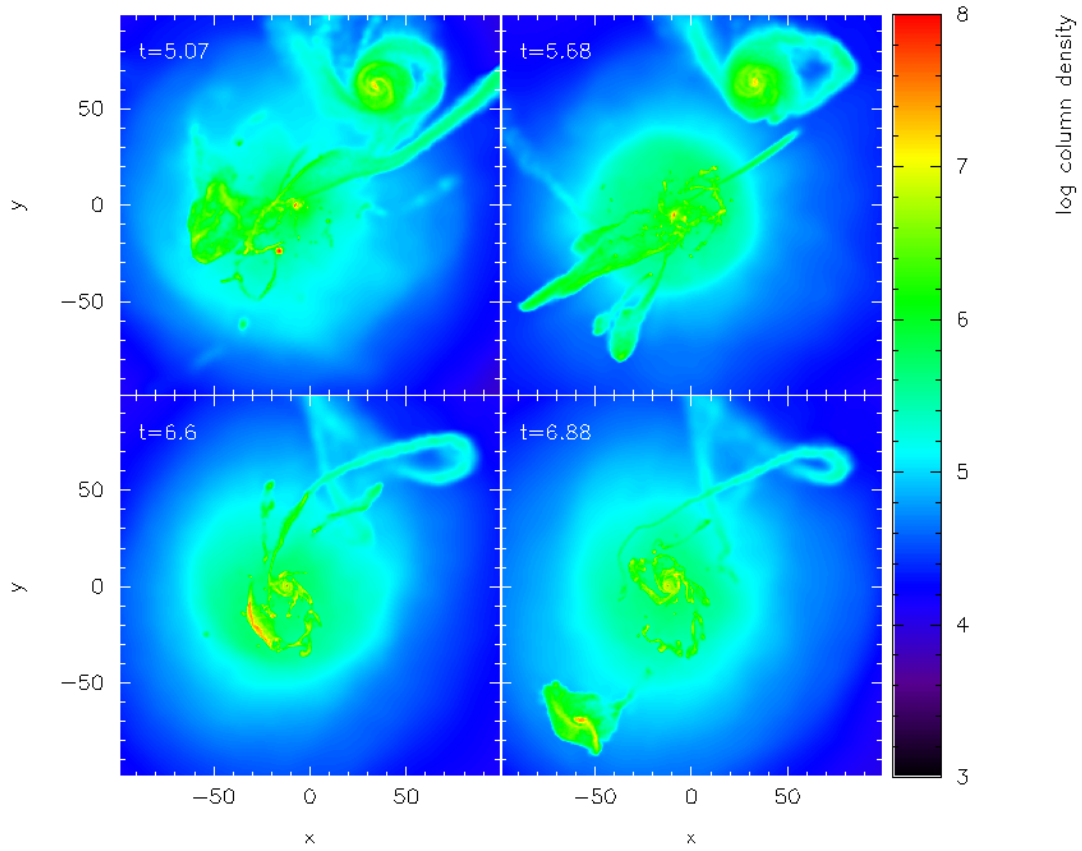

Figure 4.16: Final evolution of the $G1$-8s simulation. The galaxy in the lower left is heading off with a large velocity, to return only after several more Gyr. I have analysed the $G1$-8s remnant without waiting for it to come back.

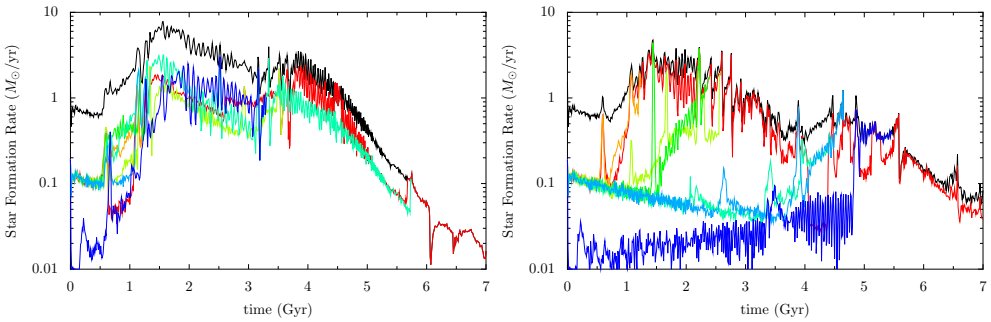

Figure 4.17: Star formation rates for the $G1$ simulations. On the left, $G1$-8b, and on the right $G1$-8s. The total star formation rates are quite low in an absolute sense, but they are elevated by more than an order of magnitude over their quiescent values for about 4 Gyr.

with the $G2$ simulations, the star formation rates are fairly low but sustained for a long period of time. The star formation rate in these simulations is of course limited by the fact that the galaxies have no way to increase their gas content after the simulation starts. Eventually nearly all of the gas is consumed and there is no cosmological environment from which it can be replenished.

As also seen in the $G2$-4s and $G2$-4b simulations, the sequential merger scheme results in star formation that is more concentrated in a single remnant rather than evenly spread among the galaxies in the simulation at any given time.

Figure 4.18 shows kinematic data for the $G1$-8b simulations. There is less overall rotation than the $G1$-8b simulation, but there is still a quite clear rotation pattern. As before, the simulation with the largest impact parameters has the least rotation of the three.

Figure 4.19 shows the same kinematic data for the $G1$-8s simulation. Here the result is dramatic and clear: the remnants have nearly exactly zero rotation. They are nearly spherical in shape. It seems that the building mass by sequential mergers as shown in Figure 4.2 is capable of giving spherical, non-rotating remnants that are required by the observations but not produced by binary mergers.

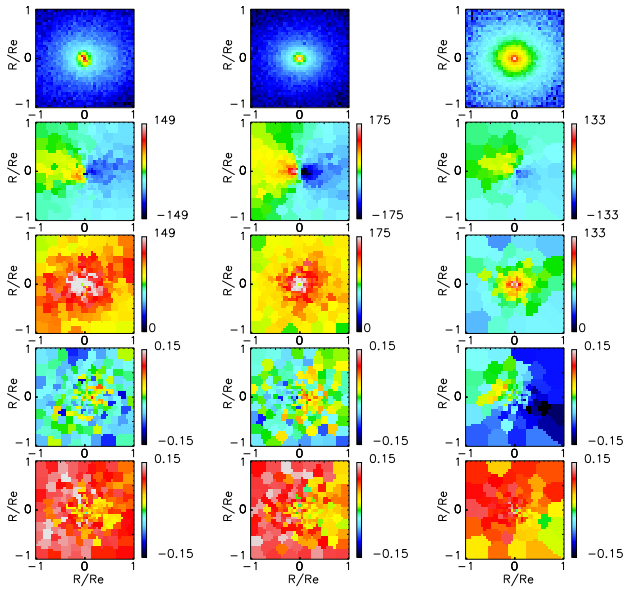

Figure 4.18: Kinematic data for the $G1$-8b simulations. From the left, the impact parameters are 1.5 kpc ($G1$-8b-1), 3.0 kpc ($G1$-8b) and 6.0 kpc ($G1$-8b-3). These remnants show rotation, with the exception of the right-most case where the rotation is not well-developed.

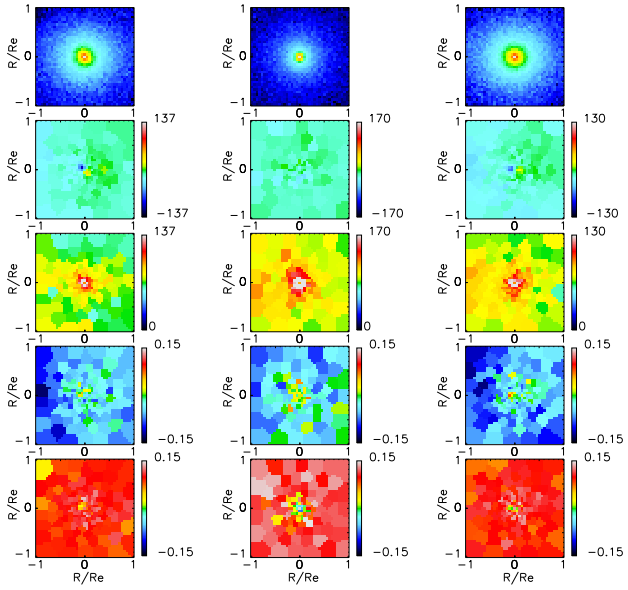

Figure 4.19: Kinematic data for the $G1$-8s simulation. These remnants are non-rotating and nearly spherical. The $G1$-8s scheme of mass build-up by sequential mergers could be the way that massive, non-rotating, nearly spherical galaxies are made.

4.4.3 Conclusions

The goal of running these idealized initial conditions is to build intuition about how the merger history of a simulated galaxy merger remnant affects its kinematics. Of particular interest is how non-rotating, nearly isotropic, nearly spherical galaxies may be produced.

We have seen that sequential mergers (Figure 4.2) result in less rotation than successive binary mergers (Figure 4.1) when starting with the same progenitors. If there are between four and eight sequential mergers, it is possible to produce a very convincing slowly rotating galaxy (Figure 4.19).

4.5 Cosmological Initial Conditions

The starting point for these simulations is a cosmological hydrodynamic simulation run by Doug Rudd with his distributed memory version of the ART code (Kravtsov et al., 1997; Rudd, 2007). The code uses the WMAP3 cosmological parameters to create a realization of an 80 h^{-1} Mpcbox using 512^3 dark matter particles.

For the dark matter, the code solves the Poisson equation using a fast Fourier Transform on the largest scales coupled with a multi-grid technique (Brandt, 1977). The mass resolution is $2.90 \times 10^8 M_\odot$ and the resolution of the most refined grid cell is 1.6 comoving kpc. For stellar material, the particles have a range of masses depending on the conditions under which they were created, but they have a nearly log-normal distribution a mean of $4.21 \times 10^5 M_\odot$, and a variance of 0.67 dex. The forces for star particles are computed using the same grid as the dark matter, so they have the same force resolution. Finally, the Euler equations are solved using an adaptive grid where the most refined cell is 1.2 comoving kpc on a side.

4.5.1 Resimulations of Subregions

The goal of this study is to explore the consequences of multiple galaxy mergers when the initial orbits and orientations of the model galaxies are cosmologically realistic. I would also like to see the effect of the dark matter and gas background material on the resulting galaxies. The intent of this study is *not* to run a "simulation to end all simulations" that is perfect in all respects. Were such a simulation even possible in principle, it would be very expensive computationally. Rather, the goal here is to employ computationally cheaper, but well-motivated, simulations to explore a range of possibilities.

Briefly, the sub-simulations are set up by selecting an "interesting" region of the cosmological simulation where the halo mass is $1 - 2 \times 10^{12} M_{\odot}$. The mass resolution of the WMAP80 simulation is too coarse for my purpose, so I define a "high-resolution" region and split the dark matter particles to achieve higher mass resolution. The "galaxies" from the WMAP80 simulation are also quite spherical and lack disks, so I replace them with model galaxies of an appropriate mass. The WMAP80 simulation tracks gas information on a grid so it is necessary to produce a particle-based realization of the density field. Finally, I include a large "low-resolution" region to provide the tidal field in the high resolution region.

In the low resolution region, the mass of the dark matter particles is increased to account for the fact that stars and gas are not present. For most of the simulations, the high resolution region is 1 proper megaparsec in diameter and the low resolution region is 5 proper megaparsecs in diameter.

4.5.2 Splitting Particles

I generate higher-resolution initial conditions for sub-regions of this simulation by splitting particles. The technique is obviously not self-consistent in the sense that a truly

higher-resolution cosmological simulation would contain information about the primordial power spectrum of matter fluctuations via dark matter substructure. Given that I cannot recover the lost information, I would nevertheless like my higher-resolution simulation to have the freedom to track smaller-mass-scale information as the simulation proceeds. I would like to generate a new realization of the same physical system that is in some sense faithful to the information provided by the cosmological simulation.

N-body simulations can be viewed as a Lagrangian way of solving the collisionless Boltzmann equation. Each particle represents a small volume of phase space that is integrated forward in time. Phase space is six dimensional, so even a million particle simulation would only allow ten cells per dimension if the cells are to be distributed uniformly in phase space. Given that phase space must be grossly under-sampled, N-body simulations can be seen as a Monte Carlo method of solving the CBE.

While splitting particles, I would like to be faithful to the density and velocity structure of the underlying distribution function while simply sampling it at additional phase-space points. The offspring of each particle should be smeared in position and velocity space compared to the parent particle.

The distance to the nearest neighbor particle provides a simple, adaptive estimate of the spatial resolution of the underlying distribution function, so the position of each daughter particle gets a Gaussian displacement compared to the parent particle.

It is not as obvious how to handle the velocities of the daughter particles. One strategy would be to find the nearest neighbor in phase space and give a velocity kick determined by the distance in velocity space. However, defining a distance metric on phase space requires a constant with units of time, e.g. $d^2 = \Delta x^2 + \tau^2 \Delta v^2$. We also know that our sparse sampling ensures that some particles will lack close neighbors in our simulation (though not in the real

physical system), resulting in spuriously large velocity kicks.

It is desirable for the scheme to be invariant to Galilean transformations in the sense that the procedure gives the same result even if we are splitting a particle that is falling into a larger system.

If no velocity kicks are given, then the daughter particles will recollapse into a bound structure if their free-fall time is shorter than the dynamical time of the system they inhabit. Since this essentially re-creates the parent particle, this both fails to allow the system to track finer structure as it evolves and excessively burns computer time since Gadget must integrate the orbits of the bound particles.

This observation leads to a natural way of determining the velocity kicks: The local dynamical time should be somewhat shorter than the collapse time of the daughter particles so that their evolution is determined by the global potential rather than their proximity to each other. Ideally the daughter particles should initially be gently unbound so that they soon "forget about" each other and phase mixing can erase their common origin.

4.5.3 Creating the gas density field

From the ART code I know the density, temperature, position, and size of gas cells. Given a background gas particle mass, I find the number of particles required to represent the mass in a given cell and then distribute the particle coordinates randomly with a uniform distribution within each cell. Since all of the gas particles are coming from a single cell with a single velocity, this is conceptually similar to the dark matter particle splitting discussed above. Therefore I give the gas particles a small, normally distributed velocity dispersion to prevent them from recollapsing into a single effective particle. This calculation takes into account the pressure support the particles receive via their temperatures. In practice, the temperature

correction is small and the velocity dispersions are a few percent of the peculiar velocities.

The number of gas particles in each cell is close to an exponential distribution with a mean of about five gas particles per cell. The adaptive grid ensures that the dynamic range in the number of particles per grid cell is much smaller than the dynamic range in densities.

4.5.4 Cosmology

I perform these simulations in physical coordinates. Therefore the Hubble expansion velocity is explicitly added to the dark matter and gas background particles. Furthermore an overall Hubble expansion velocity is added to each model galaxy (but there is no expansion within each model galaxy itself since they are bound structures). The simulation does not include dark energy, so the cosmological expansion will cease to be correct when dark energy comes to dominate the energy density of the universe around $z \sim 0.4$. This will not be too much of a problem since the high-resolution region is bound and hence will not feel the cosmological acceleration. The low resolution region and the tidal field it provides will suffer, however.

A more pressing problem for carrying the simulation to low redshift is the fact that the simulation becomes unrealistic when dark matter particles from the low-resolution region start to reach the galaxy forming at the center of the high-resolution region. This depends on the size of the high-resolution region and happens between 3 and 5 Gyr for the simulations presented here.

4.5.5 Inserting Model Galaxies

The process of inserting the model galaxies is straightforward but tedious. The tedium results from attempting to at the same time be faithful to the underlying cosmological simulation and the model galaxies.

Finding high density regions is much aided by the fact that the WMAP80 simulation includes a recipe for star formation. Stars are only formed in the central regions of the highest density peaks, therefore the stellar halos are readily identifiable and separable.

By contrast, identifying dark matter halos within a simulation is much more difficult because the halos are less dense and often overlap. The standard tool is a simple friend-of-friends halo finder (Davis et al., 1985) (technically the transitive closure of the adjacency graph where particles are adjacent if the distance between them is less than the linking length). For use in dark matter halo finding, there have been a wide variety of refinements to avoid, for example, two separate halos being joined because of a thin bridge of particles connecting them (e.g. Kravtsov et al., 1997; Diemand et al., 2006; Bett et al., 2007).

The higher density and spatial separation of stellar halos in the WMAP80 simulation permits the use of the simple FOF algorithm.

The list of stellar halos is processed in descending order by mass to ensure a sane allocation of mass to model galaxies. I find the effective radius of the stellar FOF halo and define the baryonic mass of the galaxy to be all stellar and baryonic mass within 5 times the effective radius. For a Hernquist profile, 85% of the mass is included withing 5 times the (3D) effective radius.

Given a baryonic mass, I choose an appropriate galaxy from the G series where the boundaries in baryonic mass between one galaxy model decision and another are equidistant in log space from the actual baryonic mass of the model galaxies. The orientation of the model galaxy is set so that the angular momentum vectors of the mass in the simulation and in the model galaxy are parallel.

To make room for the model galaxy, I remove all of the star particles attributed to the galaxy under consideration, and remove gas particles using a Gaussian window function

with a radius calculated to ensure that the total baryonic mass removed is equal to that in the model galaxy.

Making room for the dark matter is somewhat trickier because of the large, sometimes overlapping halos. As each WMAP80 simulation particle is "used up" by the insertion of a model galaxy, it is marked as such so that the total mass in the simulation is conserved. Therefore, if inserting galaxy A results in much of the dark matter near galaxy B to be marked as used, then when it comes time to insert a model for galaxy B, distant mass belonging to a third galaxy will again be needed. Therefore having one galaxy mark too much dark matter as used causes a cascading failure to reasonably represent the matter distribution.

On the other hand, the G series galaxies were carefully constructed to be in equilibrium. Maintaining equilibrium requires that the dark matter density near the center of the model galaxy not change.

Therefore the WMAP80 simulation mass removed for each model galaxy should be as much as possible (up to the total mass of the dark matter in the model galaxy) without removing mass that rightfully belongs to another galaxy. The maximum allowed radius of the Gaussian window function is determined to be the largest radius r at which the mass to be removed has a center of mass that falls withing $0.35r$ of the center of the galaxy (corresponding to 4.3% of the volume under consideration).

This does not behave well when one galaxy is significantly more massive than the other, so there is an additional constraint that the center of mass of a thin shell of radius r should fall within $0.35r$ of the center of the galaxy.

The dark matter mass to be removed from the WMAP80 simulation is now determined, so we must trim the model dark matter to fit. This uses the same Gaussian window function with a radius calculated to leave the correct dark matter mass in the model galaxy.

Generally half of the model dark matter survives, but in some cases as little as 20% survives.

The important point is that the dark matter near the center of the model galaxy is nearly undisturbed, even when 4/5 of the dark matter mass is trimmed from the model. Furthermore, the *total* mass of the galaxy halo must be considered to be the *combined* mass of the model dark matter and WMAP80 simulation dark matter that survive. That is, even if a nearby satellite prevents much dark matter mass from being removed from the WMAP80 simulation (and therefore forces the model dark matter to be trimmed aggressively), then the outer part of the galaxy's halo hasn't gone away—it's simply realized in terms of WMAP80 simulation particles instead of model galaxy particles.

4.5.5.1 Two Sets of Realizations

In section 4.6, I present two realizations of the these simulations which differ in the algorithm used to insert model galaxies. The first set of realizations is denoted cos1, cos2, and so on. In those realizations, I *do not* trim the model galaxy dark matter halos. This has the effect of moving most or all of the dark matter in the high resolution region to the model galaxy halos. That is, most of the dark matter filaments are "reassigned" to model galaxy halos.

I made two changes when generating the second set of realizations, denoted cos1-2, cos2-2, and so on. The first change is that when choosing which model galaxy to insert based on the baryonic mass in the a density peak in the WMAP80 simulation, I process the galaxies in order of descending mass. In the first set of realizations I simply processed the galaxies in the order in which they were found. This difference sometimes results in a different decision being made about which model galaxy to insert, because baryonic mass already assigned to one of the model galaxies is removed from the WMAP80 simulation before further processing.

The second change is that I attempt to trim the outer parts of the dark matter halos in the model galaxies to preserve the filamentary structure of the dark matter in the high resolution region, and leave the equilibrium of the central model galaxy undisturbed. This second set of realizations is more faithful to the larger-scale cosmological simulation and is presumably more realistic. However, these simulations are currently running and are in various states of completion, so I present results from both the old and the new sets of simulations in Section 4.6.

The algorithm to generate the second set of simulations (e.g. cos1-2) is described in detail below. The algorithm to generate the first set (cos1) is the same, except that the dark matter halos of the model galaxies are not trimmed. I conserve mass in both cases. The primary affect of this change is that the cos1 simulation evolves much faster than the cos1-2 simulation (and similarly for the other cases).

4.6 Results

I initially started nine simulations with cosmological initial conditions, numbered cos1 through cos9. Some of them turned out to be less interesting, so there are gaps in the numbering of simulations presented here. Table 4.2 shows the number of model galaxies that went into each realization of the simulations starting from cosmological initial conditions.

To provide some orientation, Figures 4.20 and 4.21 show the projected density for the cos9 simulation at various times.

4.6.1 Mass Accretion and Star Formation

In order to quantify the mass accretion and star formation histories of the simulations with cosmological initial conditions, I construct a simple merger tree. For every simulation

	$G3$	$G2$	$G1$
cos1		3	3
cos2		2	1
cos3	1	4	1
cos5	1	1	2
cos8	1	4	1
cos9	2	1	1
cos1-2	1	1	6
cos2-2		2	4
cos3-2	1	4	2
cos5-2	1	1	2
cos8-2	1	3	4
cos9-2	2	1	1

Table 4.2: Model galaxies used in each realization of the simulations from cosmological initial conditions.

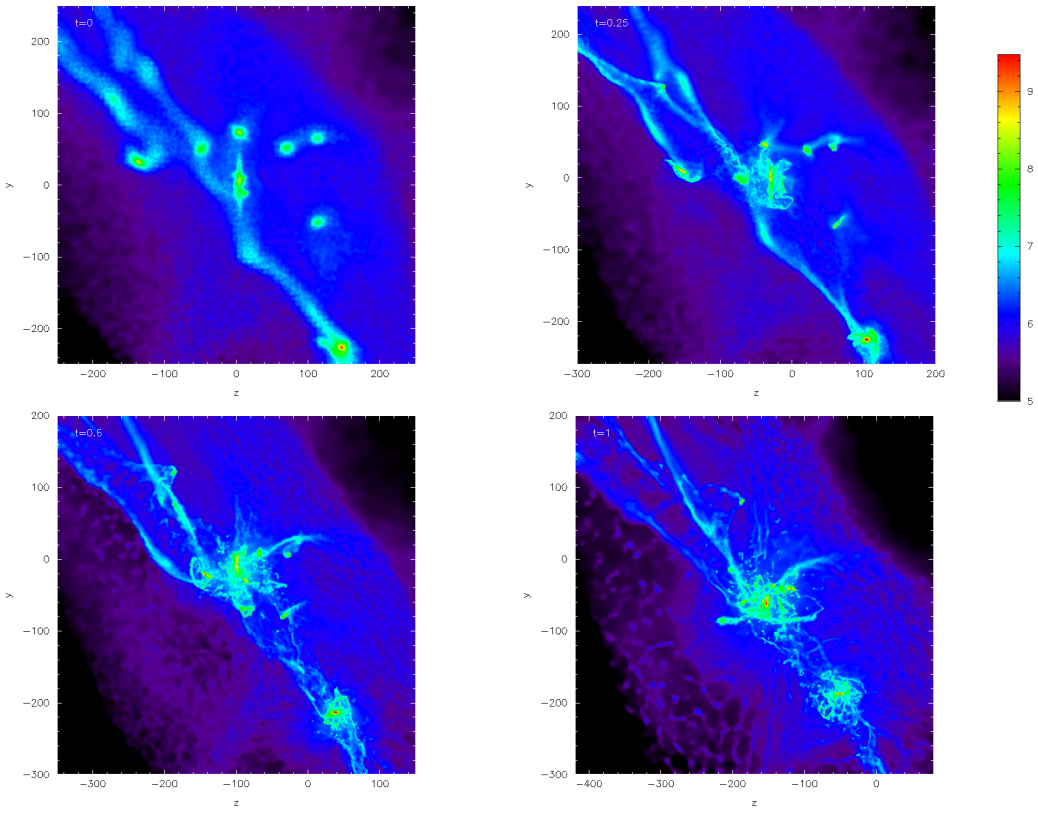

Figure 4.20: Time evolution of the cos9 simulation up to 1 Gyr. This include the first encounter with two of three of the model in the simulation along with three lumps of gas that do *not* include model galaxies.

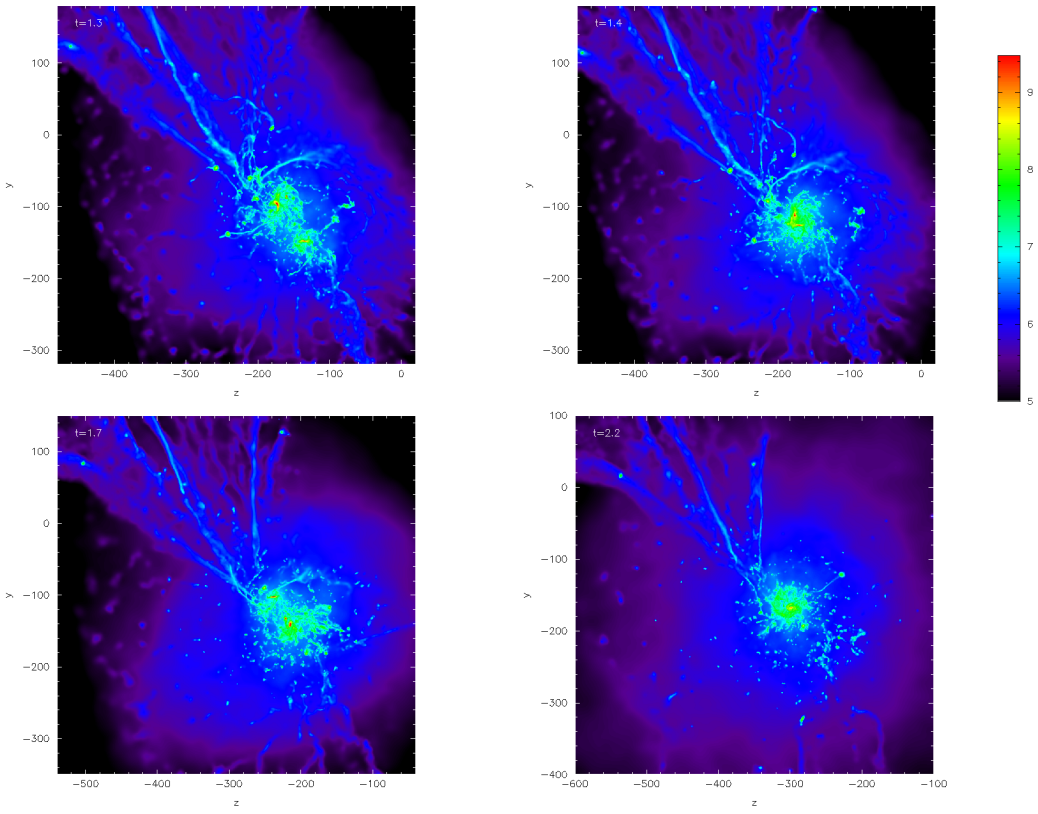

Figure 4.21: The final evolution of the cos9 simulation. The central remnant is developing a spherical halo of hot gas along with a rotating gas disk.

snapshot, I use the star particle identity numbers to compute the center of mass and effective radius of all of the star particles that *started out* in each of the model galaxies. For each pair of model galaxies, if the distance between their centers is less than twice the mean effective radius, then they have either merged or are having a close encounter.

To construct the merger tree, for each group of merged model galaxies I look for the last snapshot in which they have an independent identity by the definition given above. That is, they are at least two effective radii away from any other object. This defines the fork in the merger tree and prevents model galaxies from being considered to have merged by virtue of a close passage.

I would also like to identify the main progenitor of the final remnant at at each fork in the merger tree. At each such fork, I denote the main progenitor to be the object that contains the largest number of model galaxies. If two or more progenitors contain the same number of model galaxies, then I choose the more massive progenitor.

Choosing the progenitor that contains the largest number of model galaxies is almost the same as always choosing the most massive progenitor. However, there are times when the most massive progenitor is not the center of interest of the simulation. Choosing the progenitor that contains the largest number of model galaxies does a better job of ensuring that the main progenitor corresponds to the center of interest in the simulation.

Throughout this chapter, "Cold" gas refers to gas that it at least 50% neutral. This version of Gadget calculates the equilibrium ionized gas fraction as described by Katz et al. (1996). This makes the cutoff between cold and hot gas $\sim$25,000 Kelvin.

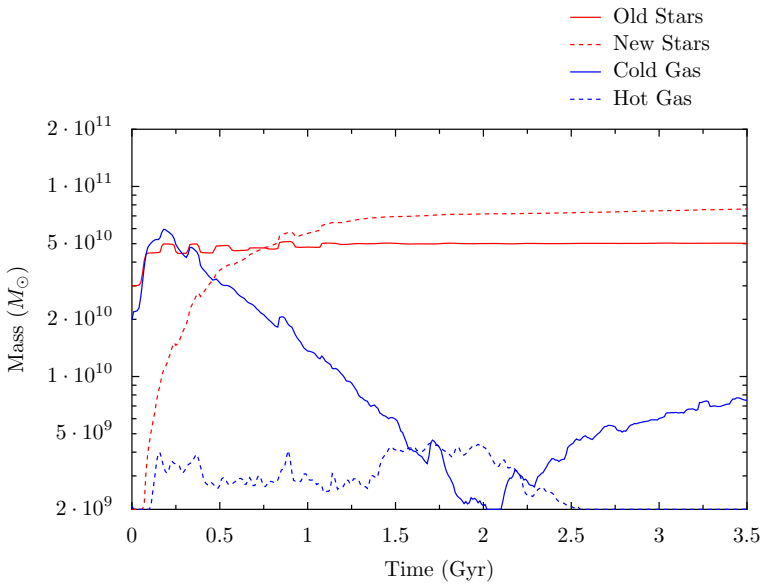

Figure 4.22: Baryonic mass of the main progenitor in the cos1 simulation as a function of time. Stellar mass is represented by red lines, gas mass by blue lines. Old stars (red solid line) are those stars that were present in the simulation initial conditions. New stars (dashed red line) are those that were formed during the simulation. Cold gas (solid blue line) is gas below 25,000 degrees Kelvin, other gas is labeled "hot" and represented with a dashed red line.

4.6.1.1 Cos1

The cos1 simulation starts off with 3 $G2$ galaxies and 3 $G1$ galaxies. After a flurry of activity in the first 500 Myr, the remnant passively accretes cold gas for 3 Gyr. This remnant thus provides an example of the effect of a long period of passive evolution.

Figure 4.22 shows the matter content of the main progenitor of the final remnant in the cos1 simulation as a function of time. At the start of the simulation, the gas fraction of the model galaxy at the center of the simulation is 24%. However, nearby cold gas quickly flows into the galaxy, giving it a gas fraction of $\sim 60\%$ within 100 Myr. This gas is quickly converted to stars over the next 2 Gyr, building up the mass of stars formed in the simulation until they dominate the mass of stars that started out in the model galaxies.

Close passes of other model galaxies are visible as "square-wave" patterns in the solid

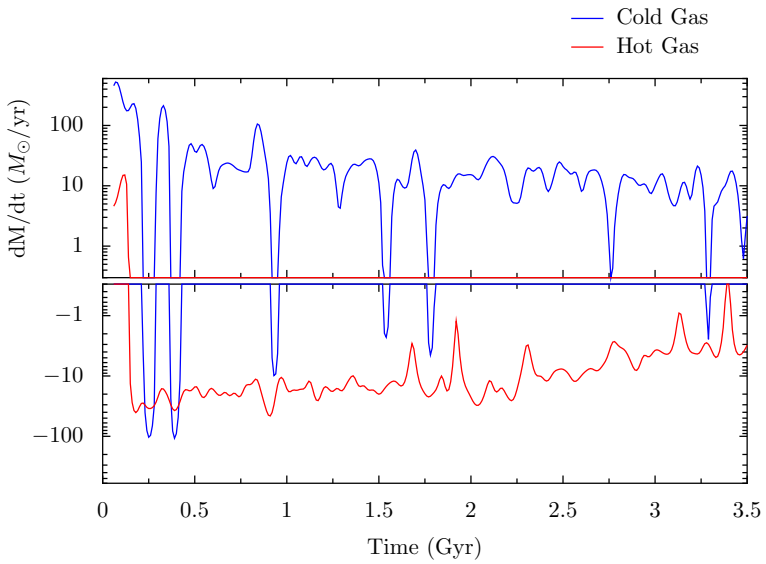

Figure 4.23: Accretion rate of the main progenitor in the cos1 simulation as a function of time by type of matter.

red line representing stars that started out in model galaxies. Another model galaxy passes by, temporarily increasing the old stellar mass. Mergers are visible in the solid red line as "step-function" patters, where the old stellar mass increases permanently.

After 1.25 Gyr, this galaxy passively evolves without experiencing additional mergers.

Figure 4.23 shows the accretion rate of different types of matter as a function of time. This is produced by comparing pairs of simulation snapshots to see which particles have entered a sphere of 15 kpc around the galaxy and which have left that sphere. Particles that have entered or exited are split by type and the difference between mass entering and mass exiting is plotted.

It is quite clear from the animations of the simulations that mass falling into the galaxy usually makes several passes before finally settling down and entering the galaxy. This means that the mass flux into and out of a galaxy is quite large compared to the difference. A net accretion rate of $10 M_\odot$/yr means that of order 10 particles have been added to the galaxy

since the last snapshot (spaced every 10 Myr), compared to of order 10^5 particles already in the galaxy. Therefore the mass accretion plot is quite noisy and it is necessary to smooth it with a 100 Myr sliding average.

Nevertheless, the plot is informative. A close pass of a model galaxy falling into the main progenitor shows up as rapid inflow and then outflow of cold gas and stars together (blue and green lines). The final merger is the last inflow of the gas and stars, but in this example the mergers and close-passes overlap until 1.25 Gyr, so it is difficult to identify the final mergers in this plot. After 1.25 Gyr, cold gas continues to flow into the galaxy at a rate of a few tens of solar masses per year, while hot gas is blown out of the galaxy at about the same rate.

Figure 4.24 shows mass conversion rates for material in the galaxy. Gas can be converted into stars, gas can be heated, or it can be cooled. This plot is produced by looking at simulation snapshots adjacent in time, finding all particles within a 15 kpc sphere of the center of mass of the galaxy in *both* snapshots, and then tallying up which of those particles have undergone the given change of state. For the first 1.25 Gyr, the dominant process is star formation. Several tens of solar masses of gas per year cool within the galaxy, and a small amount is heated within the galaxy.

Comparing Figures 4.23 and 4.24, it is clear that the hot gas outflow is *not* driven by gas heating due to star formation feedback, since only $\sim 1 M_\odot$ of gas is heated within the galaxy per year. Rather, what must be happening is that cold gas is streaming into the galaxy, shock heated, and then most of it flows out of the galaxy again.

Figure 4.25 shows the star formation rates in a 15 kpc aperture around all of the model galaxies as well as the total star formation rate in the simulation volume. The main progenitor has a star formation rate of $\sim 100 M_\odot$/yr for about 500 Myr at the beginning of the

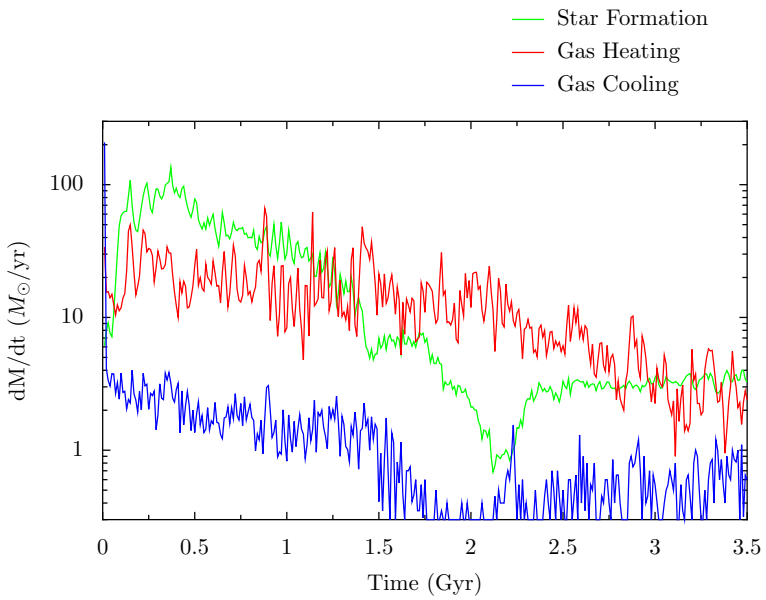

Figure 4.24: Conversion between different types of matter within the cos1 main progenitor.

simulation, making it a candidate to be identified as a Luminous InfraRed Galaxy (LIRG).

Figure 4.25 shows star formation rates in spherical apertures around model galaxies, so when a small galaxy passes by a large galaxy, the aperture around the small galaxy will pick up the star formation in the large galaxy. The two will appear to have the same star formation rate until the small galaxy moves away. I chose this way of making the plot in part because it is simple to understand and in part because it is somewhat ill-posed to try to decide which gas particles belong to which galaxy when two galaxies are close. When two model galaxies are determined to have merged, the star formation line for the smaller galaxy ends.

Two of the model galaxies have not made it into the final remnant by the time 3.5 Gyr have elapsed. Their star formation rate simply declines as they consume their gas. It is also interesting to note that the star formation rate for the whole simulation volume levels off to 10 $M_\odot$/yr after 2 Gyr, and the bulk of this star formation is taking place *outside* of the

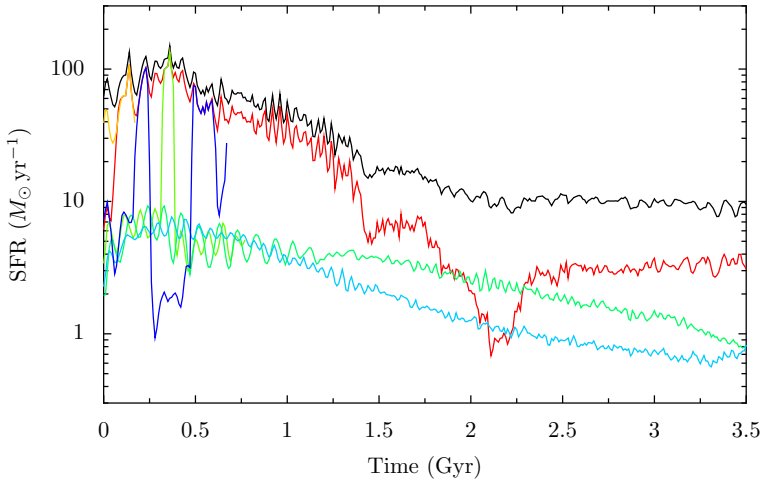

Figure 4.25: Star formation rate in the cos1 simulation. The black line is the total star formation rate in the simulation volume, and the star formation rate in a 15 kpc aperture around each model galaxy is one of the colored lines.

model galaxies.

4.6.1.2 Cos2

The cos2 simulation starts out with two $G2$ galaxies and a $G1$ galaxy. It is on the whole much more sedate than the cos1 simulation, and the simulation ends up with a less massive final galaxy.

Figures 4.26 and 4.27 show the mass content and accretion history of the main progenitor. The evolution is on the whole quite similar to the cos1 simulation. The main progenitor gains a larger fraction of its mass by mergers, but the cold and hot gas accretion rates are fairly similar.

Figure 4.28 shows the mass conversion rates as a function of time. Again, it is clear from the comparison of Figures 4.27 and 4.28 that the hot gas outflow is not the result of gas heating *within* the galaxy, but rather the result of gas being heated as it passes through the galaxy as a result of shocking. This is simply because the gas heating rate within the galaxy

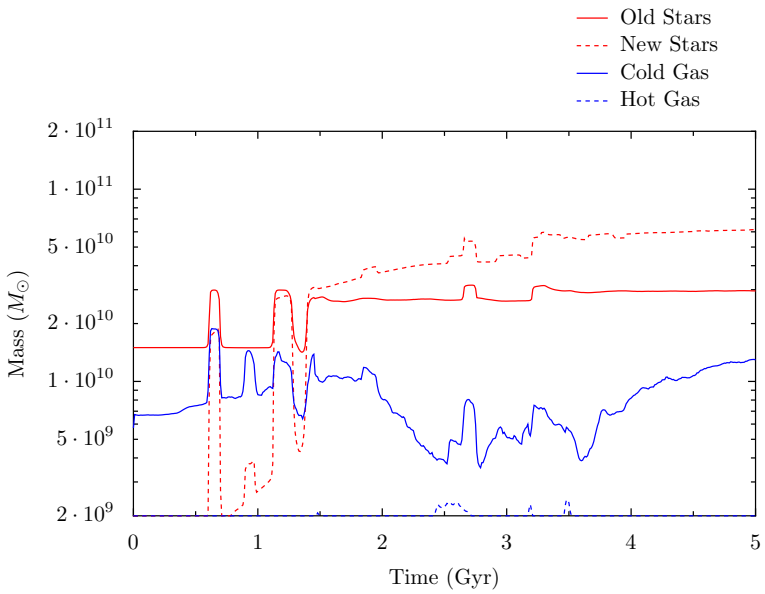

Figure 4.26: Mass content of the cos2 main progenitor. There is a major merger around 1.25 Gyr, followed by a minor merger around 3.4 Gyr.

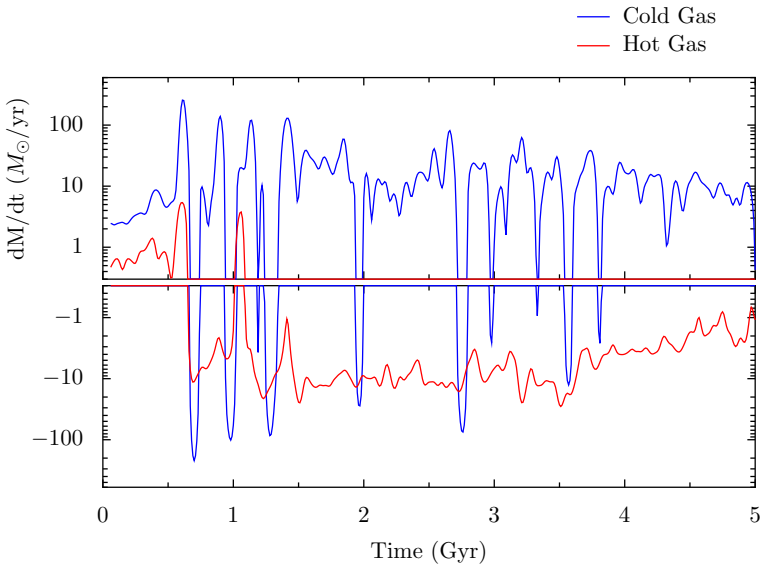

Figure 4.27: Mass accretion rates for the cos2 main progenitor. The model galaxy mergers at 1.25 and 3.4 Gyr are visible, along with cold gas inflows and hot gas outflows similar to that seen in the cos1 simulation.

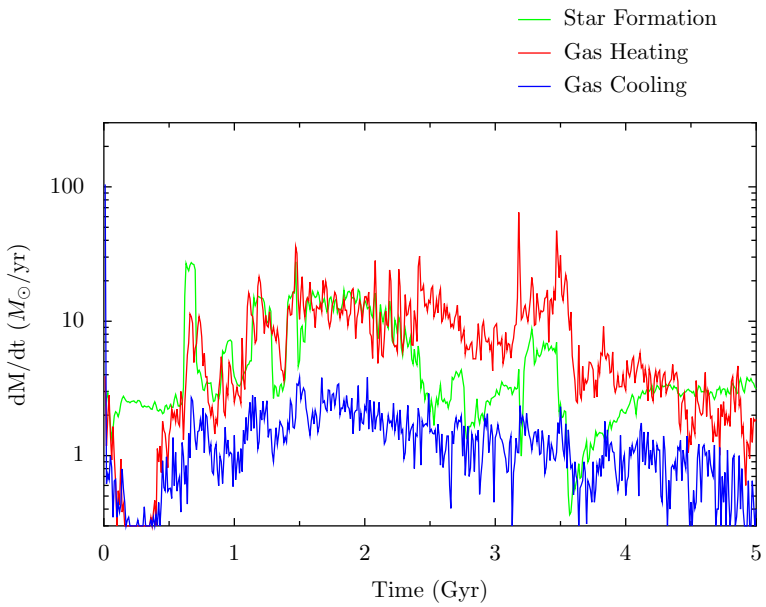

Figure 4.28: Mass conversion rates in the cos2 simulation.

is too low to account for the total hot gas outflow rate.

Figure 4.29 shows the star formation rate for the four model galaxies. The peak star formation rate of $\sim 30 M_\odot$/yr is similar to that seen in binary merger simulations (Cox et al., 2008), although the duration of the elevated star formation rate is longer in this simulation. The fact that the star formation rate is somewhat elevated for a long period of time in this simulation recalls the Noeske et al. (2007) result that the specific star formation rates of galaxies at $z \sim 1$ are quite uniform, indicating elevated quiescent star formation rates rather than bursts with short duty cycles.

4.6.1.3 Cos3

The cos3 simulation starts off with one $G3$ galaxy, four $G2$ galaxies, and one $G1$ galaxy. This simulation a character close to the successive mergers depicted in 4.2.

Figure 4.30 shows that the $G3$ galaxy merges with two of the $G2$s within 500 Myr

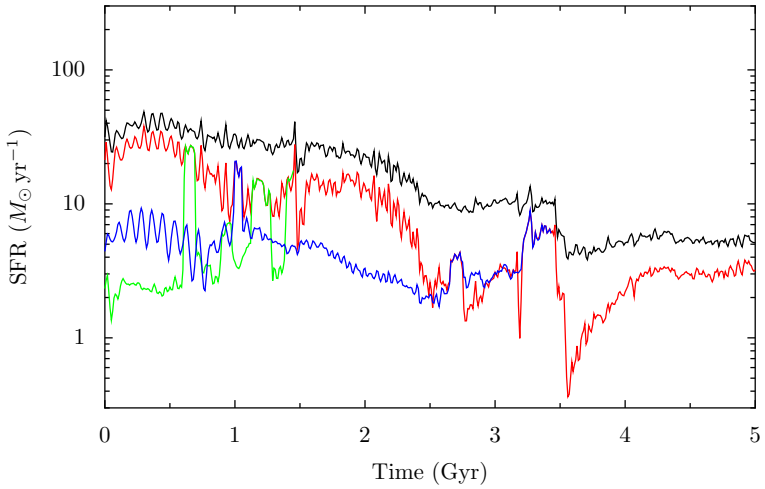

Figure 4.29: Star formation rates in cos2 for all model galaxies.

and has a close pass with a third at 600 Myr, resulting in a merger at 1.6 Gyr. After that, the main remnant passively evolves. The other $G2$ galaxy and the two $G1$s do not merge with the main galaxy within 3.5 Gyr.

Figures 4.31 and 4.32 show essentially the same pattern we've already seen: lots of accretion of both stars and gas in the form of model galaxies in the first Gyr, followed by inflow of cold gas and outflow of hot gas once things settle down.

Figure 4.33 shows the star formation rate for all of the progenitors in the cos3 simulation. The peak star formation rate in one galaxy briefly surpasses 100 $M_\odot$/yr.

4.6.1.4 Cos5

The cos5 simulation consists of 1 $G3$ galaxy, 1 $G2$ galaxy, and 2 $G1$ galaxies. In this case the two $G1$ galaxies merge while the $G3$ and $G2$ galaxies merger *separately*. Finally, the two combined galaxies merge into the final remnant at 2.8 Gyr. This situation is a nice combination of the mass build-up scenarios we've discussed so far: there's one equal mass

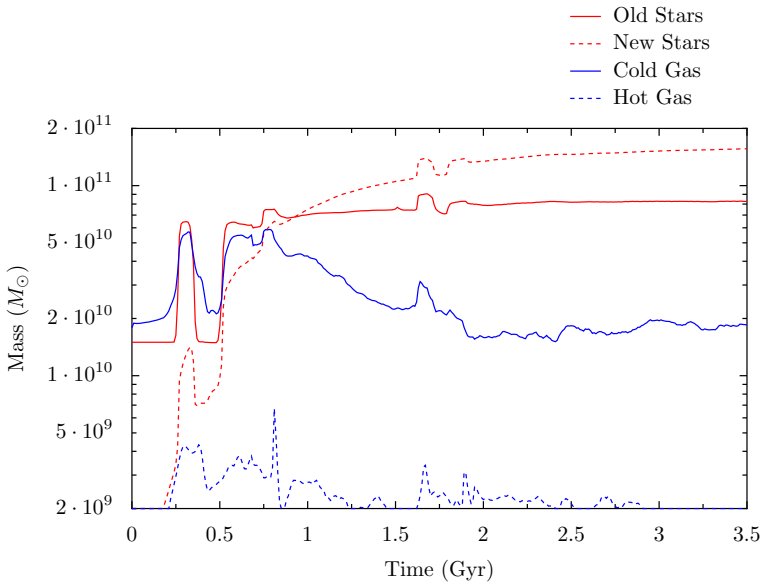

Figure 4.30: Mass content of the main progenitor in cos3.

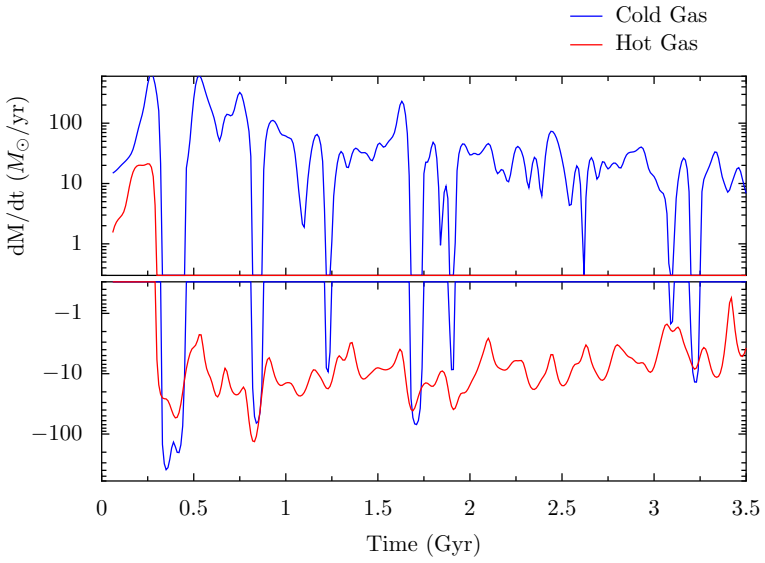

Figure 4.31: Mass accretion rates in the cos3 simulation.

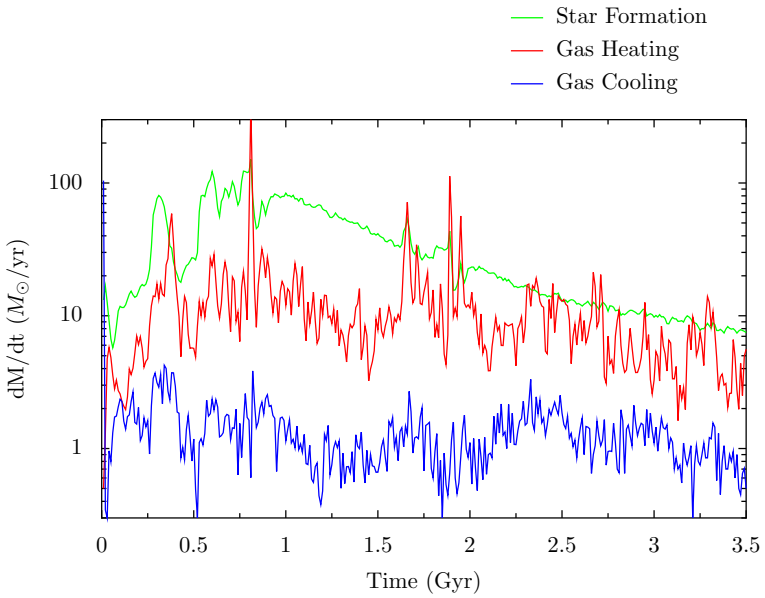

Figure 4.32: Mass conversion rates in the cos3 simulation.

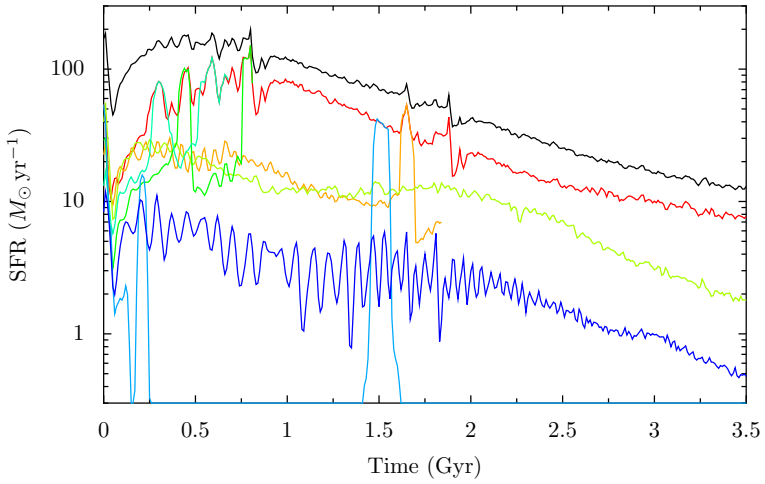

Figure 4.33: Star formation rate for all of the progenitor galaxies in the cos3 simulation.

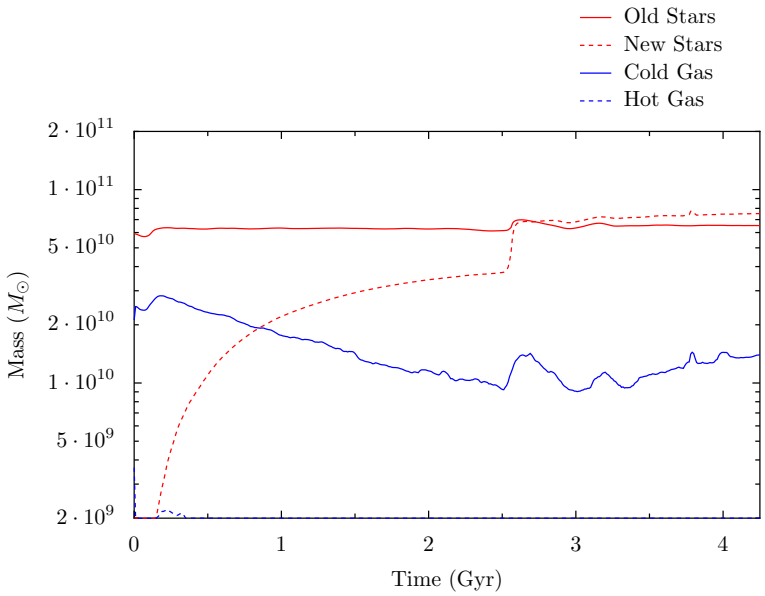

Figure 4.34: Mass content of the cos5 main progenitor.

major merger and one unequal mass major, all involving disk galaxies, followed by the minor merger of the two remnants.

Figures 4.34, 4.35, and 4.36, show the mass content, mass accretion rate, and mass conversion rates for the main progenitor, respectively. This simulation is quite interesting in that by far the dominant form of matter accreted is as stars, but the accretion is smooth, lasting from 0.5 to 2.5 Gyr. This indicates that in this simulation, gas is forming stars *before* falling into the remnant and then flowing in in a relatively smooth stream. There is also significant star formation in the remnant, but the star formation rate is less than the stellar mass accretion rate.

Figure 4.37 shows the star formation rate for this simulation, which is relatively sedate. It is interesting to note that the star formation rate is elevated by about a factor of 2 for 300 Myr when the two remnants merge at 2.8 Gyr. This would perhaps look like at E-E

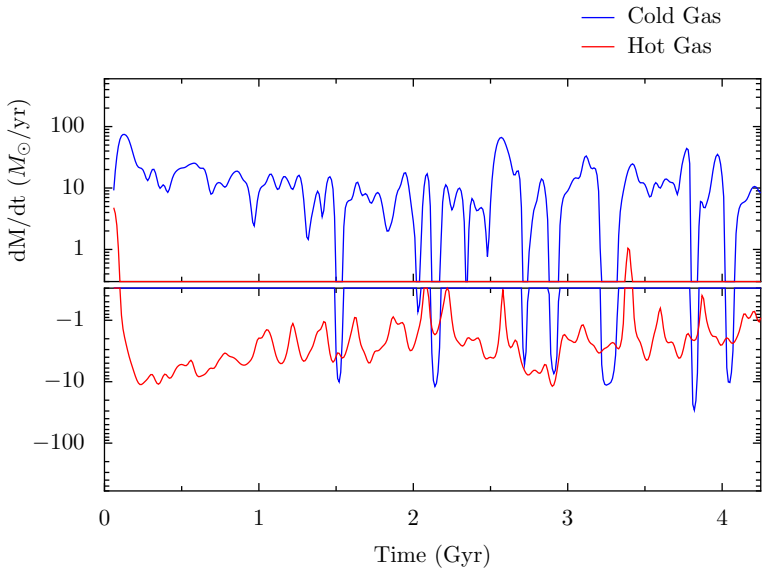

Figure 4.35: Mass accretion rate of the cos5 main progenitor.

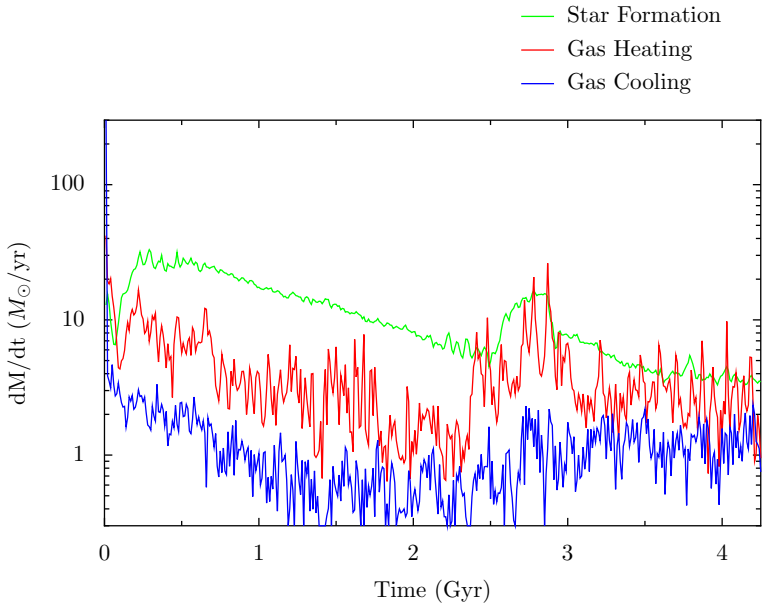

Figure 4.36: Mass conversion rates in the cos5 main progenitor.

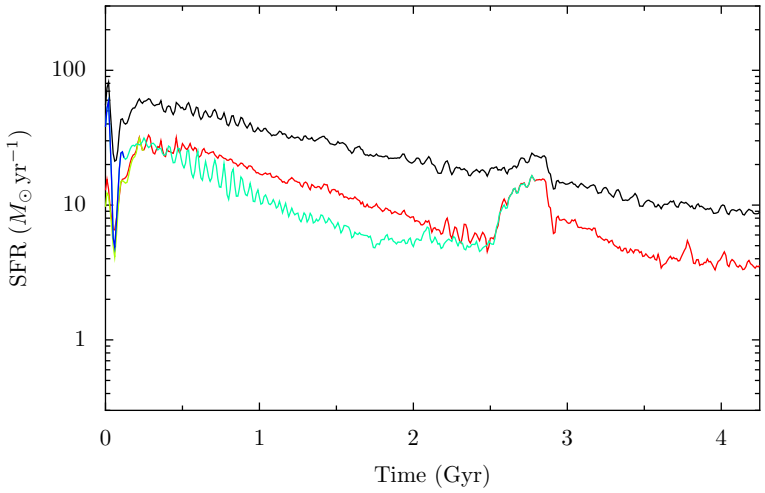

Figure 4.37: Star formation rates for the cos5 model galaxies.

merger, but there is enough cold gas in the remnants to trigger a burst of star formation.

4.6.1.5 Cos8

Figure 4.38 shows that the cos8 simulation is nearly quiescent for 2.25 Gyr. It starts out with one $G3$ galaxy, three $G2$ galaxies, and 1 $G1$ galaxy. There are a few close passes, but the only merger that eventually happens is between the $G3$ galaxy and the $G1$.

Figures 4.39 and 4.40 show the mass accretion and conversion rates. Notably, the cold gas content only drops by 30% from $3 \times 10^{10} M_\odot$ to $2 \times 10^{10} M_\odot$ in spite of forming $5 \times 10^{11} M_\odot$ of stars during the simulation. Obviously the gas accretion rate and the star formation rate are nearly in equilibrium for the duration of the simulation.

Figure 4.41 shows that the star formation rate in the main progenitor is nearly constant at 20 $M_\odot$/year. No one model galaxy dominates the star formation rate within the simulation volume, but nearly all of the star formation in the volume is taking place in model galaxies. That is, the star formation is nearly equally distributed among the many model

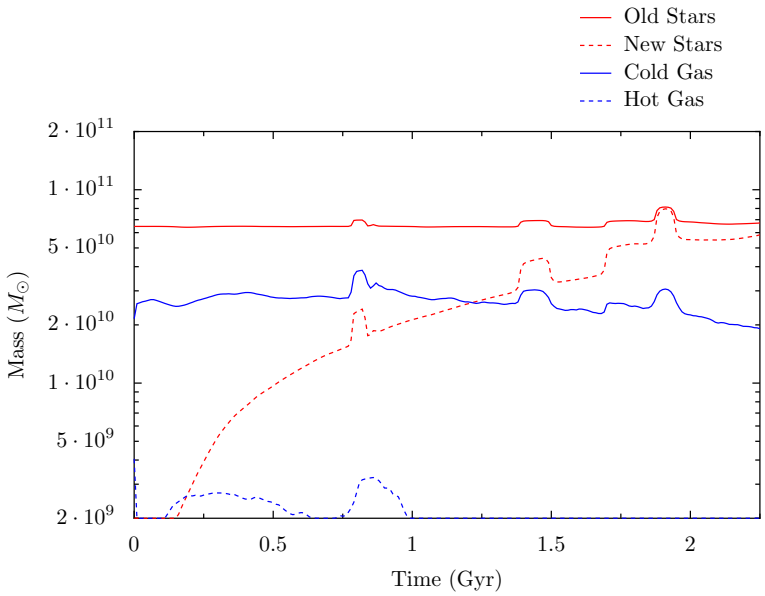

Figure 4.38: The mass content of the main progenitor in the cos8 simulation.

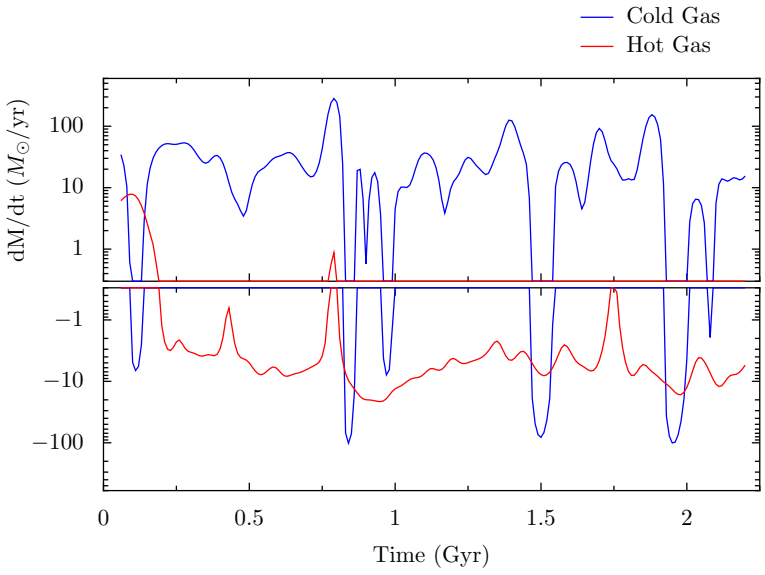

Figure 4.39: Mass accretion rate for the main progenitor in the cos8 simulation.

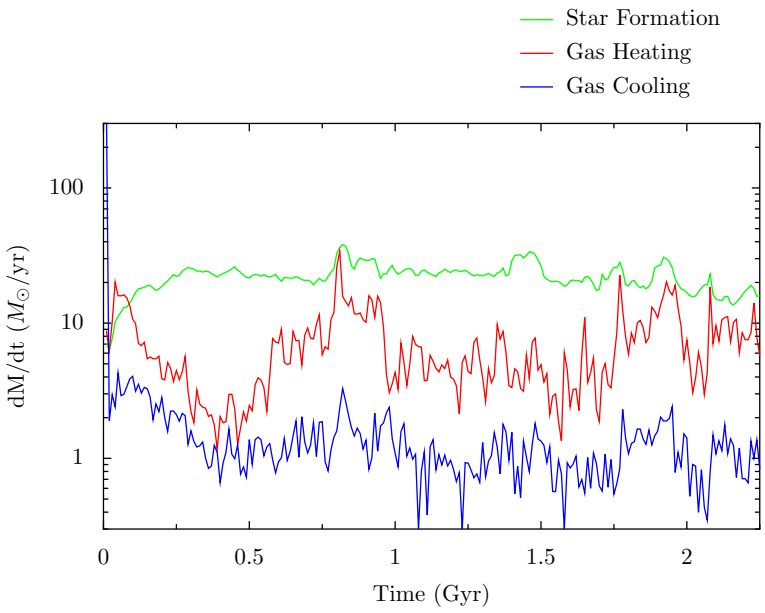

Figure 4.40: Mass conversion rates in the cos8 simulation.

galaxies.

4.6.1.6 Cos9

The cos9 simulation initially has two $G3$ galaxies, one $G2$ galaxy, and one $G1$ galaxy. The main progenitor is one of the $G3$ galaxies and it consumes the $G2$ galaxy around 1.25 Gyr, the $G1$ galaxy around 1.6 Gyr, and the other $G3$ galaxy around 2 Gyr. Figure 4.42 shows the mass content of the cos9 main progenitor. That figure shows that the incoming galaxies have roughly doubled their stellar mass via star formation during the simulation by the time the final merger at 2 Gyr happens.

Figures 4.43 and 4.44 show pattern similar to those we've already seen: significant accretion of cold gas accompanied by a hot gas outflow. Most of the mass coming into the cos9 main progenitor is in the form of model galaxies containing stars and cold gas—the blue

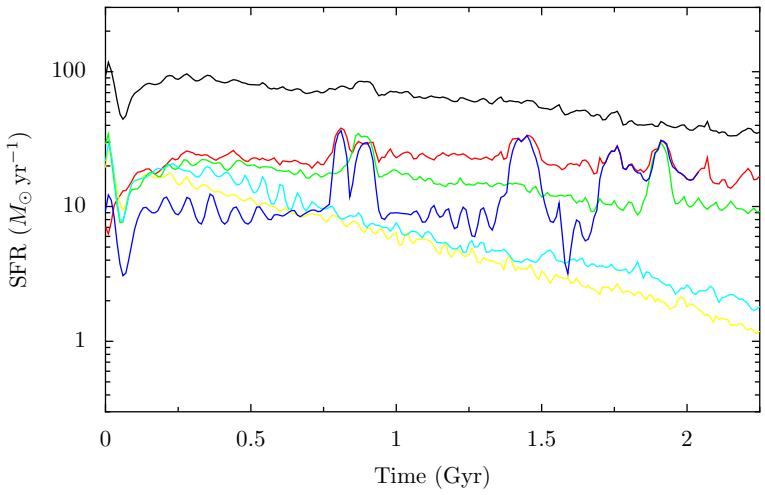

Figure 4.41: Star formation rate for all of the progenitors in the cos8 simulation.

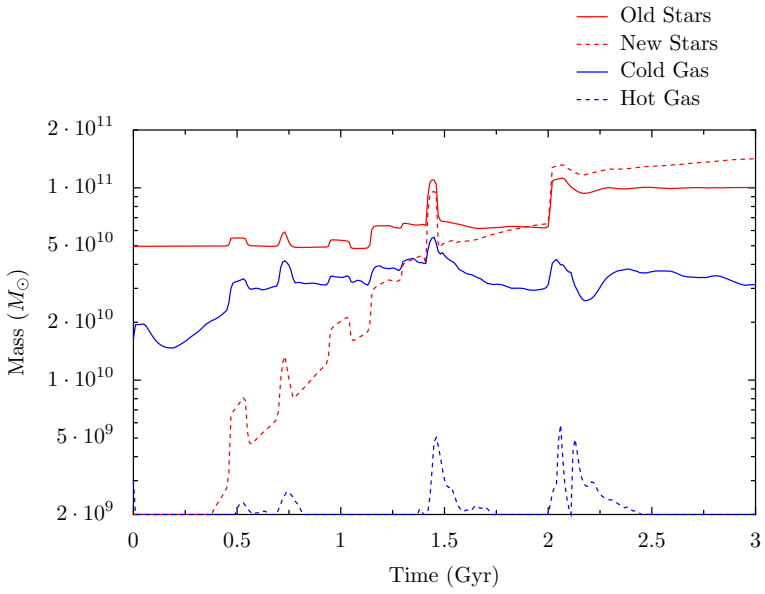

Figure 4.42: Mass build-up in the cos9 simulation.

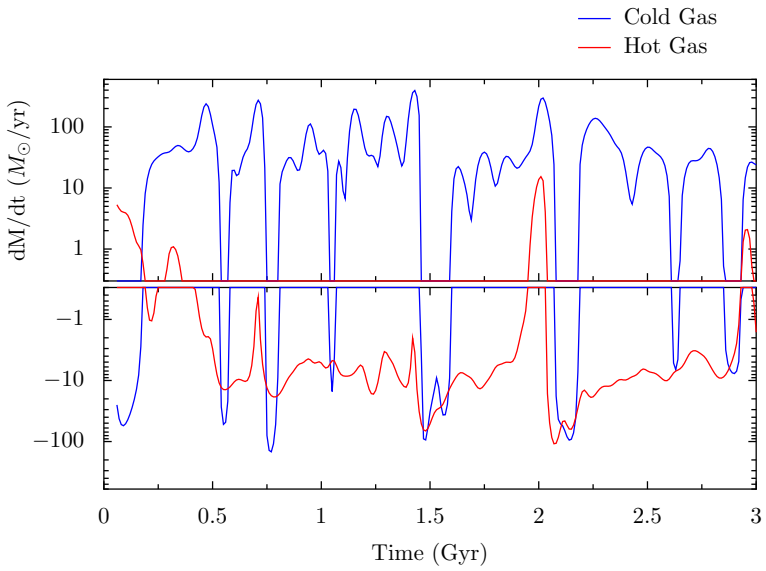

Figure 4.43: Mass accretion rates in the cos9 simulation.

and green lines in Figure 4.43 are closely correlated.

Figure 4.45 shows the star formation rate for all of the model galaxies.

4.6.1.7 Cos1-2

The initial conditions for this simulation are the same as the cos1 simulation except for the improved handling of the dark halos of the model galaxies described in Section 4.5.5.1

Figure 4.46 shows the mass content of the main progenitor in the simulation. It looks quite similar so far except for the fact that it's evolving with a much longer timescale. This can be attributed to the more massive halo leading to more efficient gas accretion in the cos1 simulation.

Figures 4.47 and 4.48 show mass accretion and conversion as a function of time. These also look fairly similar with attenuated values due to the increase in evolution timescale.

Figure 4.49 shows the star formation rate as a function of time for all of the model

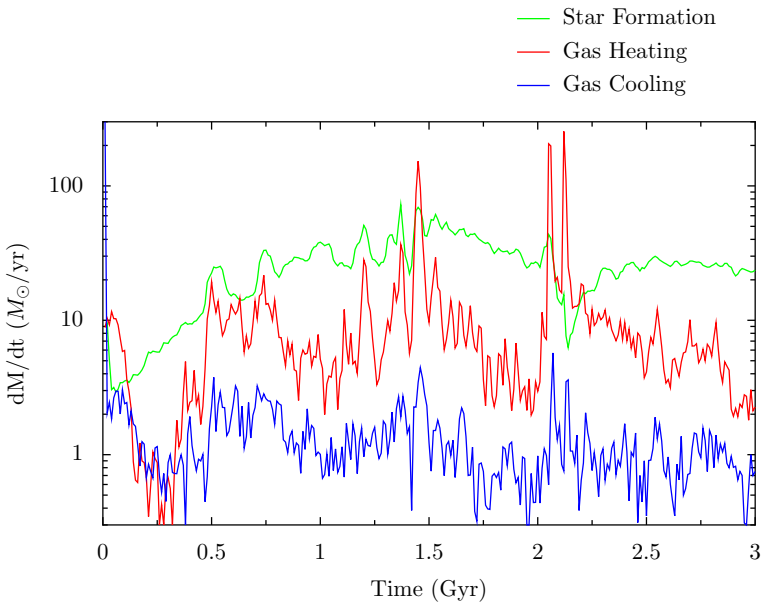

Figure 4.44: Mass conversion rates in the cos9 simulation.

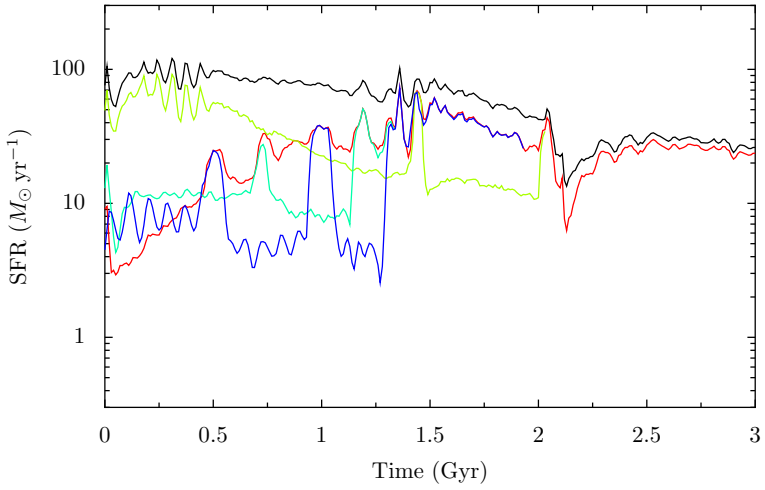

Figure 4.45: Star formation rates for the cos9 model galaxies.

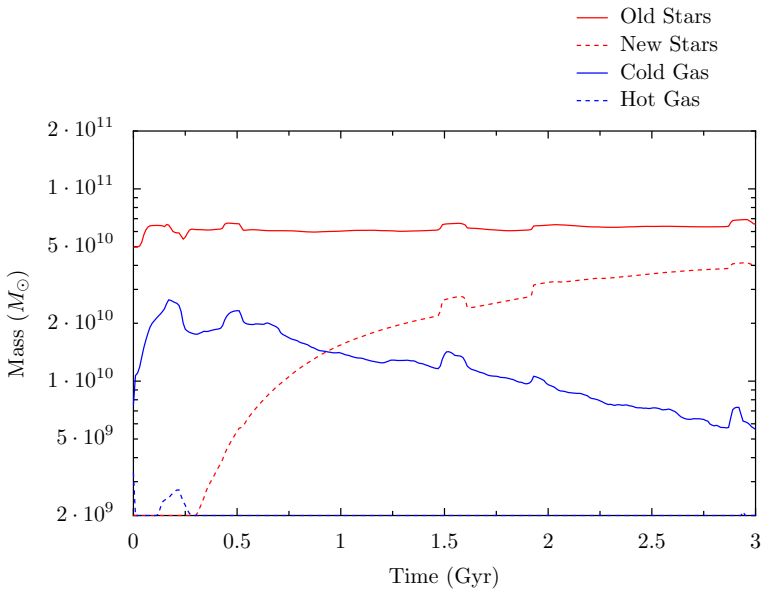

Figure 4.46: Mass evolution of the main progenitor in the cos1-2 simulation.

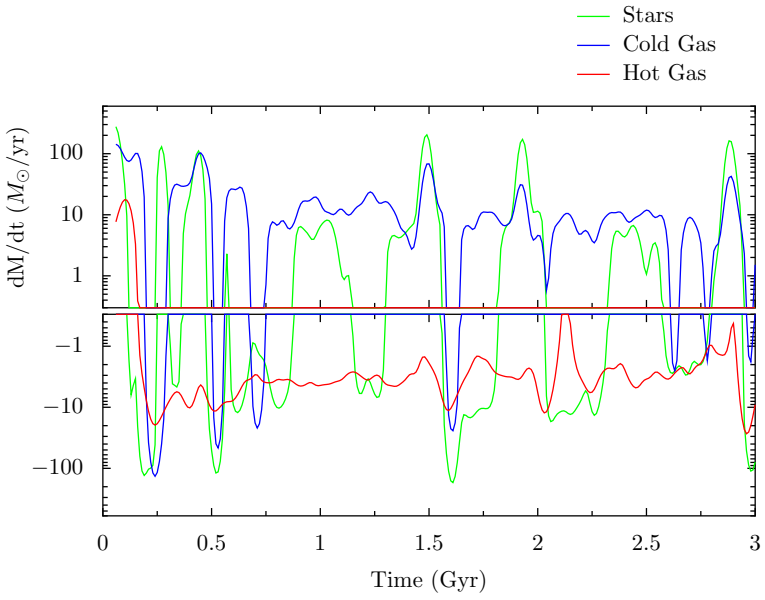

Figure 4.47: Mass accretion rates in the cos1-2 simulation.

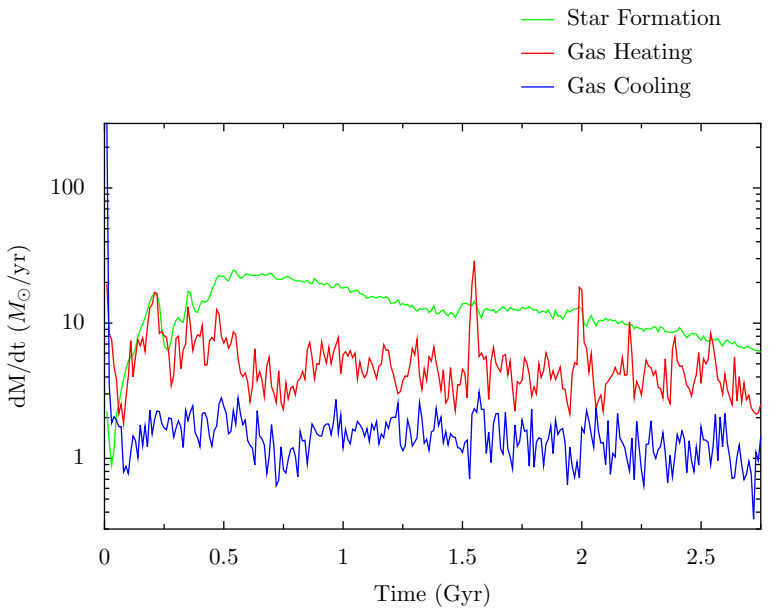

Figure 4.48: Mass conversion rates in the cos1-2 simulation.

galaxies in cos1-2. The star formation rate has dropped by about a factor of three due to the decrease in the gas accretion rate compared to cos1.

4.6.1.8 Cos2-2

The cos2-2 simulation is quite similar to the cos2 simulation. Figure 4.50 shows that the merger activity happens between 1 and 1.5 Gyr in both cases. The main difference is that the main progenitor in cos2-2 converts less of its gas to stars, maintaining a gas fraction of about 25%.

Figures 4.51, 4.52, and 4.53 are also similar the corresponding figures 4.27, 4.28, and 4.29. The exception is that star formation takes longer to get going in the cos2-2 simulation.

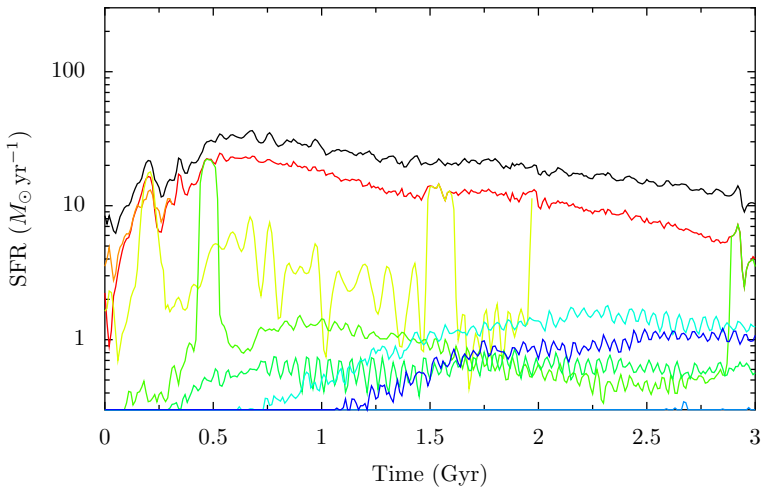

Figure 4.49: Star formation rates for model galaxies in the cos1-2 simulation.

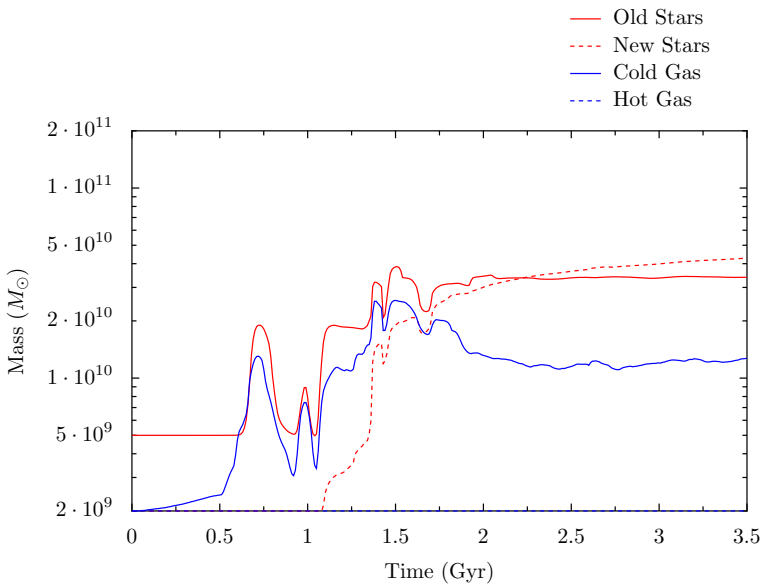

Figure 4.50: Mass evolution of the main progenitor in the cos2-2 simulation.

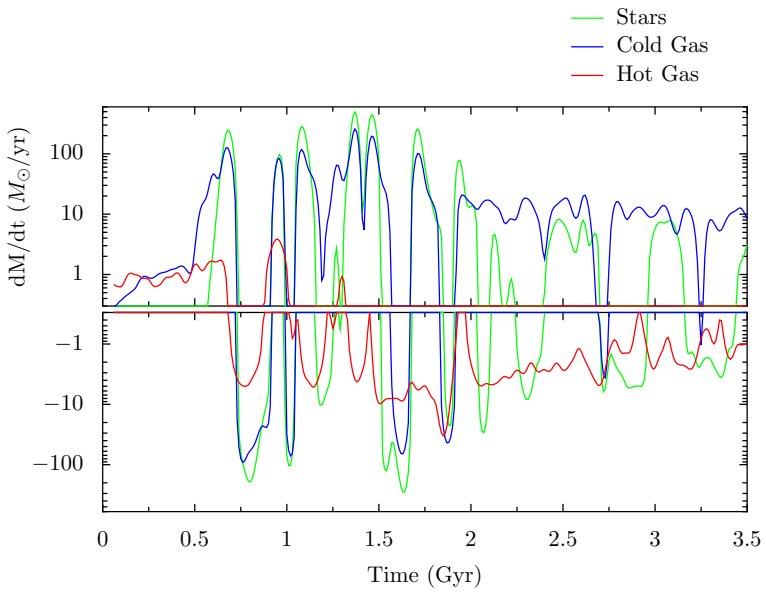

Figure 4.51: Mass accretion rates in the cos2-2 simulation.

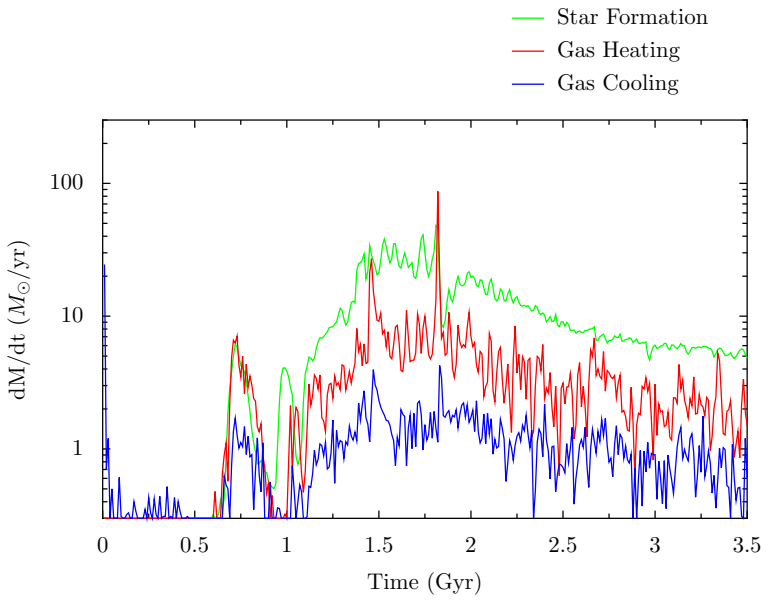

Figure 4.52: Mass conversion rates in the cos2-2 simulation.

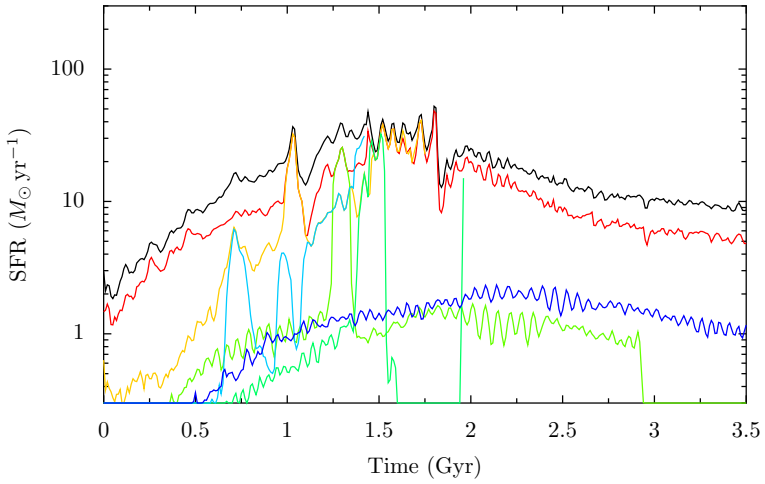

Figure 4.53: Star formation rates for model galaxies in the cos2-2 simulation.

4.6.1.9 Cos3-2

The cos3-2 simulation evolves with a timescale similar to cos3. Figures 4.30 and 4.54 both show that there is a burst of merger activity between 0.25 and 1 Gyr. Figure 4.55 shows the mass accretion history of the main progenitor in the cos3-2 simulation. There is sustained cold gas accretion of almost 100 $M_\odot$/yr. The mass conversion rates shown in Figure 4.56 indicate that the vast majority of this inflow is converted to stars. About 10 $M_\odot$/yr of gas is heated and blown out of the galaxy.

Figure 4.57 shows the star formation rate as a function of time. The main difference between the star formation rate in cos3 and in cos3-2 is that cos3-2 has a star formation rate that is 30-50% lower and takes 500 Myr to get going.

4.6.1.10 Cos5-2

The cos5-2 simulation evolves at a much slower rate compared to cos5. In the cos5 simulation, two of the pairs of galaxies merge almost immediately, and then the two remnants

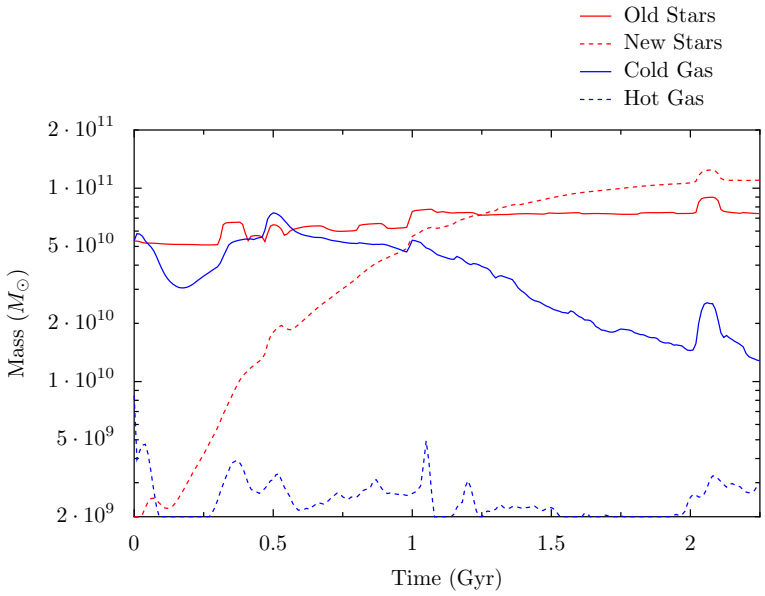

Figure 4.54: Mass evolution of the main progenitor in the cos3-2 simulation.

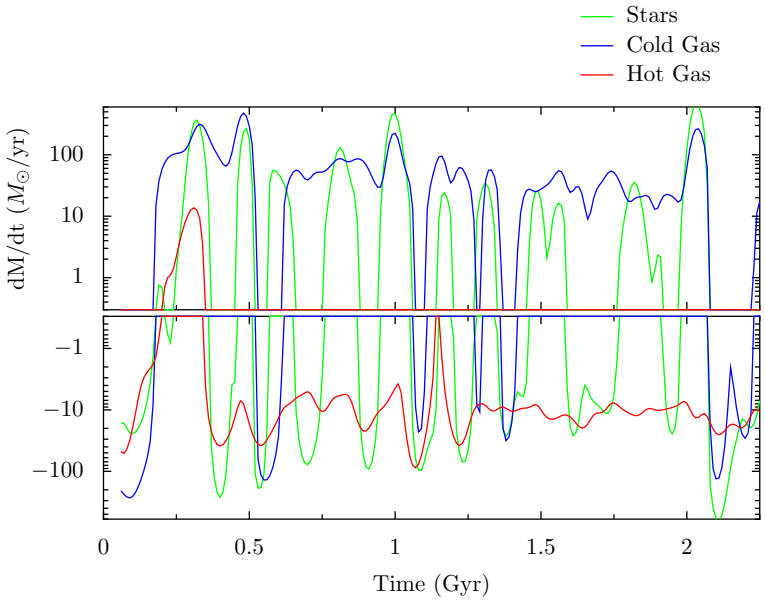

Figure 4.55: Mass accretion rates in the cos3-2 simulation.

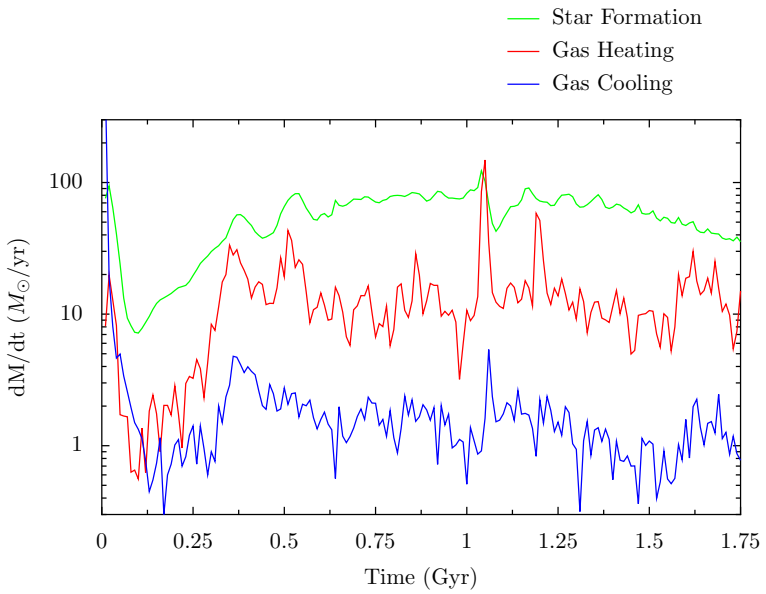

Figure 4.56: Mass conversion rates in the cos3-2 simulation.

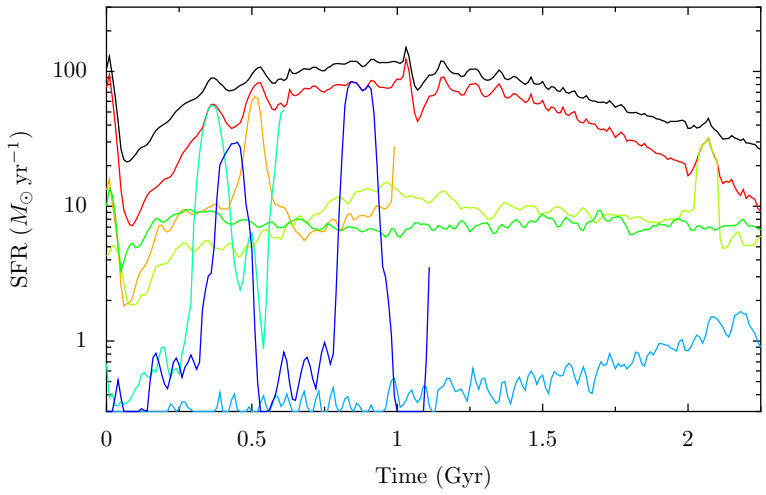

Figure 4.57: Star formation rates for model galaxies in the cos3-2 simulation.

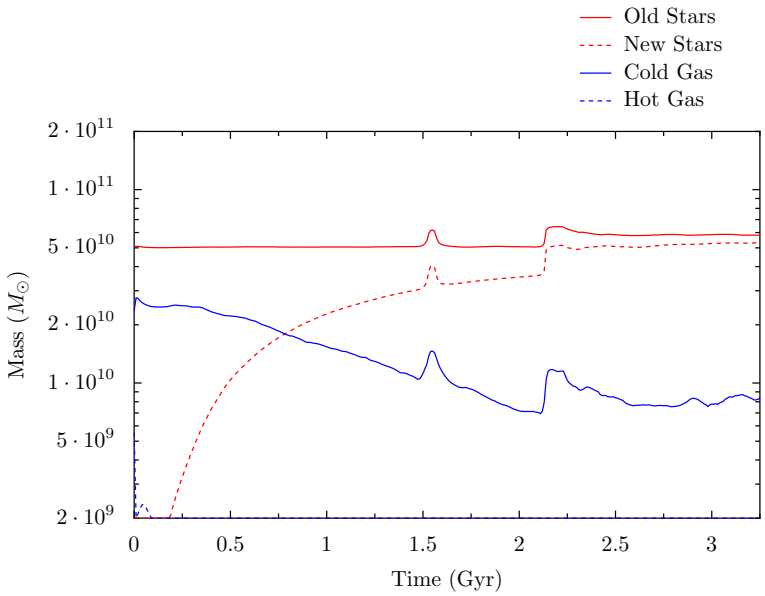

Figure 4.58: Mass evolution of the main progenitor in the cos5-2 simulation.

merge after 2 Gyr. However, Figure 4.58 shows that in cos5-2, the *first* merger happens after about 2 Gyr and there are still two other model galaxies in the simulation.

Figure 4.59 shows the rather modest cold gas accretion rate of 10 $M_\odot$/yr. Figure 4.60 shows the star formation rate is much higher, at several tens of solar masses per year. Hence the cos5-2 main progenitor steadily consumes its gas and the star formation rate drops for lack of gas.

Figure 4.61 shows *rising* star formation rates in the two lower-mass progenitor galaxies. Their gas content is being replenished by the cosmological environment. This will result in a relatively gas-rich encounter when these two galaxies finally merge with the main progenitor.

4.6.1.11 Cos8-2

The cos8-2 simulation has not run for very long but is included as an example of nearly quiescent cold gas accretion onto one of the model galaxies. Figures 4.62 and 4.63 show

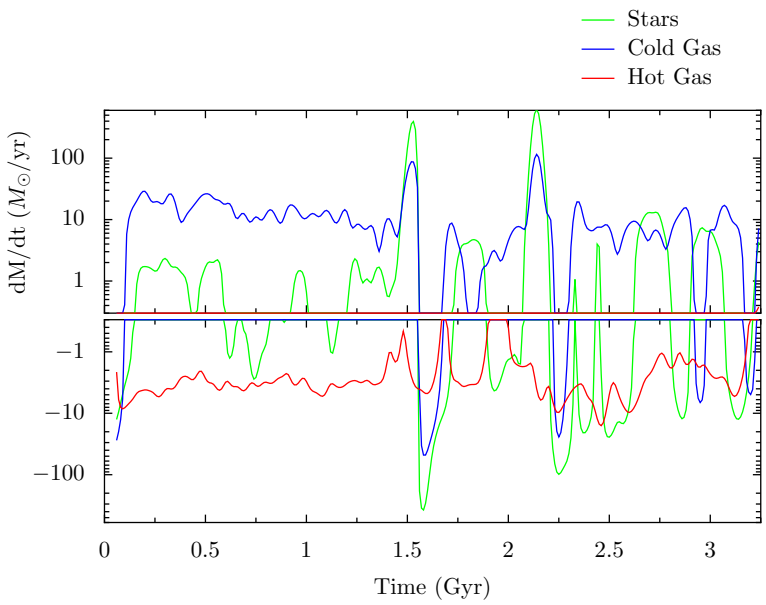

Figure 4.59: Mass accretion rates in the cos5-2 simulation.

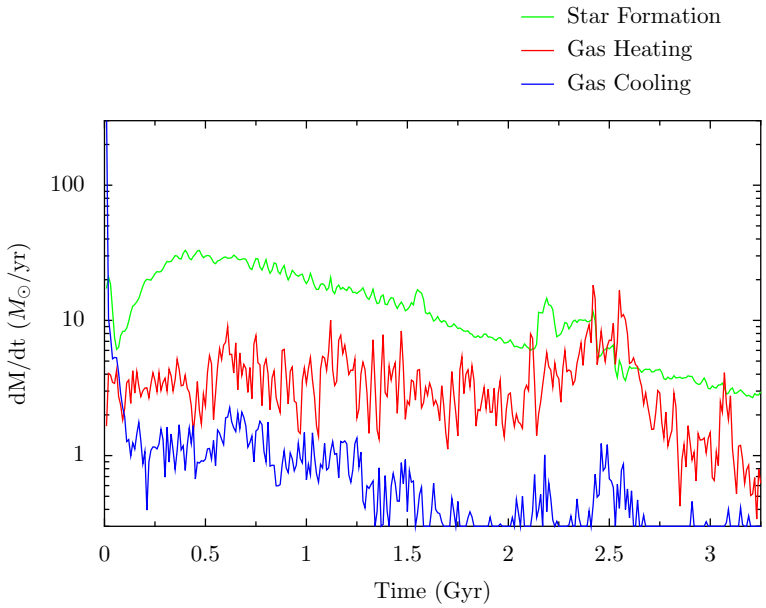

Figure 4.60: Mass conversion rates in the cos5-2 simulation.cos5-2

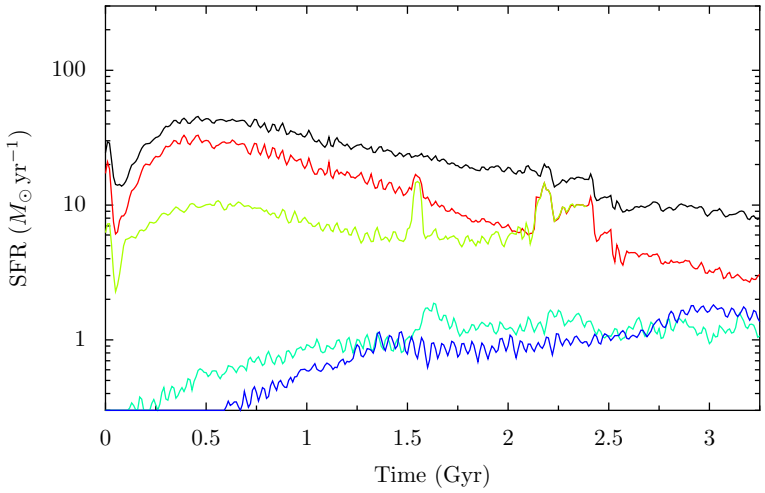

Figure 4.61: Star formation rates for model galaxies in the cos5-2 simulation.

the main progenitor in cos8-2 accreting cold gas at many tens of solar masses per year. Figures 4.64 and 4.65 show that the gas is converted to stars at a steady 20 $M_\odot$/yr. Figure 4.65 also shows the star formation rates of the multitude of model galaxies in the cos8-2 simulation that have not yet disturbed the most massive model galaxy.

4.6.1.12 Cos9-2

The cos9-2 simulation is quite similar to cos9 except that everything happens about 500 Myr later. Figure 4.66 shows that there are close passes and mergers at times of 2 and 2.5 Gyr instead of 1.5 and 2 Gyr as in Figure 4.42. Figure 4.67 shows that the cos9-2 simulation experiences significant cold gas accretion along with several mergers. Figure 4.68 shows spikes in gas heating rate that coincide with close passes or mergers. Figure 4.69 shows the star formation rates for cos9-2. These are lower than in cos9, at about 30 $M_\odot$/yr in the main progenitor instead of 90 $M_\odot$/yr.

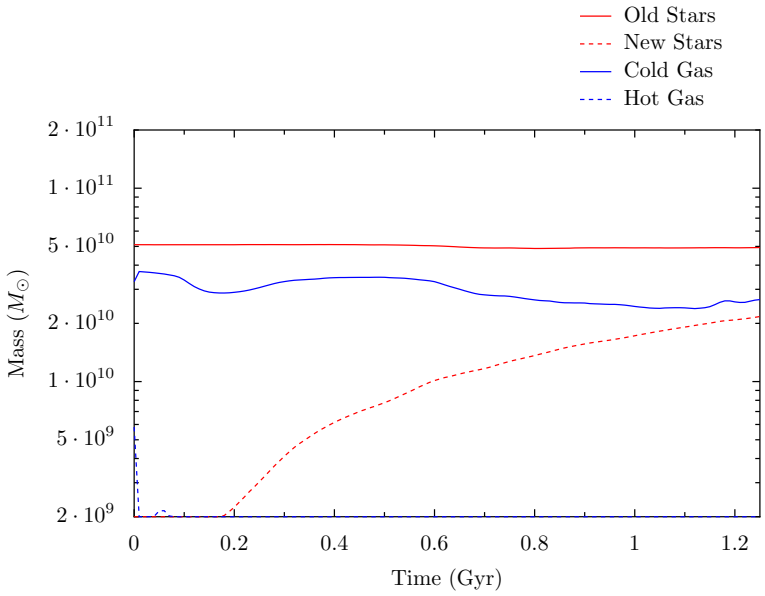

Figure 4.62: Mass evolution of the main progenitor in the cos8-2 simulation.

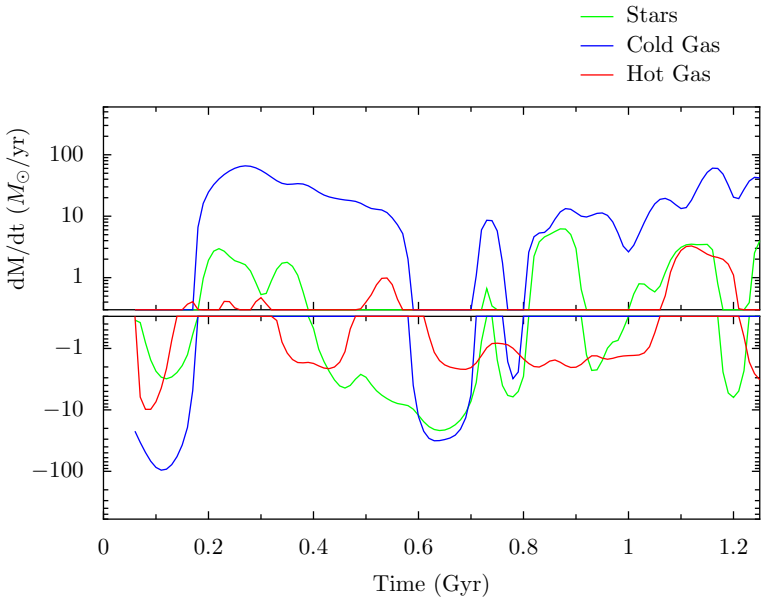

Figure 4.63: Mass accretion rates in the cos8-2 simulation.

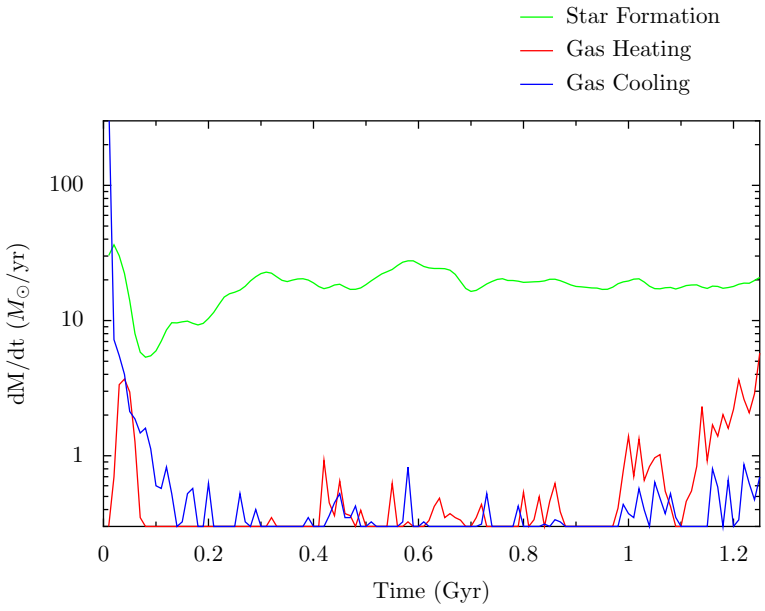

Figure 4.64: Mass accretion rates in the cos8-2 simulation.

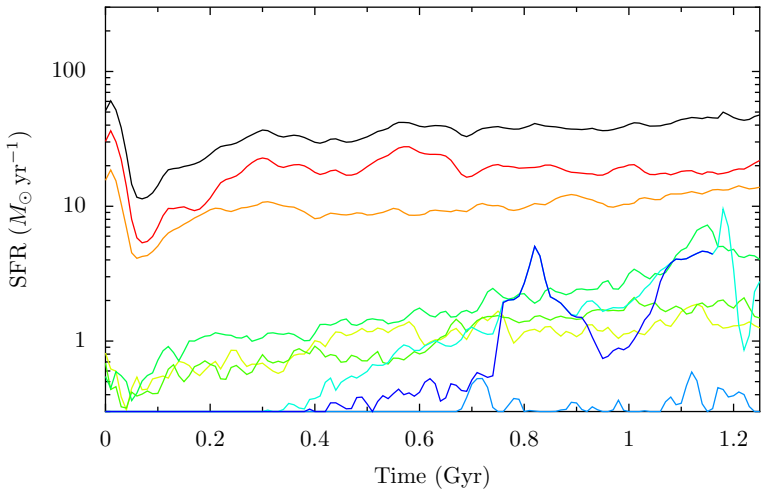

Figure 4.65: Star formation rates for model galaxies in the cos8-2 simulation.

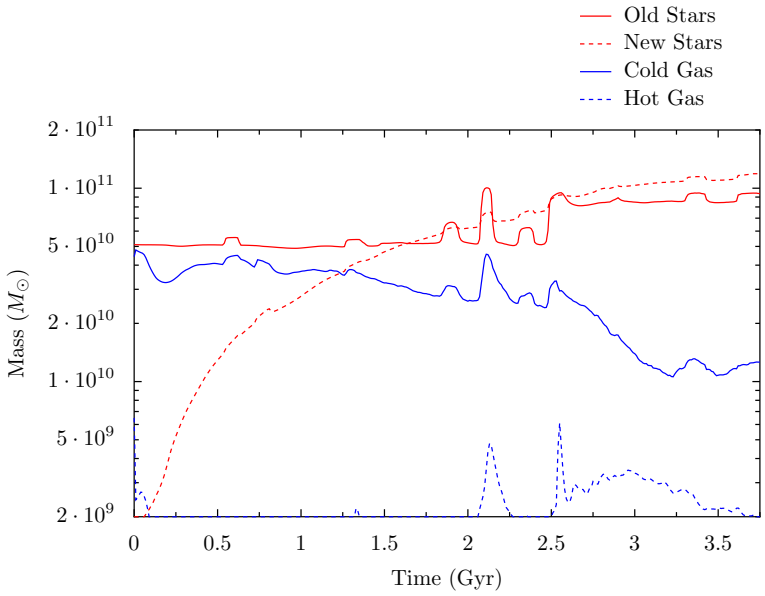

Figure 4.66: Mass evolution of the main progenitor in the cos9-2 simulation.

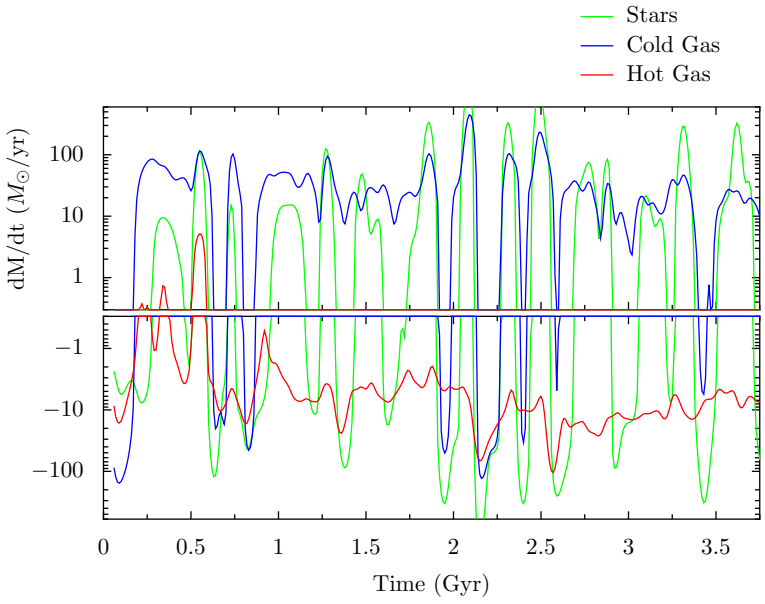

Figure 4.67: Mass accretion rates in the cos9-2 simulation.

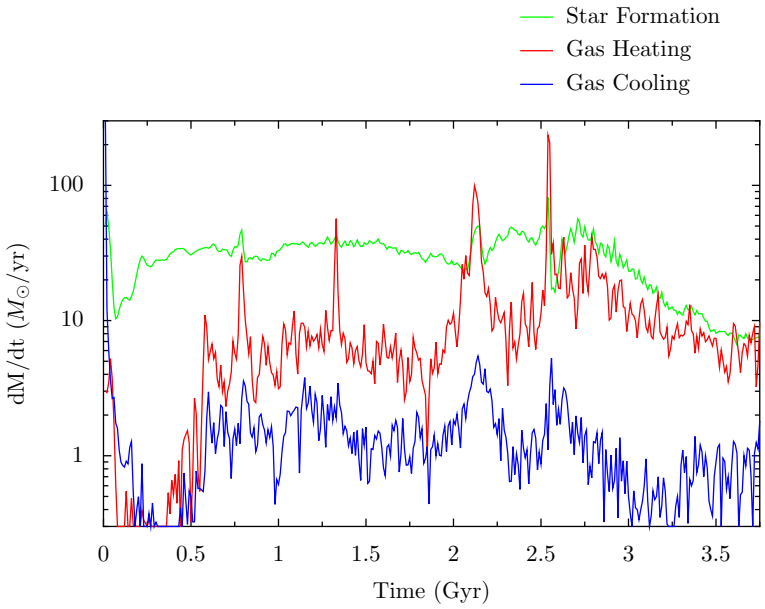

Figure 4.68: Mass conversion rates in the cos9-2 simulation.

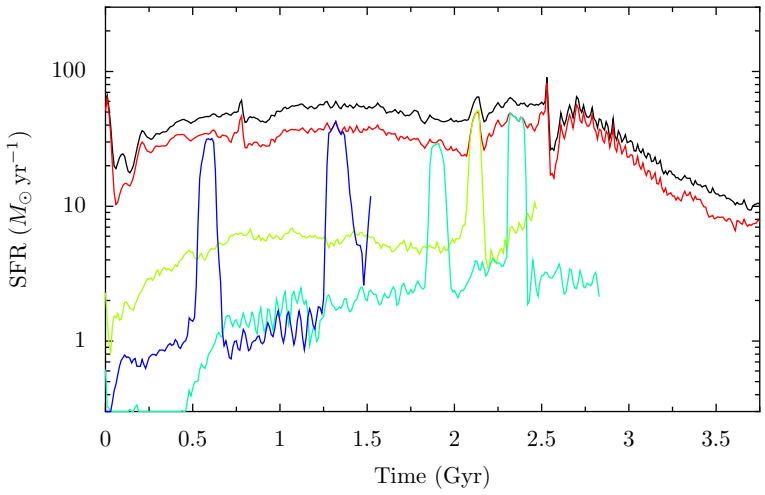

Figure 4.69: Star formation rates for model galaxies in the cos9-2 simulation.

4.6.2 Effect of Feedback Scheme

One of the major uncertainties in hydrodynamic simulations of stellar systems is how to handle feedback from supernovae. As described in Section 2.2.1, this work makes use if the Cox et al. (2006b) parameterization of the effects of supernovae feedback, where the free parameters n, are the effective polytropic index of the equation of state of star forming gas , and τ_{fb}, the timescale over which energy from supernovae is thermalized. The polytropic index takes the values 0, 1, or 2, and the thermalization timescale takes the values 0.82 Myr (low), 8.2 Myr (med), and 82 Myr (high). Most of the simulations presented here use the $n2med$ parameter set.

In order to asses the effect of the different feedback parameter sets on the multiple merger simulations presented here, I have run simulations for at least 1 Gyr with each of the nine combinations of parameters. The rather short simulation time is due to the fact that the simulations are quite expensive for the low value of τ_{fb}. Star formation rates for these nine simulations are shown in Figure 4.70. The initial conditions are those for the cos9-2 simulation.

Low values for the thermalization timescale lead to much higher star formation rates peaked at earlier times, and therefore faster gas depletion times. Changing the n, also affects the star formation rates, but not nearly as dramatically as changing τ_{fb}.

The star formation rates are the quantity most directly affected by the feedback scheme. However, the fast star formation timescales will also affect the structure of the remnants by changing the gas fractions of incoming galaxies. I am leaving the effect of the feedback scheme on the remnants for the future.

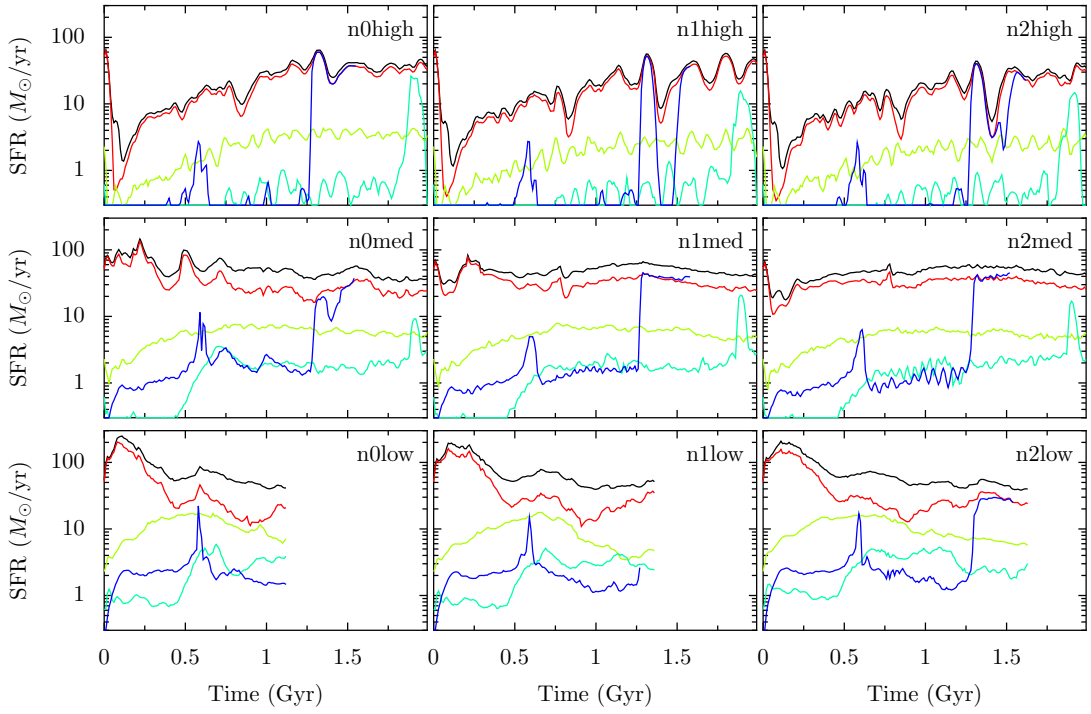

Figure 4.70: Effect of different supernova feedback parameters in the cos9-2 simulation. The most dramatic difference occurs when changing τ_{fb} (low, med, and high). Low feedback leads to higher star formation rates, peaked at earlier times. Changing the value of n has a comparatively small effect.

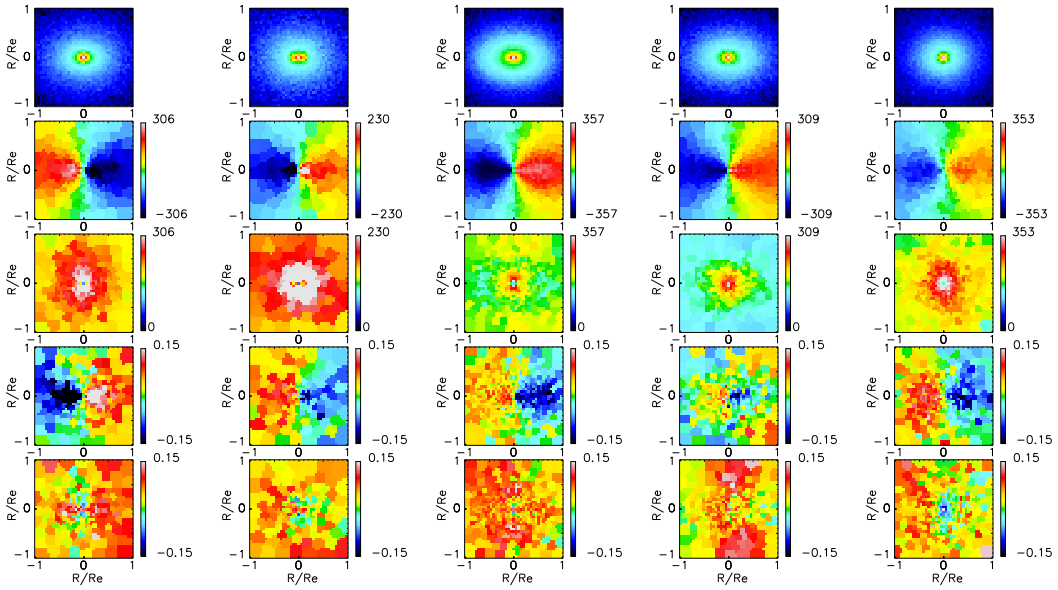

Figure 4.71: Kinematic data for the simulations from cosmological initial conditions. From the left, cos1, cos2, cos3, cos5, and cos9.

4.6.3 Kinematic Data

Figures 4.71 and 4.72 show simulated integral field data for simulates starting from cosmological initial conditions. All of the remnants are clearly fast rotators.

In section 4.4 I showed that the merger history of a galaxy has an effect on its final kinematics: Galaxies that are built up by sequential mergers have less rotation than those that experience an equal mass major merger. The cosmological simulations have a variety of merger histories, with the mass growth of some dominated by mergers, and the mass growth of others dominated by quiescent accretion. The cosmological simulations do not display the same relationship between merger history and kinematic structure as the idealized simulations.

The most obvious difference between the idealized and the cosmological simulations is that the cosmological ones include gas replenishment from the intergalactic medium. Therefore, it seems likely that continued infall of cold gas is the most important factor in the kinematics

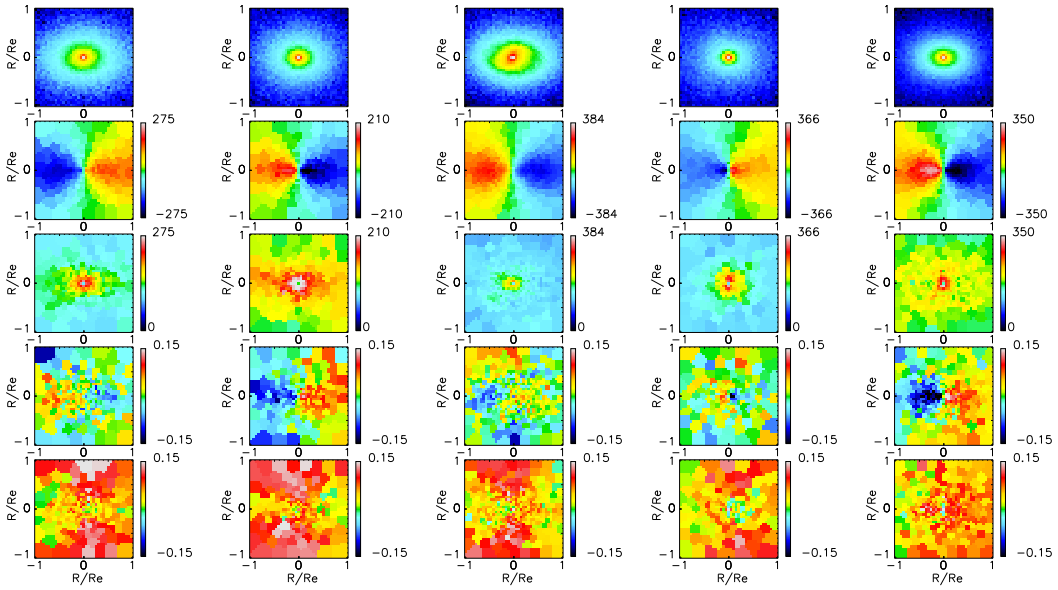

Figure 4.72: Kinematic data from the second series of simulations from cosmological initial conditions. From the left, cos1-2, cos2-2, cos3-2, cos5-2, and cos9-2.

of the remnants and results in fast rotators.

If the reason for the rotation is in fact cold gas infall, then the fact that *all* of the cosmological simulations display robust rotation, while essentially all of the most massive elliptical galaxies are slow rotators indicates that gas infall must be shut off in the real universe. A few possible processes that might shut off cold gas accretion are strong supernova feedback, feedback from active galactic nuclei, or shock heating of gas as it passes through a virial shock.

Strong supernova feedback is not a good candidate because it requires ongoing star formation, which is inconsistent with the observed old stellar populations in massive elliptical galaxies. Gas heating due to "radio-mode" feedback from low-luminosity active galactic nuclei (Croton et al., 2006) is a reasonable possibility. The simulations presented here do not include central black hole feedback in any form. Gadget includes shock heating via artificial viscosity, and the simulated galaxies are above the transition mass where the virial shock is thought to be stable (Birnboim & Dekel, 2003; Dekel & Birnboim, 2006). However, shock heating does

not seem to be effectively shutting off cold gas accretion in these simulations.

4.7 Conclusions

We saw in Chapter 3 that hydrodynamics simulated binary galaxy merger remnants nearly always produce fast-rotating early-type remnants by virtue of their large orbital angular momentum. In this chapter, I have shown that if mass is built up via successive binary equal mass major mergers, then the remnant is also a fast-rotator. This is because the orbital angular momentum in the last encounter has a dominant effect on the kinematics of the remnant.

Starting with the same progenitors and varying only the order in which galaxies merge, the opposite end of the spectrum of possibilities is to let the galaxies merge one after another, one at a time. This is a series of sequential mergers of decreasing mass ratio as the mass of the central galaxy is built up.

This sequential merger case robustly produces non-rotating remnants. The orbital angular momentum of the incoming galaxies averages to zero and the remnant is left with no net rotation. This is a plausible formation mechanism for the SAURON slow-rotators.

I have also run a series of simulations starting from a large, lower-resolution cosmological simulation. I selected compact groups and re-simulated them at higher resolution in order to explore the kinematics of the remnants after the members of the groups have merged. I found uniformly high rotation in these cosmological cases.

The cosmological initial conditions have a variety of merger histories, so it would seem that the constant inflow of gas from the intergalactic medium is the decisive factor in making the remnants rotate.

I have not yet run the simulations down to low redshift. The observational constraint from the SAURON survey is that there exists a population of galaxies that do not rotate

today, not at $z = 1$. It is possible that continued harassment and mergers will average away the significant rotation that the simulated remnants display at $z = 1$. If the rotation goes away by $z = 0$, then these simulated galaxies could still be identified as the SAURON slow rotators.

Even if these simulated galaxies are *not* identified as the source of the SAURON slow rotators, they were produced from reasonable cosmological initial conditions, and the simulation was done with a code that can be expected to reasonably represent the actual evolution of the system. Shouldn't these galaxies exist?

This constitutes a prediction that early-type galaxies at $z = 1$ should rotate. van der Marel & van Dokkum (2007) presents tantalizing evidence that this may indeed be the case. However, van der Wel & van der Marel (2008) indicates that this result may not be robust. Either way, the question will be decided observationally very soon.

4.7.1 Future Work

Simulating multiple galaxy mergers is a natural next step in the progression of study of numerical simulations of galaxy formation, and several groups have recently done or are currently doing similar work Naab et al. (2007); Martig et al. (2008). Each group has only simulated a small number of cases and has made different decisions about how to simulate gas physics and how to handle star formation and supernova feedback. These studies are quite complementary to each other and it will be interesting to analyze the similarities and differences between the simulations of different groups in more detail.

The primary question that needs to be decisively addressed in immediate future work is: Is the late infall of cold gas the primary reason that the cosmological simulations are rotating? If so, why does this make such a big difference? Is radiative gas cooling the

important physical process? Is it the fact that the matter is coming in as a stream rather than as lumps?

The idealized simulations were informative and the results are fairly well-understood. Nevertheless, the conclusion would be more convincing if I run a few additional random realizations of each case. I could bias the orientations of the merger planes so that the galaxies tend to be co-linear. This is to simulate the accretion along filaments that occurs in cosmological simulations.

Starting from the same progenitors, the "binary tree" method of mass build-up finishes faster than the "sequential mergers" method. Therefore sequential mergers have consumed more of their gas by the time the final merger takes place. Does the fact that the sequential mergers produced slow rotators due to their merger history or due to their lower gas fractions when the final few mergers took place? This could be answered by changing the orbits of the progenitors to adjust the time when the final events happen.

The realization that most of our simulated galaxies are rotating led to the question of whether they would continue to rotate at lower redshift. I have started a version of cos9-2 that has a high-resolution region twice as large cos9-2. The cos9-2 simulation runs for 4 Gyr ($z = 0.7$) before the low-resolution region starts to enter the central part of the high resolution region. The larger high-resolution region will allow the simulation to run to at least a redshift of 0.4, and hopefully as low as 0.2 before the low-resolution region begins to interfere.

Two extreme cases of initial conditions that will build intuition are to simulate the same cosmological halos, but with all gas turned into stars, and then again with all stars turned into gas. Finally, it would be useful to run a third simulation intermediate between these two where the gas fraction of each density peak does not change. I have run such a realization of the cos9 halo where I have not replaced the baryonic density peaks with model galaxies.

This last simulation is finished, but not yet analyzed. Taken together, these three simulations should provide guidance in determining what physical processes are important to include in simulations that are supposed to come close to the real universe.

It would be interesting to vary the properties of the model galaxies both in the idealized simulation and in the cosmological cases. I add angular momentum to the cosmological cases when I insert model galaxies because the model galaxies have much higher specific angular momenta than the galaxies they replace. The simulation without model galaxy replacement will provide some insight into whether or not this makes a difference, but it will not provide a definitive answer because other things are changing as well (such as the gas fraction of the galaxies). One way to test whether or not this makes a difference would be to use model galaxies with lower specific angular momenta instead of the *G*-series galaxies.

Other items for immediate future work are:

- Ensure that the cosmological and idealized simulations follow the observed global trends obeyed by early-type galaxies such as the Fundamental Plane.
- I need a more well-digested understanding of the mass accretion history of the cosmological simulations.
- Certain cosmological simulations experience a prolonged period of gas starvation. Is this because of a virial shock?
- Look at the λ parameter defined by Emsellem et al. (2007) to quantify the rotational state of the remnants.
- Organize the cosmological cases according to their characteristics rather than according to their names. This will help readers follow the different cases.
- Draw merger trees for each of the simulations.

- The discussion of the setup of the cosmological initial conditions would benefit from a more precise, quantitative discussion of how it is done, along with plots of density profiles of the the halos in the WMAP80 simulation before and after model galaxy replacement.
- Look at time evolution of structure and kinematics during bouts of undisturbed cold gas accretion and mergers.

Some items for future work on an intermediate timescale are:

- Choose halos to simulate more carefully based on their merger history and environment.
- Explore a greater range of halo masses.
- Start the sub-region simulations at progressively higher redshifts in order to see how the remnants change. This will also be useful to eventually make contact with the Naab et al. (2007) simulations for comparison.
- Naab (2008) claims to find that slow rotators form in $10^{13} M_{\odot}$ halos, which are 10 times more massive than the galaxies I have simulated in this chapter. However, the physical reason that $10^{12} M_{\odot}$ halos are different from $10^{13} M_{\odot}$ is not clear. It could be the dynamical effect of the massive halo itself (for example, merging galaxies would approach each other at much higher velocities), or it could be that the surrounding matter behaves in a systematically different way (for example, higher mass halos may experience more minor mergers).
- The mass build-up of several of the cosmological simulations are dominated by in-situ star formation. These remnants rotate but they are not thin stellar disks. Is the thickening of the stellar disk due to bombardment by infalling clumps? Or is it because the filaments feeding the gas disk change over time, the orientation of the gas disk changes in turn,

and the stellar disk is thick because it is the "time integral" of the past positions of the thin gas disk?

- The galaxies formed in the cosmological simulations have halos of hot gas that would emit x-rays. It may be possible to compare their x-ray temperatures and surface-brightness profiles to observed galaxies.

- What are the masses and Toomre Q parameters in the gas disks that formed in some of the cosmological simulations?

- It seems increasingly relevant to produce simulated integral-field data for in-progress mergers Genzel et al. (motivated by 2006, for example). It will be difficult to provide information that is useful to observers because merging systems have complex geometries and look very different from different viewing angles.

- Increasing evidence seems to point to early-type galaxies at high redshift having very small sizes (e.g. van Dokkum et al., 2008). The galaxies formed from cosmological initial conditions have half mass radii of 2-3 kpc, while van Dokkum et al. sees half mass radii of 1 kpc. This raises two interesting questions: Do the galaxies formed in my simulations have anything to do with the van Dokkum et al. galaxies? Is there a physical process that will "puff up" the van Dokkum et al. galaxies so that they look more like ellipticals at low redshift?

- One is a comparison of the star forming disks in several of the cosmological simulations to the galaxies seen by Genzel et al. (2006) at $z = 2$.

- What is the effect of different star formation feedback parameters on the final structure of the remnants? I have started these simulations, but they are not yet finished.

- What is the effect of feedback from black hole accretion on the gas inflow rates and resulting structure of the remnants?

- High resolution SPH simulations from several groups presented at the Santa Cruz Galaxy Formation Workshop in 2008 seem to robustly show very thin, pressure-confined filaments of cold gas feeding halos (Keres, 2008; Brooks, 2008). After the first pass through the center of the forming galaxy, these streams break up into clumps that persist for a long time. Grid codes do not seem to display this behavior (Dekel, 2008). Is this because grid codes are too diffusive or because SPH codes suppress instabilities that would dissolve these clumps? Why is there a difference in filaments sizes between the two types of codes?

- Filaments of cold gas often seem to be remarkably straight over long distances and seem to hit the very center of the forming galaxy. How can this be?

Chapter 5

Homology

> "I shall not today attempt further to define the kinds of material I understand to be embraced within that shorthand description [of pornography] ... But I know it when I see it[.]"
>
> — United States Supreme Court Justice Potter Stewart

> "Saying that initial conditions are non-Gaussian is like saying that an animal is a non-dog."
>
> — Sergei Shandarin (related by Joel Primack)

Are galaxies homologous? The discovery of the Fundamental Plane (FP) of elliptical galaxies distinctly sharpened this question because galaxies showed a regularity that almost, but not quite, followed that expected from the Virial Theorem for systems in dynamical equilibrium. The Virial Theorem holds in any case, but if each galaxy were unique, then the FP would have a large scatter. If all galaxies were simply scaled copies of one another, then the FP would follow the virial expectation. In either of these cases, the FP would likely not have generated the interest that it has because it would either be less useful (in the former case) or less interesting (in the latter case). Actual galaxies seem to be in between these two possibilities: they are quite regular in structure, but do not quite follow the simple virial expectation. An understanding of the origin of the FP requires at least one ingredient aside from the Virial

Theorem, and the search for that missing ingredient has been the focus of many papers.

In this chapter I will develop a precise definition of homology starting from the several informal definitions that seem to be in common use. My definition will involve choosing a set of three scaling constants for each galaxy. The best choice for the definition of the scaling constants is unclear, so I explore a wide range of possibilities, using them to draw dimensionless density, velocity dispersion, and kinetic energy profiles for a large set of hydrodynamic binary galaxy merger simulations. The best definition of the scaling constants is the one that makes the dimensionless profiles of the simulated merger remnants have the least variation from remnant to remnant. I find that one particularly simple definition does a remarkable job of making a wide variety of merger remnants look similar.

The next step in this study is to look at a wider set of simulations to see if they, too, share the same properties as the binary merger remnants analysed here. Finally, the last step is to consult observations of real galaxies to assess the usefulness of my definitions of the scaling constants.

5.1 Theoretical preliminaries

Unfortunately the definition of the term homology is unclear. Everyone has the intuitive sense that it means that galaxies are somehow similar to each other, but precise definitions seem to vary widely. People feel that they know it when they see it, but not everyone agrees on what *it* is.

I will develop precise definitions that I believe capture the common usage, and I will endeavor to use my precisely defined terms over the bare word itself in order to avoid confusion. My own intuitive sense is that homology means that galaxies are scaled copies of each other. For single-component models, it is fairly clear how to express this concept precisely.

The first obvious point is that the property of homology applies to a set of galaxies, not to individual galaxies. The statement that a set of galaxies is homologous is a very strong claim about their structure. The statement that they are non-homologous conveys almost no information about them. All homologous galaxies are the same, but every non-homologous galaxy is non-homologous in its own way.

The usual method is to define structure constants relating true values of a galaxy's mass and luminosity to "virial estimates" obtained using scaling constants. From Bender et al. (1992):

$$L = c_1 I_e r_e^2 \tag{5.1}$$

$$M = c_2 \sigma_0^2 r_e \tag{5.2}$$

where L is the galaxy's luminosity, r_e is the projected half-light radius, I_e is the mean surface brightness inside r_e, σ_0 is the projected aperture velocity dispersion, and c_1 and c_2 are structure constants defined by these two equations. The important point is that M is the true mass of the galaxy where σ_0 and r_e are scale quantities combined in such a way as to dimensionally produce a mass (up to physical constants, in this case G_N^{-1}). Therefore variation of c_2 from galaxy to galaxy indicates that mass profiles of the two galaxies differ to produce a different relationship between the virial estimator and the actual mass. One definition of homology holds that these structure constants are the same for all galaxies. I denote this definition *structure-constant homology.*

Another definition is that the distribution functions of all galaxies are scaled versions of some "master" distribution function. That is, there exists a function F such that all galaxies have distribution functions f obtainable from F via:

$$f(x, v) = \frac{M}{R^3 V^3} F(x/R, v/V) \tag{5.3}$$

where R, V, and M are arbitrary scale constants, different for each galaxy. That is, if one knows the universal distribution function, three numbers suffice to completely describe a galaxy. This will be called *scaling homology*.

We shall see that all galaxies that are scaling-homologous are also structure-constant-homologous, but not vice versa. That is, scaling homology is a stronger concept.

5.1.1 The Virial Theorem

I treat the simple case of a single component galaxy explicitly for clarity of comparison with the multi-component case.

The scalar virial theorem says:

$$2K + W = 0 \tag{5.4}$$

where K is the total kinetic energy of the system and W is the total potential energy of the system. Putting this into the language of distribution functions,

$$\rho(x) = \int f(x,v)\, d^3x\, d^3v \tag{5.5}$$

the total kinetic energy is

$$\mathrm{KE} = \frac{1}{2}\int |v|^2 f(x,v)\, d^3x\, d^3v \tag{5.6}$$

and the total potential energy is:

$$\mathrm{PE} = -\frac{1}{2}\int \frac{G_N \rho(x)\rho(y)\, d^3x\, d^3y}{|x-y|} = -\frac{1}{2}\int \frac{G_N f(x,v) f(y,w)\, d^3x\, d^3y\, d^3v\, d^3w}{|x-y|} \tag{5.7}$$

The virial theorem is then:

$$\int |v|^2 f\, d^3x\, d^3v = \frac{1}{2}\int \frac{G_N f(x,v) f(y,w)\, d^3x\, d^3y\, d^3v\, d^3w}{|x-y|} \tag{5.8}$$

Define three arbitrary scaling constants R, V, and M, and non-dimensionalized coordinates $\tilde{x} = x/R$ and $\tilde{v} = v/V$.

$$V^2 R^3 V^3 \int |\tilde{v}|^2 f(x,v)\, d^3\tilde{x}\, d^3\tilde{v} = \frac{G_N R^6 V^6}{2R} \int \frac{f(x,v) f(y,w)\, d^3\tilde{x}\, d^3\tilde{y}\, d^3\tilde{v}\, d^3\tilde{w}}{|\tilde{x} - \tilde{y}|} \tag{5.9}$$

Finally define the non-dimensionalized distribution function F to be:

$$F(\tilde{x}, \tilde{v}) = \frac{R^3 V^3}{M} f(R\tilde{x}, V\tilde{v}) \tag{5.10}$$

The virial theorem is now:

$$MV^2 \int |\tilde{v}|^2 F(\tilde{x}, \tilde{v})\, d^3\tilde{x}\, d^3\tilde{v} = \frac{G_N M^2}{2R} \int \frac{F(\tilde{x}, \tilde{v}) F(\tilde{y}, \tilde{w})\, d^3\tilde{x}\, d^3\tilde{y}\, d^3\tilde{v}\, d^3\tilde{w}}{|\tilde{x} - \tilde{y}|} \tag{5.11}$$

Therefore define the structure constants

$$\alpha := \int |\tilde{v}|^2 F(\tilde{x}, \tilde{v})\, d^3\tilde{x}\, d^3\tilde{v} = \frac{1}{M} \int |v/V|^2 f(x,v)\, d^3x\, d^3v \tag{5.12}$$

and

$$\beta := \int \frac{F(x,v) F(y,w)\, d^3\tilde{x}\, d^3\tilde{y}\, d^3\tilde{v}\, d^3\tilde{w}}{|\tilde{x} - \tilde{y}|} = \frac{1}{M} \int \frac{f(x,v) f(y,w)\, d^3x\, d^3y\, d^3v\, d^3w}{|x/R - y/R|} \tag{5.13}$$

With these definitions, the Virial Theorem becomes:

$$\alpha V^2 = \beta \frac{G_N M}{2R} \tag{5.14}$$

and comparing to equation 5.2 reveals that:

$$c_2 = \left(\frac{2\alpha}{G_N \beta}\right) \left(\frac{\bar{M}}{M}\right) \left(\frac{R}{r_e}\right) \left(\frac{V}{\sigma_0}\right)^2 \tag{5.15}$$

where $\bar{M}$ refers to the total mass of the galaxy.

Finally, the virial theorem places a constraint on galaxies in equilibrium so that if they are homologous, then the quantity of numbers required to fully specify a galaxy goes from three to two.

5.1.2 Two Component Galaxies

Describing a galaxy that contains both stellar and dark matter requires specifying two distribution functions, f and g, with corresponding non-dimensionalized functions F and G.

$$MV^2\left(\int|\tilde{v}|^2F(\tilde{x},\tilde{v})\,d^3\tilde{x}\,d^3\tilde{v}+\int|\tilde{v}|^2G(\tilde{x},\tilde{v})\,d^3\tilde{x}\,d^3\tilde{v}\right) \tag{5.16}$$
$$=\frac{G_NM^2}{2R}\int\frac{(F(\tilde{x},\tilde{v})+G(\tilde{x},\tilde{v}))(F(\tilde{y},\tilde{w})+G(\tilde{y},\tilde{w}))\,d^3\tilde{x}\,d^3\tilde{y}\,d^3\tilde{v}\,d^3\tilde{w}}{|\tilde{x}-\tilde{y}|}$$

$$MV^2\left(\int|\tilde{v}|^2F(\tilde{x},\tilde{v})\,d^3\tilde{x}\,d^3\tilde{v}+\int|\tilde{v}|^2G(\tilde{x},\tilde{v})\,d^3\tilde{x}\,d^3\tilde{v}\right) \tag{5.17}$$
$$=\frac{G_NM^2}{2R}\int\frac{(F(\tilde{x},\tilde{v})(F(\tilde{y},\tilde{w})+2F(\tilde{x},\tilde{v})G(\tilde{y},\tilde{w})+G(\tilde{x},\tilde{v})(G(\tilde{y},\tilde{w})\,d^3\tilde{x}\,d^3\tilde{y}\,d^3\tilde{v}\,d^3\tilde{w}}{|\tilde{x}-\tilde{y}|}$$

defining

$$\gamma:=2\int\frac{F(\tilde{x},\tilde{v})G(\tilde{y},\tilde{w})\,d^3\tilde{x}\,d^3\tilde{y}\,d^3\tilde{v}\,d^3\tilde{w}}{|\tilde{x}-\tilde{y}|}=\frac{2}{M}\int\frac{f(x,v)g(y,w)\,d^3x\,d^3y\,d^3v\,d^3w}{|x/R-y/R|} \tag{5.18}$$

we at last have the virial theorem in the form:

$$(\alpha_f+\alpha_g)V^2=(\beta_f+\beta_g+\gamma)\frac{G_NM}{2R} \tag{5.19}$$

From this expression it is clear that for multi-component galaxies:

- Scaling homology implies structure-constant homology.
- Structure-constant homology does not imply scaling-homology because structure-constant homology only requires a small number of constraints on the definite integrals defining α, β, and γ.
- A galaxy being structure-constant homologous does not imply that each component is separately structure-constant homologous. Structure-constant-homologous galaxies can be built from non-homologous components if the change in α_f compensates for the change in α_g and similarly for β.

- The components of galaxies being structure-constant-homologous does not imply that the galaxies are structure-constant-homologous.

- The structure constants for multi-component galaxies are not simply the sum of the structure constants of the individual components owing to the cross term γ.

Finally, similar considerations for scaling-homology yield:

- Scaling-homology of galaxies implies scaling-homology of the components.

- Scaling-homology of the components does not imply scaling-homology of galaxies. The whole galaxy is scaling-homologous only if the ratios of the scaling constants for each component are the same for all galaxies. That is, R_f/R_g is the same for all of the galaxies.

One may wonder whether the dark and luminous components should be allowed their own scaling constants. The problem is that scaling the components separately disturbs the dynamical equilibrium of the galaxy. Consider a galaxy in dynamical equilibrium where the baryonic scale radius is allowed to shrink to zero, making the baryons into a point mass. The dark matter far outside the original baryonic scale radius will not be significantly affected, but the dark matter inside the original baryonic scale radius will not have more mass enclosed. This will obviously disturb equilibrium. Therefore the question of whether each component of a set of galaxies is separately homologous is of little practical importance.

The discussion of scaling constants makes it clear that scaling-homology is closely related to systems of units. It means that all galaxies are the same if one works with the correct system of units, where the units are allowed to change from galaxy to galaxy.

5.1.3 Observational Complications

The only observationally accessible quantities are projected ones. Therefore for example, the measured mean surface brightness within the effective radius involves an integral along the light of sight and therefore implicitly mixes information about the entire mass/light profile at all radii.

A second complication involves mass-to-light ratios, where much confusion has resulted from imprecision in the use of terminology. There are two contributions to the observed mass-to-light ratio—one is the stellar population and the other is the dark matter fraction. The problem is that these two contributions are generally observationally degenerate. Therefore there is a tendency to simply refer to the mass-to-light ratio without specifying whether to quantity under consideration is due to stars or dark matter fraction.

5.1.4 Three ways to tilt the FP

There are three independent ways to generate the tilt in the fundamental plane. Any or all of them may be at work.

The first is a systematic change in the stellar mass-to-light ratio with the mass of the host galaxy via trends in the age and/or metallicity of the stellar population. In this case the stellar and dark matter distribution functions are scaling (and therefore structure-constant) homologous because the masses of stars and dark matter components are unaffected.

The second is a systematic change in the dark matter fraction near the center of the galaxy. This is a mild form of non-homology which is achieved by changing the ratio of the mass scaling constants M_{sm}/M_{DM} with galaxy mass. Overall scaling- and structure-constant homology are violated, but the baryonic components by themselves may be nearly scaling- and structure-constant-homologous. Furthermore, as long as the stellar and dark matter remain

nearly decoupled by the very different half mass radii, then changing the dark matter fraction should not greatly disturb the dynamical equilibrium of the stellar material. In this case the stellar population mass-to-light ratio is identical for all galaxies, but the total mass-to-light (both for the entire galaxy and within any radius) ratio changes systematically with mass.

The third possibility is that homology is flagrantly violated and the baryonic components of galaxies are neither scaling nor structure-constant homologous. Even if the stellar population mass-to-light ratio is always the same, there is still total freedom in the total mass-to-light ratio owing to the total freedom in the choice of dark matter profile for each galaxy. It may change or be constant as a function of radius, and the total mass-to-light ratio may change or be constant for the entire set of galaxies.

As a concrete example, this is the case if more massive galaxies are more centrally concentrated than lower mass galaxies. One has the choice to give all galaxies the cosmological baryon fraction or change the baryon fraction from galaxy to galaxy, determining the overall mass-to-light ratio. Even if all galaxies have the same baryon fraction, changing the radial structure of the dark matter halo can change the mass-to-light ratio as a function of radius.

A great source of confusion is that the first and second possibilities are very different theoretically but nearly degenerate observationally. Everyone agrees that the first possibility involves homology and the third possibility involves non-homology. However, the second possibility is *observationally* very similar to the first possibility but *theoretically* very similar to the third possibility. This unfortunate circumstance makes it difficult to decide this issue.

5.1.5 Variable dark matter fraction and equilibrium

There are two contributions to a total mass-to-light ratio—one from the characteristics of the stellar population and one due to the accompanying dark matter. This allows

researchers, through the sloppy use of terminology, to labor under the false impression that they agree with one another.

If the mass-to-light ratio changes with galaxy mass because of a changing stellar population, then the FP will be tilted but the mass distribution may still be homologous. However, if the mass-to-light ratio changes due to changing dark matter fraction, then the galaxies *must* be non-homologous.

Consider the spherically symmetric Jeans equation (e.g. Binney & Tremaine, 1987):

$$\frac{\ln \nu}{\ln r} + \frac{\ln \sigma_r^2}{\ln r} + 2\beta + \frac{1}{\sigma_r^2}\frac{d\Phi}{\ln r} = 0 \tag{5.20}$$

where ν is the number density of tracer particles, σ_r is the radial component of the velocity dispersion, Φ is the total gravitational potential, and $\beta = 1 - \sigma_\theta/\sigma_r$ is the anisotropy parameter.

The matter density is provided by two components, ρ_b and ρ_d. The Poisson equation is linear so if we find two potential functions Φ_b and Φ_d that separately satisfy it, then the potential for the sum of the mass densities is the sum of the potentials. So:

$$\nabla^2\Phi_b = 4\pi G_N \rho_b \qquad \text{and} \nabla^2\Phi_d = 4\pi G_N \rho_d \tag{5.21}$$

implies

$$\nabla^2(a\Phi_b + b\Phi_d) = 4\pi G_N(a\rho_b + b\rho_d) \tag{5.22}$$

is also a solution to the Poisson equation. Changing the dark matter fraction, then corresponds to setting $a = 1$ and allowing b to change. Putting this into the Jeans equation results in:

$$\frac{\ln \nu}{\ln r} + \frac{\ln \sigma_r^2}{\ln r} + 2\beta + \frac{1}{\sigma_r^2}\left(\frac{d\Phi_b}{\ln r} + b\frac{d\Phi_d}{\ln r}\right) = 0 \tag{5.23}$$

That is, if a galaxy is in equilibrium with b=1, then *any* change to b *must* be compensated by a change in the anisotropy β or a change in the radial fall-off of density or velocity dispersion.

The dark matter and baryons separately satisfy their own Jeans equations, so there is no possibility of compensating changes that will preserve equilibrium. A final hope would be

to carefully define the scale constants in equation 5.3 to depend on b so that homology would be preserved. However, we are working with the Jeans equation in dimensionless form, so any changes to units or scale constants cancel out and have no effect on the equation.

We are left with the conclusion that varying dark matter fraction and non-homology are the same concept. If the tilt in the FP is *not* due to systematic changes in the stellar population mass-to-light ratio, then it *must* be due to non-homology. There is no separate case where "only" the dark matter fraction and therefore the observed mass-to-light ratios are changing.

5.2 Previous Work

This subject has a long history and this section only covers the recent notable observational and theoretical developments.

5.2.1 Observational Studies

Cappellari et al. (2006) used Schwarzschild modeling of SAURON early-type galaxies to show that the so-called virial mass estimator ($5r_e\sigma^2/G$) is an excellent estimator of the dynamical mass within one effective radius. The SAURON survey also has stellar spectra over the whole galaxy image out to $\sim r_e$, and is thus excellently placed to use stellar population synthesis to finally break the degeneracy between dark matter fraction and stellar population mass-to-light ratio. The key plot is their Figure 17, reproduced here as Figure 5.1 and it is unfortunately completely ambiguous. For dynamical mass-to-light ratios below 2.8, there is basically a linear relationship between the stellar mass-to-light ratio and the dynamical mass-to-light ratio. For larger mass-to-light ratios, there is essentially a single stellar mass-to-light ratio, independent of the dynamical mass-to-light ratio.

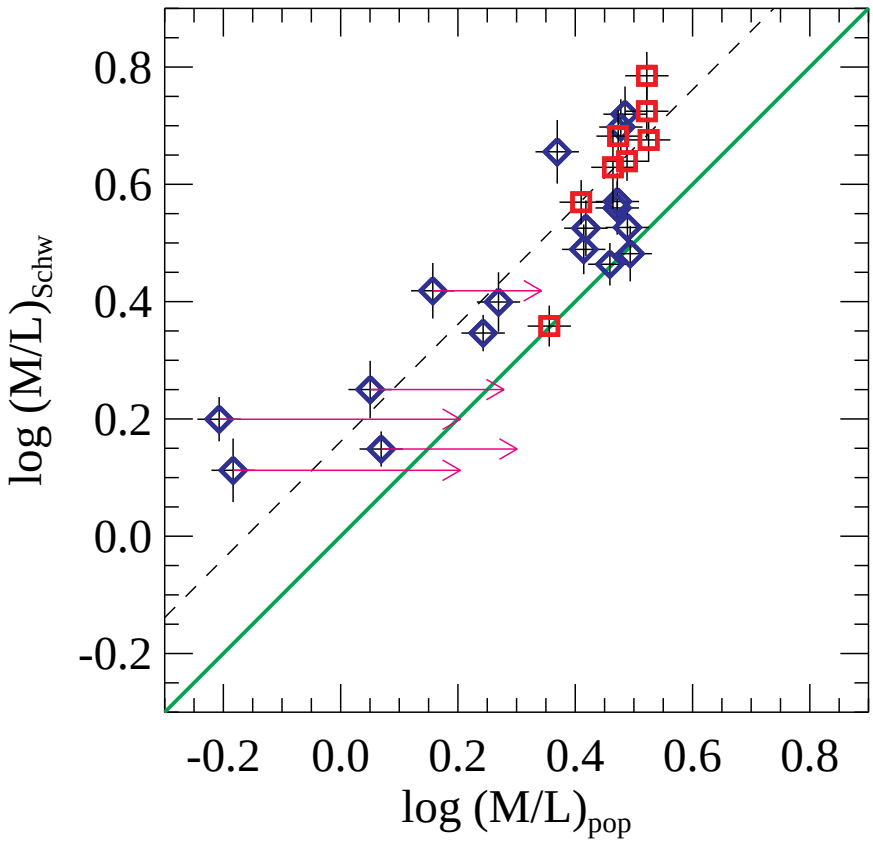

Figure 5.1: Dynamical mass-to-light ratio versus stellar mass-to-light ratio from Cappellari et al. (2006). The red points are slow-rotators, the blue points are fast-rotators, and the pink arrows indicate the uncertainty due to modeling the stellar population with a single age or multiple ages.

It seems that the easiest conclusion to draw is that for mass-to-light ratios below 2.8, stellar populations are solely responsible for variations, whereas for mass-to-light ratios above 2.5, dark matter fraction is solely responsible for variations. An unfortunate state of affairs, but the universe is under no obligation to be simple.

Bolton et al. (2008) used strong gravitational lenses to argue that if one replaces the luminosity surface density in the FP with the mass surface density, one gets an untilted fundamental mass plane that is in full agreement with the virial expectation. Therefore the tilt in the FP must be due to variations in mass-to-light ratio, but this study is unfortunately

mute on whether the variations are due to dark matter fraction or stellar populations.

Graves is using Sloan data on nearby galaxies to look at dynamical and stellar mass-to-light ratios (personal communication, 2008). She finds large variation in dynamical mass-to-light ratios with little variation in stellar population mass-to-light ratios. This indicates a changing dark matter fraction/non-homology.

5.2.2 Theoretical Studies

González-García & van Albada (2003) and Boylan-Kolchin et al. (2005) studied dissipationless merger simulations to determine whether mergers leave the FP intact. González-García & van Albada (2003) started with structure-constant homologous systems and found that their remnants did not share the property. The merger remnants *do* lie on the FP, evidently because the two structure are able to undergo compensating changes since they only appear in a multiplicative combination in the FP relation (their Equation 6). Boylan-Kolchin et al. (2005) studied a smaller number of much higher resolution simulations and found that both structure-constant homology and the FP were preserved by the merger process at the 10% level. They did, however, find a significant violation of homology for radial-orbit mergers.

Dekel et al. (2005) showed that simulated hydrodynamics merger share many of the observed properties of elliptical galaxies, with special emphasis on the large-radius ($\sim 2-5r_e$) kinematics.

Dekel & Cox (2006) studied dissipation as the potential origin of the FP tilt. They assumed that all observable galaxy properties are power-law functions of the mass of the galaxy and the gas fraction, and then used several merger simulations with different gas fractions and masses in order to fix the power-law exponents and constants in their model. They were left with a set of constraints on the power-law exponents such that for any observed FP tilt, one

could solve for the properties of the progenitor galaxies (e.g., gas fraction) as a function of mass. This of course depends on their merger simulations being good representatives of all mergers of that mass and gas fraction.

Robertson et al. (2006) assumed a constant stellar mass-to-light ratio and concluded that with a sufficient amount of gaseous dissipation, merger remnants naturally produce a tilted FP. Since they assumed a constant stellar mass-to-light ratio, this tilt must have been caused by structural non-homology/varying dark matter fraction.

Hopkins et al. (2008a) performed an extensive study of dissipation and the origin of the fundamental plane. They seem to be concerned with structure-constant homology, but dismiss non-homology as the source of the FP tilt. They assert that gas dissipation causes a varying dark-matter fraction inside the effective radius, which in turn tilts the FP. They note that a varying dark matter fraction implies non-homology, but somewhat confusingly still claim that the varying dark matter fraction is the overriding consideration.

5.3 Results

In this section I search for the definitions of the scaling constants that result in the least variation among the remnants produced by gas-rich binary major mergers.

5.3.1 Choice of Units

As we've seen, deciding whether a set of galaxies is scaling-homologous boils down to finding a system of units in which all galaxies look the same. The different density profile slopes and central dark matter fractions mean that the present set of simulated remnants cannot be perfectly homologous. However, the question continues to be interesting because of the remarkably consistent total mass density profile shown in Figure 2.2.

We seek mass, radius, and velocity (hence time) scales that can be used to non-dimensonalize the remnant density and velocity profiles. Typically, the projected stellar half mass radius and central velocity dispersion are used. The nearly power-law total mass density profile is scale-free, but other possibilities for a scale radius include the dark matter half-mass radius, the radius where dark matter and baryonic densities are equal, or the radius where the enclosed dark matter and enclosed baryonic matter masses are equal. Candidate scale masses are the total baryonic mass or total dark matter mass. Finally, for scale velocities it may be advantageous to include the velocity anisotropy in the definition. For now we are obviously leaving aside the issue of observationally determining the scale quantities once we have determined our favorites by analyzing simulated remnants.

5.3.1.1 Density Profiles

Figure 5.2 shows the non-dimensionalized density profiles for the usual choice of the stellar effective radius for the length scale and the total stellar mass for the mass scale. To avoid complications due to viewing angles, we use the 3D half mass radius, not the observationally accessible projected half mass radius.

Figure 5.3 shows a different choice of length and mass scales. The length scale is r_{eq}, the radius at which the enclosed stellar and dark masses are equal, and the mass scale is the stellar mass enclosed within r_{eq}. In comparing to the mass profiles shown in Figure 5.2, we must ensure that the same physical radial range of the galaxies are probed. Multiplying the chosen units by a factor common to all galaxies does not change the result, so we normalize to the *Sbc*201a-u4 simulation. For this simulation, $r_e = 0.437 r_{eq}$ and $M_{stars} = 1.54 M(< r_{eq})$.

We arrived at after looking at eight possible radius scales including stellar, dark, and total effective radii and projected effective radii, the radius where stellar mass density and dark

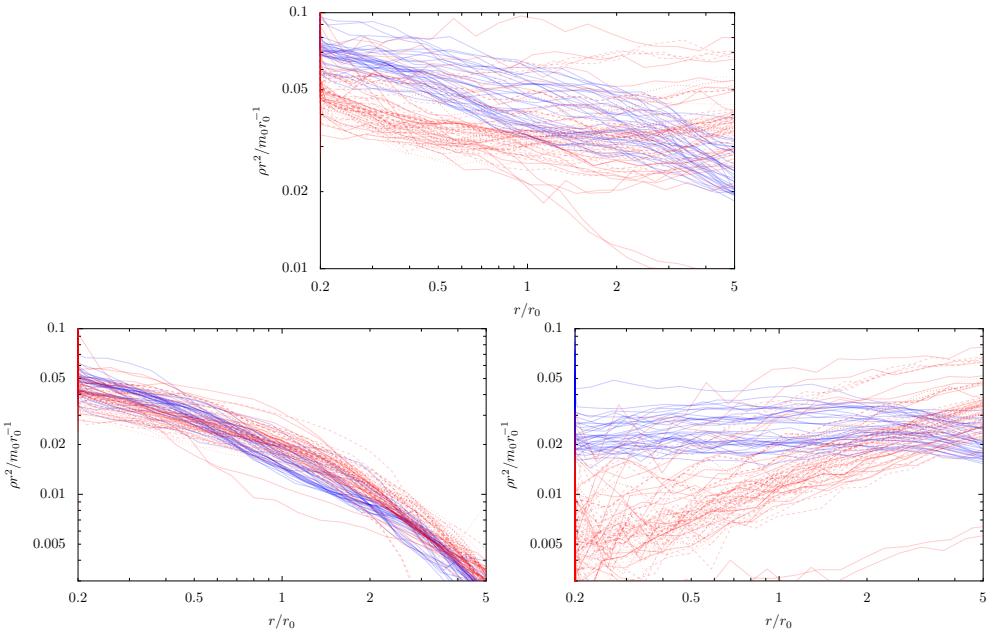

Figure 5.2: The total non-dimensionalized mass density profiles for all G and *Sbc* series simulations. Above, the total mass density, on the bottom left, the stellar mass density, and on the bottom right the dark matter mass density. All mass profiles have been multiplied by r^2 to flatten them out. The length and mass scales are the typical observationally motivated choices of stellar half mass radius and stellar mass. The stellar components of all of the simulations are strikingly similar. However, the chosen mass and length scales have nothing to do with the dark matter, so there is significant variation among the dark matter profiles of the different simulations. There is also a systematic change in the slope of the dark matter profiles between *Sbc* and G series simulations. No change of units will remove this difference.

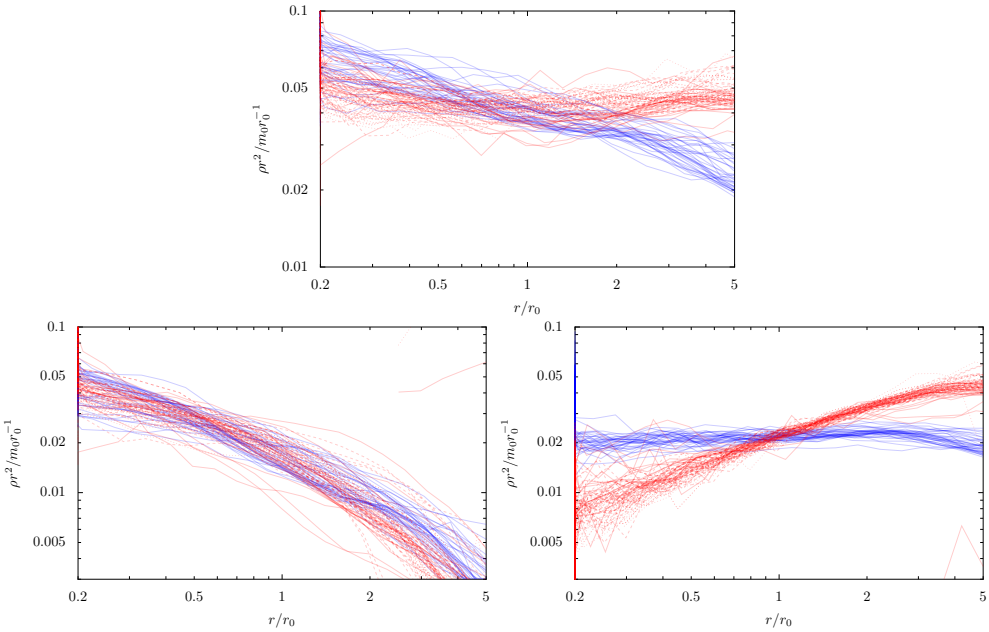

Figure 5.3: The same as Figure 5.2 except for a different choice of radius and mass scales. Here, the radius scale is $0.437 * r_{eq}$, where r_{eq} is the 3D radius where the enclosed stellar mass and dark mass are equal, and the mass scale is the 1.54 times the stellar mass enclosed within r_{eq}. The factors of 0.437 and 1.54 are chosen to ensure that these plots cover nearly the same physical region of the galaxy as Figure 5.2. With this choice of length and mass scale, the merger remnants show truly remarkable regularity. The dark matter mass profiles show $\sim 10\%$ variation and the baryonic mass profiles show $\sim 40\%$ variation in spite of a wide range of masses, gas fractions, orbits, and feedback recipes employed in these simulations.

mass density are equal, and finally the radius where the enclosed stellar mass and enclosed dark mass are equal. We evaluated thirty mass scales including total stellar, dark, and total mass, the total of each type of mass within each of four radii (stellar effective radius, dark effective radius, radius where stellar and dark densities are equal, and r_{eq}), and the mass scale that sets each of the three types of mass density to one at each of the four radii.

The simulated galaxy merger remnants analysed here are not perfectly scaling-homologous. This is clear as soon as one realizes that the central slopes of the dark matter profiles are different between the G and *Sbc* series of simulations. Changing the scale radius can only shift curves from side-to-side in Figures 5.2 and 5.3—it cannot change the slopes.

Even so, the radius and mass scale choice made in Figure 5.3 represents essentially the maximum regularity among galaxy merger remnants that one can hope for by judiciously choosing a system of units for each galaxy.

It is also surprising that the dark matter mass profiles for *Sbc*-series simulations is extremely close to an isothermal $\rho \propto r^{-2}$ profile (indicated that the relevant curves in Figure 5.3 are nearly flat). The dark matter profiles of *G*-series remnants are somewhat shallower, and the stellar remnants in both cases are somewhat steeper. In the case of the *G*-series remnants, the balance between the dark and stellar profiles leads to a total mass density very close to an isothermal profile. The *Sbc* series remnants have steeper total mass density profiles, but only slightly so.

This is in contrast with the widely known result from dissipationless cosmological dark matter simulations that the inner density slope of dark matter halos is between 1 (Navarro et al., 1996) and 1.5 (Moore et al., 1998). In these binary galaxy merger simulations, dark halos end up with even steeper profiles in spite of starting with shallower, NFW profiles.

5.3.1.2 Velocity Profiles

Having seen that the density profiles of simulated galaxy merger remnants are very consistent when scaled by a particular choice of constants, the next question is whether such behavior is also seen in the velocity profiles.

Figure 5.4 shows remnant stellar velocity profiles for the typical choice of scaling constants: the stellar half-mass radius and the central projected velocity dispersion. The 1σ variation near the half-mass radius is $\sim 20\%$.

Figure 5.5 shows the results of using the dynamical time at the half mass radius as the relevant timescale. Note that does *not* introduce a new galaxy-dependent quantity in

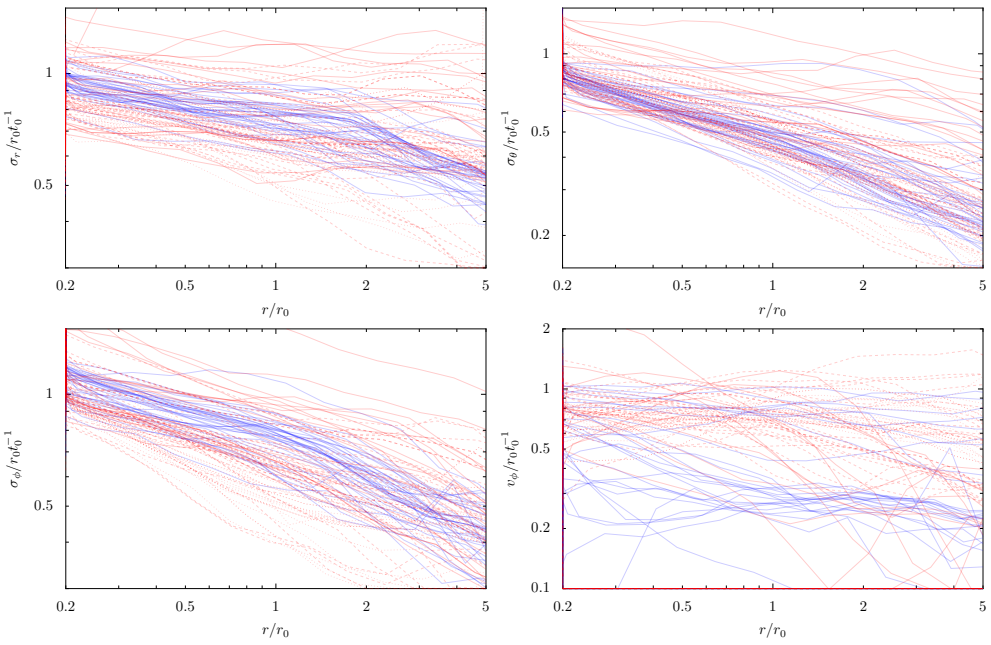

Figure 5.4: Non-dimensionalized stellar velocity profiles for G and Sbc series simulated merger remnants. The choice of scale radius and time here are the usual observationally motivated ones: r_0 is the is the stellar half-mass radius and t_0 is r_0/σ_p where σ_p is the projected velocity dispersion within an aperture of $r_e/8$. Top left: 3D radial velocity dispersion; top right: 3D velocity dispersion in the θ direction; bottom left projected velocity dispersion in the azimuthal direction; bottom right: mean streaming velocity in the azimuthal direction. This figure shows significant diversity in the velocity structure of simulated galaxy merger remnants.

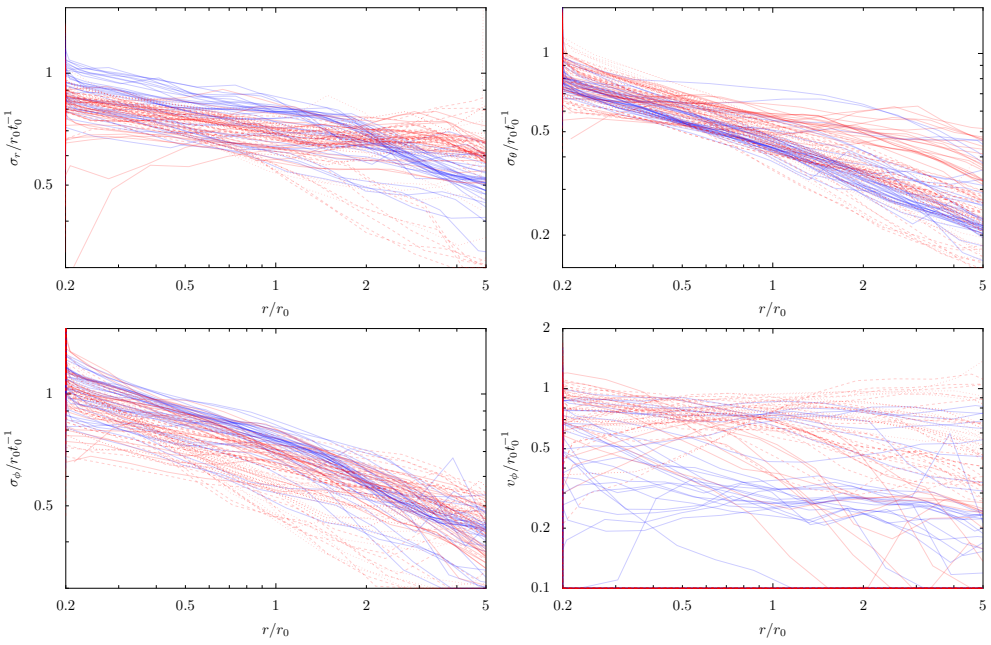

Figure 5.5: Same as Figure 5.4, except that the time scale is the dynamical time at the 3D stellar half-mass radius. This is the best choice for the timescale of the possibilities explored herein. The velocity profiles are significantly more similar than those shown in Figure 5.4, but the similarity is nowhere near as striking as that of the density profiles shown in Figure 5.2

.

addition to the radius and mass scales already defined. This choice simply uses the gravitational constant to turn the radius and mass scales into a timescale. This makes the velocity dispersion profiles of the various remnants significantly more similar, reducing the 1σ scatter to $\sim 10\%$. There remains significant variation in the rotation velocities of the remnants. The dynamical time at the half mass radius is the best choice of possibilities analysed here for the purpose of bringing the scaled stellar velocity profiles of merger remnants into agreement with one another.

However, the stellar/dark-matter equality radius r_{eq} has significant advantages over the stellar half-mass radius with respect to remnant density profiles. It would be advantages to avoid introducing a separate length scale for use with velocity profiles, so Figure 5.6 shows

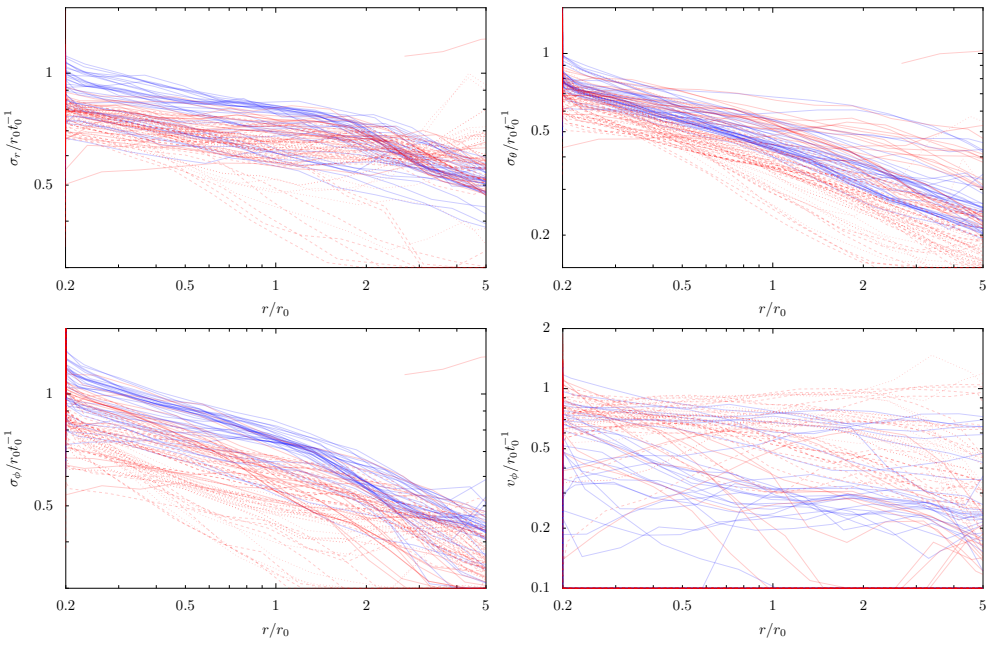

Figure 5.6: Same as Figure 5.4, except that the time scale is the dynamical time at the mass-equality radius r_{eq}. The velocity profiles shown here are significantly more similar than those in Figure 5.4, but not as similar as those shown in Figure 5.5. This set of velocity profiles is presented because this choice of timescale is only slightly worse than the dynamical time at the stellar half-mass radius (shown in Figure 5.5), and making this choice has the advantage that it no additional measurements must be made for each galaxy if one has already decided to use r_{eq} because if its dramatic advantage with regard to mass density profiles.

stellar velocity profiles when scaled by the dynamical time at r_{eq}. The results are only slightly worse than the velocity profiles shown in Figure 5.5.

Figure 5.7 shows dark matter velocity profiles for the three choices of radius and timescales under discussion. This is of marginal observational utility since the dark matter velocity dispersion as a function of radius is nearly impossible to observe, but is interesting from a theoretical perspective. This figure shows that using the dynamical times at either the stellar half-mass or mass-equality radius results in a significant reduction in the variation in velocity profiles of the dark matter halos. The velocity profile using the dynamical time at r_{eq} shows as little as 5% variation among *Sbc*or G series simulations, although there is an offset

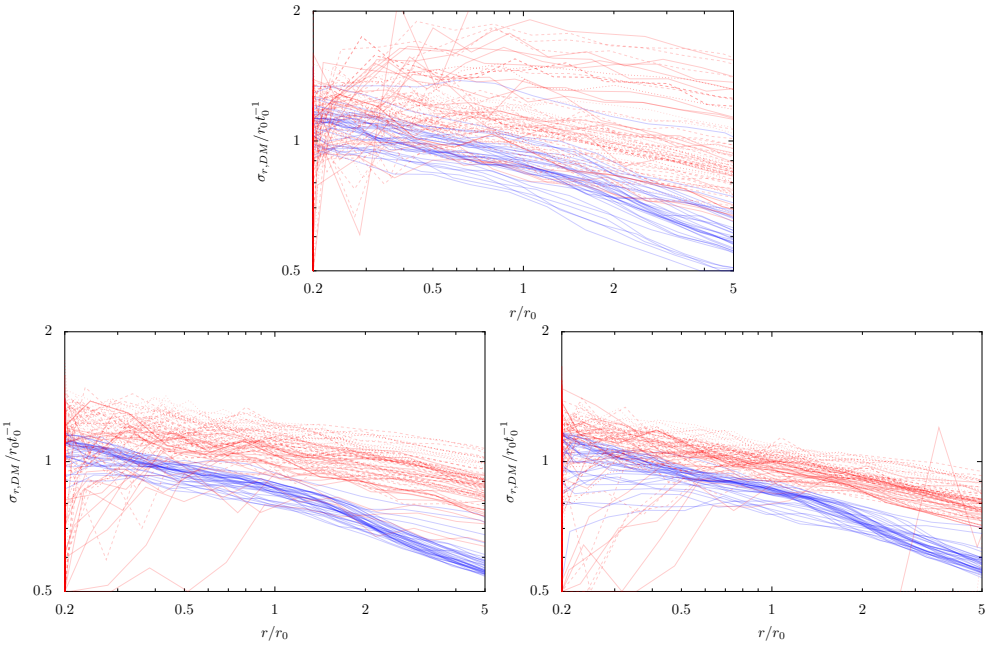

Figure 5.7: Dark matter velocity profiles for three choices of length and time scales. Top: r_0 is the stellar half mass radius and t_0 is r_0/σ_p; bottom left: r_0 is the same and t_0 is the dynamical time at the stellar half mass radius; bottom right: $r_0 = r_{eq}$ and t_0 is the dynamical time at r_{eq}. The lower panels are a significant improvement over the top panel, and the lower right panel is somewhat improved over the lower left panel. We only show the radial dark matter dispersion profiles because the dark matter anisotropy is small and nearly independent of radius.

between the two sets of simulations.

Analyzing anisotropy profiles is a convenient way to put a limit on the extent to which the velocity structure of the simulated remnants can be brought into a common system. This is because the anisotropy is unitless, hence the only choice to be made is the length scaling constant.

The anisotropy β is usually defined for a spherically symmetric object. In that case, $\sigma_\theta = \sigma_\phi$ and $v_r = v_\theta = v_\phi = 0$ so

$$\beta_\theta = 1 - \sigma_\theta^2/\sigma_r^2 = \beta_\phi = 1 - \sigma_\phi^2/\sigma_r^2 \tag{5.24}$$

The merger remnants presented here are not spherically symmetric so Figure 5.8 shows both

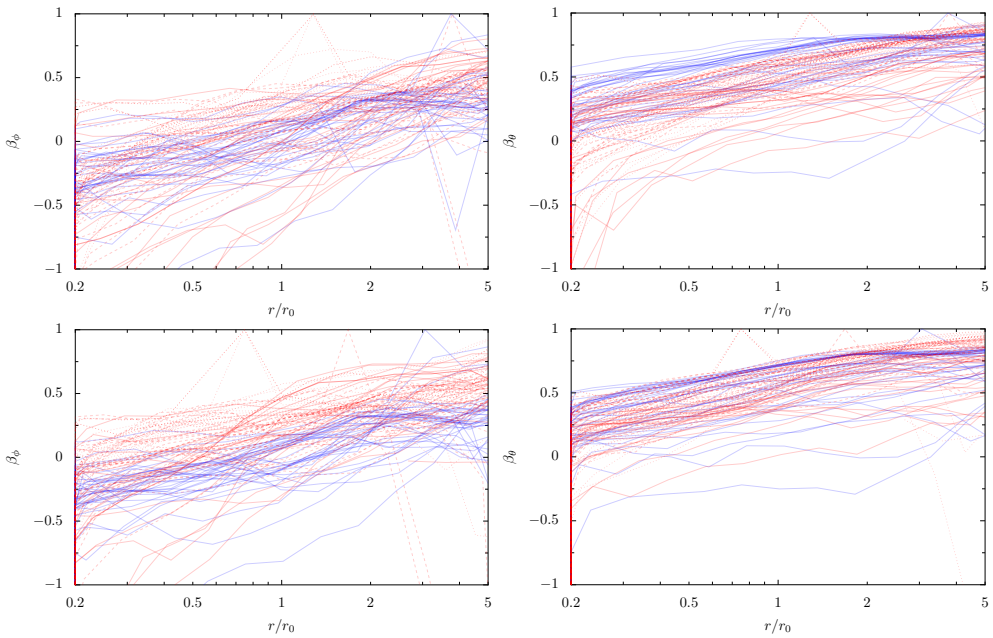

Figure 5.8: Stellar Anisotropy profiles for two choices of scale radius. In the top two panels, r_0 is the stellar half-mass radius. In the bottom two panels, r_0 is the stellar-dark mass equality radius r_{eq}. The left two panels show the azimuthal anisotropy and the right two panels show the anisotropy associated with the polar angle. This plot shows part of the reason why there is diversity in the velocity profiles of galaxy remnants in spite of the striking regularity in the density profiles. The Virial Theorem constrains the total kinetic energy of the system, but does not determine the *direction* of the velocities of the stars. Therefore it is impossible to choose scaling constants so that, for example, the σ_r profile looks the same for all remnants.

β_θ and β_ϕ.

Virtually all of the remnants show stellar anisotropy profiles that rise with radius, in some cases to values near 1 (completely radial velocity dispersion). This is easily understood in terms of the dynamical origin of the stars at large radius (Dekel et al., 2005). Stars that end up at large radius are stars that were flung out from near the center be gravitational slingshot in interaction with the merging nuclei. They have low angular momentum because they started out within $\sim 1r_e$, so the orbits of those stars must pass close to the center of the remnant. The large aspect ratio of the orbits of these stars manifests itself as highly radial anisotropy.

In spite of the similar slopes of the anisotropy profiles, there is significant variation in the zero-point. The slopes of the anisotropy profiles are similar from galaxy to galaxy, but they are shallow. Changing the scale radius slides the curves horizontally, so any scale radius that would bring all the curves into agreement would be forced to vary dramatically from galaxy to galaxy. The lower two panels of the figure show that going from the stellar half-mass radius to the mass-equality radius makes hardly any difference.

We have seen that the density profiles of simulated remnants are remarkably consistent, but the velocity profiles show significant variation. Figure 5.8 suggests that the reason for the variation in the velocity profiles is the direction of the velocities of the stars. That is, there is a common *kinetic energy* profile, but the velocity profiles are different because some remnants are radially anisotropic, some are tangentially anisotropic, and some are rotating.

The specific kinetic energy is:

$$E_k/m = \frac{1}{2}(v_\phi^2 + \sigma_r^2 + \sigma_\theta^2 + \sigma_\phi^2) \tag{5.25}$$

where we have assumed Gaussian velocity distributions and neglected v_r and v_θ because the remnants are in steady-state.

Figure 5.9 shows kinetic energy profiles using the stellar half-mass radius and central projected velocity dispersion as scale constants. A common kinetic energy profile is not apparent with this choice of scale constants.

Figures 5.10 and 5.11 show kinetic energy using effective radius and dynamical time at the effective radius, or the mass-equality radius and the dynamical time there, respectively. Now the common energy structure of the merger remnants comes dramatically into focus. In the case of the *Sbc*simulations there is as little as 3% 1σ variation in the *Sbc*series of simulations. There is again, an offset between the two sets of simulations but nevertheless the lack of variation between simulations of a given set is remarkable.

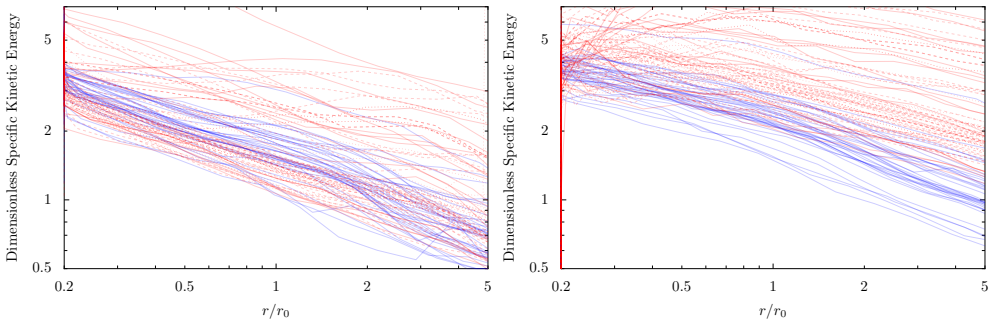

Figure 5.9: Specific kinetic energy profiles with scale constants r_0 equal to the stellar half mass radius and $t_0 = r_0/\sigma_p$. There appears to be great diversity in the kinetic energy profiles of galaxy remnants.

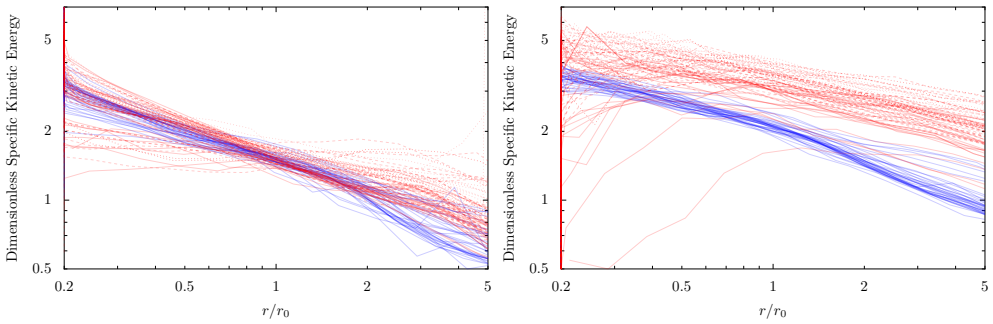

Figure 5.10: Specific kinetic energy profiles with r_0 being the stellar half-mass radius and t_0 being the dynamical time at that radius. Compared to Figure 5.9 there is very little diversity in the kinetic energy profiles of different remnants. This confirms the idea that the source of diversity in the dimensional velocity profiles is the diversity in the directions of the stellar velocities in the different remnants.

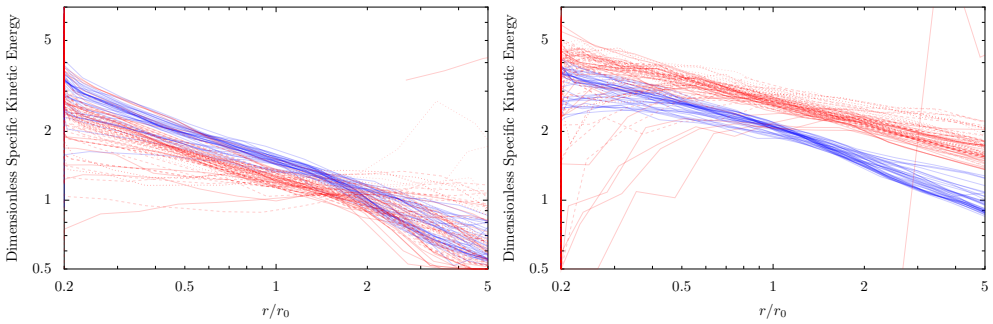

Figure 5.11: Same as Figure 5.10, but the scale radius is r_{eq} and the scale time is the dynamical time at r_{eq}. These kinetic energy profiles also show extremely consistent behavior given the great diversity of the origins of the remnants.

5.4 Conclusions

In this chapter I developed precise definitions of the various informal concepts of homology that seem to be in common use. I explored the precise meaning of the definitions in terms of the distribution functions that describe galaxies.

I have shown that simulated gas-rich binary galaxy merger remnants show remarkably regular structure when the correct scale constants are used to plot non-dimensional density and kinetic energy profiles. The direction of the motion of stars is essentially the sole source of the variation in the kinematic structure of these simulated merger remnants.

The scaling constants that result in the least variation among this population of merger remnants are r_{eq}, m_{eq}, and τ_{eq}, where r_{eq} is the the radius at which the enclosed dark and luminous matter are equal, m_{eq} is the mass within r_{eq}, and τ_{eq} is the dynamical time at r_{eq}.

Dark halo concentration, and progenitor gas fraction contribute to a systematic difference between the *Sbc* and *G* series simulations, but within each set of simulations the structure is remarkably consistent.

The fact that r_{eq} plays such a prominent role in these scaling constants immediately recalls the disk-halo conspiracy arising from the study of spiral galaxy rotation curves (Bahcall & Casertano, 1985; Burstein & Rubin, 1985; Kent, 1987). Blumenthal et al. (1986) argued that such a conspiracy will arise naturally if the dissipational collapse of baryons is limited by their initial angular momentum and if the baryon fraction is roughly equal to the spin parameter $\lambda = JE^{1/2}G^{-1}M^{-5/2}$. This result appears to be another manifestation of this phenomenon.

5.4.1 Future Work

Issues that should be addressed in immediate future work in order to publish this chapter include:

- *Why* do simulated merger remnants look so similar when scaled by r_{eq}, m_{eq}, and τ_{eq}? Is this related to the Blumenthal et al. (1986) result that provided an explanation for the featureless rotation curves of spiral galaxies? A few additional simulations of galaxy mergers with different merger orbits should resolve this question.

- Why are the *G*-series and *Sbc*-series simulations different from each other, but so similar within each series? The two most obvious possible explanations are the difference in gas fractions and the difference in dark halo concentrations. A few additional binary merger simulations with different progenitors should answer this question.

- This chapter analyzes only binary merger remnants. Do multiple merger remnants have the same dimensionless density and kinetic energy profiles as binary mergers?

- It would be useful to develop a set of rules that

- It would be informative to analyze the remnants in terms of the Jeans equations in order to see exactly which terms of the equations are important.

Chapter 6

Implications of the Mass Plane for Galaxy Structure

I compare a large suite of numerical simulations to gravitational lensing data from Bolton et al. (2007). This has the virtue that essentially no ad-hoc assumptions are needed to directly compare simulated galaxies to the observed ones. I find that for velocity dispersions below 200 km/s, simulated binary merger remnants and observed galaxies are compatible. When the velocity dispersion reaches 250 km/s, simulated binary merger remnants are systematically less concentrated than observed galaxies. Merger remnants produced by simulations starting from cosmological initial conditions have velocity dispersions 250 to 350 km/s, and they have enough mass enclosed within the Einstein radius to bring them into agreement with observations. Galaxies with velocity dispersions of 250 km/s or above do not seem to have been produced by binary mergers of gas-rich spiral galaxies, but they may have been produced by more complicated merger histories and continued gas accretion that occur in simulations starting from cosmological initial conditions.

6.1 Introduction

The fundamental plane (FP) of elliptical galaxies (Djorgovski & Davis, 1987; Dressler et al., 1987) has long been of interest to astronomers, who have debated whether the so-called tilt of the plane arises due to a systematic change of the mass-to-light ratio (either stellar or dynamical) with galaxy mass, or due to structural non-homology of galaxies with mass. Recently Bolton et al. (2007) (henceforth B07) obtained mass surface density estimates of elliptical galaxies from gravitational lenses that allowed the construction of a separate plane in terms of mass surface density rather than luminosity surface density. This indicates that the tilt in the FP is solely as mass-to-light effect. These observations are unfortunately mute on the question of whether the changing mass-to-light ratio is attributable to systematic changes in the stellar populations of galaxies or to systematic changes in the dark matter fractions. As we saw in Chapter 5, the first possibility would mean that galaxies are homologous, while the second possibility would mean that galaxies are not homologous.

The result from B07 agrees with Cappellari et al. (2007), who used integral-field spectroscopy and Schwarzschild dynamical modeling of nearby elliptical galaxies to conclude that the dynamical mass of galaxies is given accurately by the so-called virial mass estimator, $M \propto R_e\sigma^2/G$ where M is the mass of the galaxy, R_e is the half-light radius, σ is the velocity dispersion, and G is the gravitational constant. Cappellari et al. also analyzes the stellar populations of the SAURON galaxies and it seems that for at galaxies with large mass-to-light ratios, the stellar population mass-to-light ratio is nearly constant while the dynamical mass-to-light ratio changes significantly. This indicates that galaxies these have changing dark matter fractions and hence are not homologous.

When analyzing the remnants produced in hydrodynamic merger simulations, the most common course of action is to assume a constant stellar mass-to-light ratio. In that case

a tilted FP will only arise if galaxies are non-homologous, and studies of simulated gas-rich merger remnants indeed robustly predict tilted FPs (Dekel & Cox, 2006; Robertson et al., 2006).

A pleasant fact about gravitational lensing measurements is that the observationally accessible quantities are also the theoretically accessible quantities. I construct Bolton et al.'s mass plane from simulations and show that, in agreement with previous studies, hydrodynamic galaxy merger simulations show non-homology that reproduces the FP given constant mass-to-light ratio. This implies that they disagree with Bolton et al.'s mass plane measurements.

6.2 Methods

The quantity well-constrained by B07's measurements is the projected mass contained within the Einstein radius of the lens. Thus from the raw lensing measurements one does not learn anything about homology because one is probing different radii depending on the redshifts of the lens and source as well as the properties of the lens. For example, if all galaxies are homologous and at the same redshift, then the Einstein radius in units of the half-light radius will be smaller if the mean surface mass density of the galaxy (M/R_e^2) is smaller.

In order to learn anything about homology it is necessary to measure length in units of a scale radius which is usually taken to be the projected half-light radius. B07 adopted an isothermal density profile in order find masses and velocity dispersions within a common aperture, $R_e/2$. Although the authors carefully point out that their conclusions are independent of the specific mass model, it is necessary to adopt *some* mass model in order to measure quantities at a common radius.

Therefore I consider two aspects of the relationship between the simulations and the data. First, I simply extract the observationally accessible quantities from the simulations and

plot them without regard for learning anything about homology. Second, I construct Bolton et al.'s mass plane from the simulated galaxies in order to learn about homology.

In order to find the Einstein radii associated with the simulations, I find the root of the equation:

$$\frac{4GM(<r)d_{LS}d_L}{c^2 d_S} - r^2 = 0 \tag{6.1}$$

where r is the projected radius, $M(<r)$ is the projected mass within projected radius r, and d_{LS}, d_L, d_S are angular diameter distances from the lens to source, observer to lens, and observer to source, respectively. I assume that $z_S = 2z_L$, where z_L and z_S are the redshifts of the lens and source, respectively. close to the "ideal" lensing geometry. The value of r that solves this question is the Einstein radius, $R_{\rm Ein}$.

6.3 Results

One of the great complications of comparisons between simulated galaxies and observed ones is that observers measure fluxes and linewidths of light processed by dust, while simulators measure masses and velocities from models that often do not account for dust. Gravitational lensing data make the situation much simpler because the observationally accessible quantities are also theoretically accessible.

Figures 6.1 and 6.2 show the basic observed quantities from B07 and the same quantities extracted from simulations. Each simulated galaxy actually describes a line through each of the plots since the Einstein radius and the mass enclosed within the Einstein radius both depend on the redshift of the lens and the redshift of the source. The velocity dispersion is the aperture dispersion within $R_e/2$, so it does not depend on the lensing geometry and hence the line for each simulation would be vertical if Figure 6.2.

The lenses in B07 have redshifts between 0.2 and 0.4, and most of them are close to

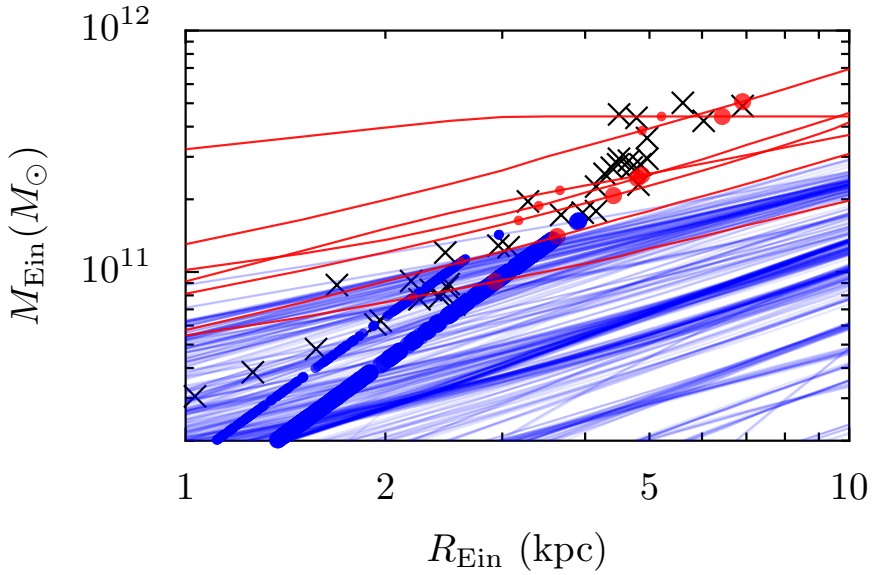

Figure 6.1: Einstein radius versus mass enclosed within the Einstein Radius. Black Xs are data from B07. Each line shows the mass profiles of one simulation. Blue lines indicate binary merger simulations and red lines indicate simulations with cosmological initial conditions. Given a lensing geometry, each simulation will produce a point somewhere along its line. The small (large) dots correspond to a particular lensing geometry for each simulation where $z_L = 0.2$ (0.4) and $z_S = 0.4$ (0.8). There is little information in this panel and it is primarily reflects redshift distribution of lenses.

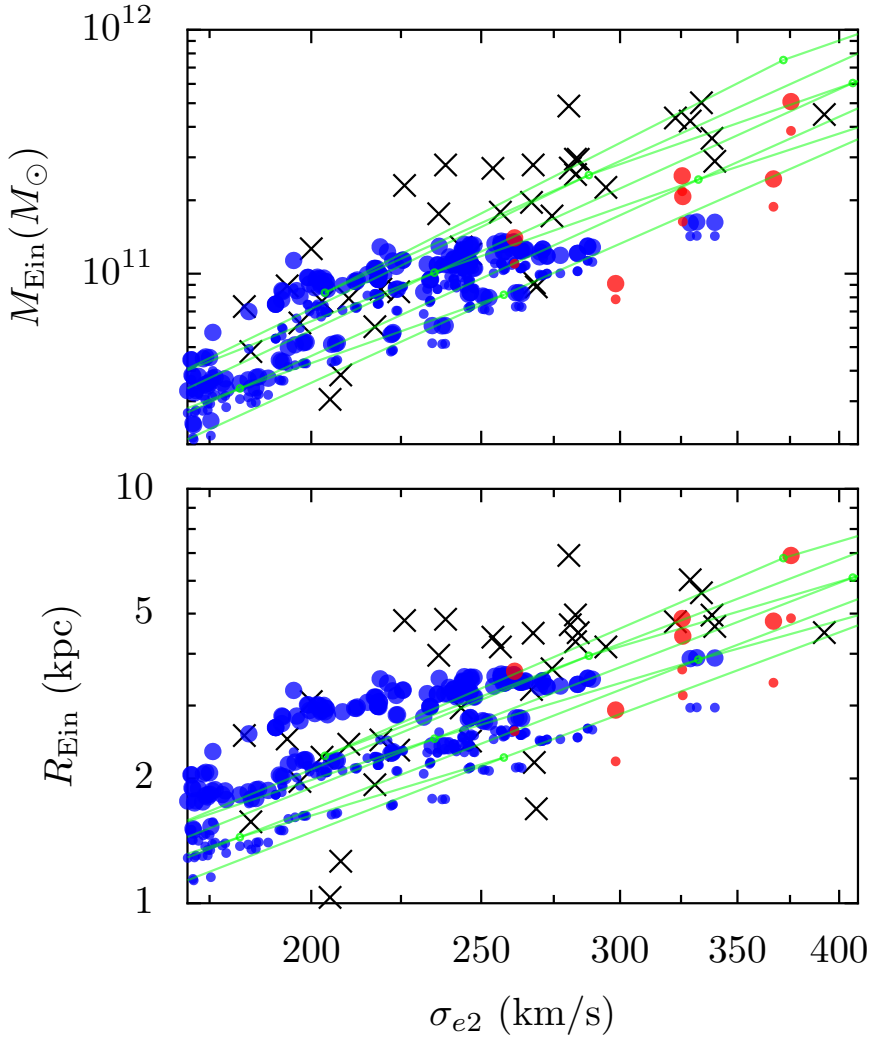

Figure 6.2: Gravitational lensing observables versus velocity dispersion. Top: Mass enclosed within the Einstein radius versus the velocity dispersion within $r_{eff}/2$. Again, black Xs are observed galaxies, blue points are simulated binary galaxy mergers, and red points are simulated merger remnants from cosmological initial conditions. The green grid shows a set of homologous Hernquist + NFW models described in the text. Near 200 km/s, observations and simulated binary merger remnants occupy the same region of the plot. Near 250 km/s, the binary merger simulations have systematically less mass enclosed within the Einstein radius when compared to observations. The merger remnants from cosmological initial conditions, however, have both larger velocity dispersion and higher values of M_{ein} when compared to the binary merger remnants. The cosmological merger remnants are in tentative agreement with the lensing observations. Changing the redshift of the lens makes very little difference. Bottom: Mass enclosed within the Einstein radius versus the velocity dispersion within $r_{eff}/2$. The information conveyed in this panel is essentially the same as in the top panel, except that this panel is more sensitive to the redshift distribution of the lenses.

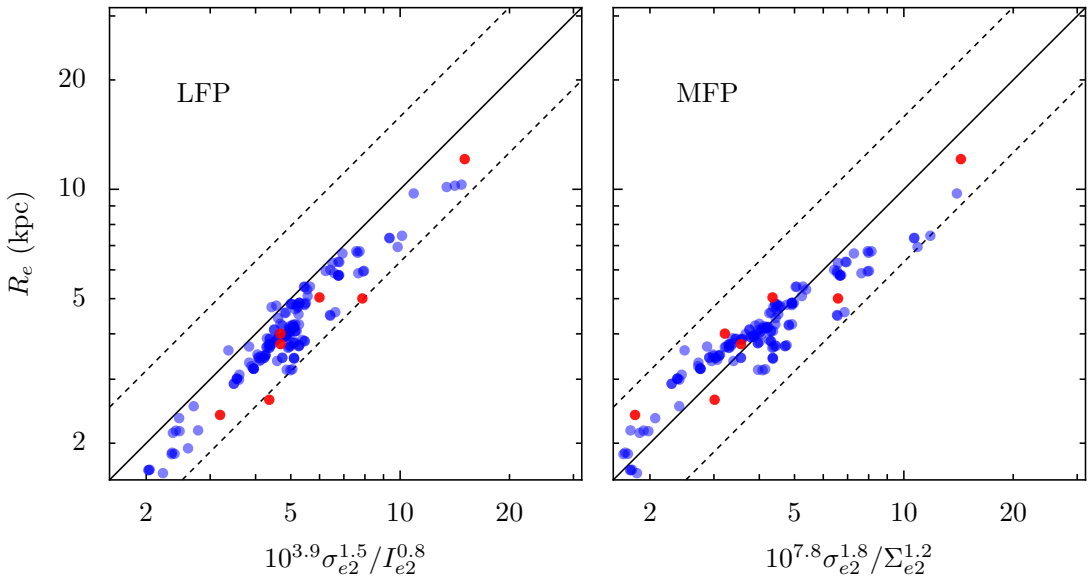

Figure 6.3: Left: The luminosity plane for simulated galaxies. A combination of velocity dispersion and surface brightness designed to give a virial estimate of effective radius versus measured effective radius. The exponents come from the fit in (B07). Blue points are simulated remnants assuming a constant stellar mass-to-light ratio. Blue points are simulated remnants from cosmological initial conditions with the same assumption of constant stellar mass-to-light ratio. The solid line is the 1:1 relation and the dotted lines show the approximate spread in the data points shown in B07. In agreement with previous studies, I find that the simulated galaxies closely resemble the observations, in particular reproducing the tilt of the FP. Since simulated galaxies reproduce the tilted FP with a constant stellar mass-to-light ratio, they are not homologous (recalling from Chapter 5 that a changing central dark-matter fraction implies non-homology). One is led to infer from this panel that simulated galaxies reproduce the observations, that real galaxies *are not* homologous, and that non-homology is the source of the tilt in the FP of real galaxies. Right: The mass plane of B07. As above, except that mass surface density replaces luminosity density for the observed galaxies. For simulated galaxies, our assumption of constant stellar mass-to-light ratio means that the only difference between the luminosity surface density and the mass surface-density is the fact that the mass surface-density includes the dark matter. Simulated galaxies are clearly *not* reproducing the mass plane, but they are not far off. The combination of exponents is again from B07 and is only $\sim 1.5\sigma$ away from that expected from the virial theorem. The axes of both panels are chosen to be exactly the same as the corresponding plots in B07.

the "ideal" lensing geometry where the lens is approximately halfway between the observer and the source. When placing simulated remnants at a particular redshift, I assume the standard cosmology ($\Omega_m = 0.3, \Omega_\Lambda = 0.7, h = 0.7$) and that $z_S = 2z_L$. This is not quite the ideal geometry when the effects of cosmology are included but it is not far off for these relatively low redshift lenses.

Figures 6.1 and 6.2 provide the most unadulterated comparison between simulations and observations, but one cannot draw conclusions about homology from it because quantities are not measured as at a consistent radius. Homology is here understood to mean that there is a universal distribution function F for all galaxies such that:

$$f(r, v) = M_0 F(r/R_0, v/V_0) \tag{6.2}$$

where f is the distribution function for a particular galaxy while R_0, V_0, and M_0 are scaling constants that are different for each galaxy. For a given galaxy, the scaling constants are related through the virial theorem so that it is only necessary to specify two of the three. Thus if a population of galaxies is homologous and one knows the universal distribution function, two numbers suffice to completely specify the galaxy. In practice these two numbers are often taken to be the effective radius and the velocity dispersion measured within some fixed fraction of the effective radius such as σ_{e2}, measured within $R_e/2$.

I include a grid of homologous model galaxies motivated by the structure of real galaxies. The models consist of a spherical, isotropic Hernquist model (Hernquist, 1990) representing the baryons and a spherical, isotropic NFW profile (Navarro et al., 1996) representing the dark matter. The fundamental parameters are the virial radius and mass, R_{vir} and M_{vir}. For the halo I assume that $r_s = R_{vir}/10$ and set central density so that the total mass (dark matter and baryons) within R_{vir} is M_{vir}. For the Hernquist profile, I assume that the total mass is $0.1M_{vir}$ and that the 3D half mass radius is $R_{vir}/50$. There is no adiabatic contraction.

I numerically integrate the Jeans equation to find the radial velocity dispersion, the projected velocity dispersion, and the aperture velocity dispersion, all as a function of radius.

Figure 6.2 shows a grid of these models for $M_{vir} = 1, 3, 10, 30, 100 \times 10^{11} M_{\odot}$ and $R_{vir} = 25, 50, 100, 200, 400, 800$ kpc. The grid of models is nearly, but not quite, degenerate in the parameters R_{vir} and M_{vir}. This confirms that raw gravitational lensing data does indeed probe the mass profile at different points and thus does not by itself permit conclusions regarding homology. It is worth noting that both the Hernquist component and the NFW component are necessary to come reasonably close to the data because the NFW component by itself does not have a high enough central mass density, while the Hernquist component by itself does not have enough total mass to give reasonable agreement with the data and simulations.

The tilt of the FP is the deviation of the exponents relating the scaling variables of a galaxy from the virial expectation. From the virial theorem, one expects that $R_e \propto \sigma^2/\Sigma$, but the observed FP is closer to $R_e \propto \sigma^{1.5}/I^{0.75}$ (Bernardi et al., 2003). The difference between the exponents is the tilt in the FP

Figure 6.3 shows the traditional FP (based on luminosity) and the mass plane from B07. In the absence of observational data to construct the mass plane, Robertson et al. (2006), Dekel & Cox (2006) and others made the reasonable decision to assume a constant stellar mass-to-light ratio to see if simulated galaxies reproduced the observed tilt in the FP. The satisfying result at the time was that, indeed, simulated galaxies did reproduce the tilted plane without the need for a systematically varying mass-to-light ratio.

It is important to realize that although the simulations are not reproducing this aspect of the data, they are not dramatically wrong. It is interesting and important to identify where the simulations and data disagree wherever possible, but this result does *not* indicate

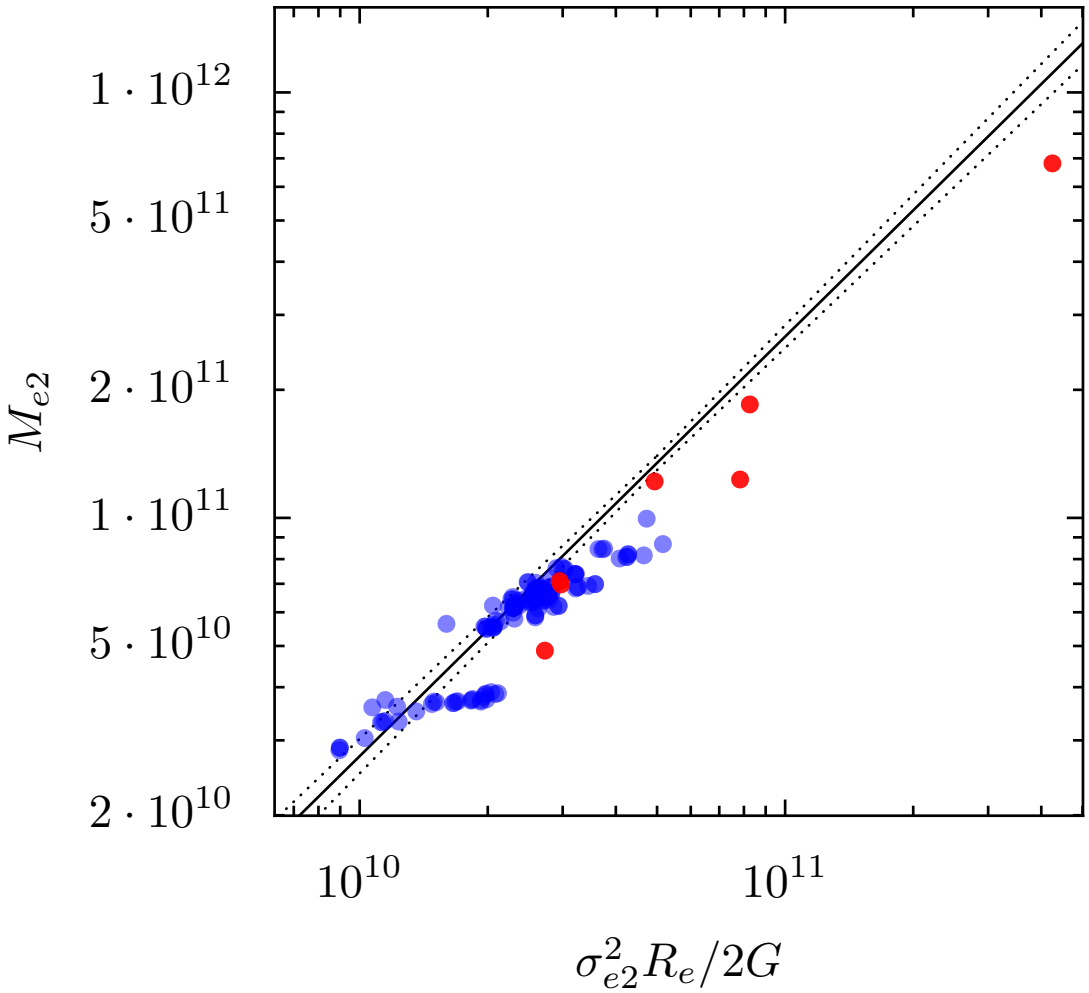

Figure 6.4: Virial mass versus observed mass within half of the effective radius. Blue dots are simulated binary merger remnants and red dots are simulated merger remnants from cosmological initial conditions. The solid line shows a fit to the data from B07 and the dotted lines show 1σ errors in the fit. Clearly the simulated galaxies have a slope different from observed galaxies and different from unity. Homologous galaxies must have a slope of unity in a plot like this because the mass within a fixed fraction of the half-mass radius must also be a fixed fraction of the total mass of the system. The axes of the plot are chosen to be exactly the same as the corresponding plot in B07.

that the simulations are completely incorrect. I have simply learned something unexpected and important about how real galaxies must have been put together.

Figure 6.4 is a second representation of the mass plane. Simulated galaxies clearly have a slope that is different from the observations. The slope of the observational fit is 1, indicating homology, while the simulated galaxies have a slope lower than 1.

6.4 Conclusions

I have compared a large suite of numerical simulations to gravitational lensing data from B07. This has the virtue that no ad-hoc assumptions are needed to directly compare simulated galaxies to the observed ones. I find that at a velocity dispersion of 200 km/s, simulated binary merger remnants and observed galaxies are compatible. When σ reaches 250 km/s, simulated binary merger remnants have systematically less mass enclosed within the Einstein radius compared to observations. However, simulated remnants starting from cosmological initial conditions tentatively agree with the observations for velocity dispersion between 250 and 350 km/s.

I also find, in agreement with previous studies, that simulated galaxies reproduce a tilted FP with the assumption of a constant stellar mass-to-light ratio.

6.4.1 Future Work

Issues that must be addressed in immediate future work in order to publish this chapter include:

- I need to think more carefully about what Bolton et al. actually found. Under what circumstances would they have found anything *other* than the virial mass plane? What role does the assumption of an isothermal ellipsoid play?

- This chapter does not make firm contact with Chapter 5 even though the Bolton et al. lensing data was the motivation for thinking about homology.

Chapter 7

Conclusions

In this thesis, I have explored how a galaxy's merger history influences its structure and kinematics. Using first binary merger remnants, then multiple merger remnants, and finally galaxies formed by taking initial conditions from a larger scale cosmological simulation, I have determined that gas-rich binary mergers nearly always form fast rotating remnants and that multiple mergers *can* form slow rotators. The simulations with cosmological initial conditions are all fast rotators at $z = 1$, and it remains to be seen if they lose their rotation by $z = 0$.

In Chapter 2, I characterized the three-dimensional shapes and density profiles of remnants produced by hydrodynamic simulations of binary galaxy mergers. Stellar remnants are nearly all oblate, with a few examples of triaxiality in the most gas-poor mergers. Dark matter halos are either prolate or triaxial, and the short axis of the baryons is perpendicular to the long axis of the dark matter. All of these facts can be understood in terms of the effects of angular momentum and dissipation during the merger.

Real galaxies in a ΛCDM universe are thought to have experienced many mergers

over the course of their history, and these multiple mergers can be expected to weaken the relationship between the shapes of galaxies and their halos described here. The extent to which the effects of large-scale structure, such as mass accretion along filaments, tend to preserve the relationship between galaxies and their halos is an open question.

The density profiles of remnants are quite regular in their structure. The slopes of the baryonic and total density profiles are confined to a small range near -2. The dark matter density profiles of the *Sbc* simulations are significantly different from the *G* series, attributable to the initial configuration of the halos of the progenitors.

In Chapter 3, I showed that the current sample of gas-rich hydrodynamic merger remnant simulations plausibly correspond to the SAURON fast-rotators by virtue of their large orbital angular momentum, in agreement with Cox et al. (2006a). However, there are very few galaxies in the sample with little rotation, and none at the upper end of the mass range. The origin of massive, non-rotating early-type galaxies remains mysterious.

Chapter 4 explored the properties of galaxies that result from multiple mergers. I have showed that if mass is built up via successive binary equal mass major mergers, then the remnant is also a fast-rotator. This is because the orbital angular momentum in the last encounter has a dominant effect on the kinematics of the remnant. Starting with the same progenitors and varying only the order in which galaxies merge, the opposite end of the spectrum of possibilities is to let the galaxies merge one after another, one at a time. This is a series of sequential mergers of decreasing mass ratio as the mass of the central galaxy is built up.

This sequential merger case robustly produces non-rotating remnants. The orbital angular momentum of the incoming galaxies averages to zero and the remnant is left with no net rotation. This is a plausible formation mechanism for the SAURON slow-rotators.

The second part of Chapter 4 was devoted to running a set of "realistic" simulations where the initial conditions were taken from a larger-scale, lower-resolution cosmological simulation. I found uniformly high rotation in these cosmological cases. The cosmological initial conditions have a variety of merger histories, so it would seem that the constant inflow of gas from the intergalactic medium is the decisive factor in making the remnants rotate.

I have not yet run the simulations down to low redshift to see if they stop rotating by the present day. It is possible that continued harassment and mergers will average away the significant rotation that the simulated remnants display at $z = 1$. If the rotation goes away by $z = 0$, then these simulated galaxies could still be identified as the SAURON slow rotators.

Even if these simulated galaxies are *not* identified as the source of the SAURON slow rotators, they were produced from reasonable cosmological initial conditions, and the simulation was done with a code that can be expected to reasonably represent the actual evolution of the system. Shouldn't these galaxies exist?

This constitutes a prediction that early-type galaxies at $z = 1$ should rotate. van der Marel & van Dokkum (2007) presents tantalizing evidence that this may indeed be the case. However, van der Wel & van der Marel (2008) indicates that this result may not be robust. Either way, the question will be decided observationally very soon.

In Chapter 5 I developed precise definitions of the various informal concepts of homology that seem to be in common use. I explored the precise meaning of the definitions in terms of the distribution functions that describe galaxies. I then showed that simulated gas-rich binary galaxy merger remnants show remarkably regular structure when the correct scale constants are used to plot non-dimensional density and kinetic energy profiles. The direction of the motion of stars is essentially the sole source of the variation in the kinematic structure of these simulated merger remnants.

The scaling constants that result in the least variation among this population of merger remnants are r_{eq}, m_{eq}, and τ_{eq}, where r_{eq} is the the radius at which the enclosed dark and luminous matter are equal, m_{eq} is the mass within r_{eq}, and τ_{eq} is the dynamical time at r_{eq}.

Dark halo concentration, and progenitor gas fraction contribute to a systematic difference between the *Sbc* and *G* series simulations, but within each set of simulations the structure is remarkably consistent.

In the last chapter, I compared a large suite of numerical simulations to gravitational lensing data from B07. This has the virtue that no ad-hoc assumptions are needed to directly compare simulated galaxies to the observed ones. I find that at a velocity dispersion of 200 km/s, simulated binary merger remnants and observed galaxies are compatible. When σ reaches 250 km/s, simulated binary merger remnants have systematically less mass enclosed within the Einstein radius compared to observations. However, simulated remnants starting from cosmological initial conditions tentatively agree with the observations for velocity dispersion between 250 and 350 km/s.

At the closing session of the workshop on galaxy mergers at the Space Telescope Science Center in 2006, Brad Witmore said "We're on the verge of understanding it all at once," Rather than understanding isolated pieces of the galaxy merger/galaxy formation puzzle in isolated contexts, it is becoming possible to put together a comprehensive understanding of how mergers, cosmological environment, and feedback from star formation and AGN influence galaxies.

Bibliography

Alam, S. M. K. & Ryden, B. S. 2002, *ApJ*, **570**, 610

Allgood, B., Flores, R. A., Primack, J. R., Kravtsov, A. V., Wechsler, R. H., Faltenbacher, A., & Bullock, J. S. 2006, *MNRAS*, **367**, 1781

Arp, H. 1966, *ApJS*, **14**, 1

Bacon, R., Copin, Y., Monnet, G., Miller, B. W., Allington-Smith, J. R., Bureau, M., Carollo, C. M., Davies, R. L., Emsellem, E., Kuntschner, H., Peletier, R. F., Verolme, E. K., & de Zeeuw, P. T. 2001, *MNRAS*, **326**, 23

Bahcall, J. N. & Casertano, S. 1985, *ApJ*, **293**, L7

Bender, R., Burstein, D., & Faber, S. M. 1992, *ApJ*, **399**, 462

Bender, R., Doebereiner, S., & Moellenhoff, C. 1988, *A&AS*, **74**, 385

Bender, R., Saglia, R. P., & Gerhard, O. E. 1994, *MNRAS*, **269**, 785

Bendo, G. J. & Barnes, J. E. 2000, *MNRAS*, **316**, 315

Bernardi, M., Sheth, R. K., Annis, J., Burles, S., Eisenstein, D. J., Finkbeiner, D. P., Hogg, D. W., Lupton, R. H., Schlegel, D. J., SubbaRao, M., Bahcall, N. A., Blakeslee, J. P.,

Brinkmann, J., Castander, F. J., Connolly, A. J., Csabai, I., Doi, M., Fukugita, M., Frieman, J., Heckman, T., Hennessy, G. S., Ivezić, Ž., Knapp, G. R., Lamb, D. Q., McKay, T., Munn, J. A., Nichol, R., Okamura, S., Schneider, D. P., Thakar, A. R., & York, D. G. 2003, *AJ*, **125**, 1866

Bett, P., Eke, V., Frenk, C. S., Jenkins, A., Helly, J., & Navarro, J. 2007, *MNRAS*, **376**, 215

Binney, J. & de Vaucouleurs, G. 1981, *MNRAS*, **194**, 679

Binney, J. & Tremaine, S. 1987, *Galactic dynamics*, Princeton, NJ, Princeton University Press, 1987, 747 p.

Birnboim, Y. & Dekel, A. 2003, *MNRAS*, **345**, 349

Blumenthal, G. R., Faber, S. M., Flores, R., & Primack, J. R. 1986, *ApJ*, **301**, 27

Bolton, A. S., Burles, S., Koopmans, L. V. E., Treu, T., Gavazzi, R., Moustakas, L. A., Wayth, R., & Schlegel, D. J. 2008, *ApJ*, **682**, 964

Bolton, A. S., Burles, S., Treu, T., Koopmans, L. V. E., & Moustakas, L. A. 2007, *ApJ*, **665**, L105

Borne, K. D., Bushouse, H., Lucas, R. A., & Colina, L. 2000, *ApJ*, **529**, L77

Bournaud, F. & Combes, F. 2002, *A&A*, **392**, 83

Bournaud, F., Jog, C. J., & Combes, F. 2005, *A&A*, **437**, 69

Bournaud, F., Jog, C. J., & Combes, F. 2007, *A&A*, **476**, 1179

Boylan-Kolchin, M., Ma, C.-P., & Quataert, E. 2005, *MNRAS*, **362**, 184

Boylan-Kolchin, M., Ma, C.-P., & Quataert, E. 2006, *MNRAS*, **369**, 1081

Brainerd, T. G. 2005, *ApJ*, **628**, L101

Brandt, A. 1977, *Mathematics of Computation*, **31**, 333

Brooks, A. 2008, *The Role of Cold Gas Accretion in the Early Growth of Galaxies*, Santa Cruz Galaxy Formation Workshop

Burkert, A. & Naab, T. 2005, *MNRAS*, **363**, 597

Burkert, A., Naab, T., & Johansson, P. H. 2007, *astro-ph/0710.0663*, 710

Burstein, D. & Rubin, V. C. 1985, *ApJ*, **297**, 423

Cappellari, M., Bacon, R., Bureau, M., Damen, M. C., Davies, R. L., de Zeeuw, P. T., Emsellem, E., Falcón-Barroso, J., Krajnović, D., Kuntschner, H., McDermid, R. M., Peletier, R. F., Sarzi, M., van den Bosch, R. C. E., & van de Ven, G. 2006, *MNRAS*, **366**, 1126

Cappellari, M. & Emsellem, E. 2004, *PASP*, **116**, 138

Cappellari, M., Emsellem, E., Bacon, R., Bureau, M., Davies, R. L., de Zeeuw, P. T., Falcón-Barroso, J., Krajnović, D., Kuntschner, H., McDermid, R. M., Peletier, R. F., Sarzi, M., van den Bosch, R. C. E., & van de Ven, G. 2007, *MNRAS*, **379**, 418

Cappellari, M. & McDermid, R. M. 2005, *Classical and Quantum Gravity*, **22**, 347

Cole, S., Aragon-Salamanca, A., Frenk, C. S., Navarro, J. F., & Zepf, S. E. 1994, *MNRAS*, **271**, 781

Cole, S., Lacey, C. G., Baugh, C. M., & Frenk, C. S. 2000, *MNRAS*, **319**, 168

Contopoulos, G. 1956, *Zeitschrift fur Astrophysik*, **39**, 126

Cox, T. J. 2004, *Ph.D. thesis*, University of California, Santa Cruz

Cox, T. J., Dutta, S. N., Di Matteo, T., Hernquist, L., Hopkins, P. F., Robertson, B., & Springel, V. 2006a, *ApJ*, **650**, 791

Cox, T. J., Jonsson, P., Primack, J. R., & Somerville, R. S. 2006b, *MNRAS*, **373**, 1013

Cox, T. J., Jonsson, P., Somerville, R. S., Primack, J. R., & Dekel, A. 2008, *MNRAS*, **384**, 386

Croton, D. J., Springel, V., White, S. D. M., De Lucia, G., Frenk, C. S., Gao, L., Jenkins, A., Kauffmann, G., Navarro, J. F., & Yoshida, N. 2006, *MNRAS*, **365**, 11

Davies, R. L., Efstathiou, G., Fall, S. M., Illingworth, G., & Schechter, P. L. 1983, *ApJ*, **266**, 41

Davis, M., Efstathiou, G., Frenk, C. S., & White, S. D. M. 1985, *ApJ*, **292**, 371

de Zeeuw, P. T., Bureau, M., Emsellem, E., Bacon, R., Carollo, C. M., Copin, Y., Davies, R. L., Kuntschner, H., Miller, B. W., Monnet, G., Peletier, R. F., & Verolme, E. K. 2002, *MNRAS*, **329**, 513

Dekel, A. 2008, *Formation of Galaxies at High Redshift With Cold Flows*, Santa Cruz Galaxy Formation Workshop

Dekel, A. & Birnboim, Y. 2006, *MNRAS*, **368**, 2

Dekel, A. & Cox, T. J. 2006, *MNRAS*, **370**, 1445

Dekel, A., Stoehr, F., Mamon, G. A., Cox, T. J., Novak, G. S., & Primack, J. R. 2005, *Nature*, **437**, 707

Diemand, J., Kuhlen, M., & Madau, P. 2006, *ApJ*, **649**, 1

Djorgovski, S. & Davis, M. 1987, *ApJ*, **313**, 59

Dressler, A., Lynden-Bell, D., Burstein, D., Davies, R. L., Faber, S. M., Terlevich, R., & Wegner, G. 1987, *ApJ*, **313**, 42

Dubinski, J. & Carlberg, R. G. 1991, *ApJ*, **378**, 496

Emsellem, E., Cappellari, M., Krajnović, D., van de Ven, G., Bacon, R., Bureau, M., Davies, R. L., de Zeeuw, P. T., Falcón-Barroso, J., Kuntschner, H., McDermid, R., Peletier, R. F., & Sarzi, M. 2007, *MNRAS*, **379**, 401

Emsellem, E., Cappellari, M., Peletier, R. F., McDermid, R. M., Bacon, R., Bureau, M., Copin, Y., Davies, R. L., Krajnović, D., Kuntschner, H., Miller, B. W., & de Zeeuw, P. T. 2004, *MNRAS*, **352**, 721

Franx, M., Illingworth, G., & de Zeeuw, T. 1991, *ApJ*, **383**, 112

Fukugita, M. & Peebles, P. J. E. 2004, *ApJ*, **616**, 643

Genzel, R., Tacconi, L. J., Eisenhauer, F., Förster Schreiber, N. M., Cimatti, A., Daddi, E., Bouché, N., Davies, R., Lehnert, M. D., Lutz, D., Nesvadba, N., Verma, A., Abuter, R., Shapiro, K., Sternberg, A., Renzini, A., Kong, X., Arimoto, N., & Mignoli, M. 2006, *Nature*, **442**, 786

Gerhard, O. E. 1993, *MNRAS*, **265**, 213

González-García, A. C. & Balcells, M. 2005, *MNRAS*, **357**, 753

González-García, A. C., Balcells, M., & Olshevsky, V. S. 2006, *MNRAS*, **372**, L78

González-García, A. C. & van Albada, T. S. 2003, *MNRAS*, **342**, L36

Governato, F., Willman, B., Mayer, L., Brooks, A., Stinson, G., Valenzuela, O., Wadsley, J., & Quinn, T. 2007, *MNRAS*, **374**, 1479

Hernquist, L. 1990, *ApJ*, **356**, 359

Hernquist, L., Spergel, D. N., & Heyl, J. S. 1993, *ApJ*, **416**, 415

Hoekstra, H., Yee, H. K. C., & Gladders, M. D. 2004, *ApJ*, **606**, 67

Hopkins, P. F., Cox, T. J., & Hernquist, L. 2008a, *astro-ph/0806.3974*, 806

Hopkins, P. F., Hernquist, L., Cox, T. J., Dutta, S. N., & Rothberg, B. 2008b, *ApJ*, **679**, 156

Jesseit, R., Naab, T., Peletier, R. F., & Burkert, A. 2007, *MNRAS*, **376**, 997

Jing, Y. P. & Suto, Y. 2002, *ApJ*, **574**, 538

Katz, N., Weinberg, D. H., & Hernquist, L. 1996, *ApJS*, **105**, 19

Kennicutt, R. C. 1998, *ApJ*, **498**, 541

Kent, S. M. 1987, *AJ*, **93**, 816

Keres, D. 2008, *Galaxy Buildup by Gas Accretion*, Santa Cruz Galaxy Formation Workshop

Khochfar, S. & Burkert, A. 2006, *A&A*, **445**, 403

Kormendy, J. & Bender, R. 1996, *ApJ*, **464**, L119+

Krajnovic, D., Bacon, R., Cappellari, M., Davies, R. L., de Zeeuw, P. T., Emsellem, E., Falcon-Barroso, J., Kuntschner, H., McDermid, R. M., Peletier, R. F., Sarzi, M., van den Bosch, R. C. E., & van de Ven, G. 2008, *astro-ph/0807.1505*, 807

Krajnović, D., Cappellari, M., de Zeeuw, P. T., & Copin, Y. 2006, *MNRAS*, **366**, 787

Kravtsov, A. V., Klypin, A. A., & Khokhlov, A. M. 1997, *ApJS*, **111**, 73

Li, Y., Hernquist, L., Robertson, B., Cox, T. J., Hopkins, P. F., Springel, V., Gao, L., Di Matteo, T., Zentner, A. R., Jenkins, A., & Yoshida, N. 2007, *ApJ*, **665**, 187

Lynden-Bell, D. 1967, *MNRAS*, **136**, 101

Mandelbaum, R., Hirata, C. M., Ishak, M., Seljak, U., & Brinkmann, J. 2006a, *MNRAS*, **367**, 611

Mandelbaum, R., Seljak, U., Kauffmann, G., Hirata, C. M., & Brinkmann, J. 2006b, *MNRAS*, **368**, 715

Martig, M., Bournaud, F., & Teyssier, R. 2008, *astro-ph/0807.1693*, 807

Mihos, J. C. & Hernquist, L. 1996, *ApJ*, **464**, 641

Moore, B., Governato, F., Quinn, T., Stadel, J., & Lake, G. 1998, *ApJ*, **499**, L5+

Naab, T. 2008, *The Formation of Massive Star Forming Disks at High Redshift*, Santa Cruz Galaxy Formation Workshop

Naab, T. & Burkert, A. 2001, *ApJ*, **555**, L91

Naab, T. & Burkert, A. 2003, *ApJ*, **597**, 893

Naab, T., Jesseit, R., & Burkert, A. 2006a, *MNRAS*, **372**, 839

Naab, T., Johansson, P. H., Ostriker, J. P., & Efstathiou, G. 2007, *ApJ*, **658**, 710

Naab, T., Khochfar, S., & Burkert, A. 2006b, *ApJ*, **636**, L81

Naab, T. & Trujillo, I. 2006, *MNRAS*, **369**, 625

Navarro, J. F., Frenk, C. S., & White, S. D. M. 1996, *ApJ*, **462**, 563

Navarro, J. F. & White, S. D. M. 1993, *MNRAS*, **265**, 271

Noeske, K. G., Weiner, B. J., Faber, S. M., Papovich, C., Koo, D. C., Somerville, R. S., Bundy, K., Conselice, C. J., Newman, J. A., Schiminovich, D., Le Floc'h, E., Coil, A. L., Rieke,

G. H., Lotz, J. M., Primack, J. R., Barmby, P., Cooper, M. C., Davis, M., Ellis, R. S., Fazio, G. G., Guhathakurta, P., Huang, J., Kassin, S. A., Martin, D. C., Phillips, A. C., Rich, R. M., Small, T. A., Willmer, C. N. A., & Wilson, G. 2007, *ApJ*, **660**, L43

Parker, L. C., Hoekstra, H., Hudson, M. J., van Waerbeke, L., & Mellier, Y. 2007, *ApJ*, **669**, 21

Price, D. J. 2007, *Publications of the Astronomical Society of Australia*, **24**, 159

Puech, M., Hammer, F., Flores, H., Östlin, G., & Marquart, T. 2006, *A&A*, **455**, 119

Robertson, B., Cox, T. J., Hernquist, L., Franx, M., Hopkins, P. F., Martini, P., & Springel, V. 2006, *ApJ*, **641**, 21

Robertson, B. E. & Kravtsov, A. V. 2008, *ApJ*, **680**, 1083

Romanowsky, A. J., Douglas, N. G., Arnaboldi, M., Kuijken, K., Merrifield, M. R., Napolitano, N. R., Capaccioli, M., & Freeman, K. C. 2003, *Science*, **301**, 1696

Rubin, V. C., Graham, J. A., & Kenney, J. D. P. 1992, *ApJ*, **394**, L9

Rudd, D. H. 2007, *Ph.D. thesis*, The University of Chicago

Sales, L. & Lambas, D. G. 2004, *MNRAS*, **348**, 1236

Schmidt, M. 1959, *ApJ*, **129**, 243

Schwarzschild, M. 1979, *ApJ*, **232**, 236

Shapiro, K. L., Genzel, R., Förster Schreiber, N. M., Tacconi, L. J., Bouché, N., Cresci, G., Davies, R., Eisenhauer, F., Johansson, P. H., Krajnović, D., Lutz, D., Naab, T., Arimoto, N., Arribas, S., Cimatti, A., Colina, L., Daddi, E., Daigle, O., Erb, D., Hernandez, O.,

Kong, X., Mignoli, M., Onodera, M., Renzini, A., Shapley, A., & Steidel, C. 2008, *ApJ*, **682**, 231

Shu, F. H. 1978, *ApJ*, **225**, 83

Somerville, R. S. & Primack, J. R. 1999, *MNRAS*, **310**, 1087

Springel, V. 2000, *MNRAS*, **312**, 859

Springel, V. 2005, *MNRAS*, **364**, 1105

Springel, V. & Hernquist, L. 2002, *MNRAS*, **333**, 649

Springel, V., Yoshida, N., & White, S. D. M. 2001, *New Astronomy*, **6**, 79

Toomre, A. 1977, in B. M. Tinsley & R. B. Larson (eds.), *Evolution of Galaxies and Stellar Populations*, p. 401

Toomre, A. & Toomre, J. 1972, *ApJ*, **178**, 623

van Albada, T. S. 1982, *MNRAS*, **201**, 939

van der Marel, R. P. & Franx, M. 1993, *ApJ*, **407**, 525

van der Marel, R. P. & van Dokkum, P. G. 2007, *ApJ*, **668**, 738

van der Wel, A. & van der Marel, R. P. 2008, *astro-ph/0804.4228*, 804

van Dokkum, P. G., Franx, M., Kriek, M., Holden, B., Illingworth, G. D., Magee, D., Bouwens, R., Marchesini, D., Quadri, R., Rudnick, G., Taylor, E. N., & Toft, S. 2008, *ApJ*, **677**, L5

Vazdekis, A. 1999, *ApJ*, **513**, 224

Vincent, R. A. & Ryden, B. S. 2005, *ApJ*, **623**, 137

Weil, M. L. & Hernquist, L. 1996, *ApJ*, **460**, 101

Yang, X., van den Bosch, F. C., Mo, H. J., Mao, S., Kang, X., Weinmann, S. M., Guo, Y., & Jing, Y. P. 2006, *MNRAS*, **369**, 1293

York, D. G. et al. 2000, *AJ*, **120**, 1579